Radiation dose reduction in diagnostic neonatal x-ray imaging

by

Annemari Groenewald

Thesis presented in partial fulfilment of the requirements for the degree of
Master of Science in Medical Science (Medical Physics)
of the Faculty of Health Sciences
at
Stellenbosch University

Supervisor: Dr Willem Adolf Groenewald

March 2013

Declaration

I declare that the entirety of this thesis, submitted electronically, is my own, original work, that I am the sole author of it (except where any other source is acknowledged), that reproduction and publication of it by Stellenbosch University will not infringe upon the rights of third parties and that I have not previously submitted this dissertation in its entirety or part of it with the aim of obtaining any qualification.

Date: March 2013

Abstract

Introduction

X-ray imaging is used to diagnose and follow up various conditions in neonates (i.e. pre-term babies and babies up to the age of 28 days). Chest anterior-posterior (AP) radiographs are used to check the condition of the lungs and heart. Acceptable images requiring lower doses of radiation can be produced digitally by using a computed radiography (CR) system. Radiation can induce cancer in the young child. Lower doses are therefore important since neonates are more sensitive to radiation and have a relatively longer life expectancy. To minimise the risk of inducing cancer in neonates, x-ray exposures must adhere to the principle of ALARA (i.e. as low as reasonably achievable). Reducing radiation doses during a radiographic examination of a neonatal chest often results in reduced image quality. Dose reduction while maintaining optimum image quality and the risk of inducing cancer must therefore be considered in conjunction with one another.

Aim

The aim of this study is to develop an anatomical and radiological simulation phantom of a real neonatal chest and, using the phantom, to derive methods of decreasing the radiation dose while maintaining acceptable quality of the clinical image at a reduced cancer induction risk.

Materials and methods

Following guidelines in literature on the subject, as well as principles of medical physics, a phantom simulating a real neonatal chest anatomically and radiologically was developed. Anatomical equivalence was based on a computed tomography (CT) scan of a neonatal cadaver. Radiological equivalence was obtained by

matching density, elemental composition, attenuation, scatter and absorption characteristics of real neonatal tissues to possible substitute materials. The phantom was used to derive x-ray imaging protocols to decreased radiation dose, as well as the risk of cancer induction, while maintaining acceptable quality of the image. To achieve this exposure technique factors, such as tube voltage and current, exposure time and filtration, were varied experimentally. Image quality was evaluated quantitatively in a physics image quality assessment phantom, by calculating signal-to-noise ratios and modulation transfer functions. Images were ranked according to measured doses, visual and quantitative image quality and cancer induction risks.

Results

The simulation phantom acceptably matched a real neonatal chest anatomical and radiologically. The radiation dose and image quality of various exposures were compared with the standard exposure for neonatal chest AP x-ray imaging. In eight different exposures the dose was decreased to below the standard. The largest dose reduction was approximately 63%. Seven of these images had an improved visual image quality compared with the standard. The greatest improvement being about 21%. In two of the eight options a cancer induction risk analysis showed that, despite reduced doses, the risk could be greater than the standard exposure risk.

Discussion and conclusion

In six different exposure options a decrease in the dose was achieved while maintaining, and even improving, image quality and lowering the cancer inducing risk. These exposure protocols were recommended to be used in the Diagnostic Radiology Division of Tygerberg Academic Hospital.

Opsomming

Inleiding

X-straalbeelding word gebruik om verskeie siektes te diagnoseer en op te volg. In die geval van neonate (i.e. vroeg-gebore babas en babas van geboorte tot ouderdom 28 dae) word anterior-posterior (AP) x-straalondersoeke van die borskas gedoen om die toestand van die longe en hart te evalueer. Bevredigende beeldkwaliteit wat laer dosisse x-strale nodig het, kan digitaal verkry word met behulp van 'n rekenaar-radiografiese (i.e. Computed Radiography (CR)) sisteem. By die jong kind kan blootstelling aan bestraling kanker veroorsaak. In die geval van neonatale blootstellings is dit belangrik, want neonate is meer sensitief vir bestraling en het relatief 'n langer lewensverwagting. Om die risiko vir kankerinduksie te minimaliseer moet daar aan die beginsel van ALARA ("as low as reasonably achievable") voldoen word. Dosisverlagings gaan gewoonlik gepaard met verlies van beeldkwaliteit. Die doelwit tydens die radiografiese ondersoek van 'n neonaat moet egter altyd verlaging van die bestralingsdosis met optimum beeldkwaliteit en verlaagde risiko van kankerinduksie in die neonaat wees.

Doelwit

Die doelwit van hierdie studie is om 'n gesimuleerde fantoom te ontwikkel wat 'n regte neonatale borskas anatomies en radiologies voorstel. Deur die fantoom te gebruik word metodes ontwikkel om bestralingsdosisse te verminder met die doel om die kankerinduksierisiko te verlaag, maar steeds aanvaarbare visuele beeldkwaliteit te behou.

Materiaal en metodes

Riglyne en aanbevelings uit literatuur oor die onderwerp en basiese mediese fisika beginsels is aangewend om ’n fantoom te maak wat ’n neonatale borskas anatomies en radiologies naboots. Anatomiese ekwivalensie is verkry deur ’n neonatale kadawer rekenaar-tomografies te skandeer. Radiologiese ekwivalensie is behaal deur digtheid, elementale komposisie, attenuasie, absorpsie en verstrooiing-karakteristieke van ‘n regte neonatale borskas te vergelyk met dié van moontlike vervangingsmateriale. Die fantoom is gebruik om x-straalbeeldprotokolle af te lei wat die bestralingsdosis en die kankerinduksierisiko verlaag terwyl die beeldkwaliteit behoue bly. Dit is bereik deur blootstellingsfaktore, soos x-straalbuisspanning en stroom, blootstellingstyd en filtrasie, eksperimenteel te varieer. Beeldkwaliteit is ook kwantitatief ge-evalueer in ’n fisikafantoom, deur sein-tot-geruisverhoudings en modulasie-oordragsfunksies te bereken. Die beelde is georden volgens gemete ingangsdosisse, visuele en kwantatiewe beeldkwaliteit en kankerinduksierisiko.

Resultaat

Die simulasiefantoom van die neonatale borskas was ’n aanvaarbare anatomiese en radiologiese voorstelling van ‘n ware neonatale borskas. Die bestralingsdosis en beeldkwaliteit van verskillende blootstellings is vergelyk met die standaard blootstelling wat gewoonlik op neonate tydens borskas AP blootstellings gebruik word. Agt verskillende blootstellings is afgelei met dosisse laer as die standaard. Die grootste afname was ongeveer 63%. Sewe van die blootstellings het ’n beter visuele beeldkwaliteit as die standaard gehad, waarvan die grootste verbetering ongeveer 21% was. In twee van die agt beelde het ’n analise van die kankerinduksierisiko getoon dat die risiko hoër as die standaard blootstelling kan wees, selfs al was die dosis laer.

Bespreking en gevolgtrekking

Ses verskillende blootstellings is bepaal wat die dosis en kankerinduksierisiko verlaag het, met behoud of verbetering van beeldkwaliteit. Hierdie blootstellingsprotokolle word aanbeveel vir gebruik in die Diagnostiese Radiologie-afdeling in Tygerberg Akademiese Hospitaal.

Dedication

This thesis is dedicated to Blue.

Acknowledgements

I am grateful to my supervisor, Dr Wilhelm Groenewald, for his guidance, valuable input and much appreciated support.

I thank the personnel of iThemba LABS for their assistance in designing and manufacturing the phantom, in particular Mr Evan de Kock, Mr Basil Martin, Mr Phillip Beukes and Me Melina Loubser.

I also thank the staff of the radiology and medical physics departments at Tygerberg Academic Hospital for their assistance and for allowing me to conduct the study in their departments. Special thanks to Me Lee Mintoor and Me Melanie Grobler.

Grateful acknowledgement is made to the following instances:
Netcare for the use of their dosimeter.
Equra Health for allowing me to do research and work on the thesis during office hours.

Table of contents

List of Figures

List of Tables

Chapter 1

Introduction

In the medical environment ionising radiation is applied, for instance, when x-ray images of parts of the human body are required in the diagnostic process. An x-ray image is a two-dimensional representation of the area under investigation. X-ray investigation of the chest and other parts of the neonate's body serves as an aid in the diagnostic process, treatment and follow-up of these tiny, vulnerable patients. X-ray studies of neonates play a vital role in the treatment of these babies. At the same time these procedures pose an increased risk of cancer induction since each x-ray delivers a dose of ionising radiation to the neonate, who is particularly sensitive to radiation. Since neonates under radiological investigation may receive large numbers of x-ray exposures, the total dose of radiation at this young age could be clinically significant, i.e. it can increase the risk of a malignancy developing in the young child or even in its later life. Clearly the risk should be minimised and kept as low as reasonably achievable, i.e. according to the ALARA principle. Since treatment of neonates is undertaken by Tygerberg Academic Hospital it is necessary to evaluate the doses of radiation delivered through x-ray imaging to these neonates and to derive methods to decrease these doses.

At Tygerberg Academic Hospital computed radiography (CR) x-ray imaging is applied as a non-invasive investigative tool which, however, exposes these small patients to radiation. These doses should be minimised, but dose reductions are generally associated with the loss of image quality. In this dissertation these concepts are investigated and protocols are derived with the aim of decreasing the delivered radiation dose per x-ray image, while maintaining acceptable clinical image quality. The risk of inducing cancer in the young child is also considered.

CR x-ray imaging is a form of digital imaging in which a photo-stimulable phosphor (PSP) plate, enclosed in an imaging cassette, is used. Exposing the plate to radiation creates a latent image on the plate by storing the absorbed radiation intensity at each location on the plate as excited electron energies. In the CR reader unit a red laser light stimulates the release of the trapped electron energy as emission of visible light. The visible light in turn is detected by a photo-multiplier tube (PMT) that creates an electronic signal proportional to the released visible light at each location. The result is a digital image that is viewed on a digital display monitor. After the read-out process and the registration of the image the plate is exposed to bright white light in the reader unit to erase any residual image data and is ready for re-use.

CR imaging is chemical free, compared with film-screen imaging. Digital processing is quicker and allows for post-image manipulation. CR imaging has a wider dynamic range, or region of exposure, in which image quality is acceptable, which means that retakes when using this technique are fewer.[1] The physical nature of CR imaging therefore implies that dose reductions may be possible although reducing the dose of radiation often leads to unacceptable image quality. Image quality is expressed in terms of contrast, (i.e. the difference in the grey scale display of adjoining regions in an image), spatial resolution, (i.e. the distinction between small and closely spaced objects in an image) and noise (i.e. a random constituent in an image that gives it a mottled appearance). The aim is to obtain an image with an acceptable image quality at a reduced dose of radiation.

According to Huda[2], depending on the area of interest where a radiation dose is measured, different terminology and units are used to describe the delivered doses of radiation. Radiation exposure is a measure of the amount of radiation that is delivered by an x-ray beam on a certain area. It does not take an absorbing medium into account. The associated absorbed radiation dose (in gray (Gy)) is a measure of the energy deposited per unit mass of the absorbing medium by the radiation exposure. It depends on the characteristics of the absorbing material, for example high atomic number materials absorb more radiation that low atomic number materials. The biological harm caused by the absorbed radiation dose is expressed in terms of the equivalent dose (in sievert (Sv)). Here the type of radiation used to

make the exposure is taken into account. The stochastic, i.e. cancer induction and hereditary risk from a dose of radiation, is indicated by the effective dose (in Sv). It accounts for the radiosensitivity of the organs exposed to the radiation. Effective doses can be estimated from exposures by taking certain dose-influencing factors into account. These factors include patient size, the exposed organs and area and the energy of the radiation beam used.[2]

Any x-ray examination, regardless of the age group it is performed on, delivers a radiation dose. This thesis focuses on the neonatal age group and attention is given only to anterior-posterior (AP) chest x-ray imaging of these babies. Prematurely born and new-born babies up to the age of 28 days are referred to as neonates. Neonates are often born with respiratory and cardiac problems and their treatment and monitoring call for regular x-ray radiographs to be taken. Although each of these radiographs delivers only a small dose of radiation to the neonate, the large number of radiographs that are taken results in a larger total delivered dose. The number of radiographs depends on the gestational age, birth weight, clinical conditions at birth and length of time that the baby stays in hospital.

Neonates are more radiosensitive than adults due to rapid cell division and growth and a longer life expectancy. Because they are small in physical size their radiosensitive organs are closer to or in the primary x-ray beam. Makri et al[3] state that x-ray exposures may increase the risk of a cancer, especially leukaemia, developing in the young child.[3] The magnitude of the risk depends on the age at which a neonate is exposed to radiation. As premature babies are included in this category, radiation protection and shielding is therefore a special concern. Consequently, it is important to ensure that exposures are justified and that the delivered dose per radiograph is as low as reasonably achievable, adhering to the principle of ALARA, which should be implemented and upheld in any radiology department.[2] The benefit of x-ray investigations on neonates far outweigh the associated risks, provided that each exposure is justified and in accordance with the ALARA principle. The goal should therefore be clinically acceptable, rather than best or maximal, image quality.

In the case of the neonate during its stay in hospital every effort should be made to minimise the delivered dose of x-ray radiation. It is equally important that dose reduction does not compromise the image quality to such an extent that the image is clinically useless, resulting in retakes which add to the total delivered radiation dose, and in such a way missing the initial goal.

Which x-ray exposure parameters to use with a CR imaging system in the effort to decrease the radiation dose according to the ALARA principle while maintaining clinical image quality must be established. The advantage of reducing radiation to minimise the risk of inducing childhood cancer must also be considered.

Dose reduction, by changing x-ray beam parameters such as tube kilovoltage (kV), current-time product (mAs), exposed field size, distance from x-ray source to the detector and beam filtration, is described in literature, and discussed in section 2.2.[4,11,15,21,25,28] Reference is also made to dose reduction with added extra lead equivalent shielding. Equations and programs for calculating organ doses and relating it to cancer induction risk increases are also discussed. In much of the literature consulted reference is made to film-screen systems. Although these concepts are also applicable to CR systems, the physics of CR imaging must be considered when exposure protocols are designed for these systems.

According to Dougeni et al[4] the size of the exposed neonate will influence the dose, as an increased exposure is needed to obtain a satisfactory image of a greater mass, and bigger, neonate.[4] An investigation of how image quality and radiation dose change with varying exposure technique factors allows for optimisation of these parameters. If the dose is kept constant, the best procedure would be the one that maximises image quality. If image quality is kept constant, the most optimal procedure would be the one that delivers the lowest radiation dose. The first step in dose optimisation is determining what radiation dose is delivered to a neonate per x-ray investigation. Published reference doses exist[21,28] and facilities can investigate the doses they deliver to see if it is below the recommended reference doses. Technique and equipment changes are encouraged to ensure that reference levels are adhered to. Such studies can also serve as justification for dose increases in order to improve image quality, if the initial doses are well below reference levels.

Different x-ray investigations are performed for different disease conditions. The current study focuses on chest AP x-rays only. Optimised x-ray exposure protocols, which decrease the delivered radiation dose while maintaining acceptable clinical image quality, could decrease the risk of childhood cancers developing. At present, such optimised protocols have not been designed and implemented at Tygerberg Academic Hospital.

Two aims are identified for this thesis. Firstly, a neonatal chest simulation phantom which simulates a real neonatal chest anatomically and radiologically is to be designed and constructed. Chest AP x-ray image quality and delivered radiation dose will be evaluated simultaneously, using the proposed phantom. The second aim is to develop optimised x-ray exposure protocols that decrease the radiation dose, delivered by chest AP x-ray investigations to neonates, while maintaining the required image quality for diagnostically useful images. How to reduce the risk of inducing childhood cancer should be the result of this investigation. The optimised protocols will then be recommended to the Division of Diagnostic Radiology at Tygerberg Academic Hospital.

In the current study a phantom representing a real neonatal chest is developed and used. Recommendations from literature are followed to analyse the methods used for neonatal chest AP x-rays at Tygerberg Academic Hospital. The research shows that an increase in kV, added filtration and a reduction in mAs can be used to decrease the delivered radiation dose, while maintaining acceptable image quality with digital image processing. With certain combinations of exposure factors visual image quality can even be improved at a reduced radiation dose, compared with the exposure used routinely in Tygerberg Academic Hospital.

A review of literature on the subject of this dissertation summerises the recommendations referred to in this literature. The anatomical and radiological equivalence determination of the phantom and the process of validation of the phantom are discussed. Image quality is quantified with a physics image quality assessment phantom, and its construction is explained. Different methods of dose reduction are employed and these, and the obtained results, are presented. The obtained clinical and physical image quality results are presented and discussed.

Recommendations to the Division of Diagnostic Radiology at Tygerberg Academic Hospital are concluded and presented for implementation in the Division. The limitations of the project, possible improvements and future advancements are communicated and conclusions are drawn from the presented data.

Chapter 2

Literature review

Extensive research on dose reduction with film screen systems was done by McParland et al[5]. However, limited research in this field using CR systems was reported. Therefore much of the literature study refers to film-screen research. The principles of dose reduction and image quality maintenance remain the same, regardless of the imaging system used. Only the combinations of exposure factors and achieved radiation doses and image quality will differ, due to the increased dynamic range and post processing and image manipulation capabilities with CR.

As this thesis focused on neonatal chest AP radiographs, an understanding of neonatal anatomy in the chest area was needed. It was also of importance for the construction of the neonatal chest simulation phantom. The different x-ray imaging techniques and associated doses had to be understood in order to gain knowledge about the radiation dose range applicable to these exposures, which influenced the radiation dosimeter that should be used for dose measurements. Dose reduction was the main goal of the current study, therefore the physics of the interaction of radiation with matter and the associated delivered radiation doses were studied. It was important that the obtained results were applicable to real neonatal patients, so that the conclusion from this dissertation could be used as recommendations on neonatal chest AP exposures in Tygerberg Academic Hospital. Therefore neonatal tissue equivalent materials and possible simulation phantoms were investigated. The recommendations and results from the literature review were used to construct the experimental part of this thesis.

2.1 Neonatal anatomy and imaging

White et al[6] define the term “foetus” as a baby 8 - 40 weeks post conception. A foetus is called a neonate as soon as it is exposed to the environment external to the uterus. Babies born preterm are therefore included. These babies are still in a maturational process and exposure to an aerated environment, where temperatures vary and gravity and disease-causing organisms are present, causes rapid maturing and compensatory growth. A new-born infant is not equivalent to a small adult. Likewise a preterm neonate differs from a full-term one. Full-term neonates are typically 48 - 53 cm long from crown to heel, and weigh 2700 - 3800 g. Birth mass is classified as low birth weight if it is less than 2500 g, very low birth weight for less than 1500 g and less than 1000 g are extremely low birth weight neonates.[7]

The development of the body systems is described by Gray in the 39th edition of Gray’s anatomy[7]. It is shown in Figures 2.1 and 2.2 below, reproduced from the book by Gray. In Figure 2.1.each row, from left to right, shows the development of individual systems and each column, from top to bottom, shows the organs at risk at a certain development time.[7] Figure 2.2 shows the embryonic development on the top scale, counted from the fertilisation date. Clinical estimation of pregnancy is determined from the last menstrual cycle, as shown on the bottom scale.[7]

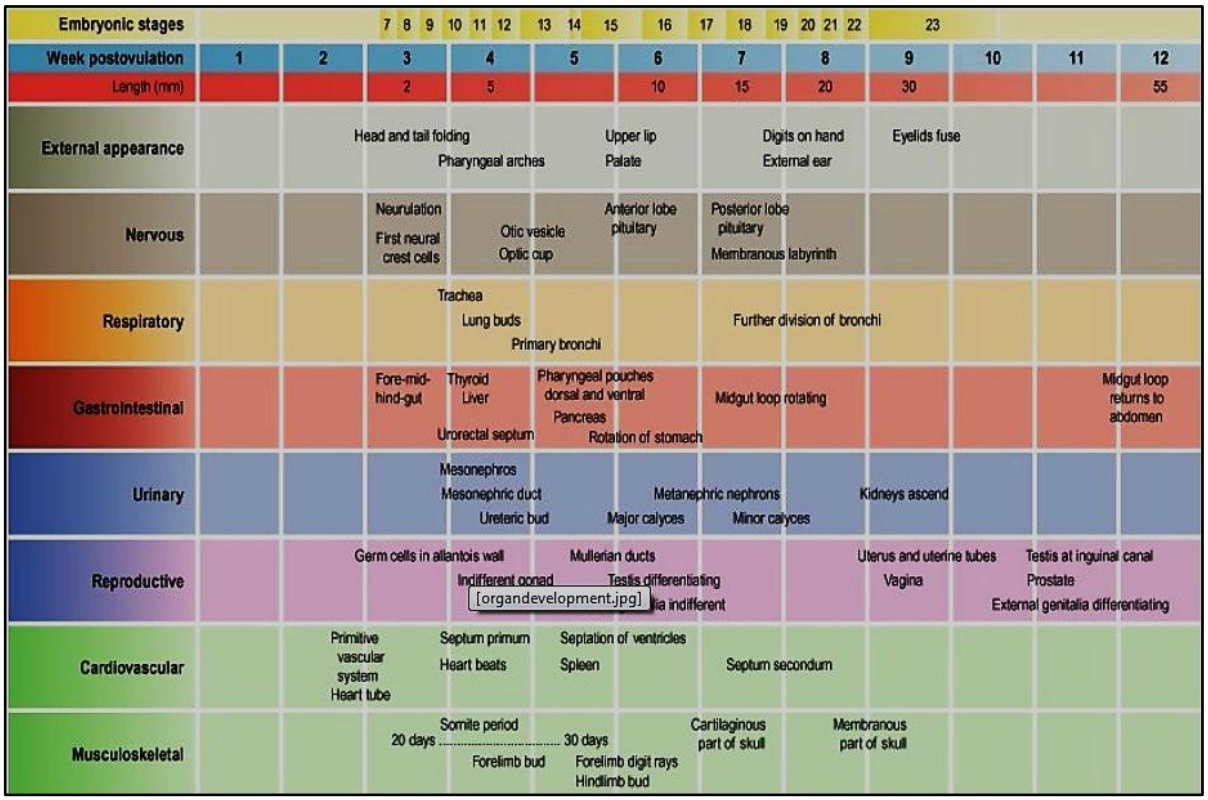

Figure 2.1: Timetable showing the development of the different systems of the body.[7]

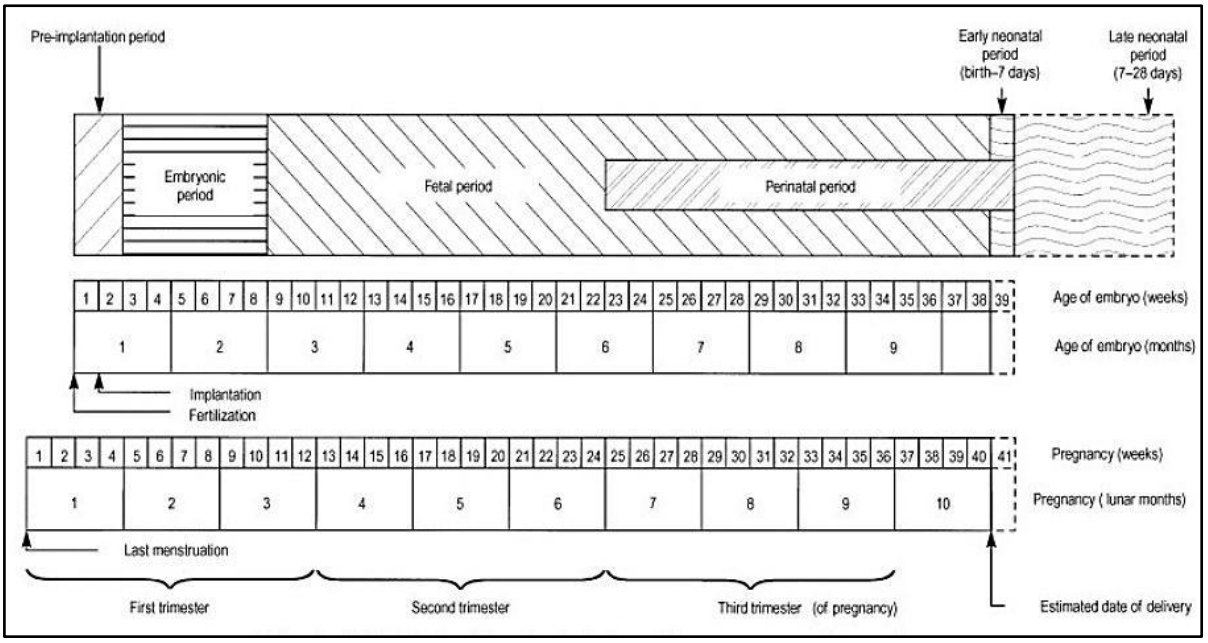

Figure 2.2: Human development timescales.[7]

Gestational age can also be determined from the ossification of the sternum. At a gestational age of 30 weeks or more, at least two sternal segments are ossified, including the manubrium. Three to four ossified segments indicate a gestational age of 34 - 37 weeks according to Odita et al[8].

At this early stage of life, especially when born prematurely, various problems and diseases can occur. X-rays of the chest are taken when the condition of the lungs and/or heart need to be examined. Chest x-rays are used to confirm or exclude certain disease conditions, such as pneumothorax, hyaline membrane disease, meconium aspiration syndrome and respiratory distress syndrome, to check the position of various tubes, catheters and the placement of intravenous long lines and to monitor pulmonary inflation and the development of complications, as mentioned by Arthur et al[9] and Dougeni et al[4].

Neonatal abnormalities that are best diagnosed and followed up with chest x-rays can be divided into aeration, circulation and development abnormalities. For optimal treatment of these, numerous x-rays are needed, but it is important to keep the neonate's radiation exposure ALARA in order to account for the small but important risk of childhood cancer induction. Normal neonatal lungs are aerated after two or three respiratory cycles. A normal chest AP x-ray, as in Figure 2.3, reproduced from Sophomore paediatric chest[10], shows symmetrical lung fields with the diaphragm at the level of the 8th posterior and 6th anterior ribs.

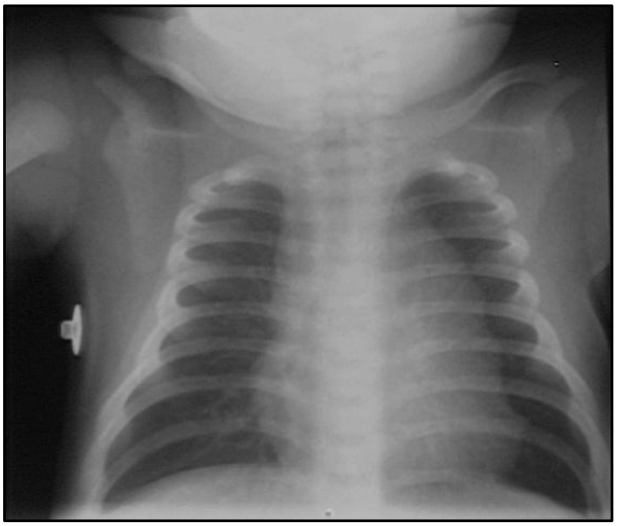

Figure 2.3: Normal neonatal chest AP x-ray.[10]

Smans et al[11] report that prematurely born babies often have morphologically and physiologically immature lungs, that lead to respiratory distress syndrome.[11] Aeration disorders include air leaks after alveolar rupture, pulmonary haemorrhage, meconium aspiration syndrome, neonatal pneumonia, pleural effusions, chronic lung disease and hyaline membrane disease, which arise from a lack of pulmonary surfactant leading to collapse of the lung. It shows up as a “white” lung on an x-ray, as in Figure 2.4 below, reproduced from Arthur[9]. The condition is simulated with a solid water tissue equivalent substitute in the neonatal chest simulation phantom. To diagnose and follow up these diseases regular chest x-rays are justified, but the principle of ALARA has to be maintained.[11]

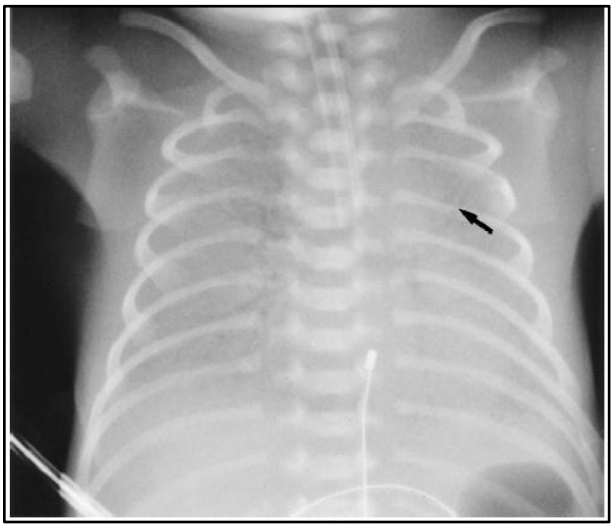

Figure 2.4: Severe hyaline membrane disease resulted in a “white” lung on an x-ray.[9]

Arthur[9] also discusses circulation and developmental disorders. Congenital heart disease is an example of a circulation disorder. Developmental abnormalities include trachea-oesophageal fistulae, congenital diaphragmatic hernia and malformation of the lungs.[9]

The organs at risk, according to Makri et al[3], that are considered with chest AP x-rays on neonates are the breasts, lungs, bone marrow and surface, stomach, liver, skin, thyroid, reproductive organs (uterus, ovaries and testes), small intestines, bladder, spleen and adrenals.[3] Huda[2] reports that the chest is relatively easy to penetrate with x-rays, so chest AP x-ray effective doses are low compared to that of skull and abdomen examinations.[2]

According to Ono et al[12], neonates with a low birth weight stayed in the neonatal intensive care unit (NICU) for a longer period and received more frequent x-ray examinations. The frequency of x-ray examinations depended on the birth weight, disease and gestational age of a neonate. Radiological investigations were most commonly needed for respiratory distress syndrome, meconium aspiration syndrome and chronic lung disease. Chest x-rays were the most common investigation in the NICU. The maximum number of radiological examinations on a single neonatal

patient in the NICU was 72, with an average per neonate of 26, at an entrance surface dose of 0.017 - 0.034 mGy per exposure. From epidemiological data, i.e. a life span study on Hiroshima and Nagasaki atomic bomb survivors, it was seen that children had a higher incidence of radiation-related cancer if exposed to radiation as a baby.[12] In this study the dose to the patient that received 72 exposures was between 1.2 and 2.4 mGy.

Gutteling et al[13] found that chest radiographs were most commonly performed for respiratory distress syndrome and lung hypoplasia, which was caused by lungs that were underdeveloped. The severity and follow-up of the disease were assessed with radiographs. Neonates were typically classified into three groups based on birth weight, i.e. extremely premature with birth weights less than 1 kg, premature with birth weights of 1 - 2.5 kg and full-term with birth weights greater than 2.5 kg. The extremely premature group had a bigger chance of having underdeveloped lungs and the time from birth to term was longest for this group, therefore they often required the most radiographs.[13]

Compared to film, image quality could be maintained at a lower radiation dose if CR was used. Modified exposure factors must therefore be established for CR exposures and CR should be used instead of film-screen, if available.[14] Research by Brindhaban and Al-Khalifah[15] showed that neonates with respiratory problems typically underwent 20 - 25 x-ray investigations. They mention that dose reduction with CR compared with film screen was possible due to the linear response of CR's photo-stimulable phosphor plates and post-processing image manipulation.[15] The current study aims to utilise the physical characteristics of CR imaging systems to decrease the delivered radiation dose, with consideration to image quality maintenance and cancer induction risks. However, mention was made in literature of dose increases with CR.

Malekzadeh et al[16] reported that digital systems, such as CR, have a fixed resolution, but these systems could operate with acceptable images over a wide range of delivered doses. The resolution performance of these systems is determined by the thickness of the detector and the size of a pixel. In the case of these systems the level of image noise is inversely proportional to the amount of

radiation, or the delivered dose, used to form the image. It is therefore possible to choose the level of noise in an image that would be acceptable by varying the exposure used to form the image by changing the technique factors used. Spatial resolution would not be affected. The amount of transmitted radiation that reaches a digital image receptor depends on the energy or quality of the x-rays used and on the size and composition of the patient. The transmitted, or exit, dose is proportional to the incident dose, but it is difficult to use exit dose to calculate patient dose.[16]

Digital systems exhibit a linear response over a wide range of exposures to radiation. The blackening of the image receptor is decoupled from the amount of radiation used to form the image. For these reasons it is important to monitor the receptor dose indicator to maintain an acceptable image quality level without overexposing a patient. The number of x-ray photons used to form an image determines the noise of the image. For a certain exposure the efficiency of the image receptor would determine the number of incident photons that are absorbed. Generally CR systems are less efficient than film-screen systems as CR systems need to be thin to limit the scatter of light with the read-out process. CR systems therefore absorb less of the incident photons and require larger doses for optimal image formation, compared to film screen. Huda[2] stated that, for a comparable level of image quality, the nominal receptor dose for CR was about 10 µGy and for film-screen it was about 5 µGy.[2] A study on 15 patients by Malekzadeh et al[16] revealed no dose reduction in moving from film-screen to CR. Instead, a slight increase in dose was found, 68.72 µGy and 94.46 µGy for film-screen and CR respectively. The study group in the report was small.[16]

As different opinions existed in literature, specific research on the CR system at Tygerberg Academic Hospital was therefore necessary in order to determine if a dose reduction per radiograph was indeed possible. It was important to have a baseline or standard for comparison, which was set as the standard exposure of 50 kV, 2 mAs, 100 cm focus-to-film distance (FFD) and inherent filtration, currently used to image neonatal chests at Tygerberg Academic Hospital. Using the baseline it was then possible to determine if a dose reduction or increase was obtained with CR when clinically acceptable image quality, i.e. the image quality associated with the current standard exposure, was maintained.

2.2 Neonatal radiation dosimetry

Neonates often undergo many x-ray investigations during their stay in hospital. The x-ray field size used is usually large to compensate for movement. Because neonates are more radiosensitive than adults and have a relatively longer life expectancy the stochastic risks, like cancer induction especially leukaemia, are higher. The organs at risk are in or close to the primary beam in neonates, because of small physical size. For these reasons neonatal exposures and doses must be kept as low as reasonably achievable (ALARA) and radiation doses must be justified. A number of researchers emphasise this.[4,15,16,17,18]

An x-ray investigation on a neonate is justifiable if the benefit from the investigation outweighs its risk. Benefits of these investigations are not yet quantified and have to be defined for each examination. Risk could be assessed in terms of the effective radiation dose.

Effective dose is defined as the weighted sum of the equivalent radiation dose delivered to different organs. The weighting is accomplished by published tissue-weighting factors.[14] It allows for the estimation of the risk of inducing cancer. The effective dose, E, in units of Sievert (Sv), can be calculated using Equation 2.1, according to Roebuck[19].

$$E = \sum w_T \times H_T \qquad \text{[Equation 2.1]}$$

where H_T is the equivalent tissue dose and w_T is the weighting factor for that tissue. There are uncertainties in the tissue weighting factors and it is difficult to measure the equivalent doses accurately. According to Roebuck[19] it means that the effective dose could vary over a range for the same investigation.[19] Skin dose could predict deterministic effects, like skin burns, but these have a threshold dose of about 2 Gy, below which they do not occur and therefore are not seen frequently in radiology. Patient risks in radiology are mostly stochastic, with no threshold dose, and these

cannot be expressed in terms of a skin dose. Skin doses do not account for the field size of the exposure, the type of radiation used for the exposure or the radiosensitivity of the organs exposed.

Huda[2] states that effective doses account for these and are therefore good indicators of stochastic risks.[2] Tissue-weighting factors for adults are widely published and readily available in literature. Another advantage of effective dose is that it can be compared with natural background radiation levels, which is about 3 mSv per year, and with regulatory dose limits, which is 1 mSv per year for the general public. Effective doses can be converted into approximations for stochastic risk with published International Commission on Radiological Protection (ICRP) risk factors. There are huge uncertainties associated with these risk factors and the factors for babies are much higher than those for adults.[2]

In the publication by Roebuck[19] the ICRP published coefficients for the calculation of cancer induction risk are mentioned. These are 0.05 Sv^{-1} for the overall population and 0.10 - 0.15 Sv^{-1} for children. Cancer induction risk is calculated as the product of the effective dose and the ICRP coefficient. These coefficients are based on data from atomic bomb survivors and are representative of the average population. Therefore it may be an overestimation for most of the population, but as some individuals are more sensitive to radiation, especially if certain disease conditions are present, it is also an underestimation for these individuals.[19]

Le Heron[20] and Brindhaban and Al-Khalifah[15] calculated effective doses from entrance surface doses with a computer program, Child Dose, based on ICRP recommendations.[15,20] Child Dose uses a newborn baby phantom for calculations, which is not representative of low birth-weight neonates. With premature lower birth-weight babies organs are closer together, therefore gonads, for example, could easily be included in the x-ray field. Effective doses for these neonates are consequently underestimated by the Child Dose program.[15] Neonates are also more prone to repeat x-ray investigations due to inadequate immobilisation and impossible communication during examinations, which adds to the already increased risk due to longer life expectancy and increased radiosensitivity.

The delivered radiation dose depends on a number of factors, including the tube voltage (kV), tube current (mA), exposure time (s), filtration, collimation, distance from tube focus to film or image plane (FFD) and image receptor. Combining these factors to achieve radiation dose reductions is discussed in literature.

In the case of prematurely born babies the radiation dose per x-ray should be minimised as they undergo a large number of x-ray investigations and are more sensitive to radiation than adults. Wraith et al[21] mention that The Commission of the European Community (CEC) Study Group recommend that neonatal exposures on a film-screen system should be made with a focal spot size smaller than 1.3 mm, added filtration of 1 mm aluminium (Al) plus 0.1 - 0.2 mm copper (Cu), a FFD of between 100 cm and 150 cm, ideally 115 cm, a tube voltage of 60 - 65 kVp and an exposure time of 1 - 4 ms. The obtained entrance dose is then 65 µGy and a reduction to 37 µGy is possible by increasing the filtration to 3.5 mm Al and the kV to 60 kVp, while maintaining acceptable image quality. The added filtration removed some of the low energy photons, which were mainly absorbed in the body, contributing to received dose and not to image quality. The assessment was done with an ionisation chamber and a TOR(RAD) test object.[21] Although the research referred to film-screen, the same principles would apply to CR systems, i.e. additional filtration and kV increase, with associated mAs decrease, should give a dose reduction, which is investigated in the current study.

Additional filtration, as a dose reduction mechanism, is also described in literature. The effect of added copper filtration on dose and image quality was assessed with Monte Carlo simulations by Smans et al[11]. Image quality was evaluated with signal-to-noise ratios (SNR) and signal difference-to-noise ratios (SDNR), as shown in Equations 2.2 and 2.3, where S_O and σ_O are the mean signal and standard deviation of the noise of the object of interest and S_B and σ_B are that of the background area.[11]

$$SNR = \frac{S_O}{\sigma_O}$$ [Equation 2.2]

$$SDNR = \frac{S_O - S_B}{\sigma_B}$$ [Equation 2.3]

The SDNR had to be optimal, i.e. a large value, in the soft tissue regions. These simulations were verified with Gammex 610 Neonatal Chest Phantom measurements and it was found that beam hardening, through increased filtration of 1 mm Al + 0.2 mm Cu, could be used to optimise the image quality versus dose relationship, at 60 kV. The SNR increased by 30% and the lung dose decreased by 25%.[11] SNR and SDNR and the concept of additional filtration are used in the current study.

In a study by Dougeni et al[4], image quality was not significantly reduced clinically with the use of higher kV and lower mAs protocols, although a significant dose reduction was found. Harder x-ray beams that had increased penetration ability were recommended, as, with the associated reduced mAs setting, entrance surface dose (ESD) values would be lower. Increasing the kV decreased image contrast. An upper limit should therefore be determined for the kV parameter.[4] As radiographs must still be clinically useful, clinical image quality assessment was very important in such a study. Dose could easily be reduced to a minimum, but the associated image quality would also be decreased, leading to retakes and therefore increased doses. There had to be a balance between dose reduction and clinically acceptable image quality.

Brindhaban and Al-Khalifah[15] found that low filtration and a lower kV gave a higher ESD. The best results, with film screen, were obtained with kV greater than 60 kV and filtration of at least 2.5 mm Al equivalence. ESD was measured as 71 ± 28 µGy and effective dose was calculated, with the Child Dose program, as 28 ± 8 µSv for a chest AP examination. Using risk factors of 2.8 - 13×10^{-2} per Sv, i.e. risk factors for pre-natal exposures, the risk for childhood cancer induction ranged between 0.34 -

$4.68x10^{-6}$ per examination.[15] One has to keep in mind that neonates often undergo numerous x-ray investigations and that the actual risk can therefore be higher.

Dose reduction can also be achieved with active shielding. A study was done by Barcham et al[22] with direct lead equivalent shielding, placed on a neonate, and shadow shielding, where lead equivalent shielding was placed on the incubator, to reduce the dose to organs outside of the primary beam, specifically the gonads. Dose measurements showed that the dose to gonads was reduced substantially with direct shielding.[22] Beam collimation, to the required area only, avoiding non-essential and repeat exposures, using highly trained staff for neonatal exposures and the use of genital shielding can also lead to dose reductions, according to Wilson-Costello et al[23].

Gonadal exposures were investigated by Egan and Dowd[24], with a water-filled phantom made from a plastic developer container. Dose was measured at testicular level with different methods of shielding, which included the use of a lead lined collimator, shadow shielding with a lead strip placed on the incubator and direct or contact shielding with a lead rubber shield on the baby's body. The disadvantages of the different methods were that lead-lined collimators were not readily available. Shadow shielding was difficult to perform accurately if ambient light levels were too high. Direct shielding that was not applied properly could increase the delivered dose to sensitive organs, like the lens of the eye, thyroid, bone marrow and gonads, through extra scatter. This leads to repeat exposures due to poor quality radiographs. It also posed a risk for cross infections. Radiographers needed proper training in the use of shielding to ensure that the ALARA principle was adhered to. Lack of knowledge could lead to shielding being omitted in order to prevent retakes. It was found that direct gonadal shielding gave a 60% dose reduction with chest AP radiographs.[24] Although not considered in this dissertation, active shielding is a recognised neonatal dose reduction technique, if applied correctly.

A radiation x-ray audit proved helpful in dose reduction for Loovere et al[25]. The results from such an audit, which looked at the demographics and logistics of x-ray exposures in a NICU, could be used for staff education and a team effort for dose reduction could result. It was found that radiographers increased collimation to

ensure that the targeted area was imaged, but extra anatomy was then also included, a misguided strategy which had to be avoided. Educational sessions with examples of such x-rays were held and proper holding of infants, acceptable extra-included anatomy and placement of leads were discussed. Loovere et al[25] recommended such audits on a regular basis.[25] The current study measures radiation doses and makes dose reduction recommendations to the Division of Diagnostic Radiology at Tygerberg Academic Hospital. If the recommendations are implemented such an audit could help to determine the success of the results of the current study.

LiF:Mg,Cu,P thermoluminescence dosimeters (TLDs) were suggested as acceptable dosimeters for neonatal radiography by Duggan et al[17,26] and Edwards et al[27]. LiF:Mg,Ti TLDs tend to over-respond at low x-ray energies. The LiF:Mg,Cu,P TLDs have a better energy response in the low diagnostic energy range,[26,27] a lower detection limit, higher sensitivity and better tissue equivalence than LiF:Mg,Ti TLDs.[17]

A study was done by Duggan et al[28], with neonatal simulation phantoms simulating a 700 g and 2000 g neonate, and LiF:Mg,Cu,P TLDs. Variations in kVp, filtration and collimation were investigated with adjustments in FFD and mAs to maintain image optical density. ESD and dose at 3 cm and 5 cm depths were measured with the TLDs. The Commission of the European Communities suggests technique factors of 60 - 65 kVp, 80 - 100 cm FFD and 1 mm Al + 0.1 mm Cu additional filtration for chest AP paediatric radiographs, which would give a reference ESD of 80 µGy for such an examination on a 1000 g neonate. Duggan et al[28] found that ESD could be decreased by increasing kVp and/or filtration. They used an additional 0.05 mm hafnium filter. An increase in kVp from 54 to 70 kVp gave an ESD reduction of 27% in the case of the 2000 g phantom. By adding the hafnium filter at 66 kVp, the ESD was reduced by 13% more. With these adjustments the image contrast was also reduced, but the clinical significance was not investigated.[28]

Clinical image quality is very important and has to be maintained. An x-ray taken at a reduced dose, but with inadequate image quality, is useless and has to be retaken. In the current study image quality and dose reduction are evaluated in conjunction.

TLDs are not readily available and are very expensive. Using TLDs is also time consuming. Special readout equipment is needed, annealing and calibration have to be performed and measurements have to be read out timeously to prevent fading. As Tygerberg Academic Hospital does not have a TLD reader available (the only available reader in the Western Cape is at Groote Schuur Hospital) and the LiF:Mg,Cu,P TLDs have to be imported at considerable cost, these detectors are not used in this thesis. Other detector options were discussed in literature.

Akahane et al[29] used film badges and glass dosimeters with a rectangular phantom (refer to Figure 2.9) to measure surface doses for chest AP radiographs. Exposures were made with 55 kV, 1.6 mAs and 90 cm FFD. The glass dosimeters and film badges measured 0.1 mSv for such an exposure.[29]

The radiation entrance surface doses were measured with a Victoreen model 660 survey meter by Brindhaban and Eze[14]. Measurements were done for the age group from birth to one-year-old infants. It was difficult to measure patient or organ doses directly, so x-ray tube output was measured using an external detector indicating the total delivered radiation dose. Such measurements would not account for backscatter and collimation, according to Gutteling et al[13]. ESDs can also be calculated.

Entrance surface dose, ESD, is calculated from free-in-air exposure measurements using Equation 2.4, where X is the measured exposure in Roentgen (R), $F_{Da,X}$ (8.7mGyR^{-1}) converts R to absorbed dose-in-air, f_{BS} corrects for backscatter, f_{Cal} is the calibration factor of the ionisation chamber used and f_D is an inverse square law correction.[14,15] If the chamber is thin enough to accurately measure the back scatter radiation from the phantom or patient, the f_{BS} factor can be ignored.[15]

$$ESD = X \times F_{Da,X} \times f_{BS} \times f_{Cal} \times f_D \qquad \text{[Equation 2.4]}$$

Brindhaban and Eze[14] reported an entrance surface dose of 32 - 176 µGy for chest AP exposures with tube voltages between 73 kV and 52 kV. The calculated effective dose range was 8 - 40 µSv, translating to a 1.2 - 6 risk per million for cancer induction. These results were in respect of newborn babies.[14]

Olgar et al[30] did a retrospective evaluation of ESD on 23 neonates. ESD was calculated from tube output measurements and with lithium fluoride TLDs. The calculation was done with Equation 2.5, where ISL is the inverse square correction factor for the difference in the distance from the tube focus to the chamber (focus-to-chamber distance) and from the tube focus-to-skin (FSD), mAs is the tube current-time product, BSF is the backscatter factor and is 1.1 for 50 - 70 kVp for a neonate with a 5 cm body thickness and $\left(\frac{\mu_{en}}{\rho}\right)_{Air}^{Tis}$ is the mass energy absorption coefficient ratio of tissue-to-air and is 1.05 for 50 - 70kVp.[30]

$$ESD = Output(\mu Gy/mAs) \times mAs \times BSF \times ISF \times \left(\frac{\mu_{en}}{\rho}\right)_{Air}^{Tis} \qquad \text{[Equation 2.5]}$$

The calculated ESD from tube output was 67 µGy and the TLD measurement was 70 µGy on average for chest radiographs. These were comparable to 80 µSv and 50 µSv published by Commission of European Communities and the National Radiological Protection Board respectively. Mean effective dose was calculated with Monte Carlo simulations and was 16 µSv per exposure. The associated cancer induction risk was calculated to be between 0.4×10^{-6} and 2×10^{-6}. According to Olgar et al[30] intense tissue proliferation and differentiation exist in a neonate, and proliferating cells are more sensitive to radiation, which increases cancer induction risks. The small body size of neonates means that a large portion of anatomy is included in the x-ray beam, resulting in a higher effective dose per x-ray.[30]

Equation 2.5 was used by Armpilia et al[31] as well. A BSF of 1.1 ± 5% was used for a neonate with a 5 cm thick body, 50 - 70 kVp and 70 - 300 cm^2 field sizes. The FSD was derived from the known FFD (100 cm) and the approximate diameter of a

neonate, which was 7.5 ± 1.4 cm for neonates in this unit. The mass energy absorption coefficient ratio for muscle, averaged over the x-ray spectrum (50 - 58 kVp) used, was 1.05. Calculated ESDs ranged between 28 - 58 µGy. These calculated ESDs were compared with those measured with LiF:Mg,Cu,P TLDs. The ESD from the TLDs ranged between18 - 58 µGy.[31]

Equation 2.6 was suggested by McParland et al[5] to calculate the diameter of a neonate. Here d is the diameter, W is the most recent weight of the neonate and L is the neonatal length at birth.[5]

$$d = 2\sqrt{\frac{W}{\pi L}} \qquad \text{[Equation 2.6]}$$

An additional multiplicative transmission factor, TF, in Equation 2.5 was recommended in a different study by Dougeni et al[4]. The factor accounted for transmission through the incubator for those neonates imaged in the incubator. It was proposed that a thickness of 5 mm perspex had to be used to measure the factor, with about 10% attenuation of the beam. Scatter was considered to be negligible.[4]

The risk of cancer induction can be calculated from ESD or from energy imparted, if one assumes that all irradiated organs are evenly distributed in the body. As most neonates are born prematurely, the risk factors for foetal irradiation are more appropriate than those for children. The risk is 2.8 - 13x10^{-2} per Sv according to ICRP Report 60. For the above mentioned study of Armpilia et al[31] the risk per radiograph was therefore 0.3 - 1.3x10^{-6}. As foetal irradiation implied whole body irradiation, and only part of a neonate was exposed to radiation, it was an overestimation.[31]

Chapple et al[32] used technique factors to calculate entrance surface dose, which was used to calculate, with Monte Carlo, energy imparted. Energy imparted was an

indicator of radiation risk. Neonatal dose measurements with TLDs are difficult, as TLDs are not very accurate in the low dose region and could also produce unacceptable artefacts on x-rays. It is also not practical to attach dose-area product (DAP) meters to mobile units. For these reasons the researchers recommend dose calculation from technique factors. As neonates are small in physical size and difficult to immobilise, organs at risk are often included in the exposures, so normalised organ doses are not completely applicable to neonates.[32]

Chapple et al[32] therefore recommend dose expression in terms of energy imparted. It represented an integral dose and could be used as a risk indicator, if one assumed that all radiosensitive organs were spread evenly in the body. Due to the small physical size of neonates, and therefore close proximity of organs, the approximation was applicable to neonates. Entrance surface dose was calculated using Equation 2.7, where BSF was calculated with Monte Carlo simulations for a 5 cm thickness of tissue-equivalent material, i.e. a typical neonatal thickness.[32]

$$Entrance\ dose\ (mGy) = Output(mGy/mAs) \times mAs \times BSF \qquad \text{[Equation 2.7]}$$

In the study by Chapple et al[32] the mean number of radiographs per neonate was found to be 5.29, but one neonate received 38 radiographs. The mean entrance dose per radiograph was 0.06 mGy and the corresponding mean energy imparted was 0.09 mJ. The whole body dose was calculated by dividing the energy imparted by the body weight, i.e. 2.5 kg, which gave 0.04 mGy on average with a corresponding maximum of 0.30 mGy. Using the ICRP risk factors for foetal cancer induction of 2.8 - 13×10^{-2} per Sv, the typical risk in the study ranged between 1.1×10^{-6} and 5.2×10^{-6}, with a maximum risk of between 8.4×10^{-6} and 3.9×10^{-5}. Lifetime risks may be 2 to 4 times higher than these, as they accounted for risks up to the age of 15 years only. Therefore the risks from radiography were quite low in general, but exceptional cases did exist. Collimation, even with extra external shielding, had to be performed. Neonatal radiographers also required specialised training.[32]

A study by Makri et al[3] employed Monte Carlo MCNP-4C2 code to simulate neonatal chest radiographs on a mathematical phantom. Equivalent doses and energy imparted were calculated using Monte Carlo simulations per unit ESD. ESDs were measured with TLDs in a NICU and used with the Monte Carlo calculations to compute effective doses. EDSs were 44 ± 16 µGy. Effective dose was 10.2 ± 3.7 µSv and imparted energy was 18.5 ± 6.7 µJ per radiograph for males and females. The total risk per radiograph was calculated to be between 1.7 and 2.9 per million neonates per film, or 22.2 and 25.8 per million neonates for an average number of radiographs, with females having a slightly higher risk. The increased risk was small, but it did exist and could therefore not be ignored. The dose per exposure had to be minimised.[3]

Although the ESD is indicative of the technique factors used in an exposure, it does not account for changes in field size or positioning of the neonate in the field. A small change in the field size or shift in the neonatal position in the field could mean that other, or more radiosensitive, organs are in the primary beam, affecting organ and effective doses. Dose area product (DAP) meters take field size into account, according to Dougeni et al[4].

Effective doses can be calculated from DAP meters. With neonatal radiography the exposed areas are small, due to the small physical size of the patients. Small DAP readings result, although the absorbed dose in the different organs is higher. Effective doses are therefore underestimated and DAP meters are not recommended for neonatal imaging by Brindhaban and Eze[14].

DAP meters are not usually present on mobile x-ray units, most commonly used for neonatal exposures. DAP readings can be approximated, if perpendicular beam incidence is assumed, as the product of the ESD and the exposed area. These factors could be determined retrospectively from the exposure parameters, correcting for demagnification of FFD to focus-to-surface distance (FSD). Such an approximation does not take the inhomogeneity of the x-ray beam, due to the heel effect and inverse square law, into account, although the significance of these effects are deemed negligible by McParland et al[5]. DAP meters are not available on the mobile unit commonly used for neonatal x-rays at Tygerberg Academic Hospital.

Wilson-Costello et al[23] did a study on 25 surviving neonates with birth weights below 750 g. On average these neonates received 31 radiographs, of which 17 were chest radiographs. They used a Victoreen 660 survey meter to measure the exposure, in milli-Roentgen per mAs (mR/mAs), and calculated the entrance skin exposure (ESE) with Equation 2.8. [23]

$$ESE = (mR/mAs\ at\ calibration\ distance) \times (mAs\ used) \times \left(\frac{calibration\ distance}{distance\ used}\right)^2$$

[Equation 2.8]

They used two methods to assess organ doses. The standard method used published organ doses for an ESE of 1 R for a 3.96 kg infant, based on beam quality and collimation. The modified method considered organ placement and scattered radiation, actual body weight and extramedullary haematopoiesis. In neonates it occurred in the liver, spleen and bone marrow. Organ doses in the primary x-ray field were calculated with Equation 2.9. The effect of scatter on organs doses outside of the main x-ray beam were calculated with Equation 2.10.[23]

$$Organ\ dose = ESE \times f \times backscatter\ factor \times e^{-ud} \quad \text{[Equation 2.9]}$$

$$Organ\ dose = ESE \times f \times backscatter\ factor \times A \times \left(\frac{100}{d1}\right)^2 \times e^{-ud1}$$

[Equation 2.10]

Here ESE is entrance skin exposure, f is the roentgen to rad conversion factor, d is the depth of an organ in the primary beam, u is the linear attenuation coefficient, A is the ratio of scattered radiation to primary radiation at a 1 m distance and $d1$ is the distance to the scatterer. The standard method gave a total body dose which

assumed uniform whole body irradiation. The modified method calculated an effective dose equivalent that took into account the different radiosensitivities of different organs with organ weighting factors. These factors are 0.25 for the gonads, 0.15 for breast, 0.12 for marrow and lung, 0.03 for the thyroid and 0.33 as an all-inclusive factor for the brain, skin, intestines, spleen and liver. These factors are defined in ICRP 60 for adults. Such factors are not available for neonates and therefore adult factors were used by the researchers.[23]

The doses from the modified method were larger than those of the standard method, except for ESE and breast and testes doses from chest radiographs. The larger doses for internal organs, like the lungs, ovaries and marrow, showed on the inability to restrict the x-ray beam to areas of interest. The higher hematopoietic dose for liver, spleen and marrow was a more accurate representation of extramedullary haematopoiesis in neonates. The dose ranged between 0.01 and 0.02 mSv per chest radiograph, with an effective dose equivalent for all radiographs of 0.72 mSv per infant. According to the United Nations Scientific Committee on the Effects of Atomic Radiation (UNSCEAR) the risk for radiation induced cancer was 12.5 - $16x10^{-2}$ excess cancer deaths per Sv. The Committee on the Biological Effects of Ionising Radiation states a risk of 0.8% per 0.1 Sv. In a worst case scenario it meant that the risk for cancer development in neonates that underwent x-ray examinations was 1 in 10 000 in the study.[23]

These risks estimations were for adults and whole body exposures. The risk for partial body exposure, which should be done on neonates, but is not always the case, should be lower. The ICRP states that the dose to the foetus from occupational exposures during pregnancy should be less than 1 mSv for the duration of pregnancy. According to Wilson-Costello et al[23] the total dose was not likely to be reached by radiographic exposures of neonates.[23] Although these dose levels were unlikely to be reached, cancer induction risks were elevated. Calculation of the risk of childhood cancer induction was done by Wraith et al[21] and was 0.2 - $2x10^{-6}$. Therefore up to two children in every 1 000 000 receiving x-rays as neonates could develop a radiation induced childhood cancer.[21]

Twin studies, by Wilson-Costello et al[23], suggest that in utero exposure to radiation did increase the risk for childhood cancer induction. It was not demonstrated by studies on the atomic bomb survivors that were exposed in utero. A relative risk factor for cancer induction of 3.77 at 1 Sv absorbed uterine dose was reported. However, atomic bomb survivor data were for a single large exposure and neonates underwent several smaller dose exposures over a period of time. The complete biological effect of exposure to radiation depends on the type and energy of the radiation, the exposed tissue, the exposure time, the presence of chemical sensitisers and the total received dose.[23]

Neonates are more sensitive to the effects of radiation than adults. The cancer induction risk, per unit effective dose, was 2 - 3 times higher for neonates than for the rest of the population.[11] Smans et al[11] report that the risk was 6 - 9 times higher than that of a 60 year old adult for the same received dose. The risks from diagnostic x-ray procedures are low compared with the risks from other procedures involving radiation, but the delivered dose should still be optimised and the principle of ALARA adhered to.[11]

2.3 The physics of x-ray imaging

The attenuation of an x-ray beam is described by Bushberg et al[1]. The linear attenuation coefficient (μ) is governed by the photoelectric effect (τ), Rayleigh scatter (σ_R), Compton scatter (σ) and pair production (π) interaction mechanisms, as shown in Equation 2.11.[1]

$$\mu = \tau + \sigma_R + \sigma + \pi \qquad \text{[Equation 2.11]}$$

The mass attenuation coefficient is the quotient of the linear attenuation coefficient by the density of the material. For a compound it is the sum of the mass attenuation coefficients of its constituent elements. In Equation 2.12, in Mak[33], $\left(\frac{\mu}{\rho}\right)_c$ is the mass

attenuation coefficient of the compound, w_i is the weight fraction and $\left(\frac{\mu}{\rho}\right)_i$ the mass attenuation of constituent material i.[33]

$$\left(\frac{\mu}{\rho}\right)_c = \sum w_i \left(\frac{\mu}{\rho}\right)_i \qquad \text{[Equation 2.12]}$$

These interaction coefficients that form the attenuation coefficient can be calculated, with the program XCOM, developed by MJ Berger et al[34]. This program and database compute photon total and partial cross sections for coherent and incoherent scattering, photoelectric effect absorption, pair production and a total attenuation coefficient. The calculations can be done for different elements, compounds or mixtures for a range of energies from 1 keV to 100 GeV. The data in the program is based on the National Institute of Standards and Technology (NIST) database[34]. The program includes free software available at http://physics.nist.gov/XCOM[34]. The current study uses the program for calculations.

According to Berger et al[34], the photon cross-sections can be calculated reasonably accurately for compounds, except at energies close to the absorption edges, using the weighted sum of the cross-sections of the atomic constituents of the compound. Such a calculation is tedious and is complicated by the discontinuities of photo-absorption cross-sections and total attenuation coefficients at absorption edges. Photon energies immediately above and below the absorption edges should therefore be included, which is done by way of interpolation. The XCOM program uses a standard energy grid, which is spaced approximately logarithmically, or another grid that is specified by the user or on a combination of these two grids. Results can be presented in tabular or graphical form. For compounds and mixtures, interaction coefficients and total attenuation coefficients are calculated as the sum of the coefficients of the constituents of the compound or mixture. Fractions by weight are either calculated by XCOM from the chemical formula or are entered as inputs by the user.[34]

An example of the data entry screen and resultant output file of the XCOM program is shown in Figure 2.5.

a.)

```
Program XCOM, Version 3.1
M.J.Berger and J.H.Hubbell, 23 June 1999

Enter name of substance: Example

Options for characterization of substance:
  1. Elemental substance, specified by atomic number
  2. Elemental substance, specified by chemical symbol
  3. Compound, specified by chemical formula
  4. Mixture of elements and/or compounds
Enter choice: 4

How many components in mixture? Enter number: 2

Enter chemical symbol or formula for component 1: H

Enter fraction by weight for component 1: 0.5

Enter chemical symbol or formula for component 2: He

Enter fraction by weight for component 2: 0.5

 Component   Fraction
             by Weight

     1   0.500000    H

     2   0.500000    He

   Sum =    1.000000

Options for accepting or rejecting composition data:
  1. Accept, but let program normalize fractions
     by weight so that their sum is unity
  2. Reject, and enter different set of fractions
Enter choice: 1

Options for energy list for output data:
  1. Standard energy grid only
  2. Standard grid plus additional energies
  3. Additional energies only
Enter choice: 3

Modes of entering additional energies:
  1. Entry from keyboard
  2. Entry from prepared input file
Enter choice: 2

Specify file that contains input energy list.
(Specification can include drive and path): range.txt
```

```
Specify file on which output (cross section table)
is to be stored. (Specification can include drive
and path): Example

Cross-section table with headings has been stored in file Example

Options for further output:
  1. No more output
  2. Selected arrays stored on disk
Enter choice:1
```

b.)

Example

Constituents (Atomic Number:Fraction by Weight)
1:0.50000 2:0.50000

Partial Interaction Coefficients and Total Attenuation Coefficients

PHOTON ENERGY	SCATTERING COHERENT	SCATTERING INCOHER.	PHOTO-ELECTRIC ABSORPTION	PAIR PRODUCTION IN NUCLEAR FIELD	PAIR PRODUCTION IN ELECTRON FIELD	TOTAL ATTENUATION WITH COHERENT SCATT.	TOTAL ATTENUATION WITHOUT COHERENT SCATT.
(MeV)	(cm2/g)	(cm2/g)	(cm2/g)	(cm2/g)	(cm2/g)	(cm2/g)	(cm2/g)
1.000E-02	4.184E-02	2.587E-01	1.596E-02	0.000E+00	0.000E+00	3.165E-01	2.747E-01
1.500E-02	2.058E-02	2.682E-01	4.004E-03	0.000E+00	0.000E+00	2.928E-01	2.722E-01
2.000E-02	1.212E-02	2.691E-01	1.501E-03	0.000E+00	0.000E+00	2.828E-01	2.706E-01
2.500E-02	7.950E-03	2.673E-01	6.996E-04	0.000E+00	0.000E+00	2.760E-01	2.680E-01
3.000E-02	5.601E-03	2.645E-01	3.745E-04	0.000E+00	0.000E+00	2.704E-01	2.648E-01
3.500E-02	4.152E-03	2.612E-01	2.207E-04	0.000E+00	0.000E+00	2.655E-01	2.614E-01
4.000E-02	3.199E-03	2.577E-01	1.397E-04	0.000E+00	0.000E+00	2.611E-01	2.579E-01
4.500E-02	2.538E-03	2.542E-01	9.332E-05	0.000E+00	0.000E+00	2.569E-01	2.543E-01
5.000E-02	2.063E-03	2.508E-01	6.506E-05	0.000E+00	0.000E+00	2.529E-01	2.508E-01
5.500E-02	1.708E-03	2.474E-01	4.695E-05	0.000E+00	0.000E+00	2.492E-01	2.474E-01
6.000E-02	1.438E-03	2.441E-01	3.486E-05	0.000E+00	0.000E+00	2.456E-01	2.441E-01
6.500E-02	1.227E-03	2.409E-01	2.652E-05	0.000E+00	0.000E+00	2.421E-01	2.409E-01
7.000E-02	1.059E-03	2.378E-01	2.059E-05	0.000E+00	0.000E+00	2.389E-01	2.378E-01

Figure 2.5: a.) XCOM input screen. b.) XCOM generated output file.

Coherent and incoherent scatter cross-section interpolation is based on log-log cubic-spline fits as functions of energy. The photoelectric cross-section is similarly interpolated, but only for energies above the K-shell absorption edge. Below the absorption edge energy, interpolation is done as the logarithm of the photoelectric cross-section fitted as a linear function of the log of the energy. The calculation is done for each shell to avoid errors in interpolation across absorption edges. Pair production cross-sections are determined for the atomic nucleus field (E'=1.022 MeV) and for the atomic electron field (E'=2.044 MeV) as the logarithm of $\left(\frac{1-E}{E'}\right)^3 \sigma_{PAIR}(E)$, where E is the photon energy, E' is the threshold energy for pair production to occur and $\sigma_{PAIR}(E)$ is the cross-section.[34]

The limitations of the XCOM program are discussed by Berger et al[34]. The cross-sections in the database refer to isolated neutral atoms. The XCOM program does not take molecular or solid state effects into account, and these can modify cross-sections especially close to the absorption edges. Small cross-sections, for example Delbruck scattering, photo-meson production and two-photon Compton scattering are not taken into account. The nuclear photo-effect is also omitted. Energy

absorption coefficients, which characterise the conversion of photon energy to kinetic energy of secondary produced electrons, are not calculated.[34]

In the current study, total attenuation coefficients and the incoherent or Compton scatter coefficients are calculated for a range of different neonatal substitute compound materials using the XCOM program. The total attenuation and Compton scatter coefficients influence image quality, by affecting image darkening and noise. Dosimetry is influenced by the mass energy absorption coefficients which are spectral weighted to account for the spectrum of energies in an incident photon beam.

The mass attenuation coefficient for a compound can be calculated from the mass attenuation coefficients of its constituent elements, according to Turgut et al[35], through the mixture rule in Equation 2.13, where w_i is the fraction by weight and $\left(\frac{\mu}{\rho}\right)_i$ is the mass attenuation coefficient of the i^{th} element in the compound. It holds true for incident photon energies that are not within 1.5 keV of the absorption edge energy of an element.[35]

$$\frac{\mu}{\rho} = \sum_i w_i \left(\frac{\mu}{\rho}\right)_i \qquad \text{[Equation 2.13]}$$

For the elements considered in the current study, the absorption edges, as obtained from XCOM data, are recorded in Table 2.1.

Table 2.1: Elemental absorption edge energies.

Element	**K-edge (MeV)**	**L3-edge (MeV)**	**L2-edge (MeV)**	**L1-edge (MeV)**
H	-	-	-	-
C	-	-	-	-
N	-	-	-	-
O	-	-	-	-
Ca	4.038E-3	-	-	-
Na	1.072E-3	-	-	-
Cl	2.822E-3	-	-	-
F	-	-	-	-
Mg	1.305E-3	-	-	-
Ti	4.966E-3	-	-	-
Zn	9.659E-3	1.020E-3	1.043E-3	1.194E-3
K	3.607E-3	-	-	-
S	2.472E-3	-	-	-
P	2.145E-3	-	-	-
Sb	3.049E-2	4.132E-3	4.380E-3	4.698E-3
Si	1.839E-3	-	-	-

The highest absorption edge energy is the K-edge for Sb, which is 30.49 keV. This is well below the incident beam energies considered in the current study. The mixture rule should therefore hold true for compounds composed of these elements.

X-ray beams used for imaging are not mono-energetic but a spectrum of different energies. These different energies interact with the material it is incident on in different ways. Therefore, for dosimetry purposes, spectral weighting has to be considered. A semi-empirical model was developed by GT Barnes and DP Chakraborty[36] to generate tungsten target x-ray spectra. The model uses measured spectra and output data from an x-ray tube to parameterise the required constants in the mathematical model. The resultant model simulates real spectra accurately[36]. It

was used by Mr EA de Kock[37] at iThemba LABS to develop a spectral weighted mass energy absorption coefficient determination program.

This program was made available by Mr EA de Kock for application in the current study. The program uses the tube kVp, anode angle, percentage rhenium in the anode, total inherent aluminium filtration, thickness of the tube cooling oil, the thickness of the glass exit window and a list of energies and mass energy absorption coefficient paired data are computed to generate an x-ray spectrum. The mass energy absorption coefficients are calculated on a finer energy grid by way of cubic spline interpolation. The x-ray spectrum for a defined thickness of attenuating human muscle is computed at the energy grid with a semi-analytical model for the x-ray tube. These results are combined to form a spectral weighted mass energy-absorption coefficient which is written to an output file.[37]

Mass energy absorption coefficients influence dosimetry. The mixture rule can be used to determine the mass energy absorption coefficient for a compound from the absorption coefficients of its constituent elements. The mass energy absorption coefficient has to be weighted by the incident x-ray spectrum, as the incident x-ray beam is not monoenergetic. It was done by applying the program written by Mr E de Kock[37]. The mass energy absorption coefficients and mass attenuation coefficients, as published by Hubbell and Seltzer[38] for energies from 1 keV to 20 MeV and elements with atomic numbers from 1 to 92, as well as for 48 additional dosimetric useful materials, were used for the calculations.[38] An example of the input file, with absorption coefficient and energy pairs, and the output file, with the spectral weighted mass energy absorption coefficient for certain thicknesses of attenuating human muscle tissue, is shown in Figure 2.6.

a.)

[X-RAY TUBE PROPERTIES]
Tube voltage (kVp) = 60.0
Angle of anode (degrees) = 12.0
Percentage rhenium in anode = 5.0
Total aluminium filtration thickness (mm) = 2.5
Tube cooling oil thickness (mm) = 1.5
Tube glass window thickness (mm) = 0.5

[ABSORPTION DATA]
[Energy (keV), Absorption Coefficient (Any unit)]
Number of data points = 16

1	3.76E+03
1.5	1.27E+03
2	5.70E+02
3	1.81E+02
4	7.73E+01
5	3.96E+01
6	2.27E+01
8	9.38E+00
10	4.68E+00
15	1.30E+00
20	5.23E-01
30	1.49E-01
40	6.67E-02
50	4.09E-02
60	3.11E-02
80	2.55E-02

b.)

X-RAY SPECTRUM WEIGHTED ABSORPTION COEFFICIENT
X-RAY TUBE PROPERTIES:

Tube voltage (kVp) = 60.0
Angle of anode (degrees) = 12.0
Percentage rhenium in anode = 5.0
Total aluminium filtration thickness (mm) = 2.5
Tube cooling oil thickness (mm) = 1.5
Tube glass window thickness (mm) = 0.5

RESULTS:

Attenuating material = Human tissue
THICK = Thickness of attenuating material (cm)
SWATTCOEFF = Spectrum-weighted absorption coefficient (units of input data)

THICK	SWATTCOEFF
0.00	1.333099E-01
1.00	1.175817E-01
2.00	1.064315E-01
3.00	9.804714E-02
3.50	9.457611E-02
4.00	9.147689E-02
5.00	8.616878E-02
6.00	8.177835E-02
7.00	7.807831E-02

Figure 2.6: a.) Energy and mass energy absorption coefficient input file. b.) Spectral weighted mass energy absorption coefficient, with muscle attenuator, output file.[37]

Bushberg et al[1] mention several factors that influence the emission of x-rays. These include the target material, tube voltage (kV), tube current (mA), exposure time (s), beam filtration and the generator waveform.[1] In the current study the target material and generator waveform could not be changed. Because of neonatal movement the exposure time has to be as short as possible to decrease the chance of motion artefacts. The product of the tube current and exposure time, in mAs, is directly proportional to dose. The factors that could be changed and varied in the current study are therefore kV, mAs and filtration.

Bushberg et al[1] describe the output of an x-ray tube in terms of beam quality, i.e. beam energy or penetrability, and beam quantity, or the number of photons in the beam. The kV influences the energy of the x-ray spectrum, thus the beam quality, but it also affects the efficiency of x-ray production. Therefore x-ray exposure is proportional to the kV^2. An increase in kV increases beam penetrability and energy and results in a contrast reduction. The mAs determines the number of electrons flowing from the anode to the cathode, and therefore influences the beam quantity. An increase in mAs gives a beam intensity increase, which affects image darkening. Filtration removes low energy photons from the x-ray spectrum, creating a hardened spectrum, i.e. increased beam quality and reduced beam quantity. If the kV is increased, mAs should be decreased to obtain the same exposure, which implies a dose reduction. A rule of thumb calculation for the relationship is shown in Equation 2.14.[1]

$$mAs_2 = mAs_1 \times \left(\frac{kV_1}{kV_2}\right)^2 \qquad \text{[Equation 2.14]}$$

Equation 2.14 was applied in this study to estimate different kV and mAs combinations that would give comparable, and therefore acceptable, image quality.

2.4 Neonatal simulation phantoms

A tissue simulating material is suitable only if it mimics the density and elemental composition of real tissue since these properties determine the radiation interaction characteristics, i.e. attenuation and absorption properties, of a material. Many readily available materials, for example perspex, metals and foams, simulate only the density of the real tissue. Such a material is acceptable if only image quality is assessed, but these materials are not suitable for radiation dosimetry. The dosimetry of an incident radiation beam is influenced by the elemental composition of a material, and therefore a tissue simulating material has to match this aspect of the real tissue as well.

Constantinou[39] states that "the following quantities must be identical for the phantom material and the tissue it simulates, if the two are to absorb and scatter any type of radiation in the same way: (1) photon mass attenuation and mass energy absorption coefficient; (ii) electron mass stopping power and mass angular scattering power; (iii) mass stopping power and angular scattering power for heavy charged particles and heavy ions; (iv) neutron interaction cross section or kerma factors…the mass densities of the two must be the same."[39] Such equivalence can only be achieved if the substitute material has the same elemental composition, in the same proportion by weight, as the real material. The elemental composition of real tissue also varies. For example, the calcium content of paediatric bone is less than that of adult bone. Since calcium content of bone decreases with ageing such differences are important in radiation dosimetry.[39]

Reliable composition and density data are needed for radiation dosimetry and tissue substitute analysis. Tables of mass density, mass attenuation and mass energy absorption coefficients are published for a range of photon energies, from diagnostic kilovolt (kV) to therapeutic megavolt (MV) energies, for different elements and compounds. These were originally published by Hubbell in the International Journal of Applied Radiation and Isotopes in 1982.[40] More recent tables have been published by Hubbell and Seltzer[38] in 1995 and these are available on the website of the National Institute of Standards and Technology (NIST).[38] The current study employs these tables.

The elemental composition of body tissue changes continuously, for example in the process of ageing, and therefore appropriate foetal or neonatal data must be considered in the current study. White et al[6] published such data, representative of the general population, and commented that skeletal muscle makes up a quarter of the mass of a neonate and can therefore be considered as the comprising body tissue. The elemental composition and mass density of foetal lung, in the age group 17 - 40 weeks of gestation, newborn skeletal muscle and newborn cortical bone are also reported. These are shown in Table 2.2.

Table 2.2: Elemental composition analysis of body tissues and bone.[6]

Tissue	**Elemental composition (% by mass)**											**Mass density (kgm^{-3})**
	H	C	N	O	Na	P	S	Cl	K	Ca	Mg	
Foetus lung (17-40 weeks)	10.6	7.6	1.8	79.2	0.2	0.2	0.1	0.2	0.1	0.0	0.0	1040
Newborn skeletal muscle	10.4	10.3	2.4	76.2	0.1	0.1	0.1	0.2	0.2	0.0	0.0	1050
Newborn cortical bone	4.4	15.3	4.1	47.7	0.1	8.5	0.2	0.1	0.0	19.4	0.2	1720

Tissue equivalence was determined by applying the elemental equivalence method by Constantinou[39]. A compound was made up of different elements or mixtures to arrive at a chemical formula almost similar to real tissue. It meant that the chemical formula for a compound could be broken down into a combination of constituent formulae. For example soft tissue, $C_5H_{40}O_{18}N$, could be written as $0.5[CH_2N_2(H_2O)] + 1.5[C_3H_2(H_2O)_3] + 13[H_2O]$. Here $CH_2N_2(H_2O) = NH_2CONH_2$, which was urea, and glycerol was $C_3H_2(H_2O)_3 = C_3H_8O_3$.[39]

Photon beam energies in diagnostic radiology are low and the tissue mimicking characteristics of a substitute material are energy dependent. Jones et al[42] developed radiographic newborn soft tissue, bone and lung tissue equivalent materials based on mass density, mass energy absorption and mass attenuation coefficients over an energy range of 10 keV to 150 keV for computed tomography (CT) scanning. Epoxy resin bases with phenolic spheres were used and the Oak Ridge National Laboratory tissue compositions were used as reference. The mass attenuation and mass energy absorption coefficients, as previously published by White et al[41], were matched iteratively by the researchers. Phenolic spheres were then added to match the mass densities. Final material composition adjustments were made to match the interaction coefficients over the desired diagnostic energy range.[42]

All the substitutes consist of Araldite GY-6010 epoxy resin with Jeffamine T-403 as hardener. The soft tissue and lung materials contained polyethylene, silicon dioxide and magnesium oxide as added materials. The bone substitute had polyvinyl chloride, silicon dioxide and calcium carbonate additives. The lung material was finished with a foaming process that used DC 1107 and DC 200/50 as foaming and surfactant agents.[42]

Mass densities of the substitute materials were calculated from the density of water and dry mass and buoyancy of the material. The radiation interaction coefficients were calculated from data published by Hubble and Seltzer[38]. The proposed material mass attenuation coefficients underestimated the reference values by approximately 3%. The agreement was better at lower photon energies. The mass energy absorption coefficients were overestimated by 1 - 2% at low energies and underestimated at higher energies. Overall, the proposed materials compared well to the reference material characteristics and the authors could construct a neonatal CT phantom using it.[42] Although Jones et al[42] reported a good match to real tissues, data on the actual manufacturing of the substitutes were not provided. Therefore, other possible phantoms, as discussed in literature, were considered.

Brindhaban and Al-Khalifah[15] used a water filled one litre bottle to simulate a 1000 g neonate. Film cassettes were placed on the mattress directly below the neonatal

phantom. ESD was measured and effective doses were calculated. The researchers reported that differences between their results and real neonates could be expected as a result of differences in physical size and mass and differences in energy absorption between real tissue and water.[15] This phantom was a crude radiological approximation and in no way anatomically representative of a real neonate. Analysis of image quality could not be done as this phantom contained no structures for inspecting visual image quality. For the purposes of this study an improvement on the phantom described by Brindhaban and Al-Khalifah was therefore essential.

In a study by Vergara et al[43] a PMMA perspex phantom with different TLDs was used. The phantom was made out of various rectangular slabs to simulate a neonate's head, chest and abdomen, as shown in Figure 2.7. To represent lungs, air gaps were created by removing the slabs that had been placed on each side of the chest area.[43]

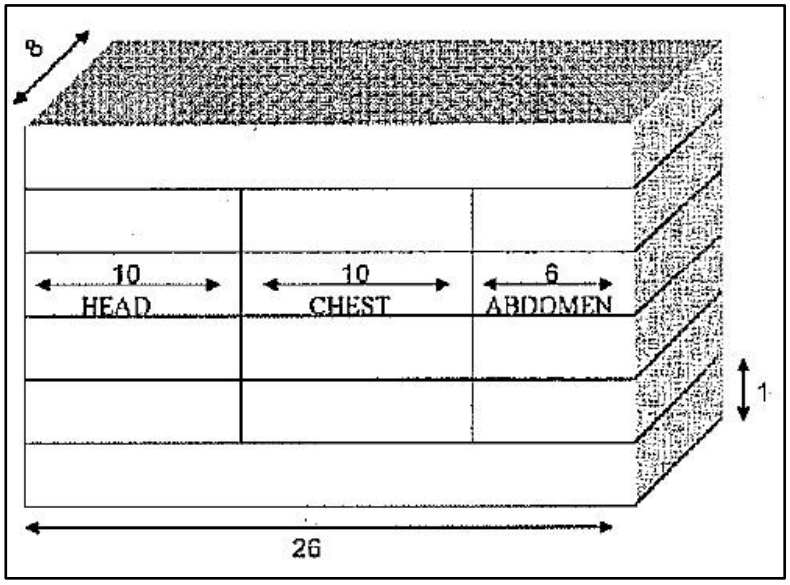

Figure 2.7: A PMMA phantom (dimensions in cm) simulating a neonate.[43]

Clearly, this was an uncomplicated simulation of a neonate. Although it was not an anatomical or radiological equivalent of a real neonate, it was a substantial improvement on the water bottle phantom of Brindhaban and Al-Khalifah[15].

Neonatal simulation phantoms were also designed by Duggan et al[28]. These phantoms simulated 700 g and 2000 g neonates. The tissue equivalent materials used were white water and lung equivalent inserts, from PTW Freiburg, Germany. Figure 2.8 shows the design for the 700 g phantom. The dimensions for the 2000 g phantom were 100 x 250 x 70 mm^3 with insert dimensions 60 x 80 x 20 mm^3. Image quality assessment tools were inserted into the phantom, which included a contrast resolution tool, made from the white water material and consisting of holes of different depths and diameters, and a line pair resolution gauge. Holes were also made in the phantom to accommodate TLDs for dose measurements.[28]

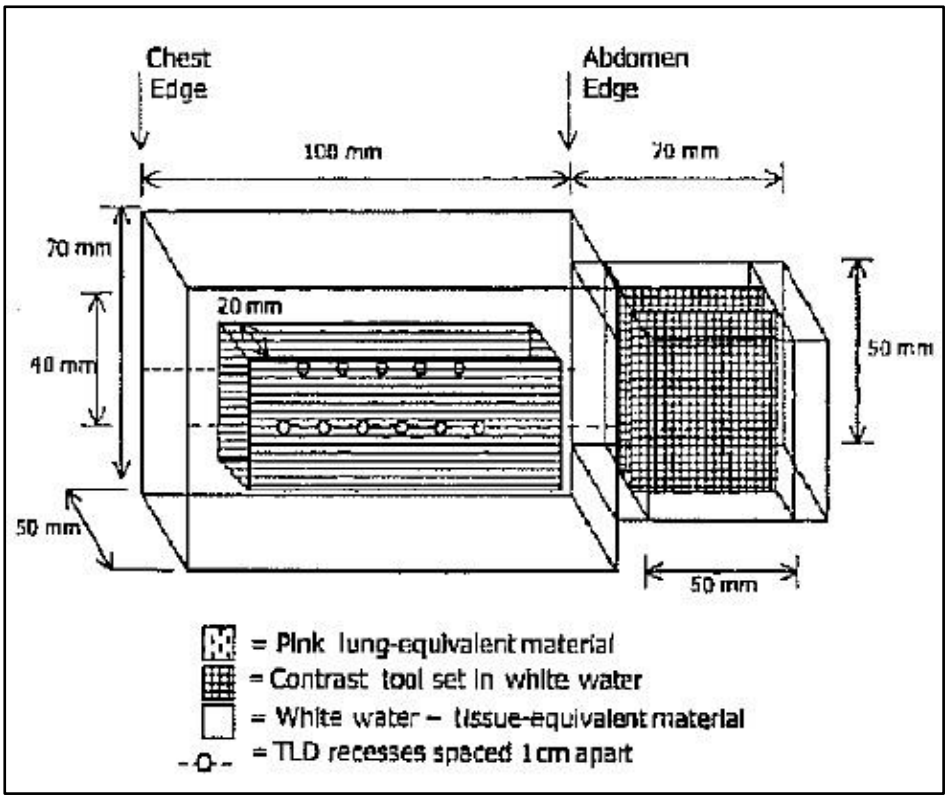

Figure 2.8: 700 g neonatal simulation phantom.[28]

Although the phantom offered an improved radiological simulation, using tissue equivalent lung material and white water, it still did not simulate neonatal anatomy accurately as it did not take the shape of lungs or the presence of bones into account. It contained image quality quantification tools, but the researchers failed to assess image quality visually. Here anatomical equivalence was improved and quantified image quality was assessed. However, clinical image quality was not considered and a low dose radiograph of poor clinical quality was unacceptable and useless.

Akahane et al[29] constructed a neonatal simulation phantom from rectangular solids, based on a mean body size, determined from head, chest and abdomen measurements of real neonates. Tough water and lung phantom materials from Kyoto Kagaku Co Ltd were used to simulate soft tissue and lungs. Bones were omitted from the phantom. The mass of the phantom was 1990.5 g and its height was 43.5 cm. Its lungs were not symmetrical due to the volume of the heart. The phantom is shown in Figure 2.9.[29]

Figure 2.9: Neonatal simulation phantom.[29]

Akahane et al[29] stated that although the phantom was sturdy and easy to handle, it did not represent the exact shape of a neonate. The lack of bones could also affect dose measurements. They mentioned that at the time of publication (IRPA 10, May 2000) of their article a "neonate physical phantom involving skeleton material has not been reported".[29] Their phantom was a further improvement on the previously mentioned phantoms since body shape was more accurately accounted for and the manubrium area was also simulated. The proposed neonatal chest simulation phantom in this thesis did not simulate a manubrium area, but it did contain bone material.

Seifert et al[44] proposed to use a rabbit as a test subject. Several x-rays were taken of a rabbit, with added filtration of 1 mm Al + 0.1 mm Cu and different mAs settings. The quality of the rabbit images was assessed by different radiologists. Images were still clinically acceptable at 66 kV with the added filtration, on a film-screen system. As real tissue was used this was possibly the closest anatomical and radiological approximation to a real neonatal chest, although slight differences would exist between neonatal and rabbit tissue. The real tissue of a rabbit is clearly a better substitute than plastic material. However, at most institutions rabbits were not readily available for research purposes and special ethical committee approval was needed for animal studies. A phantom was easier to handle, required no ethical committee approval and could be used at any institution.

The phantom designed in the current study simulates a neonate more closely than those described in literature, both anatomically and radiologically. The only phantom found in literature theoretically superior to the proposed phantom is a commercially available anthropomorphic phantom, the Gammex RMI© 610 phantom, as shown in Figure 2.10.[45] The phantom is designed for computed radiography (CR) and digital radiography (DR) diagnostic x-ray systems. It is stated that the Gammex phantom simulates a 1 - 2 kg neonate anatomically and has the same radiation attenuation characteristics as a real neonate.[45]

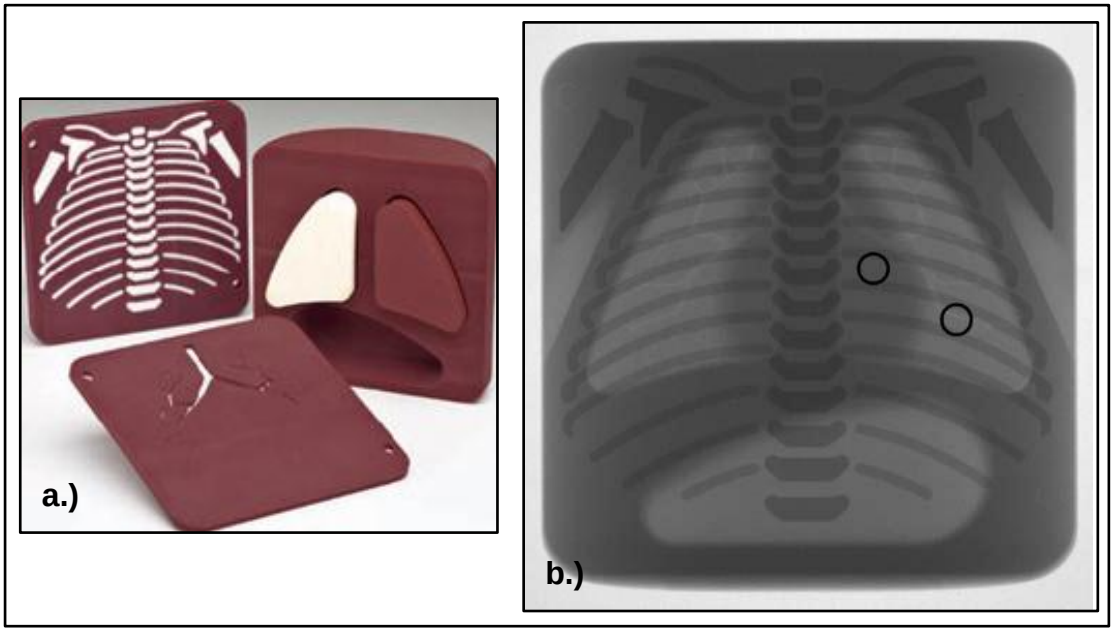

Figure 2.10: a.) The Gammex RMI© 610 Neonatal Chest Phantom.[45] b.) An inverted radiograph of the Gammex RMI© 610 Neonatal Chest Phantom.[21]

The Gammex RMI© phantom simulates a lung with pneumothorax, pleural thickening and hyaline membrane disease. The use of the phantom addressed image quality and radiation dose concerns with digital x-ray imaging, such as the greyscale scaling of over exposed images leading to “dose creeping”.[45]

In the current study, leading to a master’s degree in Medical Physics, it was decided, using basic medical physics principles, to design and develop an anatomical and radiological simulation phantom of a neonatal chest is more appropriate than using rabbit tissue as a simulated phantom of a neonate or a commercially available phantom. The phantom proposed in this thesis simulates a real neonatal chest anatomically, considering muscle as the main comprising body material, healthy and sick (hyaline membrane disease or collapsed) lung and bone (ribs and vertebrae). It is also radiologically similar to real neonatal tissues, in terms of tissue density, elemental composition and attenuation, scatter and absorption characteristics.

Chapter 3

Methods and materials

The design, construction and evaluation of a neonatal chest simulation phantom and a physics image quality assessment phantom are discussed. Dose reduction techniques, with maintenance of acceptable clinical image quality, and the possible reduction in the risk for cancer induction are recorded.

3.1 The design of a neonatal chest simulation phantom

The success of the current study depended on the construction of a phantom that was anatomically and radiologically equivalent to a real neonatal chest. As seen from literature different approaches to simulation phantoms exist but none of these phantoms satisfied both anatomical and radiological equivalence, except possibly the commercial Gammex RMI© anthropomorphic phantom[45]. It was challenging to construct a phantom that would be an exact equivalent of a neonatal chest anatomically and radiologically. The lack of a suitable neonatal chest simulation phantom led to the decision to design such a phantom that would meet the highest level of neonatal equivalence achievable.

3.1.1 Anatomical equivalence

Approval was obtained from The Health Research Ethics Committee of the University of Stellenbosch (Ethics reference number: N10/12/400) to perform a Computer Tomography (CT) scan on a neonatal cadaver. (see Appendix A) The cadaver was a seven month old preterm foetus obtained from the Anatomy and Histology Department, Faculty of Health Sciences, University of Stellenbosch. A CT scan was performed on the cadaver and used to obtain actual anatomical information that was needed to construct the neonatal chest simulation phantom for the current study.

The size and position of the lungs, sternum, ribs and vertebrae had to be established, as well as the chest circumference. A CT scan was performed on the cadaver at iThemba LABS, Faure, on a Philips Brilliance CT Big Bore configuration scanner. The quality assurance of the CT scanner was performed by a medical physicist and SANAS accredited Inspection Body. The CT scan was performed at 120 kV and 30 mA. A scan length of 400 mm was used, with 1 mm contiguous slice width. The CT reference was on the sternum of the cadaver. Reconstructions were performed with bone and soft tissue filters. A cylindrical object of known size was placed at the feet of the cadaver, to check possible scaling and magnification. Measurements were obtained with the available software tools on the CT scanner.

In Figures 3.1 to 3.6 below, arrows are used to indicate how the different measurements were obtained. In these measurements, thickness refers to the anterior-to-posterior dimension, length to the longer and width to the shorter of the remaining two dimensions.

For lung dimensions the scout views, as shown in Figure 3.1, were used. The lungs of the cadaver were not yet air filled, therefore the assumption was made that the lungs would have filled the inner cavity of the chest, from the midline to the ribs on the AP view and from the vertebrae to the ribs on the lateral view.

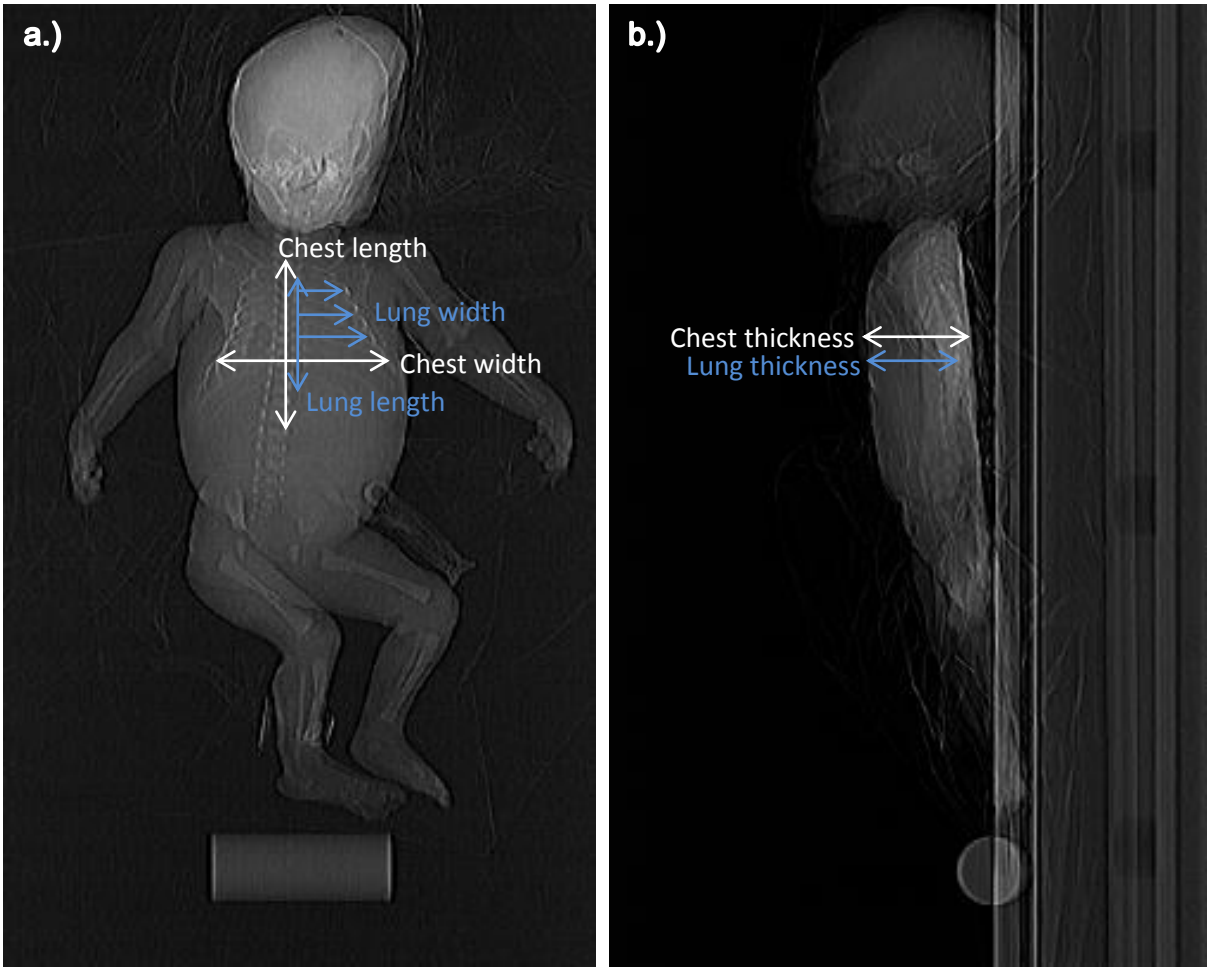

Figure 3.1: a.) AP CT scout view of neonatal cadaver. b.) Lateral CT scout of neonatal cadaver.

The sternum was measured on transverse slices of a bone reconstruction of the CT scan. In the cadaver the sternum was not yet fused and therefore consisted of three bony segments. The distance between these segments was determined by counting the number of transverse slices between appearances of the sternal segments. The thickness and width of the segments were measured on the transverse slices and the length was determined by counting the number of consecutive transverse slices on which the segment was seen. The depth of the sternal segments below the skin surface was measured from the transverse slices. Although not perfect cuboids, the sternal segments were assumed to be such for simplification of material machining for construction of the phantom. An example of the transverse slices used is shown in Figure 3.2.

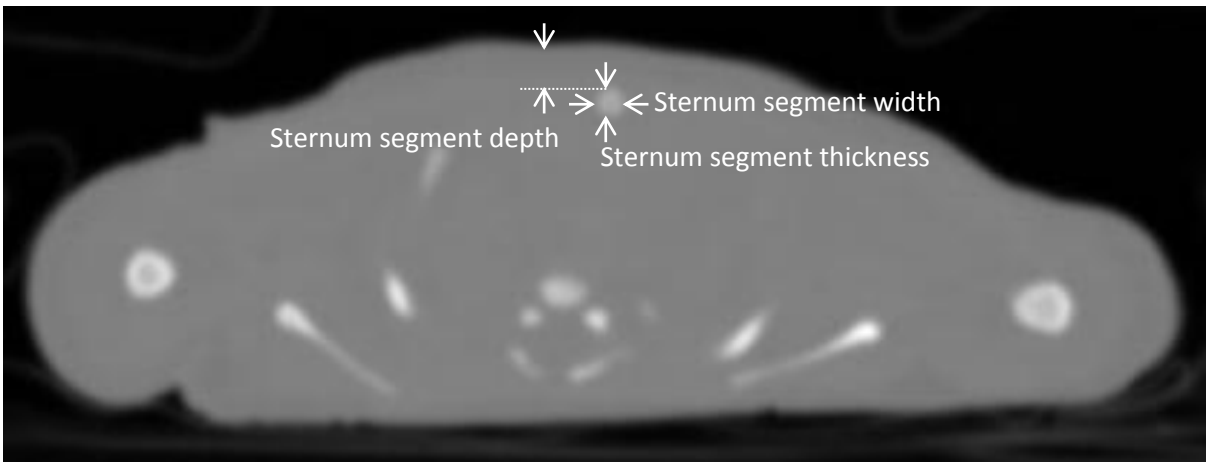

Figure 3.2: Transverse slice for sternal segment measurements.

As shown in Figure 3.3, the image of the cadaver was rotated, with software tools available on the CT scanner, to project the sternal segments centrally on the vertebral column. This view was used to measure the lengths of the anterior ribs. The anterior ribs were defined as those parts of the ribs that were projected over the lungs, i.e. those rib segments anterior to the lungs. The total distance covered by the anterior ribs in the chest cavity and the intercostal spaces were also measured from this view. The thickness of the anterior ribs was measured on the bone reconstruction transverse slices, for example as in Figure 3.4 below. Multiple measurements were performed and an average was found for simplification of phantom machining.

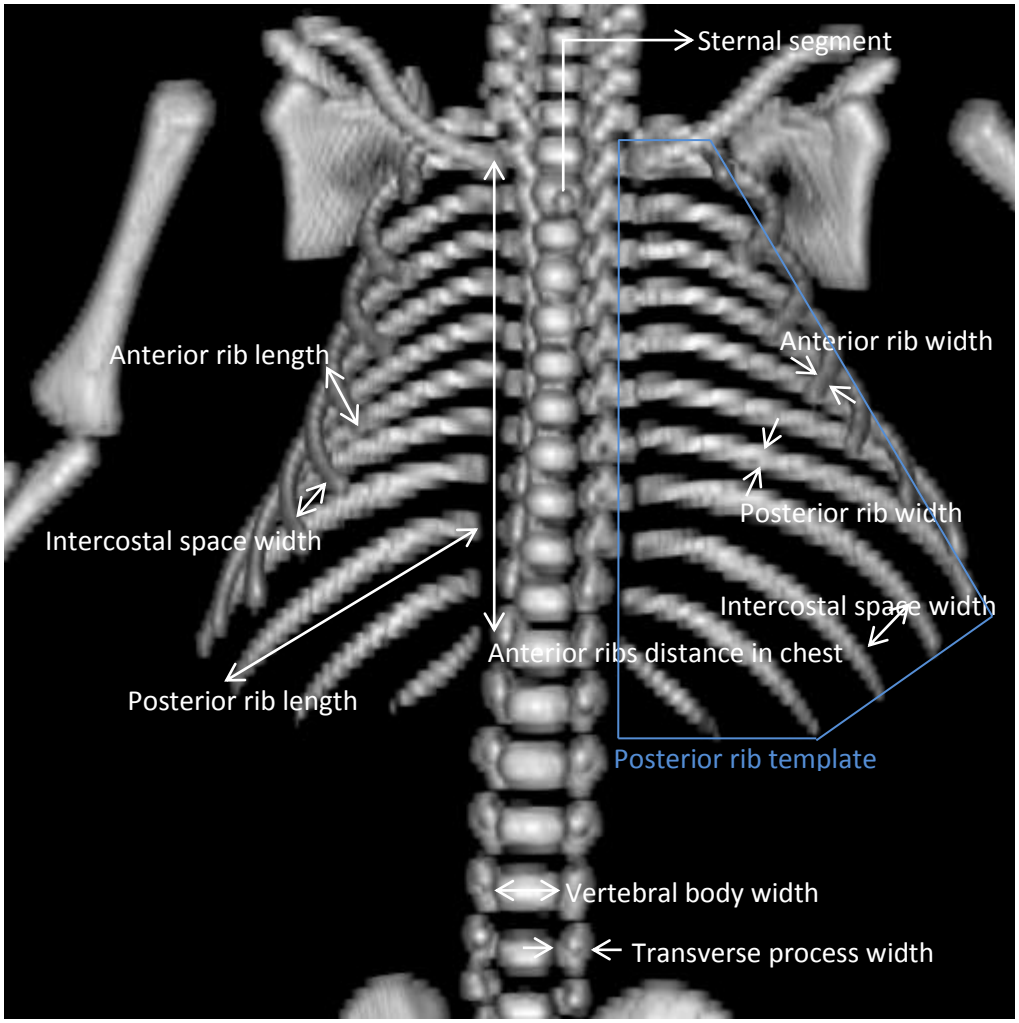

Figure 3.3: Rotated view for measurements.

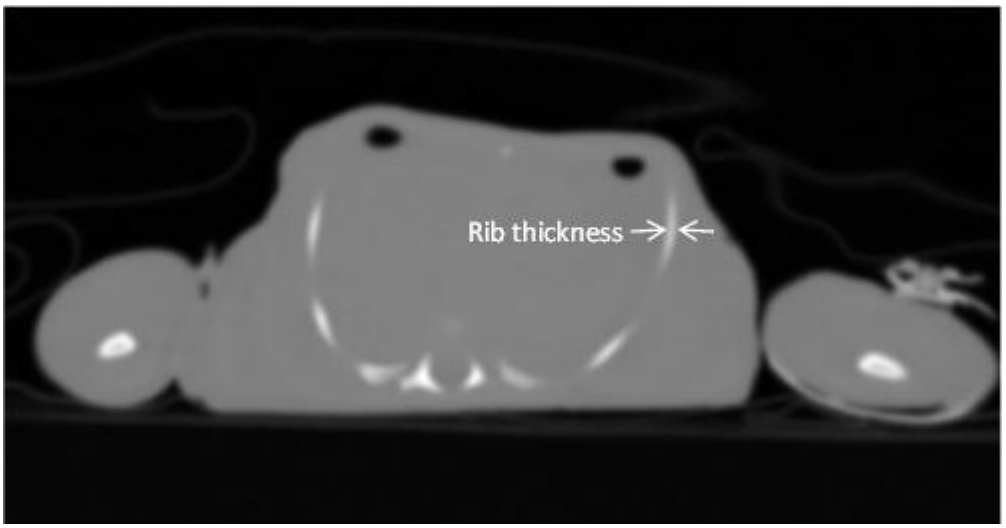

Figure 3.4: Transverse slice for measuring rib thickness.

The thickness of the posterior ribs was assumed to be the same as that of the anterior ribs. The length and width of the posterior ribs, as well as the width of the intercostal spaces, were measured on the rotated view in Figure 3.3. As a simplifying assumption the slight curvature of the posterior ribs was disregarded. These measurements were used to construct a posterior rib template, which, although simplified somewhat for machinability, simulated the posterior ribs of the cadaver quite well. Figure 3.3 shows the template outline. It was furthermore assumed that the left and right sides of the cadaver would be symmetrical if it lay in an anatomically correct AP position.

The thicknesses of the vertebral bodies and spinous processes were measured from Figure 3.5 on a spine window setting. The thicknesses of all the visible vertebrae were measured and an average was determined for phantom machining simplification. It was also assumed that the vertebral bodies and spinous processes were solid without a soft tissue gap between the two bony structures. The widths of the vertebral transverse processes and the vertebral bodies were measured on Figure 3.3 above.

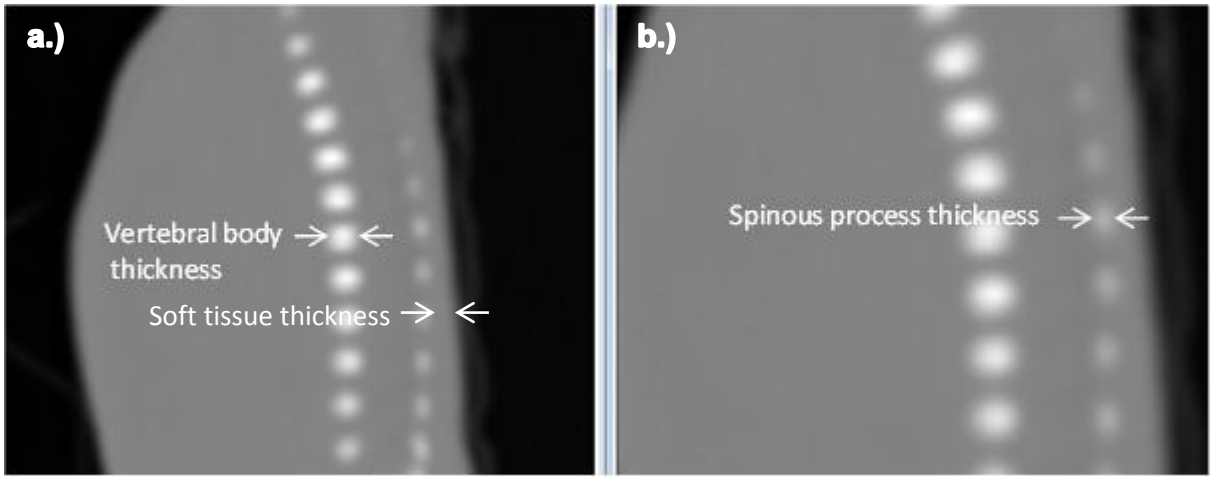

Figure 3.5: a.) Vertebral thickness measurements. b.) A zoomed in version of image a.).

As the vertebral column extended over the full length of the cadaver chest and the length of intervertebral spaces were smaller than those of the vertebrae, a simplifying assumption was again made that the vertebrae formed a solid column with a length equal to that of the entire chest. The thickness of soft tissue posterior to the vertebral column was averaged from measurements on Figure 3.5.

The chest length and width were measured on the anterior CT scout image in Figure 3.1 a.). The thickness of the cadaver chest was measured on the lateral scout image in Figure 3.1 b.). The averages of measurements at different locations were used for phantom construction.

The object placed at the feet of the cadaver for scaling and magnification checking was a cylinder of 70 mm length and 28 mm diameter. Figure 3.1 a.) and b.) were used to measure the length and diameter of the cylinder. From these measurements possible magnification or scaling could be checked.

The thickness measurements of the different structures in the chest were combined in a sectional view to show what the total overall thickness of the chest would be. It was compared to the measured chest thickness value, and also to chest thicknesses obtained from measurements at the Skills Laboratory at the Tygerberg Medical School Campus. Average sizes and dimensions were calculated from measurements at different locations for the structures incorporated into the neonatal phantom chest. Shapes of structures were also simplified into less rounded and more geometrical shapes. It was done to simplify the machining of the plastics and to take minimum achievable machining limits into account. All of these measurements and assumptions were combined to design a neonatal chest simulation phantom that simulated a real neonatal chest anatomically to a large extent.

3.1.2 Radiological equivalence

To be radiologically equivalent, the phantom had to be similar to a real neonatal chest in density, elemental composition, or mass fraction by weight, and attenuation, scattering and absorption characteristics. The substitute materials selected for the phantom had to be easily obtainable and cost had to be considered. These factors, and a range of possible substitute materials, were referred to in literature.

A variety of possible substitutes, as mentioned by White et al[6], ICRU[46] and Gammex RMI©[47], were considered for neonatal muscle, normal or healthy lung, sick or deflated lung and bone. For muscle these included Frigerio gel, RM/G1 gel, Rossi gel, Polystyrene, Temex, Gammex solid water and Agar gel mix, an in house developed option. Muscle was selected as the substance forming the body of a neonate, as it made up about 25% of the mass of a newborn and therefore contributed more to total body mass than any other structure or organ, as reported by White et al[6]. Griffith lung, LN10/75 and Gammex LN300 were considered for healthy or inflated lung. The options for sick or deflated lung were Polystyrene, Gammex CT solid water and Gammex solid water. The possible bone substitutes were SB5, B110 and Gammex SB3.

All the possible substitutes were compared to the equivalent real tissues with regard to elemental composition, density, total attenuation coefficient, Compton scatter coefficient and spectral weighted mass energy absorption coefficient. Obtainability, cost and ease of machining or working with the materials were also considered. The different substitute materials were each scored in order to determine the best possible substitute for real neonatal tissue. The scoring system is included in Table 3.1.

Table 3.1: Scoring system for neonatal chest simulation phantom substitute comparison.

Conformity to criterion	**Score**
Excellent	5
Very good	4
Fair	3
Poor	2
Not at all	1

3.1.2.1 Density and elemental composition matching

The densities, in units of kg/m^3 or g/cm^3, and elemental compositions, or mass fractions by weight, of real neonatal muscle, healthy and sick lung and bone, and those of all the different substitutes, were tabulated in literature.[6,46,47] For Agar gel mix these were calculated, as in Appendix B. The Agar gel mix consisted of 4% Agar ($C_{12}H_{18}O_9$),[48] 10% sucrose ($C_{12}H_{22}O_{11}$) and 86% water (H_2O). For the mixture the mass fraction was calculated for the chemical formulae of its constituent compounds. Its density was measured as the quotient of the mass, of a certain volume of Agar gel mix, by the associated volume.

The different substitute densities were normalised by the real tissue density by division of the substitute density by that of the corresponding real tissue. The results were displayed graphically. A value of 1 would be indicative of a good simulation of tissue density. An example of the normalisation is shown in Equation 3.1.

$$\frac{Parameter_{substitute}}{Parameter_{real\ tissue}} \qquad \text{[Equation 3.1]}$$

Elemental compositions were tabulated and plotted for a graphic display of substitute versus real tissue coincidence.

3.1.2.2 Attenuation and scatter coefficients

The total attenuation coefficients and incoherent or Compton scatter coefficients, in units of cm^2/g, were calculated from the mass fractions using the XCOM program. It was done for real and substitute materials using the mass fractions by weight as obtained from literature (refer to section 3.1.2.1). The calculations were done over an energy range of interest in neonatal chest imaging. The results were again normalised to real tissues, as demonstrated in Equation 3.1 above, and displayed graphically.

3.1.2.3 Mass energy absorption coefficients

Hubble and Seltzer[38] published in tabular form the mass energy absorption coefficients for energies from 1 keV to 20 MeV for elements with atomic numbers from 1 to 92. It was also published for 48 additional substances of interest in radiation dosimetry. For the energies of interest in the current study these tables were used to obtain the different coefficients.

As the possible tissue substitute materials were mixtures or compounds consisting of different elements, the mixture rule, as in Equation 2.13, was used to calculate the compound mass energy absorption coefficient, at a specific energy, from its constituent elemental mass fractions and mass energy absorption coefficients. The mixture rule was first proven to hold for mass energy absorption coefficient calculations by calculating the coefficient for water, A150 and adipose tissue with the mixture rule and comparing it to the published tabulated values.

The spectral weighted mass energy absorption coefficient determination program of Mr EA de Kock[37] was then used to calculate a single value for the spectral weighted mass energy absorption coefficient for each of the possible substitute materials as well as for the true body tissues. Calculations were done for the emission spectrum, i.e. with no attenuator or 0 cm muscle thickness, and for different thicknesses of muscle, to take beam hardening effects due to attenuation in the phantom into

account. The results for the possible substitute materials were normalised to that of the corresponding real neonatal tissues, as shown in Equation 3.1.

3.1.3 Obtainability and cost

The possible substitute materials were evaluated on cost and obtainability. Although some substitutes simulated the real tissues quite accurately, the chemical formulae and method of preparation were not readily available at expected sources and therefore these substitutes could not be considered for use. The majority of the substitutes of which costs could be established were very expensive. It was a requirement of this project that the phantom substitute materials should be easily obtainable and relatively economical.

3.1.4 Validation of the phantom

The average intensities and standard deviations in regions of interest (ROIs) in the healthy and sick lung, bony and muscle regions of the phantom were compared to those obtained from an x-ray of a real neonate. Averages were calculated from three ROIs in each of the structures at different locations. Both exposures were made at 50 kV, 2 mAs and inherent filtration at 100 cm FFD. The real neonatal image was obtained on a mobile imaging unit and the image of the neonatal chest simulation phantom on the fixed x-ray unit at the Oncology Division at Tygerberg Academic Hospital. This method of validation was also suggested in literature by Duggan et al[28].

3.2 The design of a physics image quality assessment phantom

Physics image quality quantification was essential. As this thesis was for a Medical Physics Master's degree, a physics phantom for image quality analysis was designed, as shown schematically in Figure 3.6.

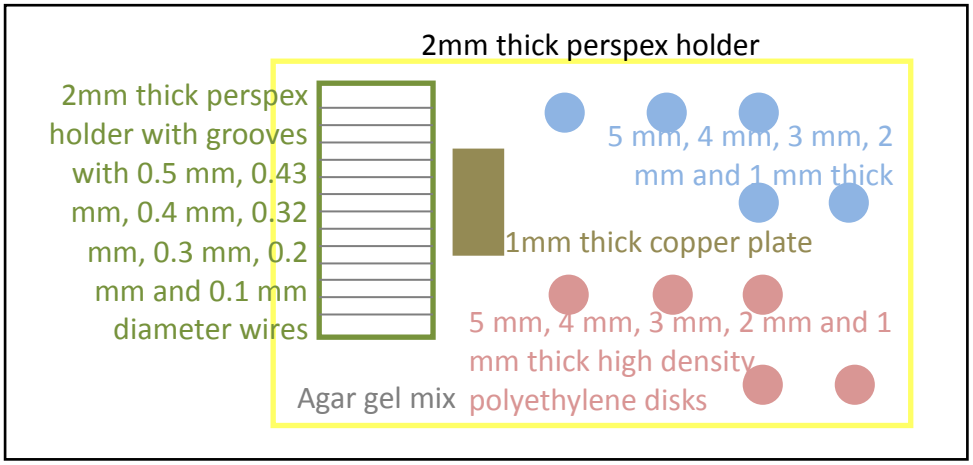

Figure 3.6: Schematic representation of physics image quality assessment phantom.

All the inserts were placed mid plane in the phantom. Agar gel mix was poured into the perspex holder to a depth of 3.5 cm. It was allowed to set. The physics test objects were then placed on the set gel and the phantom was filled with Agar gel mix. After the Agar gel mix was completely set, the phantom was wiped down with Sporekill and covered with clear plastic cling wrap to prevent contamination as Agar is a growing medium for bacteria and fungi. The phantom was then used for physics image quality quantification.

The perspex holder with the grooves housing different diameters of wires was used to determine the spatial resolution of the image in terms of the modulation transfer function (MTF) using Equation 3.2 below. In Bushberg et al[1] spatial resolution is defined as the ability of the imaging system to distinctly represent two objects as they came closer together and got smaller.[1] A MTF is an illustration of the recorded percentage contrast of an object as a function of its size. The size of an object is its

spatial frequency. Low spatial frequencies indicate large objects and small objects are represented by high spatial frequencies.[1] The spatial resolution was also determined from the copper plate, by using an edge spread function (ESF) to calculate the MTF. It was done in Microsoft Excel. The results from these two methods of MTF determination were compared.

From the Goodfellow catalogue[49], the density of torlon was 1.42 - 1.46 g/cm^3 and that of high density polyethylene was 0.95 g/cm^3.[49] These materials were selected for the image quality phantom to assess low contrast detectability, as the densities were above and below that of the Agar gel mix. Contrast is defined as the difference in the optical density or grey scale levels between two regions in an image that are next to each other.[1] By introducing different thicknesses of these materials it was possible to determine contrast resolution in terms of the thinnest disk visible. These disks were also used to calculate SNRs, SDNRs and contrast-to-noise ratios (CNRs).

3.3 Image quality analysis

Image quality was analysed for the physics image quality assessment phantom and for the neonatal chest simulation phantom.

With the physics image quality assessment phantom, only the final set of exposures, as derived in section 3.4, was considered. Quantitative image quality analysis was done by the principal investigator. It involved the calculation of MTFs, SNRs, SDNRs and CNRs. Low contrast detectability was also determined. The evaluation process is discussed in section 3.3.1.

Visual and quantitative image quality was obtained for the neonatal chest simulation phantom for the preliminary and final exposure sets, as discussed in section 3.3.2. Visual image quality was also assessed by independent medical physicists and radiographers for the final exposure set. Visual image quality analysis was a “blind” process, where the observers did not know the exposure parameters used to obtain the images, and was based on the criteria in Table 3.2 below. For quantitative

image quality analysis SNRs, SDNRs and CNRs were calculated. It is discussed in section 3.3.2.

3.3.1 Evaluation of the physics image quality assessment phantom

Image quality was quantified with the physics image quality assessment phantom and the final set of exposure parameters. The derivation of the final exposure parameter set is discussed in section 3.4 below.

MTFs were calculated from the perspex wire holder. Three wires for each diameter were included on the holder. The diameters were 0.50, 0.43, 0.40, 0.32, 0.30, 0.20 and 0.10 mm. A profile was drawn perpendicularly across the wires in ImageJ, free image processing software. The maximum and minimum intensity values of the second wire in each set were found. These were used to calculate the MTF for each wire diameter, using Equation 3.2, as suggested by Atkins[50]. The results were plotted as a function of wire thickness.

$$MTF = \frac{Maximum\ intensity - Minimum\ intensity}{Maximum\ intensity + Minimum\ intensity} \quad \text{[Equation 3.2]}$$

The ESF of the copper plate was used to calculate the MTF for each image using Microsoft Excel. In Image J a profile was drawn across the edge of the copper plate, as shown in Figure 3.7. The plot values of the profile were imported into Microsoft Excel. Background was measured in a ROI next to the copper plate. The background value was subtracted from the plot values of the profile in Microsoft Excel. The resultant values represented the ESF for the image. The number of samples was adjusted to 32, i.e. 2^5. This was necessary for the Fourier Analysis tool in Microsoft Excel to work. Zeros were added as dummy values in order to obtain the 32 data points. The Fourier Analysis tool was used to calculate the Fourier transform of the ESF. The IMABS function in Microsoft Excel was used to calculate

the absolute values of the complex numbers, which was the MTF. This method was described by Klingenberg[51].

The matrix size of the images was 3270 x 1770 pixels, which represented the image from a 24 x 18 cm cassette. The pixels/cm/interval was calculated as half of the pixels divided by the corresponding image dimension in cm divided by 32 intervals. By multiplying these values with the interval values, i.e. multiples of 2, the pixels/cm were calculated. These were the x-axis values in a graph with MTF on the y-axis. The results of the two MTF determination methods were compared.

SNRs, SDNRs and CNRs were calculated for each of the different images by the principal investigator, a medical physicist. Figure 3.7 showed the placement of the ROIs and profile lines used for the calculations.

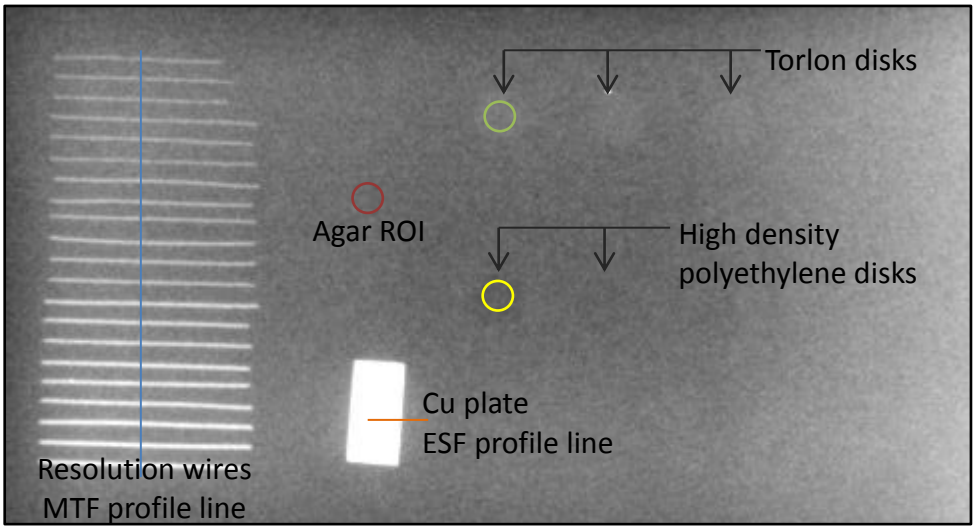

Figure 3.7: Physics image quality assessment phantom ROI and profile line locations.

SNR and SDNR were calculated with Equations 2.2 and 2.3. CNR were calculated using Equation 3.3 from Bushberg et al[1]. These calculations were done with ROIs in Image J.

$$CNR = \frac{(A-B)}{\sigma}$$ [Equation 3.3]

where A and B are the intensities in ROIs of the same size inside and right next to the disk and σ is the standard deviation or noise in the ROI next to the disk.

Low contrast detectability was evaluated with the torlon and high density polyethylene disks in the physics image quality assessment phantom. These disks had different thicknesses and their densities were 29 - 33% higher (1.42 - 1.46 g/cm^3) and 14% lower (0.95 g/cm^3) than that of Agar gel mix (1.10 g/cm^3). The thinnest visible disk was determined in each image. The thinner the visible disk was, the better the low contrast detectability was.

Image quality was deemed better if the SNR was higher, SDNR was higher, CNR was higher and the MTF graphs included more high frequency data. Based on all the analysis results images were ranked from best to worst.

3.3.2 Neonatal chest simulation phantom evaluation

The phantom was analysed visually and quantitatively by means of the preliminary and final exposure sets. No exposure factor details were present upon visual evaluation, it was therefore a “blind” process. Images were visually scored. The scoring criteria included the visibility of the central line, posterior ribs, lungs and sternal blocks, as detailed in Table 3.2 and Figure 3.8. The final exposure set images were also shown to independent medical physicists and radiographers who scored the images according to the criteria in Table 3.2.

As an example, the image in Figure 3.8 below scored 5 for sternum, as all three blocks were clearly visible, 3 for central line, as it was seen from the top of the phantom across the spinal column to the healthy lung, 3 for healthy lung as the lung was not dark and the posterior ribs were clearly visible behind the lung, 0 for sick lung as the whole lung and the medial outline were not visible and overall it obtained

a score of 5, i.e. a very good image that was usable and gave sufficient clinical data. The scoring was based on the criteria in Table 3.2 below.

Table 3.2: Clinical or visual image quality scoring criteria.

Criteria		Scoring scale	Obtained score
Sternum	All 3 blocks are clearly visible	5	
	2 blocks are clearly visible	4	
	1 block is clearly visible	3	
	1 block is partially visible	2	
	1 block is not clear	1	
	No blocks are seen	0	
Central line	Seen completely, from top of phantom across spinal column to healthy lung	3	
	Seen at top of phantom and towards healthy lung only	2	
	Seen towards healthy lung only	1	
	Not seen	0	
Healthy lung	Posterior ribs are clearly visible behind the lung	3	
	Posterior ribs are partially visisble behind the lung	2	
	Posterior ribs are not clear behind the lung	1	
	Posterior ribs are not seen/black lung	0	
Sick lung	Sick lung is totally seen	3	
	Medial outline of lung is clearly seen	2	
	Medial outline of lung is partially visible	1	
	Lung is not seen	0	
Overall	Very good	5	
	Good	4	
	Acceptable	3	
	Not good	2	
	Poor	1	
	Unusable	0	

Furthermore, the images of the neonatal chest simulation phantom were investigated quantitatively. SNRs were calculated for the sick and healthy lungs, with equal sized ROIs placed in the lungs at the same location in all of the images, as shown in Figure 3.8. SDNRs were calculated for sick and healthy lung versus Agar gel mixture and CNRs were calculated for healthy lung versus bone. It was done for the preliminary and final exposure sets. The quantitative image quality ranking for the

neonatal chest simulation phantom was compared with that of the physics image quality assessment phantom.

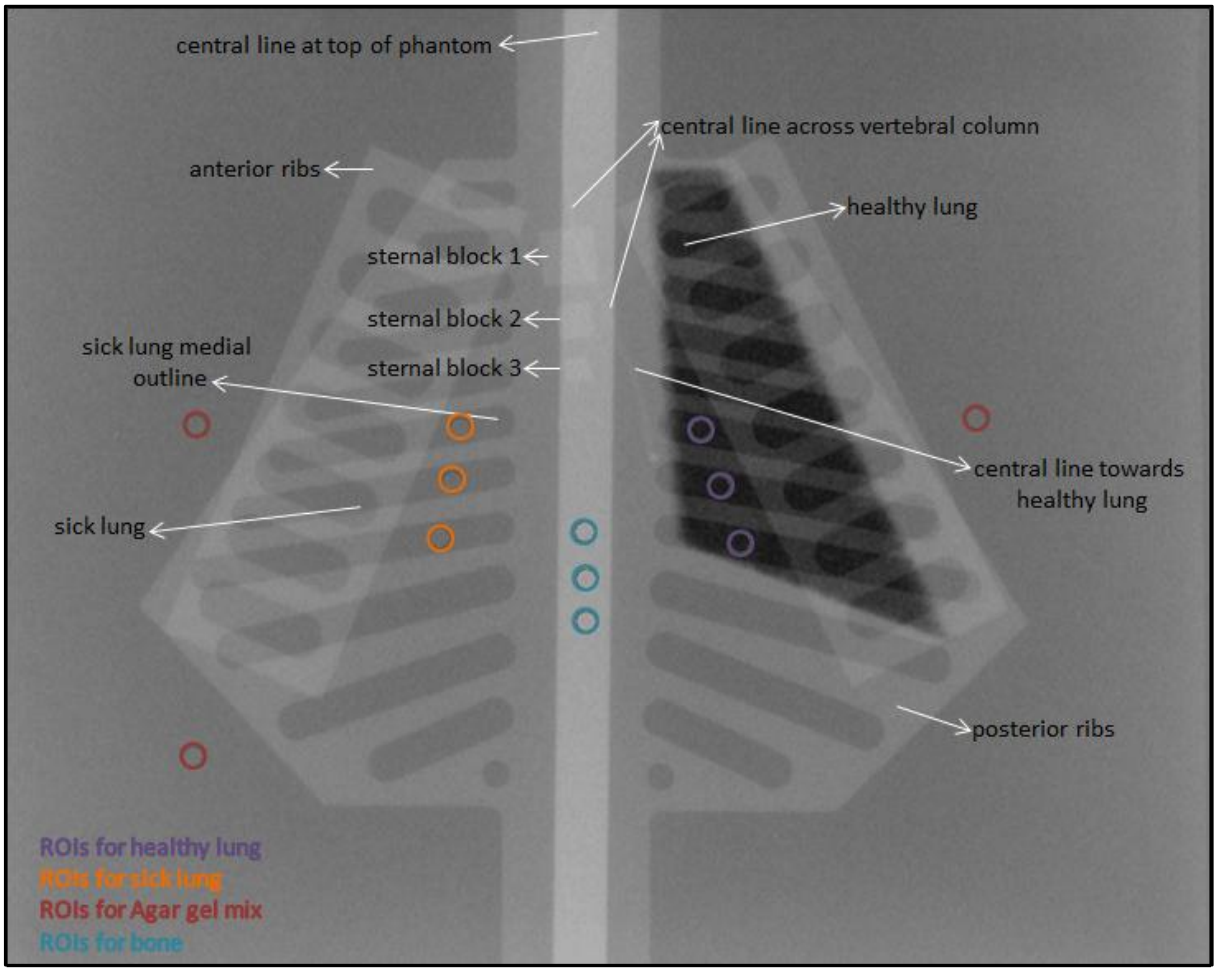

Figure 3.8: Location of quantitative ROIs and visual scoring criteria.

For the final exposure set the images were visually ranked from best to worst by independent medical physicists and radiographers. Quantitative image quality was assessed by the principal investigator. The correspondence between clinical or visual and physical image quality and delivered radiation dose was determined. The final exposure set images were ranked from best to worst based on visual and quantitative image quality and measured ESDs. These were used to make recommendations to the Diagnostic Radiology Division at Tygerberg Academic Hospital.

3.4 Dose reduction versus image quality

Various mechanisms were available to reduce the ESD, as discussed in the literature review, section 2.2. The suggestions from literature were widely ranged and mostly applicable to screen-film research. The exposure factors that did influence ESD and image quality are recorded in Table 3.3, with the ranges as suggested by the different literature studies.[13,14,15,21,28] A number of preliminary exposures were needed to determine the optimal range of exposure factors that gave a dose reduction, with little or no effect on image quality, for a CR system. It was done in a "trial-and-error" manner where doses were measured and images were acquired and analysed in order to arrive at a final set of exposures for final evaluation. The exposures of the final evaluation set were in the optimal dose reduction and image quality maintenance range.

Image analysis of the preliminary exposure sets was done on the same computer, in the same area and by the same observer. It was done in order to keep viewing conditions such as ambient light, observer eyesight and display screen resolution as constant as possible.

Table 3.3: Exposure factors and suggested ranges as found in literature.[13,14,15,21,28]

Factor	Range from literature
kV	40-80 kV
mAs	0.5-4 mAs (s as short as possible for movement)
Filtration	1-3.5 mm aluminium; 0.1 mm copper; 0.05 mm hafnium
Collimation	Tight as possible
FFD	80-115 cm

Table 3.3 was considered in four sets of preliminary exposures. Different combinations of kV and mAs settings were used and the ESD and obtained image quality were evaluated in conjunction with each other. Collimation was performed as tightly as possible, as recommended by Egan and Dowd[24] and accepted in general practice. Different FFD settings were investigated with regard to obtained ESD and

image quality, as recommended in literature.[21,28] Special attention was given to the effect of additional filtration, as the technique had proven results in literature.[21,28]

The effect of additional filtration was investigated on the fixed x-ray unit in the Oncology Division at Tygerberg Academic Hospital, although additional filtration was not available on the mobile unit routinely used to image neonates at Tygerberg Academic Hospital. This was done to obtain a full view of possible dose reductions and image quality influences. If proved effective, the research could be used as motivation for the acquisition of commercially available mobile x-ray filtration options. It included a mobile unit with additional filters on a selection dial, similar to those of the fixed unit. An example of such a unit was the Philips Practix 360, with 2 mm Al, 0.1 mm Cu + 1 mm Al and 0.2 mm Cu + 1 mm Al additional filters. Separate paediatric filters were also available from Philips. These were transparent lead containing PMMA filters, 2.4 mm or 4.3 mm thick, which were equivalent to 0.1 mm Cu + 1 mm Al and 0.2 mm Cu + 1 mm Al additional filtration at 70 kV. These could be inserted into the guide rail of the collimator of a mobile x-ray unit and would not obstruct the light field for patient setup. Another option was to fix Al and Cu plates to the exit window of the current mobile unit, although it would obstruct the light field and hinder patient setup. It therefore required extra radiographer input after patient was set up and before the x-ray was taken.

The data from each of the preliminary exposure sets were used to determine what exposures were still needed and what range of exposure factors were acceptable and useful for the current study. These preliminary exposures were made at the Oncology Division at Tygerberg Academic Hospital on a fixed Philips x-ray unit. Fujifilm FCR Fuji IP cassettes type CC 24 cm x 30 cm were used for the exposures. A PRC Eleva S Fujifilm reader was used to read out the cassettes and the images were stored on PACS. The cassette was placed below the phantom on the bed, with the required setup for that exposure. The phantom was centred on the same location repeatedly, i.e. on the manubrium for the neonatal chest simulation phantom. The images were copied from PACS onto CDs for evaluation with Image J free software. SNR, SDNR, CNR and visual image quality analysis was done on the images of the neonatal chest simulation phantom, while ESDs were also considered.

Images were acquired as raw and processed images. The raw images were obtained by selecting UM Chest Paediatrics on the reader control computer. For processed images UNIQUE Chest Portable was selected. Raw images had no inherent image processing, while image processing occurred with the processed images, to make different exposures more uniform and easier to view. Post acquisition image processing was available and used by changing window widths, i.e. contrast, and window levels, i.e. brightness, for best visualisation.

The doses for the preliminary exposure sets were measured with an Unfors XI view detector that was available at Tygerberg Academic Hospital, but the detector did not have a recent calibration traceable to a standards laboratory. These doses were therefore used for trend determination only and were not accepted as absolute doses. The detector was placed on the anterior surface of the phantom, with the same setup and parameters as used for the corresponding exposure to obtain the image. Tables 3.4 to 3.7 show the parameters for these four preliminary exposure runs. The results obtained from these exposures were used to derive the final set of exposures, which is used in image quality analysis in sections 3.3.1 and 3.3.2.

For the final set of exposures, as documented in Table 3.8, a PTW Conny II dosimeter (PTW, Freiburg), with a traceable calibration, was used for absolute ESD measurement. These exposures were made on a Shimadzu Mobile Art Evolution mobile x-ray unit using 18 cm x 24 cm Fujifilm FCR Fuji IP Cassette type CC cassettes and a Philips PCR Eleva Corado reader. The equipment was the same as that used routinely in the neonatal division at Tygerberg Academic Hospital. Here three exposures were made at each setting, i.e. the neonatal chest simulation phantom was imaged, the ESD was measured on the neonatal chest simulation phantom and an image of the physics image quality assessment phantom was obtained. The images were also stored on PACS and written to CD for evaluation with Image J.

The neonatal chest simulation phantom was set up as with the preliminary exposures and centring was done in the middle of the physics image quality assessment phantom. The quantitative image quality rankings for the two phantoms were compared. A final ranking of the neonatal chest simulation phantom images for

the final exposure set was based on visual and quantitative image quality and measured radiation dose.

Table 3.4: First preliminary exposure set.

Focus	kV	mAs	FFD (cm)	Filtration
Fine	50	2	100	Inherent
Fine	40	2	100	Inherent
Fine	70	2	100	Inherent
Fine	50	2	100	0.1 mm Cu + 1 mm Al
Fine	50	2	80	Inherent
Fine	50	2	120	Inherent

Table 3.5: Second preliminary exposure set.

Focus	kV	mAs	FFD (cm)	Filtration
Fine	50	2	100	Inherent
Fine	40	2	100	Inherent
Fine	45	2	100	Inherent
Fine	55	2	100	Inherent
Fine	60	2	100	Inherent
Fine	70	2	100	Inherent
Fine	50	2	100	0.1 mm Cu + 1 mm Al
Fine	50	2	100	1 mm Al
Large	50	2	100	Inherent
Fine	50	2	120	Inherent

Table 3.6: Third preliminary exposure set.

Focus	kV	mAs	FFD (cm)	Filtration
Fine	50	2.00	100	Inherent
Large	50	2.00	100	Inherent
Fine	50	3.20	100	1 mm Al
Fine	50	3.20	100	0.1 mm Cu + 1 mm Al
Fine	50	4.00	100	1 mm Al
Fine	50	4.00	100	0.1 mm Cu + 1 mm Al
Fine	70	2.00	100	1 mm Al
Fine	70	2.00	100	0.1 mm Cu + 1 mm Al
Fine	55	1.60	100	Inherent
Fine	55	1.25	100	Inherent
Fine	55	0.80	100	Inherent
Fine	60	1.40	100	Inherent
Fine	60	1.00	100	Inherent
Fine	60	0.80	100	Inherent
Fine	65	1.25	100	Inherent
Fine	65	0.80	100	Inherent
Fine	65	0.50	100	Inherent
Fine	70	1.00	100	Inherent
Fine	70	0.50	100	Inherent

Table 3.7: Forth preliminary exposure set.

Focus	kV	mAs	FFD (cm)	Filtration
Fine	50	2.00	100	Inherent
Fine	53	3.20	100	0.1 mm Cu + 1 mm Al
Fine	55	2.00	100	0.1 mm Cu + 1 mm Al
Fine	55	2.50	100	0.1 mm Cu + 1 mm Al
Fine	55	3.20	100	0.1 mm Cu + 1 mm Al
Fine	55	4.00	100	0.1 mm Cu + 1 mm Al
Fine	57	2.00	100	0.1 mm Cu + 1 mm Al
Fine	57	3.20	100	0.1 mm Cu + 1 mm Al
Fine	60	2.00	100	0.1 mm Cu + 1 mm Al
Fine	60	3.20	100	0.1 mm Cu + 1 mm Al
Fine	63	2.00	100	0.1 mm Cu + 1 mm Al
Fine	64	2.00	100	0.1 mm Cu + 1 mm Al
Fine	65	2.00	100	0.1 mm Cu + 1 mm Al
Fine	58	1.25	100	Inherent
Fine	58	1.00	100	Inherent
Fine	59	1.25	100	Inherent
Fine	59	1.00	100	Inherent
Fine	61	1.10	100	Inherent
Fine	61	0.80	100	Inherent
Fine	62	1.10	100	Inherent
Fine	62	0.80	100	Inherent
Fine	63	1.10	100	Inherent
Fine	63	0.80	100	Inherent
Fine	64	1.00	100	Inherent
Fine	64	0.80	100	Inherent
Fine	64	0.50	100	Inherent
Fine	68	0.80	100	Inherent
Fine	68	0.50	100	Inherent

Table 3.8: Final exposure set.

Focus	kV	mAs	FFD (cm)	Filtration	Image mode
Fine	50	2.0	100	Inherent	Processed
Fine	60	2.0	100	0.1 mm Cu + 1 mm Al	Raw
Fine	64	2.0	100	0.1 mm Cu + 1 mm Al	Raw
Fine	61	0.8	100	Inherent	Raw
Fine	62	0.8	100	Inherent	Raw
Fine	57	2.0	100	0.1 mm Cu + 1 mm Al	Processed
Fine	57	3.2	100	0.1 mm Cu + 1 mm Al	Processed
Fine	60	2.0	100	0.1 mm Cu + 1 mm Al	Processed
Fine	61	0.8	100	Inherent	Processed

3.5 Uncertainties in dose measurements

The random uncertainty in the measurement of the ESDs was determined with the PTW Conny II detector. Successive exposures were made with the neonatal chest simulation phantom, with the same exposure or technique factors, i.e. small focus, 50 kV, 2 mAs, 100 cm FFD and inherent filtration. For each exposure the positioning of the phantom and detector was redone. Random uncertainty was calculated as the standard deviation of the measured ESDs.

Systematic uncertainty was contributed by the uncertainty in the calibration of the detector. From the PTW calibration certificate this uncertainty was 5%. The total uncertainty, δ_{total}, in absolute dose measurements was the combined random, δ_{random}, and systematic, $\delta_{systematic}$, uncertainties, which was calculated with Equation 3.4.

$$\delta_{total} = \sqrt{(\delta_{random})^2 + \left(\delta_{systematic}\right)^2} \qquad \text{[Equation 3.4]}$$

The uncertainty in the calculation of the effective dose, $\delta_{Effective\ dose}$, in Table 4.24 was the product of the measured ESD uncertainty and the conversion coefficient, which was a constant. These uncertainties were calculated with Equation 3.5.

$$\delta_{Effective\ dose} = \delta_{total} \times Conversion\ coefficient \quad \text{[Equation 3.5]}$$

3.6 Cancer induction risk calculation

The risk for induction of cancer in the young child was calculated as the product of the effective dose and published ICRP risk factors. The ICRP risk factors, as mentioned by Huda[2] and Roebuck[19] are 0.1 - 0.15 Sv^{-1} for children.[2,19] Risk factors for foetal irradiation, or prenatal exposures to radiation, were also published by the ICRP in Report 60, as mentioned by Brindhaban and Al-Khalifah[15]. These are 2.8 - 13x10^{-2} Sv^{-1}.

The entrance surface dose (ESD) was measured with the PTW Conny II detector, as described in section 3.4. Conversion coefficients, which converted entrance surface dose to effective dose, as published in the National Radiological Protection Board (NRPB) Report R262[52], were used to obtain the associated effective doses. It was done for each of the exposures in Table 3.8 for the final exposure set. The calculated effective doses were multiplied with the different ICRP risk factors to obtain the cancer induction risks.

The risk per radiograph was calculated per 1 000 000 of the population. It was multiplied by the average number of radiographs a neonate received in Tygerberg Academic Hospital, i.e. 15, to obtain the average cancer induction risk per million neonates.

The tables in NRPB Report R262 consider a range of x-ray examinations, applied tube potentials (kV) and filtrations. The filtration is expressed in terms of mm aluminium. The inherent filtration of the Shimadzu Mobile Art Evolution mobile x-ray unit was 1.5 mm Al, according to the manufacturer specifications for the unit.[53] Additional filtration of 0.1 mm Cu + 1 mm Al was used in some of the exposures in Table 3.8. The additional filtration was equal to 4.5 mm Al, according to Hertrich[54]. The NRPB Report R262 tables made provision for 2 - 5 mm Al filtration only. Therefore the coefficients for 2 mm Al was used for inherent filtration of 1.5 mm Al,

and 5 mm Al values were used for additional filtration, of 6 mm Al, exposures, as further data was not available from the tables. To obtain the coefficients at kV values different to those in the tables, linear interpolation was used.

Chapter 4

Results

The work drawings for the neonatal chest simulation and physics image quality assessment phantoms are presented. Radiological equivalence and phantom validation results for the neonatal chest simulation phantom are shown. Image quality analysis results, both visual and quantitative, dose reduction and cancer induction risk analysis outcomes are included. Overall ranking of the exposures made, based on measured ESD, visual and quantitative image quality and cancer induction risks are shown, in order to determine the best option for dose reduction with image quality maintenance and cancer induction risk reduction.

4.1 The design of a neonatal chest simulation phantom

The neonatal chest simulation phantom was designed to simulate a real neonatal chest anatomically and radiologically as discussed in sections 4.1.1 and 4.1.2.

4.1.1 Anatomical equivalence

From the measurements described in section 3.1.1, scaled work drawings of the different anatomical structures of interest were made, as Figures 4.1 to 4.3 show. These were used for the machining and manufacturing of the posterior ribs, vertebral column, healthy and sick lungs, anterior ribs and sternal blocks.

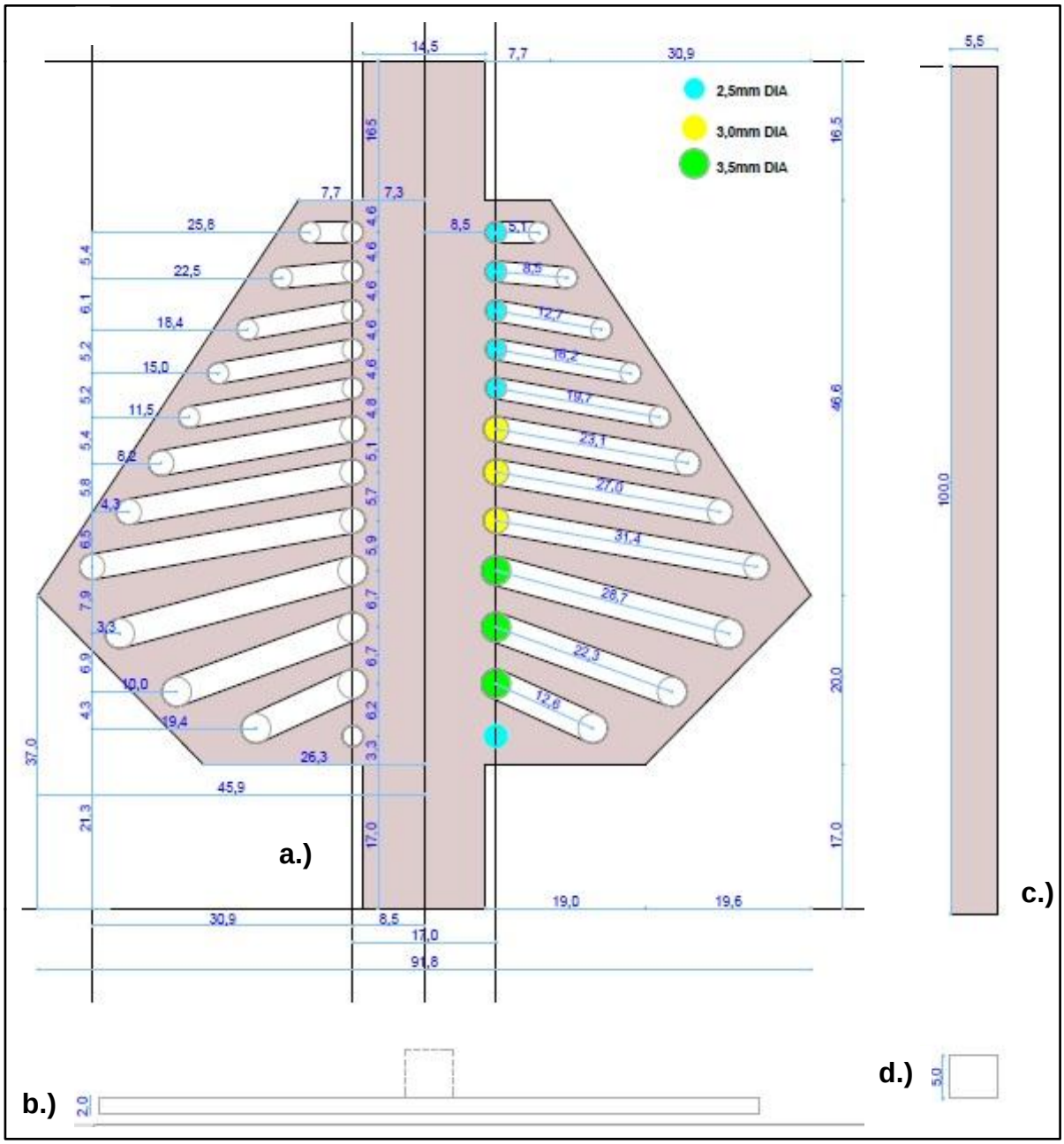

Figure 4.1: a.) Posterior ribs AP view. b.) Posterior ribs sectional view. c.) Vertebral column AP view. d.) Vertebral column sectional view.

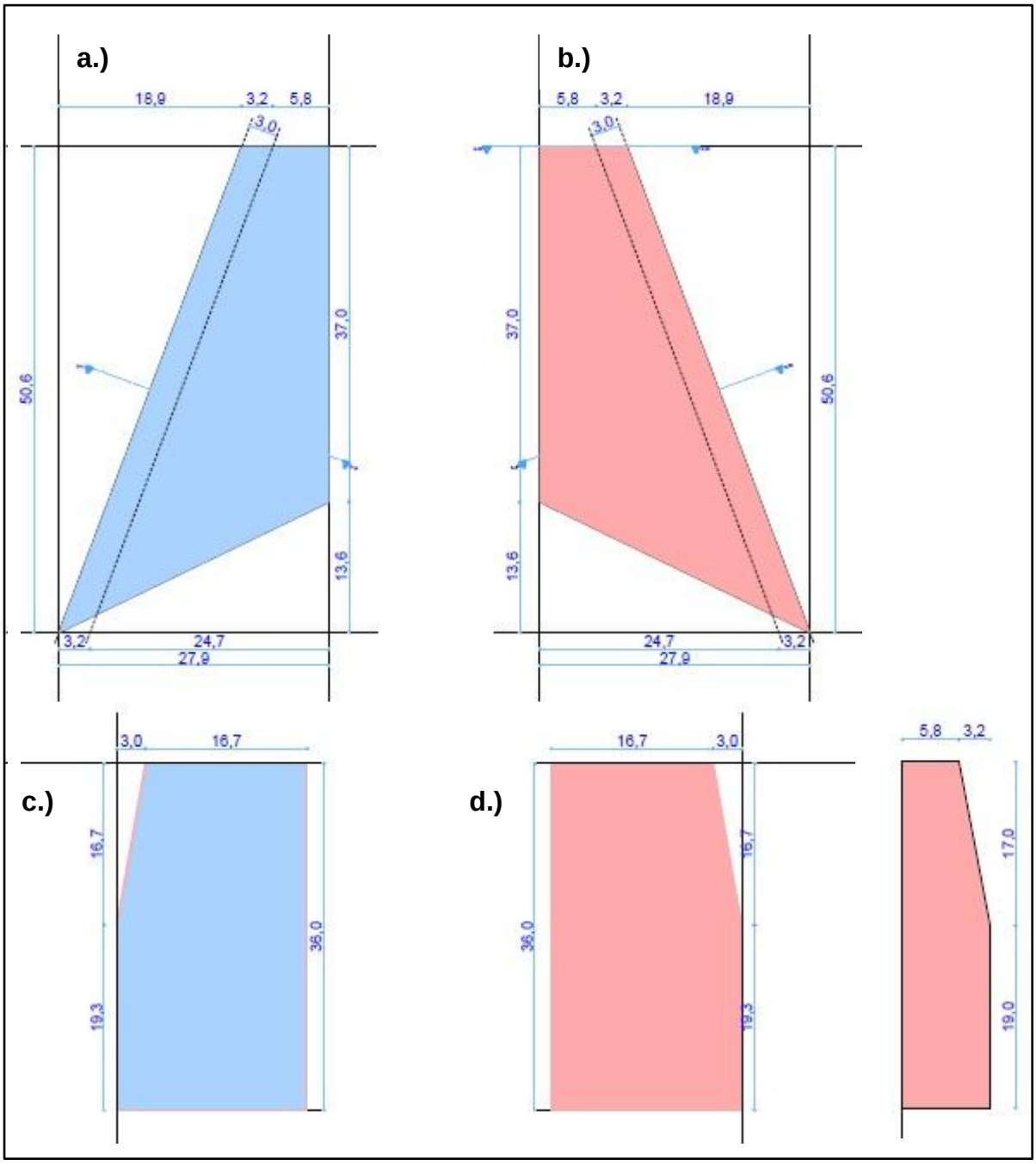

Figure 4.2: a.) Sick lung AP view. b.) Healthy lung AP view. c.) Sick lung sectional view. d.) Healthy lung sectional views.

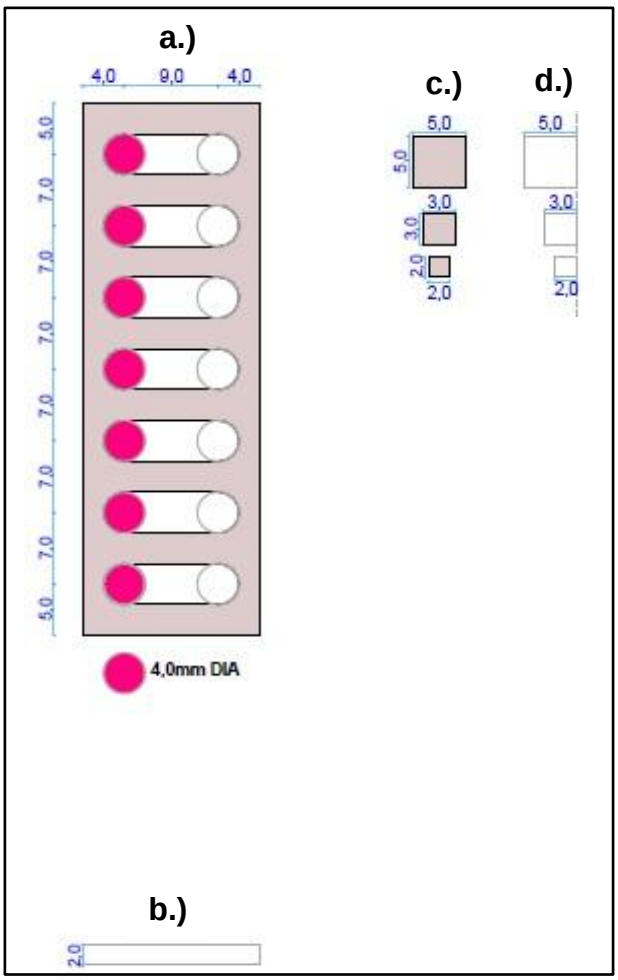

Figure 4.3: a.) Anterior ribs AP view. b.) Anterior ribs sectional view. c.) Sternal blocks AP view. d.) Sternal blocks sectional view.

A schematic AP and three-dimensional representation of the resultant phantom are shown in Figure 4.4.

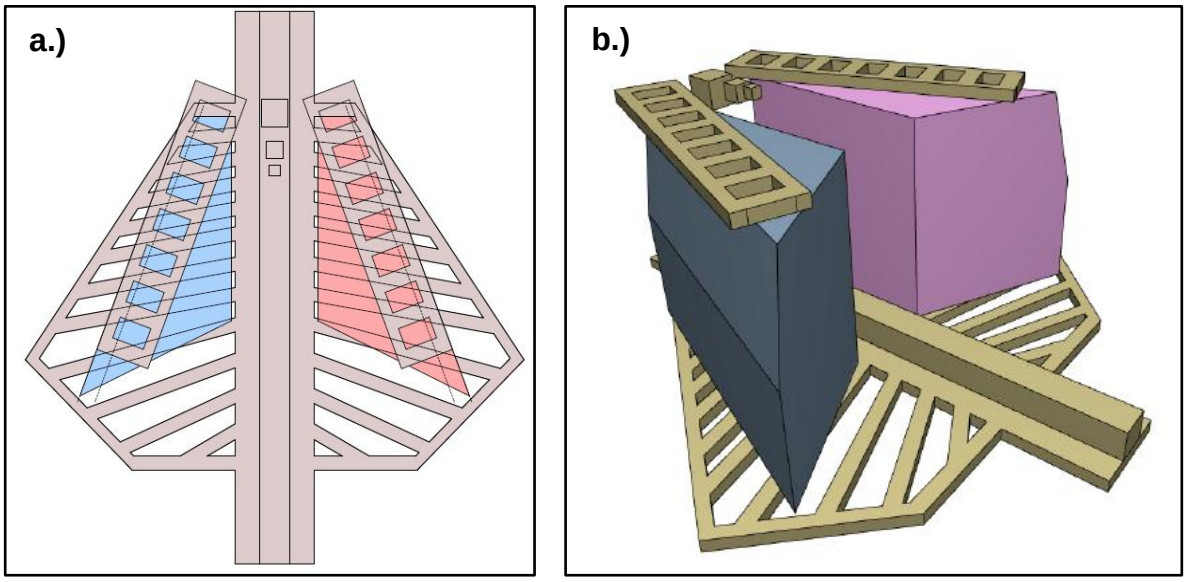

Figure 4.4: a.) Schematic AP and b.) three-dimensional representations of the designed neonatal chest simulation phantom.

The respective anatomical structures were assembled on a layer-by-layer basis in a perspex holder with the Agar gel mixture as muscle substitute material. The process is illustrated in Figure 4.5.

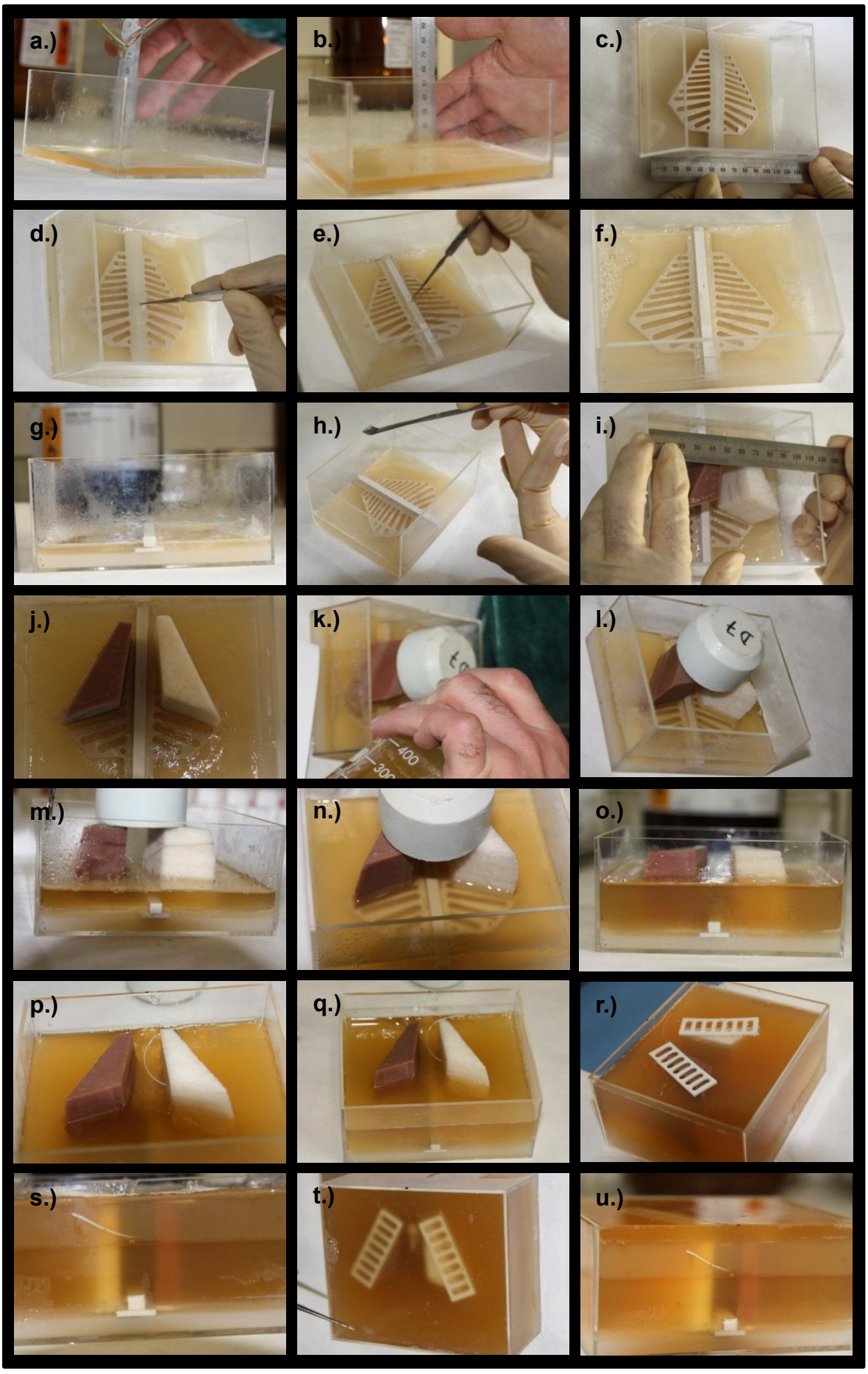

Figure 4.5: Neonatal chest simulation phantom assembly process. a.) Agar gel mix was poured into the perspex holder. b.) A ruler was used to measure the Agar gel mix thickness to be equivalent to the posterior tissue thickness. c.) After the first layer set, the posterior ribs were placed centrally in the phantom. d.) Agar gel mix was poured around the posterior ribs and the ribs were held down for the Agar gel mix to set around it. e.) The vertebral column was placed on the posterior ribs. f.) Agar gel mix was poured around the vertebral column. g.) Side view of the phantom up to this point of construction. h.) Air bubbles were removed with a spatula (it was done throughout the construction process). i.) Lungs were placed symmetrically about the centre of the phantom. j.) View of the lungs in position. k.) The healthy lung was buoyant and was held down with a lead weight. Agar gel mix was poured around the lungs layer by layer. i.) View of first layer Agar gel mix with lungs in position. m.) Side view of phantom up to this point of construction. n.) Filling of the phantom with the lungs in position. o.) Side view of phantom up to this point of construction. The central line was placed at this level. p.) Placing of the central line. q.) Thin layers of Agar gel mix were poured over the central line so that it set in position and did not float. r.) Agar gel mix was poured to the level of the lungs and the anterior ribs were placed symmetrically on the lungs. s.) Side view of phantom up to this point of construction. t.) Agar gel mix was poured to the brim of the perspex phantom. u.) Side view of phantom up to this point of construction.

The thickness of the neonatal chest simulation phantom, as determined from the constituents in the three-dimensional view in Figure 4.4 b.), was 51 mm. After construction, actual measurement with a ruler gave a thickness of 53 mm. According to measurements in the Skills Laboratory at the Tygerberg Campus Medical Faculty, neonatal chest thickness was 70 mm. The cylindrical object at the feet of the cadaver in Figure 3.1 a.) and b.) had actual dimensions of 70 mm length and 28 mm diameter. The measured results were 69.9 mm length and 27.6 mm diameter.

The final product was used for dose and image quality analysis in the current study.

4.1.2 Radiological equivalence

As discussed in the following sub sections, it was found that an in house manufactured Agar gel mix was the best substitute for neonatal muscle. Gammex LN300 lung and Gammex solid water were selected for healthy and sick lung respectively and Gammex SB3 bone was selected for bony simulations. The Gammex tissue equivalent plastics were manufactured by Gammex RMI© in the USA and were locally available from CM Nuclear Systems cc. These materials were similar to a real neonatal chest in density, elemental composition or mass fraction by weight, total attenuation coefficient, Compton scatter coefficient and spectral weighted mass energy absorption characteristics, as Table 4.1, an overall comparison of all the possible substitute materials, shows. Scoring was done based on the criteria in Table 3.1.

Each of these criteria, i.e. density and elemental composition matching, attenuation and scatter coefficient matching, mass energy absorption coefficient matching and obtainability and cost, is discussed in sections 4.1.2.1 to 4.1.2.3 and 4.1.3.

Table 4.1: Overall comparison of different substitute materials.

Substitute material	Elemental composition	Density	Total attenuation coefficient	Compton scatter coefficient	Spectrum weighted mass energy absorption coefficient	Obtainability	Cost	Machinability / Ease of working	Total
Frigerio gel	4	1	3	3	3	-	-	3	17
RM/G1 gel	4	3	4	3	4	-	-	3	21
Rossi gel	3	2	2	3	2	-	-	0	12
Polystyrene	0	4	0	0	0	Local supplier	R 68.25 per 200x100x0.1cm^3 slab	0	4
Temex	0	2	2	0	3	-	-	0	7
Gammex solid water	0	4	3	0	2	Local agent	R 4902 per 20x20x1cm^3 slab	0	9
Agar gel mix	3	2	3	4	3	Local supplier	R 1700 per kg	4	19
SB5	3	1	3	2	3	-	-	4	16
B110	2	3	3	2	3	-	-	4	17
Gammex SB3	2	2	3	3	3	Local agent	R 6726 per 20x20x1cm^3 slab	4	17
Griffith lung	3	4	2	3	3	-	-	2	17
LN10/75	2	2	3	2	2	-	-	4	15
Gammex LN300	2	3	3	2	2	Local agent	R 6726 per 20x20x1cm^3 slab	4	16
Polystyrene	1	3	2	2	1	Local supplier	R 68.25 per 200x100x0.1cm^3 slab	3	12
Gammex CT solid water	3	2	3	3	3	Local agent	R 5472 per 20x20x1cm^3 slab	4	18
Gammex solid water	3	3	3	3	3	Local agent	R 4902 per 20x20x1cm^3 slab	4	19

4.1.2.1 Density and elemental composition matching

The mass fraction by weight of the Agar gel mix was calculated from the chemical formulae of the constituent compounds, i.e. Agar $C_{12}H_{18}O_9$, sucrose $C_{12}H_{22}O_{11}$ and water H_2O. The mixture consisted of 4% Agar, 10% sucrose and 86% water, with the assumption that 1 g equalled 1 cm^3. The calculation is included in Appendix B. The calculated fractions were 0.0609 for carbon, 0.1051 for hydrogen and 0.8339 for oxygen. These values are included in Table 4.2 for further calculations.

The densities and elemental compositions of different possible substitute materials were obtained from literature[6,46,47] and entered into Tables 4.2 and 4.3 for further calculations. All the calculations that were based on elemental compositions, or mass fractions by weight, i.e. XCOM calculations, were performed using the data in Table 4.2.

Table 4.2: Elemental composition or mass fraction data of substitute and real materials.

Material	Composition (mass fraction)															
	H	C	N	O	Ca	Na	Cl	F	Mg	Ti	Zn	K	S	P	Sb	Si
Newborn skeletal muscle	0.1040	0.1030	0.0240	0.7620	0.0000	0.0010	0.0020	0.0000	0.0000	0.0000	0.0000	0.0020	0.0010	0.0010	0.0000	0.0000
Frigerio gel	0.1000	0.1200	0.0400	0.7330	0.0000	0.0040	0.0010	0.0000	0.0000	0.0000	0.0000	0.0000	0.0020	0.0000	0.0000	0.0000
RM/G1 gel	0.1020	0.0940	0.0240	0.7740	0.0000	0.0010	0.0020	0.0000	0.0000	0.0000	0.0000	0.0020	0.0010	0.0000	0.0000	0.0000
Rossi gel	0.0980	0.1570	0.0360	0.7090	0.0000	0.0000	0.0000	0.0000	0.0000	0.0000	0.0000	0.0000	0.0000	0.0000	0.0000	0.0000
Polystyrene	0.0770	0.9230	0.0000	0.0000	0.0000	0.0000	0.0000	0.0000	0.0000	0.0000	0.0000	0.0000	0.0000	0.0000	0.0000	0.0000
Temex	0.0960	0.8750	0.0010	0.0050	0.0000	0.0000	0.0000	0.0000	0.0000	0.0030	0.0050	0.0000	0.0150	0.0000	0.0000	0.0000
Gammex solid water	0.0802	0.6723	0.0241	0.1991	0.0231	0.0000	0.0014	0.0000	0.0000	0.0000	0.0000	0.0000	0.0000	0.0000	0.0000	0.0000
Agar gel mix	0.1051	0.0609	0.0000	0.8339	0.0000	0.0000	0.0000	0.0000	0.0000	0.0000	0.0000	0.0000	0.0000	0.0000	0.0000	0.0000
Newborn cortical bone	0.0440	0.1530	0.0410	0.4770	0.1940	0.0010	0.0010	0.0000	0.0020	0.0000	0.0000	0.0000	0.0020	0.0850	0.0000	0.0000
SB5	0.0260	0.3060	0.0100	0.3890	0.2680	0.0000	0.0010	0.0000	0.0000	0.0000	0.0000	0.0000	0.0000	0.0000	0.0000	0.0000
B110	0.0370	0.3710	0.0320	0.0480	0.2630	0.0000	0.0000	0.2490	0.0000	0.0000	0.0000	0.0000	0.0000	0.0000	0.0000	0.0000
Gammex SB3	0.0341	0.3141	0.0184	0.3650	0.2681	0.0000	0.0004	0.0000	0.0000	0.0000	0.0000	0.0000	0.0000	0.0000	0.0000	0.0000
Fetal inflated lung	0.1060	0.0760	0.0180	0.7920	0.0000	0.0020	0.0020	0.0000	0.0000	0.0000	0.0000	0.0010	0.0010	0.0020	0.0000	0.0000
Griffith lung	0.0800	0.6080	0.0420	0.2480	0.0210	0.0000	0.0000	0.0000	0.0010	0.0000	0.0000	0.0000	0.0000	0.0000	0.0000	0.0000
LN10/75	0.0840	0.6040	0.0170	0.1730	0.0000	0.0000	0.0010	0.0000	0.1140	0.0000	0.0000	0.0000	0.0000	0.0000	0.0000	0.0070
Gammex LN300	0.0846	0.5938	0.0196	0.1814	0.0000	0.0000	0.0010	0.0000	0.1119	0.0000	0.0000	0.0000	0.0000	0.0000	0.0000	0.0078
Fetal deflated lung	0.1060	0.0760	0.0180	0.7920	0.0000	0.0020	0.0020	0.0000	0.0000	0.0000	0.0000	0.0010	0.0010	0.0020	0.0000	0.0000
Polystyrene	0.0770	0.9230	0.0000	0.0000	0.0000	0.0000	0.0000	0.0000	0.0000	0.0000	0.0000	0.0000	0.0000	0.0000	0.0000	0.0000
Gammex CT solid water	0.0800	0.6730	0.0239	0.1987	0.0231	0.0000	0.0014	0.0000	0.0000	0.0000	0.0000	0.0000	0.0000	0.0000	0.0000	0.0000
Gammex solid water	0.0802	0.6723	0.0241	0.1991	0.0231	0.0000	0.0014	0.0000	0.0000	0.0000	0.0000	0.0000	0.0000	0.0000	0.0000	0.0000

Figure 4.6 shows the elemental composition data graphically, comparing substitute material and real tissue data. It was done for body, bone, inflated lung and deflated lung. The respective mass fractions are depicted on the y-axes and the different elements on the x-axes.

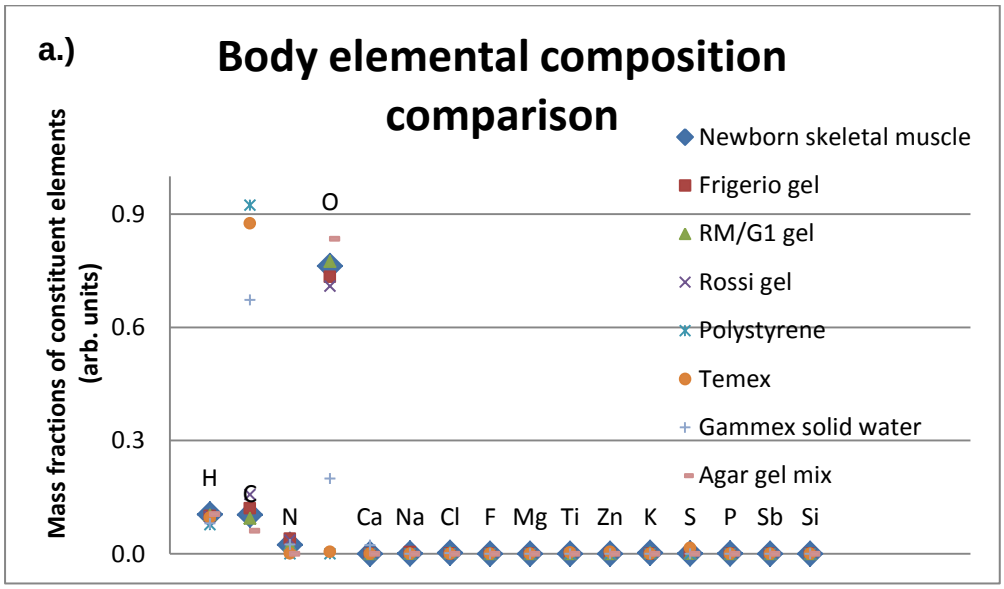

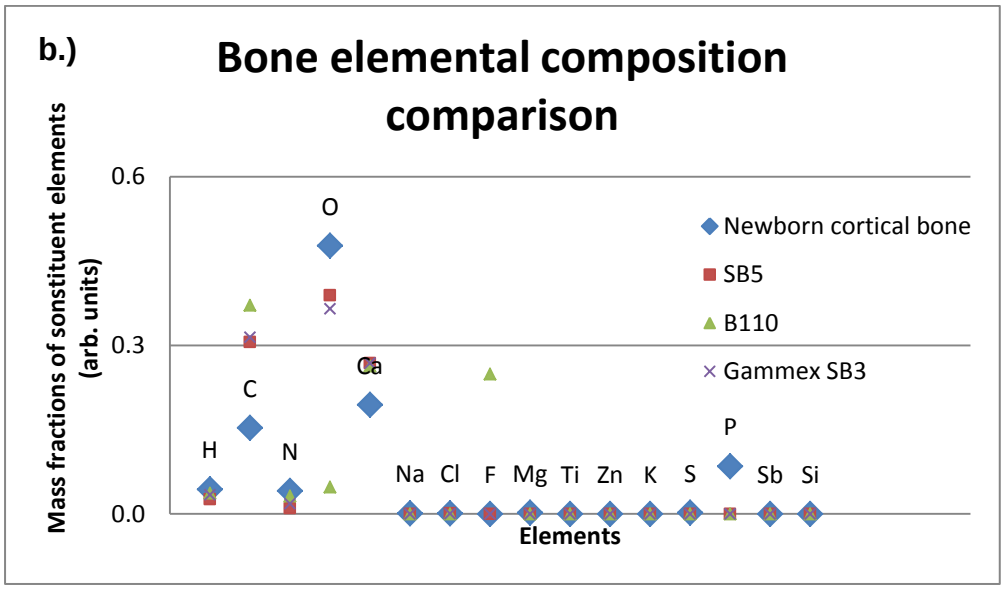

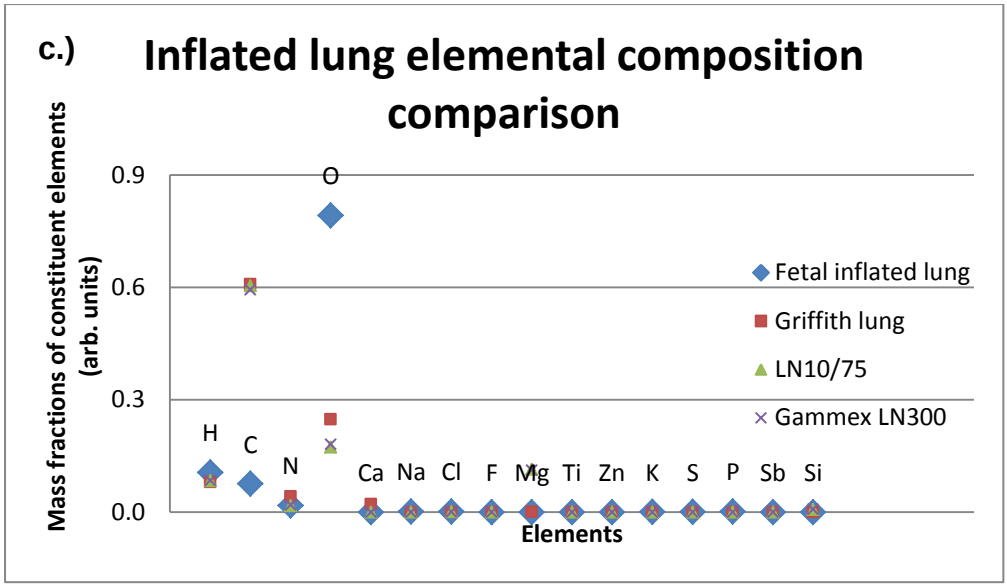

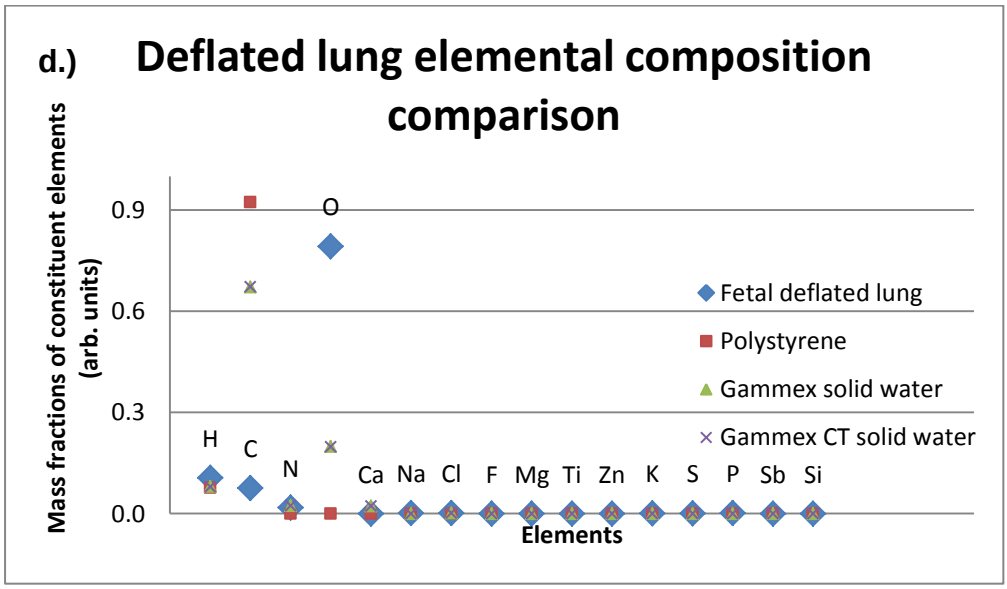

Figure 4.6: Elemental composition comparison of real neonatal tissues and possible substitute materials including a.) body (muscle), b.) bone, c.) inflated (healthy) lung and d.) deflated (sick) lung.

The various substitute and real tissue densities are recorded in Table 4.3. The densities of the possible substitute materials were normalised to that of the real neonatal tissue and the results are displayed in Figure 4.7.

Table 4.3: Density data of substitute and real materials.

Material	Density (g/cm^3)
Newborn skeletal muscle	1.05
Frigerio gel	1.12
RM/G1 gel	1.07
Rossi gel	1.10
Polystyrene	1.05
Temex	1.01
Gammex solid water	1.05
Agar gel mix	1.10
Newborn cortical bone	1.72
SB5	1.87
B110	1.79
Gammex SB3	1.82
Fetal inflated lung	0.26
Griffith lung	0.26
LN10/75	0.31
Gammex LN300	0.30
Fetal deflated lung	1.04
Polystyrene	1.05
Gammex CT solid water	1.02
Gammex solid water	1.05

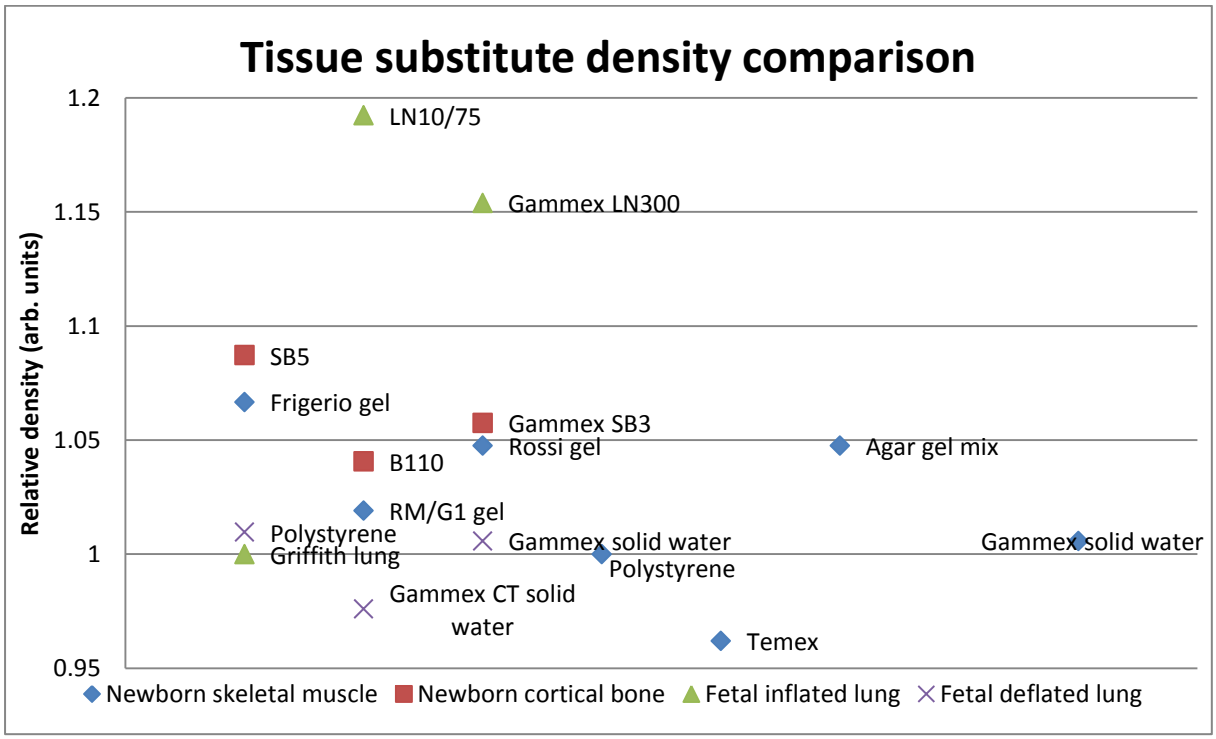

Figure 4.7: Normalised density comparison for possible substitute materials to real neonatal tissues.

4.1.2.2 Attenuation and scatter coefficients

The total attenuation and Compton scatter coefficients were calculated with the XCOM program. The results are recorded in Tables 4.4 and 4.5.

Table 4.4: Total attenuation coefficient data of substitute and real materials.

	Total attenuation coefficient in cm^2/g												
Energy (kV)	**10**	**15**	**20**	**25**	**30**	**35**	**40**	**45**	**50**	**55**	**60**	**65**	**70**
Material													
Newborn skeletal muscle	5.292	1.669	0.810	0.508	0.375	0.307	0.267	0.243	0.226	0.214	0.205	0.198	0.192
Frigerio gel	5.062	1.597	0.778	0.492	0.365	0.300	0.263	0.239	0.223	0.212	0.203	0.196	0.190
RM/G1 gel	5.301	1.671	0.810	0.508	0.375	0.307	0.267	0.242	0.226	0.214	0.204	0.197	0.191
Rossi gel	4.771	1.510	0.741	0.473	0.354	0.293	0.258	0.236	0.221	0.210	0.201	0.195	0.189
Polystyrene	2.220	0.774	0.436	0.317	0.264	0.236	0.218	0.207	0.199	0.192	0.187	0.183	0.179
Temex	4.396	1.499	0.761	0.491	0.368	0.303	0.265	0.241	0.224	0.212	0.203	0.196	0.190
Gammex solid water	5.142	1.681	0.826	0.519	0.381	0.310	0.268	0.242	0.224	0.212	0.202	0.195	0.189
Agar gel mix	5.150	1.620	0.787	0.496	0.368	0.303	0.265	0.241	0.225	0.213	0.204	0.197	0.191
Newborn cortical bone	25.150	7.966	3.539	1.920	1.193	0.820	0.608	0.479	0.396	0.339	0.299	0.270	0.248
SB5	28.180	8.986	3.995	2.160	1.333	0.908	0.667	0.520	0.425	0.360	0.315	0.282	0.257
B110	27.910	8.897	3.956	2.138	1.321	0.900	0.661	0.516	0.422	0.358	0.313	0.280	0.255
Gammex SB3	28.070	8.953	3.983	2.154	1.331	0.907	0.667	0.520	0.425	0.361	0.316	0.283	0.258
Fetal inflated lung	5.361	1.688	0.817	0.512	0.377	0.308	0.269	0.244	0.227	0.214	0.205	0.198	0.192
Griffith lung	5.095	1.660	0.816	0.513	0.378	0.307	0.267	0.241	0.224	0.211	0.202	0.194	0.188
LN10/75	5.256	1.673	0.812	0.508	0.374	0.305	0.265	0.240	0.223	0.211	0.201	0.194	0.188
Gammex LN300	5.275	1.678	0.814	0.510	0.375	0.305	0.265	0.240	0.223	0.211	0.202	0.194	0.188
Fetal deflated lung	5.361	1.688	0.817	0.512	0.377	0.308	0.269	0.244	0.227	0.214	0.205	0.198	0.192
Polystyrene	2.220	0.774	0.436	0.317	0.264	0.236	0.218	0.207	0.199	0.192	0.187	0.183	0.179
Gammex CT solid water	5.141	1.681	0.826	0.519	0.381	0.310	0.268	0.242	0.224	0.212	0.202	0.195	0.189
Gammex solid water	5.142	1.681	0.826	0.519	0.381	0.310	0.268	0.242	0.224	0.212	0.202	0.195	0.189

The possible tissue substitute data in Table 4.4 were normalised to the values for real tissues and the results are graphically displayed in Figure 4.8.

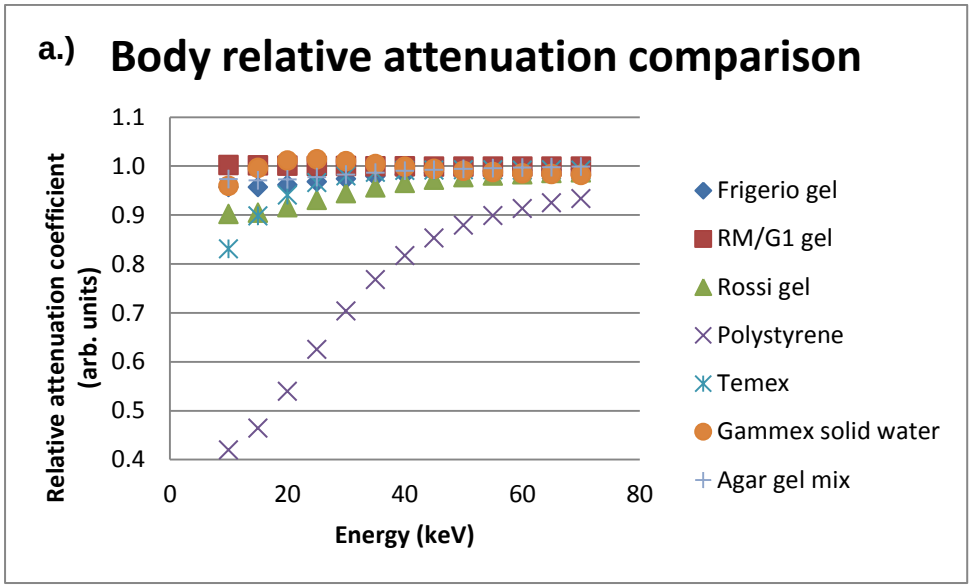

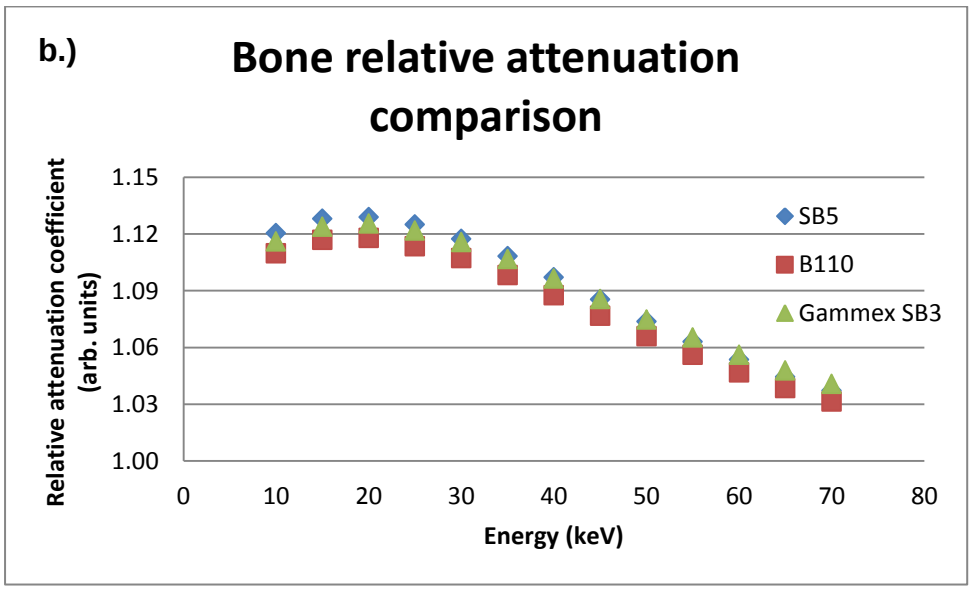

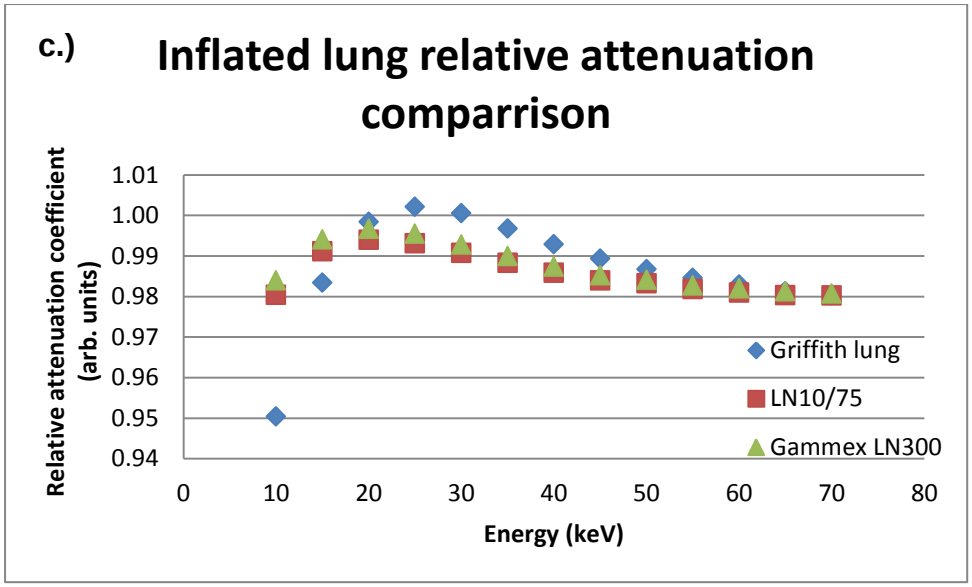

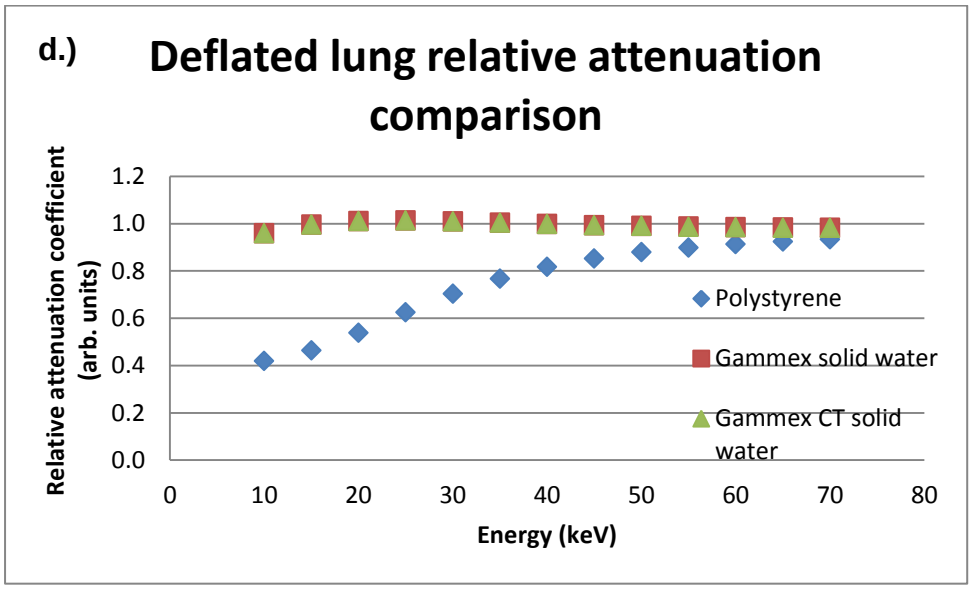

Figure 4.8: Normalised total attenuation coefficient comparison of real neonatal tissues and possible substitute materials including a.) body (muscle), b.) bone, c.) inflated (healthy) lung and d.) deflated (sick) lung.

Table 4.5 shows the Compton scatter coefficient data. The data for the substitutes were normalised to that of real neonatal tissues by dividing by the real tissue values. The results are recorded in Figure 4.9.

Table 4.5: Compton scatter coefficient data of substitute and real materials.

	Compton scatter coefficient in cm^2/g												
Energy (kV)	10	15	20	25	30	35	40	45	50	55	60	65	70
Material													
Newborn skeletal muscle	1.537E-01	1.687E-01	1.762E-01	1.800E-01	1.817E-01	1.820E-01	1.815E-01	1.805E-01	1.791E-01	1.775E-01	1.758E-01	1.740E-01	1.722E-01
Frigerio gel	1.530E-01	1.680E-01	1.755E-01	1.794E-01	1.811E-01	1.814E-01	1.809E-01	1.798E-01	1.785E-01	1.769E-01	1.752E-01	1.734E-01	1.716E-01
RM/G1 gel	1.532E-01	1.682E-01	1.757E-01	1.796E-01	1.813E-01	1.817E-01	1.812E-01	1.801E-01	1.787E-01	1.772E-01	1.755E-01	1.737E-01	1.719E-01
Rossi gel	1.529E-01	1.679E-01	1.754E-01	1.793E-01	1.809E-01	1.812E-01	1.807E-01	1.797E-01	1.783E-01	1.767E-01	1.750E-01	1.732E-01	1.714E-01
Polystyrene	1.524E-01	1.674E-01	1.752E-01	1.787E-01	1.800E-01	1.799E-01	1.790E-01	1.777E-01	1.762E-01	1.744E-01	1.726E-01	1.707E-01	1.688E-01
Temex	1.557E-01	1.707E-01	1.783E-01	1.818E-01	1.829E-01	1.828E-01	1.819E-01	1.806E-01	1.790E-01	1.772E-01	1.754E-01	1.735E-01	1.716E-01
Gammex solid water	1.511E-01	1.662E-01	1.740E-01	1.777E-01	1.792E-01	1.793E-01	1.786E-01	1.774E-01	1.759E-01	1.743E-01	1.725E-01	1.707E-01	1.689E-01
Agar gel mix	1.538E-01	1.688E-01	1.763E-01	1.801E-01	1.818E-01	1.822E-01	1.817E-01	1.806E-01	1.793E-01	1.777E-01	1.760E-01	1.742E-01	1.724E-01
Newborn cortical bone	1.329E-01	1.492E-01	1.582E-01	1.631E-01	1.656E-01	1.667E-01	1.668E-01	1.664E-01	1.655E-01	1.644E-01	1.631E-01	1.617E-01	1.602E-01
SB5	1.299E-01	1.462E-01	1.553E-01	1.603E-01	1.629E-01	1.640E-01	1.642E-01	1.637E-01	1.629E-01	1.618E-01	1.605E-01	1.592E-01	1.577E-01
B110	1.303E-01	1.466E-01	1.555E-01	1.604E-01	1.629E-01	1.639E-01	1.640E-01	1.635E-01	1.626E-01	1.615E-01	1.603E-01	1.589E-01	1.574E-01
Gammex SB3	1.319E-01	1.480E-01	1.571E-01	1.620E-01	1.645E-01	1.656E-01	1.657E-01	1.652E-01	1.643E-01	1.632E-01	1.619E-01	1.605E-01	1.590E-01
Fetal inflated lung	1.540E-01	1.689E-01	1.764E-01	1.803E-01	1.820E-01	1.823E-01	1.818E-01	1.808E-01	1.794E-01	1.778E-01	1.761E-01	1.743E-01	1.725E-01
Griffith lung	1.508E-01	1.659E-01	1.737E-01	1.775E-01	1.790E-01	1.791E-01	1.784E-01	1.773E-01	1.758E-01	1.742E-01	1.724E-01	1.706E-01	1.688E-01
LN10/75	1.499E-01	1.655E-01	1.735E-01	1.773E-01	1.788E-01	1.790E-01	1.784E-01	1.773E-01	1.759E-01	1.743E-01	1.726E-01	1.708E-01	1.690E-01
Gammex LN300	1.500E-01	1.656E-01	1.735E-01	1.774E-01	1.789E-01	1.791E-01	1.785E-01	1.774E-01	1.760E-01	1.744E-01	1.727E-01	1.709E-01	1.691E-01
Fetal deflated lung	1.540E-01	1.689E-01	1.764E-01	1.803E-01	1.820E-01	1.823E-01	1.818E-01	1.808E-01	1.794E-01	1.778E-01	1.761E-01	1.743E-01	1.725E-01
Polystyrene	1.524E-01	1.674E-01	1.752E-01	1.787E-01	1.800E-01	1.799E-01	1.790E-01	1.777E-01	1.762E-01	1.744E-01	1.726E-01	1.707E-01	1.688E-01
Gammex CT solid water	1.510E-01	1.661E-01	1.739E-01	1.777E-01	1.791E-01	1.792E-01	1.785E-01	1.774E-01	1.759E-01	1.742E-01	1.725E-01	1.707E-01	1.688E-01
Gammex solid water	1.511E-01	1.662E-01	1.740E-01	1.777E-01	1.792E-01	1.793E-01	1.786E-01	1.774E-01	1.759E-01	1.743E-01	1.725E-01	1.707E-01	1.689E-01

a.)

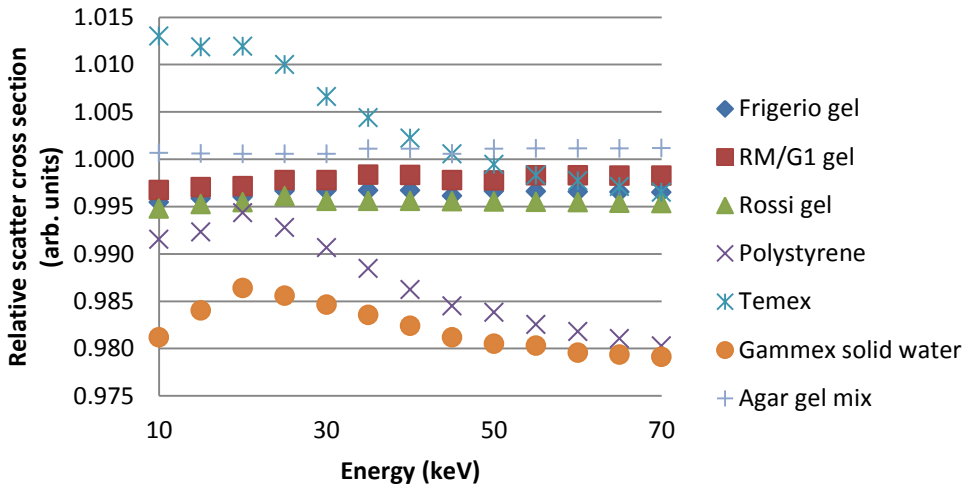

b.)

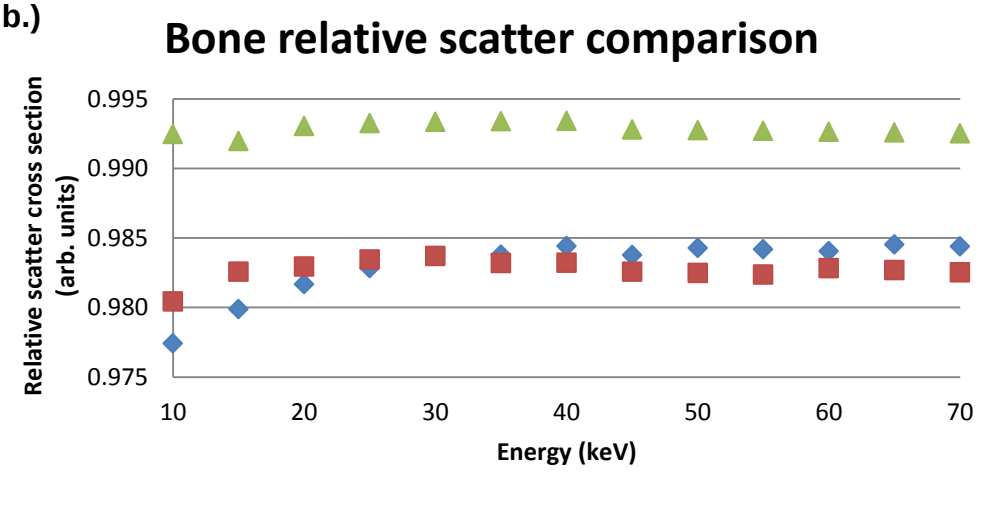

c.)

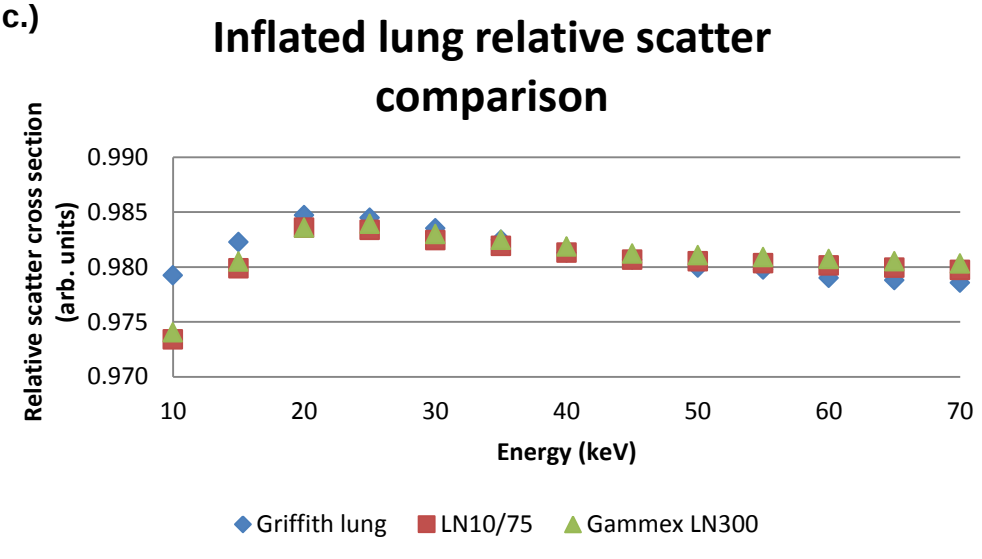

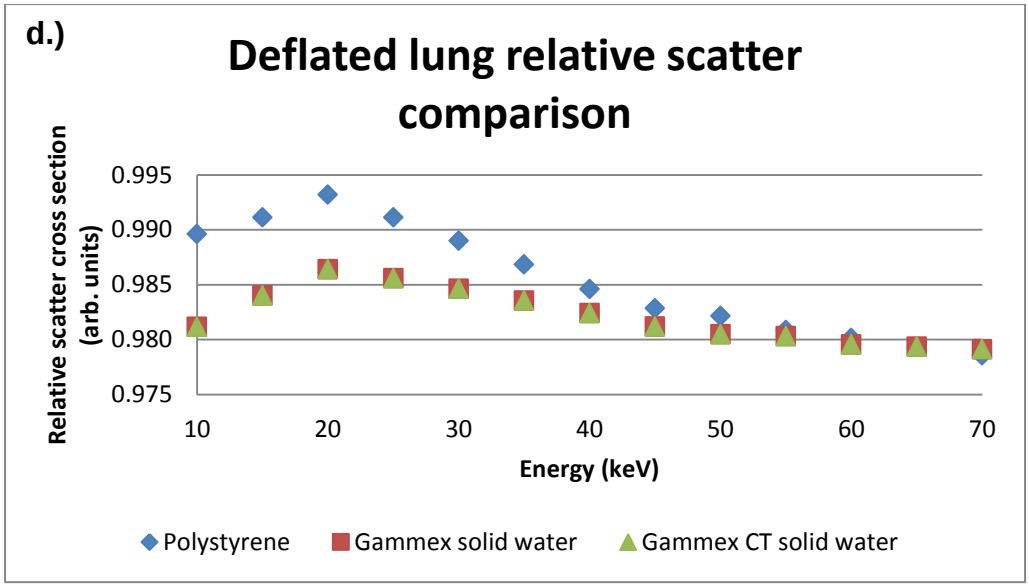

Figure 4.9: Normalised Compton scatter coefficient comparison of real neonatal tissues and possible substitute materials including a.) body (muscle), b.) bone, c.) inflated (healthy) lung and d.) deflated (sick) lung.

4.1.2.3 Mass energy absorption coefficients

Mass energy absorption coefficients were calculated with the mixture rule, i.e. Equation 2.13. For the calculation the fractions by weight, in Table 4.2, and mass energy absorption coefficients published for different elements by Hubbell and Seltzer[38], as recorded in Table 4.6, were used.

The validity of the mixture rule for such a calculation had to be proven. By calculating the mass energy absorption coefficients for water, A150 and adipose tissue using the mixture rule, and comparing the calculated results with those published in literature, this was done. The published values were obtained from Hubbell and Seltzer[38]. These results are recorded in Table 4.7. Table 4.7 shows the percentage difference between the mixture rule and published mass energy absorption coefficients, over a range of energies.

Table 4.6: Published elemental mass energy absorption coefficients (cm^2/g)[38].

Energy (kV) / Element	1.0	1.5	2.0	3.0	4.0	5.0	6.0	8.0
H	6.820E+00	1.752E+00	6.643E-01	1.693E-01	6.549E-02	3.278E-02	1.996E-02	1.160E-02
C	2.209E+03	6.990E+02	3.016E+02	8.963E+01	3.723E+01	1.866E+01	1.054E+01	4.242E+00
N	3.306E+03	1.080E+03	4.755E+02	1.447E+02	6.094E+01	3.086E+01	1.759E+01	7.170E+00
O	4.576E+03	1.545E+03	6.926E+02	2.158E+02	9.221E+01	4.715E+01	2.708E+01	1.116E+01
Ca	4.861E+03	1.710E+03	7.966E+02	2.650E+02	1.197E+02	5.373E+02	3.387E+02	1.600E+02
Na	6.522E+02	3.151E+03	1.504E+03	5.023E+02	2.238E+02	1.178E+02	6.915E+01	2.941E+01
Cl	2.829E+03	9.742E+02	4.494E+02	1.361E+03	6.626E+02	3.711E+02	2.282E+02	1.034E+02
F	5.615E+03	1.969E+03	9.005E+02	2.870E+02	1.244E+02	6.424E+01	3.716E+01	1.548E+01
Mg	9.203E+02	3.918E+03	1.899E+03	6.499E+02	2.937E+02	1.561E+02	9.227E+01	3.965E+01
Ti	5.860E+03	2.091E+03	9.824E+02	3.295E+02	1.494E+02	5.657E+02	3.691E+02	1.793E+02
Zn	1.548E+03	4.791E+03	2.359E+03	8.244E+02	3.820E+02	2.082E+02	1.261E+02	5.660E+01
K	4.053E+03	1.415E+03	6.563E+02	2.174E+02	8.304E+02	4.752E+02	2.974E+02	1.383E+02
S	2.426E+03	8.314E+02	3.828E+02	1.265E+03	6.066E+02	3.360E+02	2.046E+02	9.171E+01
P	1.910E+03	6.522E+02	2.996E+02	1.074E+03	5.079E+02	2.782E+02	1.682E+02	7.457E+01
Sb	1.567E+03	5.331E+02	2.669E+03	9.516E+02	4.427E+02	2.400E+02	1.439E+02	6.313E+01
Si	8.568E+03	3.481E+03	1.759E+03	6.469E+02	3.113E+02	8.377E+02	5.305E+02	2.518E+02
Energy (kV) / Element	**10.0**	**15.0**	**20.0**	**30.0**	**40.0**	**50.0**	**60.0**	**80.0**
H	9.849E-03	1.102E-02	1.355E-02	1.863E-02	2.315E-02	2.709E-02	3.053E-02	3.620E-02
C	2.078E+00	5.627E-01	2.238E-01	6.614E-02	3.343E-02	2.397E-02	2.098E-02	2.037E-02
N	3.545E+00	9.715E-01	3.867E-01	1.099E-01	5.051E-02	3.217E-02	2.548E-02	2.211E-02
O	5.565E+00	1.545E+00	6.179E-01	1.729E-01	7.530E-02	4.414E-02	3.207E-02	2.468E-02
Ca	8.744E+01	2.804E+01	1.220E+01	3.665E+00	1.538E+00	7.822E-01	4.520E-01	1.950E-01
Na	1.499E+01	4.313E+00	1.759E+00	4.928E-01	2.031E-01	1.063E-01	6.625E-02	3.761E-02
Cl	5.510E+01	1.700E+01	7.227E+00	2.114E+00	8.756E-01	4.433E-01	2.570E-01	1.148E-01
F	7.776E+00	2.186E+00	8.796E-01	2.451E-01	1.036E-01	5.747E-02	3.903E-02	2.676E-02
Mg	2.036E+01	5.925E+00	2.432E+00	6.855E-01	2.815E-01	1.451E-01	8.820E-02	4.671E-02
Ti	1.001E+02	3.311E+01	1.465E+01	4.488E+00	1.904E+00	9.737E-01	5.634E-01	2.422E-01
Zn	1.497E+02	6.009E+01	2.986E+01	1.018E+01	4.570E+00	2.419E+00	1.429E+00	6.203E-01
K	7.490E+01	2.370E+01	1.023E+01	3.045E+00	1.272E+00	6.454E-01	3.730E-01	1.628E-01
S	4.847E+01	1.477E+01	6.235E+00	1.809E+00	7.466E-01	3.779E-01	2.199E-01	1.000E-01
P	3.912E+01	1.179E+01	4.939E+00	1.422E+00	5.850E-01	2.965E-01	1.735E-01	8.083E-02
Sb	3.289E+01	9.794E+00	4.076E+00	1.164E+00	4.782E-01	2.430E-01	1.434E-01	6.896E-02
Si	1.396E+02	4.657E+01	2.105E+01	6.755E+00	9.789E+00	6.400E+00	4.311E+00	2.173E+00

Table 4.7: Validity of the mixture rule for compound mass energy absorption coefficient calculation.

Energy (kV)	**1**	**1.5**	**2**	**3**	**4**	**5**	**6**	**8**
Water								
Mixture rule	4.06E+03	1.37E+03	6.15E+02	1.92E+02	8.19E+01	4.19E+01	2.40E+01	9.91E+00
Hubbell	4.07E+03	1.37E+03	6.15E+02	1.92E+02	8.19E+01	4.19E+01	2.41E+01	9.92E+00
% difference	-0.02	0.01	-0.02	-0.03	-0.02	-0.02	0.00	-0.04
Energy (kV)	**10**	**15**	**20**	**30**	**40**	**50**	**60**	**80**
Water								
Mixture rule	4.94E+00	1.37E+00	5.50E-01	1.56E-01	6.95E-02	4.22E-02	3.19E-02	2.60E-02
Hubbell	4.94E+00	1.37E+00	5.50E-01	1.56E-01	6.95E-02	4.22E-02	3.19E-02	2.60E-02
% difference	-0.02	-0.06	-0.02	-0.05	-0.02	0.00	-0.01	0.00
Energy (kV)	**1**	**1.5**	**2**	**3**	**4**	**5**	**6**	**8**
A150								
Mixture rule	2.25E+03	7.26E+02	3.17E+02	9.56E+01	4.01E+01	2.88E+01	1.69E+01	7.27E+00
Hubbell	2.26E+03	7.27E+02	3.17E+02	9.58E+01	4.02E+01	2.90E+01	1.71E+01	7.34E+00
% difference	-0.10	-0.14	-0.15	-0.17	-0.20	-0.73	-0.80	-0.89
Energy (kV)	**10**	**15**	**20**	**30**	**40**	**50**	**60**	**80**
A150								
Mixture rule	3.74E+00	1.09E+00	4.55E-01	1.36E-01	6.34E-02	3.98E-02	3.07E-02	2.55E-02
Hubbell	3.77E+00	1.11E+00	4.61E-01	1.38E-01	6.41E-02	4.02E-02	3.10E-02	2.56E-02
% difference	-0.95	-1.03	-1.09	-1.13	-1.04	-0.85	-0.67	-0.41
Energy (kV)	**1**	**1.5**	**2**	**3**	**4**	**5**	**6**	**8**
Adipose tissue								
Mixture rule	2.62E+03	8.60E+02	3.79E+02	1.18E+02	4.98E+01	2.53E+01	1.45E+01	5.92E+00
Hubbell	2.62E+03	8.60E+02	3.79E+02	1.18E+02	4.98E+01	2.53E+01	1.45E+01	5.92E+00
% difference	0.00	0.01	-0.02	-0.04	-0.01	0.00	-0.01	-0.03
Energy (kV)	**10**	**15**	**20**	**30**	**40**	**50**	**60**	**80**
Adipose tissue								
Mixture rule	2.93E+00	8.10E-01	3.25E-01	9.49E-02	4.57E-02	3.08E-02	2.57E-02	2.36E-02
Hubbell	2.94E+00	8.10E-01	3.25E-01	9.50E-02	4.58E-02	3.09E-02	2.57E-02	2.36E-02
% difference	-0.03	-0.02	-0.01	-0.02	-0.02	-0.01	-0.03	-0.02

The mixture rule was then applied to the real neonatal tissues and possible substitute materials. The results are tabulated in Table 4.8.

Table 4.8: Mass energy absorption coefficients (cm^2/g) for real and substitute materials as calculated with the mixture rule.

	Energy (kV)							
Material	**1.0**	**1.5**	**2.0**	**3.0**	**4.0**	**5.0**	**6.0**	**8.0**
Newborn skeletal muscle	3.813E+03	1.285E+03	5.747E+02	1.832E+02	7.989E+01	4.102E+01	2.364E+01	9.793E+00
Frigerio gel	3.762E+03	1.275E+03	5.702E+02	1.806E+02	7.727E+01	3.955E+01	2.273E+01	9.382E+00
RM/G1 gel	3.846E+03	1.296E+03	5.800E+02	1.839E+02	8.016E+01	4.114E+01	2.370E+01	9.814E+00
Rossi gel	3.711E+03	1.244E+03	5.556E+02	1.723E+02	7.342E+01	3.747E+01	2.149E+01	8.838E+00
Polystyrene	2.039E+03	6.453E+02	2.784E+02	8.274E+01	3.437E+01	1.723E+01	9.730E+00	3.916E+00
Temex	2.021E+03	6.633E+02	2.884E+02	1.038E+02	4.456E+01	2.438E+01	1.418E+01	5.972E+00
Gammex solid water	2.592E+03	8.444E+02	3.711E+02	1.147E+02	4.854E+01	3.560E+01	2.104E+01	9.087E+00
Agar gel mix	3.951E+03	1.331E+03	5.960E+02	1.854E+02	7.917E+01	4.046E+01	2.323E+01	9.566E+00
Newborn cortical bone	3.772E+03	1.289E+03	5.826E+02	2.710E+02	1.213E+02	1.560E+02	9.615E+01	4.404E+01
SB5	3.795E+03	1.285E+03	5.804E+02	1.852E+02	8.062E+01	1.687E+02	1.049E+02	4.869E+01
B110	3.822E+03	1.308E+03	5.941E+02	1.894E+02	8.265E+01	1.675E+02	1.041E+02	4.827E+01
Gammex SB3	3.730E+03	1.262E+03	5.701E+02	1.812E+02	7.883E+01	1.678E+02	1.044E+02	4.848E+01
Fetal inflated lung	3.870E+03	1.308E+03	5.856E+02	1.877E+02	8.119E+01	4.167E+01	2.400E+01	9.936E+00
Griffith lung	2.720E+03	8.935E+02	3.938E+02	1.203E+02	5.088E+01	3.578E+01	2.107E+01	9.049E+00
LN10/75	2.350E+03	1.180E+03	5.394E+02	1.739E+02	7.580E+01	4.399E+01	2.581E+01	1.100E+01
Gammex LN300	2.380E+03	1.183E+03	5.408E+02	1.743E+02	7.599E+01	4.461E+01	2.621E+01	1.119E+01
Fetal deflated lung	3.870E+03	1.308E+03	5.856E+02	1.877E+02	8.119E+01	4.167E+01	2.400E+01	9.936E+00
Polystyrene	2.039E+03	6.453E+02	2.784E+02	8.274E+01	3.437E+01	1.723E+01	9.730E+00	3.916E+00
Gammex CT solid water	2.592E+03	8.442E+02	3.710E+02	1.147E+02	4.853E+01	3.560E+01	2.104E+01	9.085E+00
Gammex solid water	2.592E+03	8.444E+02	3.711E+02	1.147E+02	4.854E+01	3.560E+01	2.104E+01	9.087E+00
	Energy (kV)							
Material	**10.0**	**15.0**	**20.0**	**30.0**	**40.0**	**50.0**	**60.0**	**80.0**
Newborn skeletal muscle	4.903E+00	1.372E+00	5.524E-01	1.572E-01	7.027E-02	4.265E-02	3.210E-02	2.597E-02
Frigerio gel	4.683E+00	1.304E+00	5.233E-01	1.486E-01	6.672E-02	4.085E-02	3.106E-02	2.550E-02
RM/G1 gel	4.912E+00	1.374E+00	5.529E-01	1.572E-01	7.024E-02	4.261E-02	3.207E-02	2.593E-02
Rossi gel	4.400E+00	1.220E+00	4.885E-01	1.388E-01	6.272E-02	3.887E-02	2.994E-02	2.504E-02
Polystyrene	1.919E+00	5.202E-01	2.076E-01	6.248E-02	3.264E-02	2.421E-02	2.172E-02	2.159E-02
Temex	3.626E+00	1.123E+00	4.874E-01	1.521E-01	7.166E-02	4.451E-02	3.361E-02	2.677E-02
Gammex solid water	4.688E+00	1.382E+00	5.758E-01	1.706E-01	7.728E-02	4.653E-02	3.435E-02	2.671E-02
Agar gel mix	4.768E+00	1.324E+00	5.303E-01	1.502E-01	6.726E-02	4.112E-02	3.123E-02	2.563E-02
Newborn cortical bone	2.361E+01	7.368E+00	3.158E+00	9.374E-01	3.954E-01	2.058E-01	1.243E-01	6.253E-02
SB5	2.633E+01	8.315E+00	3.590E+00	1.073E+00	4.537E-01	2.356E-01	1.413E-01	6.937E-02
B110	2.608E+01	8.233E+00	3.553E+00	1.062E+00	4.488E-01	2.331E-01	1.399E-01	6.874E-02
Gammex SB3	2.621E+01	8.283E+00	3.577E+00	1.070E+00	4.524E-01	2.350E-01	1.411E-01	6.937E-02
Fetal inflated lung	4.972E+00	1.390E+00	5.591E-01	1.588E-01	7.089E-02	4.295E-02	3.228E-02	2.606E-02
Griffith lung	4.650E+00	1.362E+00	5.653E-01	1.668E-01	7.555E-02	4.561E-02	3.380E-02	2.647E-02
LN10/75	5.632E+00	1.643E+00	6.816E-01	2.008E-01	1.375E-01	8.672E-02	6.171E-02	4.064E-02
Gammex LN300	5.736E+00	1.678E+00	6.973E-01	2.059E-01	1.452E-01	9.176E-02	6.511E-02	4.236E-02
Fetal deflated lung	4.972E+00	1.390E+00	5.591E-01	1.588E-01	7.089E-02	4.295E-02	3.228E-02	2.606E-02
Polystyrene	1.919E+00	5.202E-01	2.076E-01	6.248E-02	3.264E-02	2.421E-02	2.172E-02	2.159E-02
Gammex CT solid water	4.687E+00	1.381E+00	5.757E-01	1.706E-01	7.727E-02	4.653E-02	3.434E-02	2.670E-02
Gammex solid water	4.688E+00	1.382E+00	5.758E-01	1.706E-01	7.728E-02	4.653E-02	3.435E-02	2.671E-02

The spectral weighted mass energy absorption coefficient determination program written by Mr EA de Kock[37] was used to calculate a mass energy absorption coefficient, for each material in Table 4.8, weighted over a typical incident x-ray beam spectrum. The program also has the ability to calculate spectral hardening due to muscle attenuation of the beam. Such attenuated spectral weighted mass

energy absorption coefficients were calculated for 0, 1, 2, 3, 3.5, 4, 5, 6 and 7 cm muscle attenuator. The spectral weighted mass energy absorption coefficient for the emission spectrum was equivalent to that with 0 cm muscle attenuation. The results are recorded in Table 4.9.

The spectral weighted mass energy absorption coefficients, in Table 4.9, for the possible substitute materials were normalised to that of the real neonatal tissues and the results are shown in Figure 4.10.

Table 4.9: Spectrum weighted mass energy absorption coefficients for real and substitute materials.

Material	Spectrum weighted mass energy absorption coefficient (cm^2/g)								
	0cm muscle attenuation	1cm muscle attenuation	2cm muscle attenuation	3cm muscle attenuation	3.5cm muscle attenuation	4cm muscle attenuation	5cm muscle attenuation	6cm muscle attenuation	7cm muscle attenuation
Newborn skeletal muscle	1.405E-01	1.239E-01	1.121E-01	1.032E-01	9.957E-02	9.630E-02	9.070E-02	8.606E-02	8.215E-02
Frigerio gel	1.333E-01	1.176E-01	1.064E-01	9.805E-02	9.458E-02	9.148E-02	8.617E-02	8.178E-02	7.808E-02
RM/G1 gel	1.405E-01	1.239E-01	1.121E-01	1.032E-01	9.954E-02	9.626E-02	9.064E-02	8.600E-02	8.208E-02
Rossi gel	1.246E-01	1.100E-01	9.963E-02	9.184E-02	8.861E-02	8.573E-02	8.081E-02	7.673E-02	7.330E-02
Polystyrene	5.776E-02	5.180E-02	4.761E-02	4.448E-02	4.319E-02	4.205E-02	4.009E-02	3.849E-02	3.714E-02
Temex	1.340E-01	1.195E-01	1.091E-01	1.012E-01	9.785E-02	9.489E-02	8.980E-02	8.556E-02	8.197E-02
Gammex solid water	1.512E-01	1.339E-01	1.215E-01	1.122E-01	1.083E-01	1.048E-01	9.881E-02	9.385E-02	8.965E-02
Agar gel mix	1.345E-01	1.186E-01	1.073E-01	9.883E-02	9.532E-02	9.219E-02	8.683E-02	8.240E-02	7.867E-02
Newborn cortical bone	8.109E-01	7.139E-01	6.441E-01	5.910E-01	5.689E-01	5.490E-01	5.147E-01	4.862E-01	4.619E-01
SB5	9.255E-01	8.154E-01	7.362E-01	6.758E-01	6.507E-01	6.281E-01	5.891E-01	5.566E-01	5.290E-01
B110	9.159E-01	8.070E-01	7.286E-01	6.689E-01	6.439E-01	6.216E-01	5.830E-01	5.508E-01	5.234E-01
Gammex SB3	9.239E-01	8.140E-01	7.349E-01	6.746E-01	6.494E-01	6.268E-01	5.878E-01	5.553E-01	5.277E-01
Fetal inflated lung	1.421E-01	1.253E-01	1.133E-01	1.043E-01	1.006E-01	9.731E-02	9.162E-02	8.692E-02	8.295E-02
Griffith lung	1.479E-01	1.309E-01	1.188E-01	1.097E-01	1.059E-01	1.025E-01	9.663E-02	9.178E-02	8.768E-02
LN10/75	1.984E-01	1.803E-01	1.677E-01	1.585E-01	1.547E-01	1.513E-01	1.456E-01	1.408E-01	1.368E-01
Gammex LN300	2.048E-01	1.865E-01	1.738E-01	1.645E-01	1.607E-01	1.573E-01	1.515E-01	1.467E-01	1.427E-01
Fetal deflated lung	1.421E-01	1.253E-01	1.133E-01	1.043E-01	1.006E-01	9.731E-02	9.162E-02	8.692E-02	8.295E-02
Polystyrene	5.776E-02	5.180E-02	4.761E-02	4.448E-02	4.319E-02	4.205E-02	4.009E-02	3.849E-02	3.714E-02
Gammex CT solid water	1.512E-01	1.339E-01	1.215E-01	1.122E-01	1.083E-01	1.048E-01	9.881E-02	9.385E-02	8.965E-02
Gammex solid water	1.512E-01	1.339E-01	1.215E-01	1.122E-01	1.083E-01	1.048E-01	9.881E-02	9.385E-02	8.965E-02

a.)

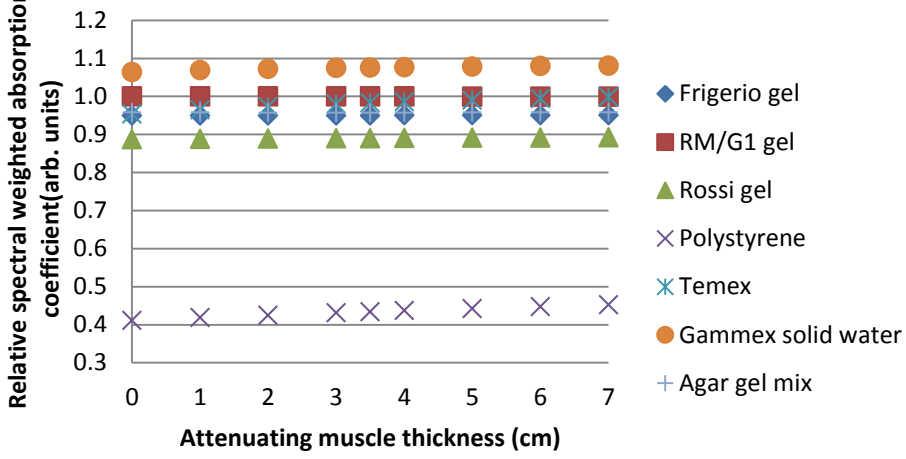

b.)

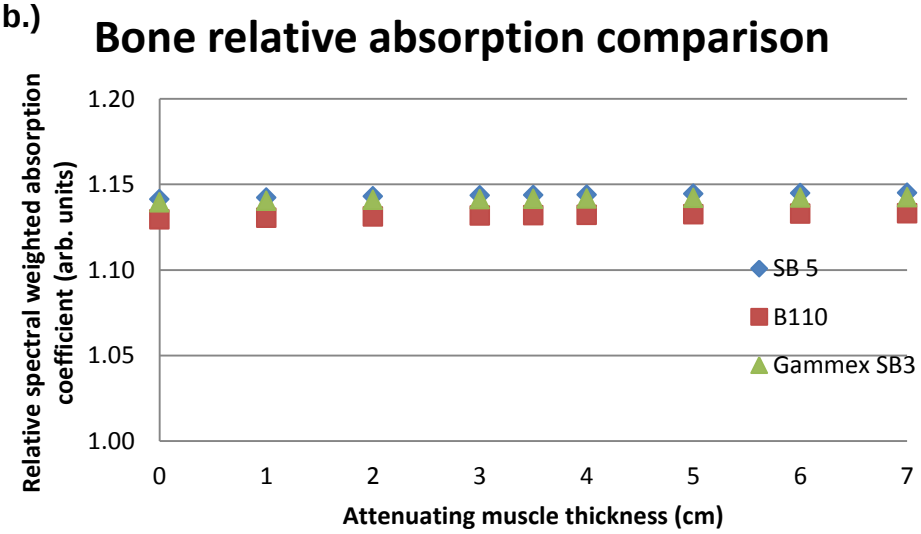

c.)

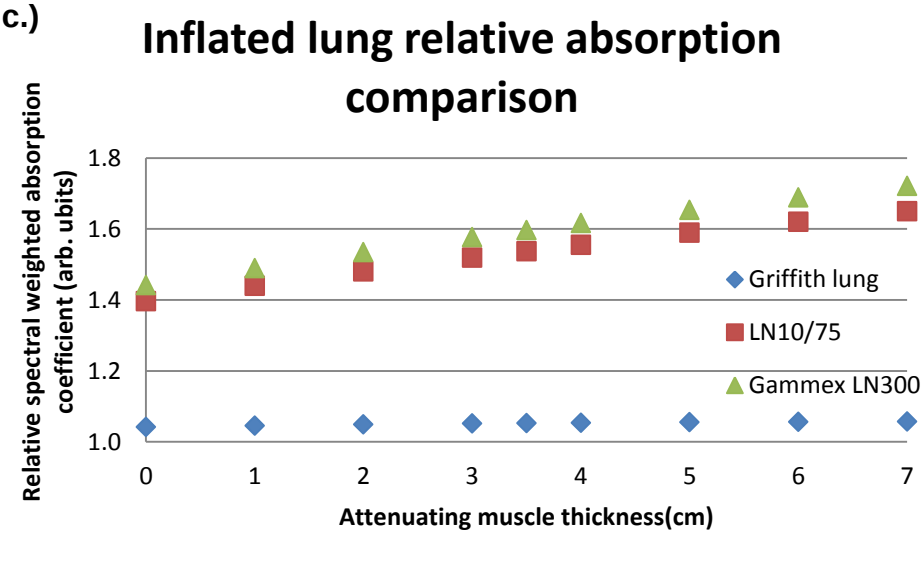

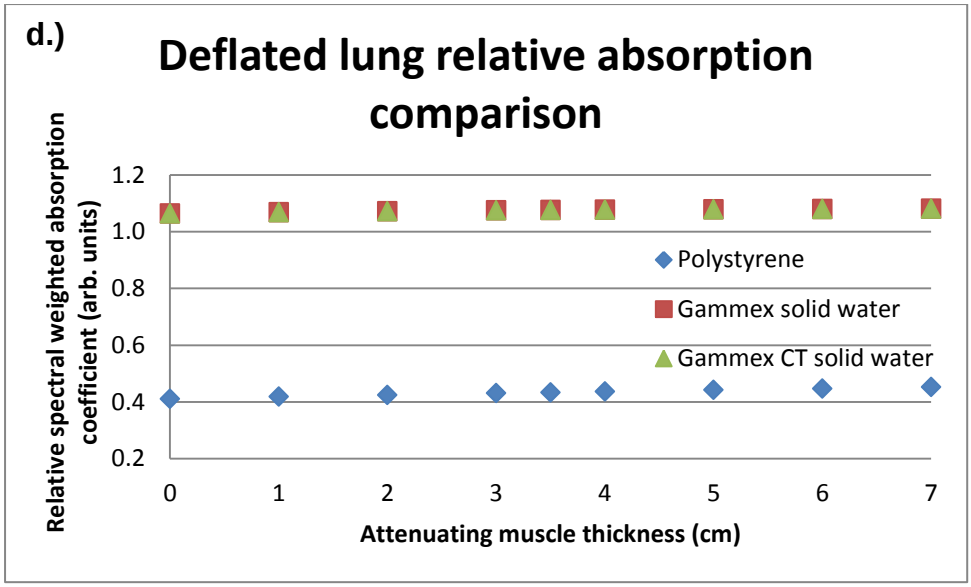

Figure 4.10: Normalised spectral weighted mass energy absorption coefficient comparison of real neonatal tissues and possible substitute materials including a.) body (muscle), b.) bone, c.) inflated (healthy) lung and d.) deflated (sick) lung.

4.1.3 Obtainability and cost

The possible substitute materials were evaluated on obtainability and cost. It was very difficult to find any information on the manufacturing of Frigerio gel, RM/G1 gel, Rossi gel, SB5, B110, Griffith lung and LN10/75 lung. The basic properties of these substitutes were discussed in the ICRU 44 report.[46] It was not possible to determine the cost for these materials.

Gammex RMI© had a representative based in South Africa and the necessary information on the composition of the different substitute materials was readily obtained. The different substitute materials could also be bought through the supplier at a quoted cost. Different sizes and thicknesses of the materials were also available. For the current study, one slab of each of Gammex SB3, Gammex LN300 and Gammex solid water material were bought. The slab size was 20 x 20 x 1 cm^3. The cost for Gammex SB3 bone and Gammex LN300 lung was R6726 per slab, for Gammex solid water R4902 and for Gammex CT solid water R5472.

Agar could be obtained locally from Merck, WhiteSci or Sigma Aldrich at about R1700 per kilogram or R560 for 250 g.

4.1.4 Validation of the phantom

The neonatal chest simulation phantom was validated by obtaining the intensities and standard deviations in ROIs placed in muscle, bone, healthy and sick lung areas of images of the neonatal chest simulation phantom and an image of a real neonatal chest. These values were compared. Figure 4.11 shows these images which were obtained using the same exposure parameters, although different imaging units were used. The results are shown in Table 4.10.

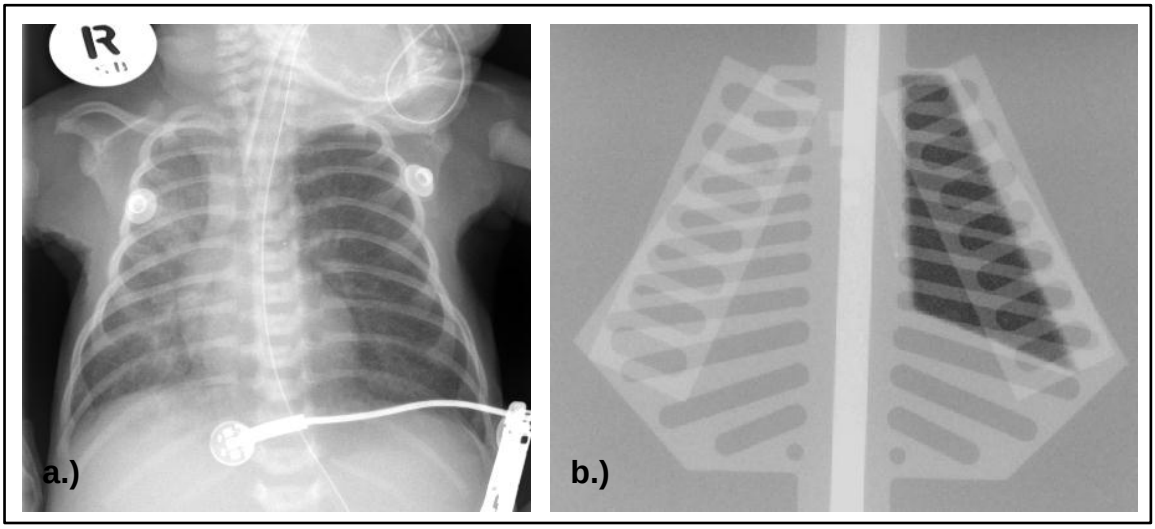

Figure 4.11: a.) Real neonatal chest x-ray and b.) x-ray of neonatal chest simulation phantom used for phantom validation.

Table 4.10: Phantom validation data.

	Muscle		Bone		Healthy lung		Sick lung	
	Mean intensity	Standard deviation	Mean intensity	Standard deviation	Mean intensity	Standard deviation	Mean intensity	Standard deviation
Real neonate image	2524.1	74.7	2812.5	125.4	1646.4	78.4	2779.1	85.0
Neonatal simulation phantom image	3374.9	25.1	3604.6	24.3	2387.8	50.3	3423.4	23.7
% difference	-33.7		-28.2		-45.0		-23.2	

4.2 The design of a physics image quality assessment phantom

The physics image quality phantom designed for the quantitative analysis of image quality in the current study is shown schematically in Figure 3.6. The work drawing for the physics image quality assessment phantom is included in Figure 4.12. These drawings were used to machine the inserts of the phantom and to construct the phantom.

.

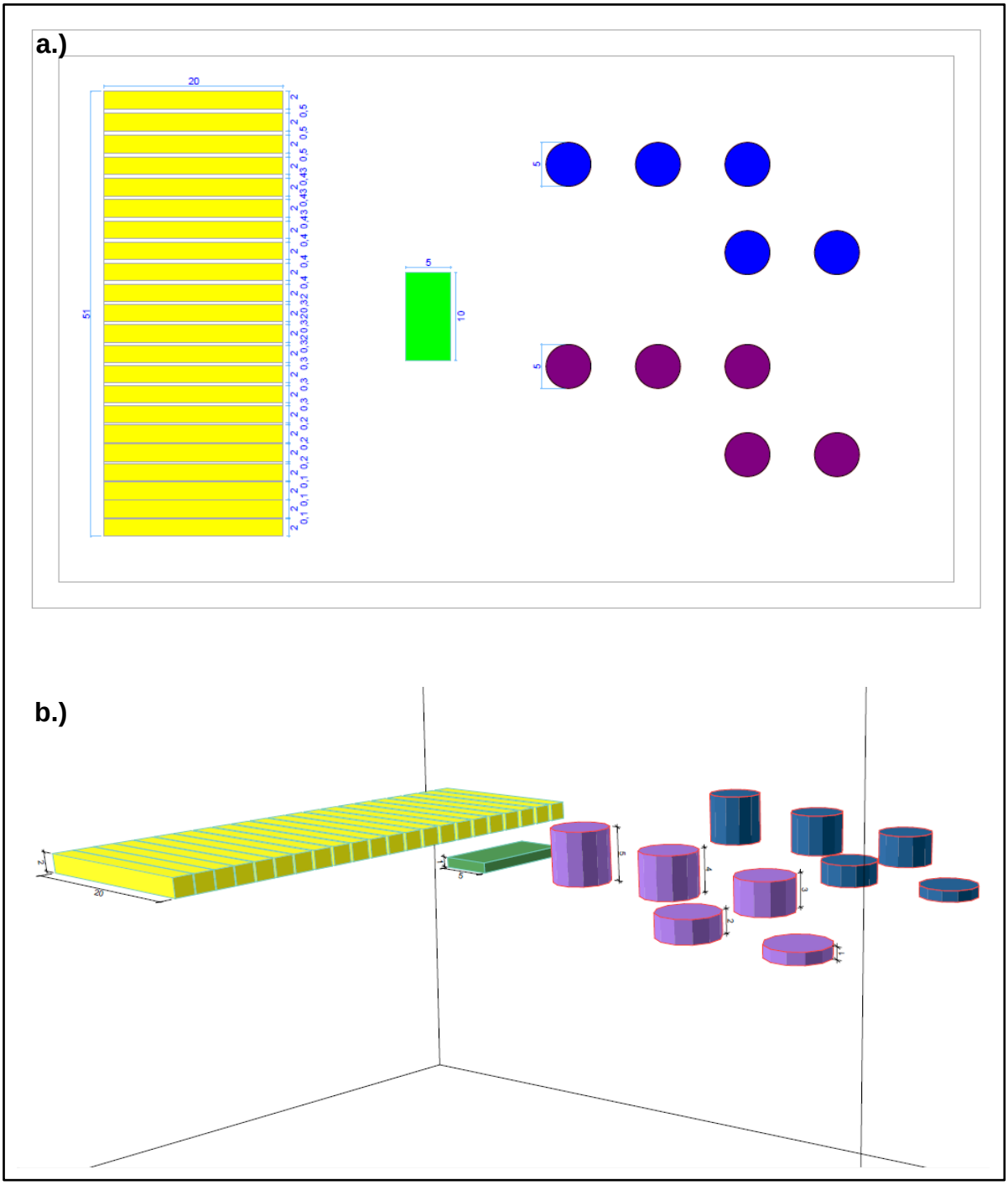

Figure 4.12: a.) AP and b.) three-dimensional views of the physics image quality assessment phantom.

The phantom was used with the final set of exposures to quantify image quality physically.

4.3 Image quality analysis

The results for quantitative image quality analysis for the final exposure set, as obtained with the physics image quality assessment phantom, are included in section 4.3.1 below. The visual and quantitative image quality results for the neonatal chest simulation phantom, for the preliminary exposures, are included in Tables 4.13 to 4.19 in section 4.4. The results of the final exposure set are recorded in Tables 4.20 and 4.21. The comparative quantitative image quality rankings for the phantoms are recorded in Table 4.22.

4.3.1 Evaluation of the physics image quality assessment phantom

The MTFs were obtained from the ESF of the copper plate in the phantom and by using Equation 3.2 and the different diameter wires in the phantom. Figure 4.13 shows the obtained MTFs.

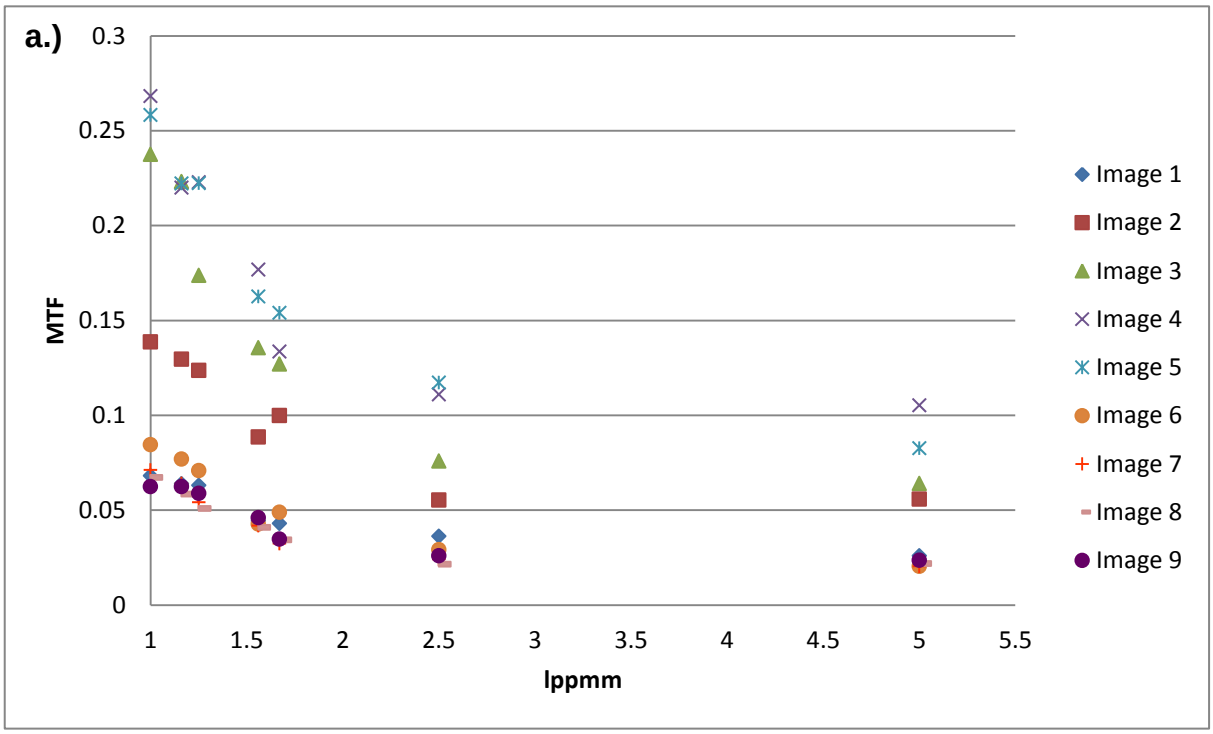
a.)
MTF
lppmm
0.3
0.25
0.2
0.15
0.1
0.05
0
1
1.5
2
2.5
3
3.5
4
4.5
5
5.5
Image 1
Image 2
Image 3
Image 4
Image 5
Image 6
Image 7
Image 8
Image 9

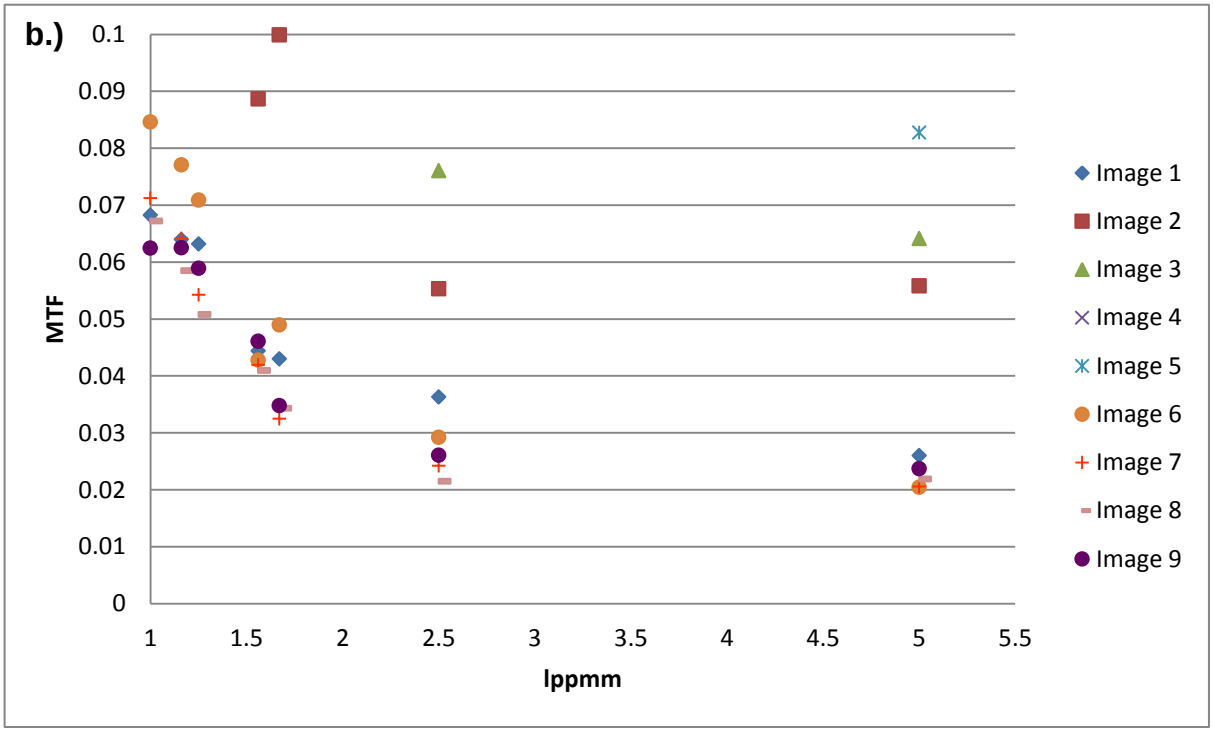
b.)
MTF
lppmm
0.1
0.09
0.08
0.07
0.06
0.05
0.04
0.03
0.02
0.01
0
1
1.5
2
2.5
3
3.5
4
4.5
5
5.5
Image 1
Image 2
Image 3
Image 4
Image 5
Image 6
Image 7
Image 8
Image 9

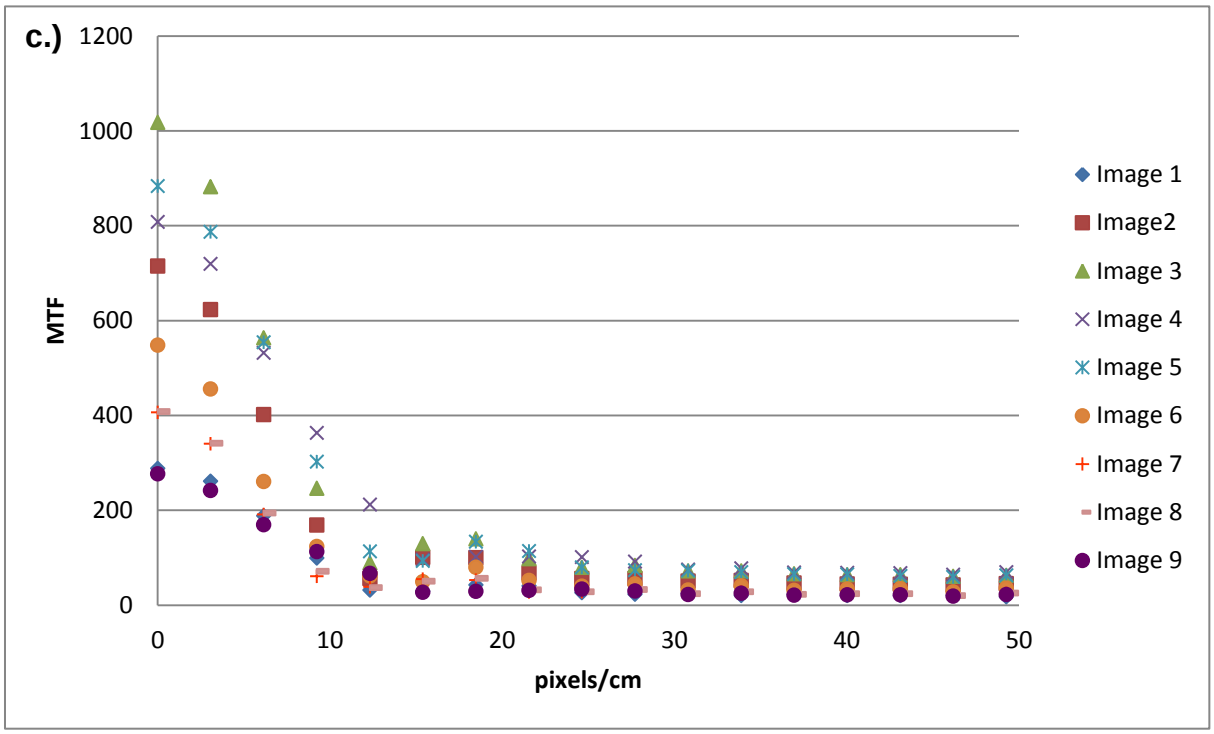

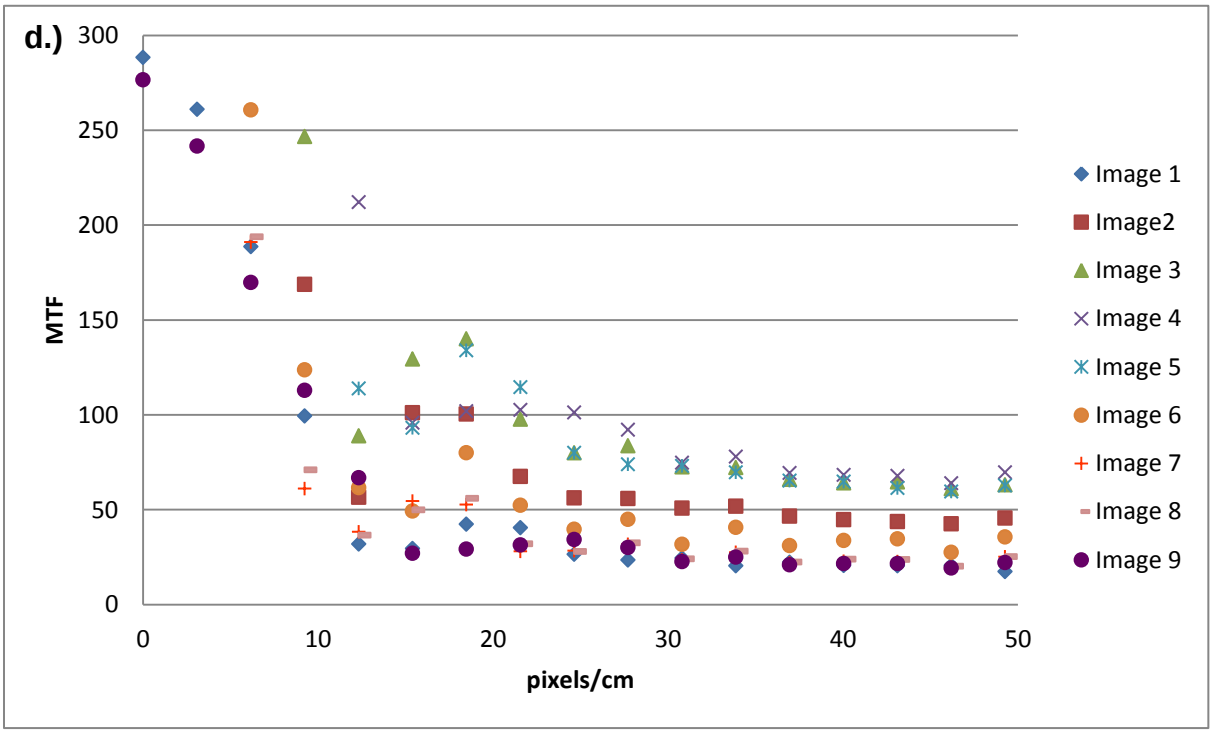

Figure 4.13: MTFs for the physics image quality phantom. a.) MTFs obtained from the perspex holder with different diameter wires. b.) Zoomed in version of Figure a.). c.) MTFs obtained from the ESF of the copper strip. d.) Zoomed in version of Figure c.).

The results for SNR, SDNR and CNR calculations are included in Table 4.11. Table 4.11 also shows the low contrast detectability results.

All the quantitative image quality analysis results for the physics image quality assessment phantom were considered and the overall ranking of the physics image quality assessment phantom images for the final exposure set is included in Table 4.11.

Table 4.11: Quantitative image quality analysis results for physics image quality assessment phantom.

Rank	Image number	Image mode	Focus	kV	mAs	FFD (cm)	Filtration	Thickness torlon disk visible (mm)	Thickness high density polyethylene disk visible (mm)	SNR torlon	SNR high density polyethylene	SDNR torlon	SDNR high density polyethylene
1	1	Processed	Fine	50	2.0	100	Inherent	3	3	86.9	80.3	2.3	7.3
7	2	Raw	Fine	60	2.0	100	0.1 mm Cu + 1 mm Al	4	5	23.2	24.0	2.0	4.1
6	3	Raw	Fine	64	2.0	100	0.1 mm Cu + 1 mm Al	3	5	24.7	22.6	1.8	5.0
9	4	Raw	Fine	61	0.8	100	Inherent	4	5	17.9	14.1	1.4	3.6
8	5	Raw	Fine	62	0.8	100	Inherent	4	5	21.5	18.4	1.2	3.9
5	6	Processed	Fine	57	2.0	100	0.1 mm Cu + 1 mm Al	5	5	60.7	54.4	2.6	0.1
2	7	Processed	Fine	57	3.2	100	0.1 mm Cu + 1 mm Al	4	5	94.6	92.5	0.7	4.0
4	8	Processed	Fine	60	2.0	100	0.1 mm Cu + 1 mm Al	5	5	83.9	85.2	0.1	4.2
3	9	Processed	Fine	61	0.8	100	Inherent	4	5	78.5	75.5	1.1	4.1

4.3.2 Neonatal chest simulation phantom evaluation

Images of the neonatal chest simulation phantom were evaluated quantitatively and visually, as in Tables 4.13 to 4.19 in section 4.4, for the preliminary exposure sets. Quantitative image quality and ESD results for the final exposure set are recorded in Table 4.20. The data in Table 4.21 for the final exposure set were used to rank the images of the neonatal chest simulation phantom based on visual or clinical image quality, determined by independent medical physicists and radiographers.

The final visual image quality ranking was compared to the quantitative image quality and absolute dose rankings, as in Table 4.12.

Table 4.12: Final overall ranking.

Image number	Absolute dose (µGy)	Absolute dose ranking	Total visual image quality score, averaged over observers	Average observer visual image quality ranking	Average quantitative image quality ranking	Overall ranking
1	44.0 ± 2.2	6	11	8	2	9
2	19.1 ± 1.0	2	13	3	9	2
3	22.8 ± 1.1	3	14	2	6	1
4	25.8 ± 1.3	4	12	7	8	7
5	26.4 ± 1.3	5	13	4	7	6
6	16.2 ± 0.8	1	12	6	1	4
7	26.3 ± 1.3	5	14	1	4	3
8	19.1 ± 1.0	2	13	5	5	5
9	25.8 ± 1.3	4	11	9	3	8

4.4 Dose reduction versus image quality

Factors that influenced the ESD also influenced image quality. These factors, focus size, kV, mAs, FFD, filtration and collimation, had to be used in combination with each other to achieve a decrease in ESD whilst maintaining acceptable clinical image quality. To determine the combination in which these factors had to be used, preliminary exposures were made, based on trial and error, in a wide range as

suggested in different publications in literature.[13,14,15,21,28] The results for the four sets of preliminary exposures which were made on a fixed x-ray unit at the Oncology Division at Tygerberg Academic Hospital are included in Tables 4.13 to 4.19. These results were used to determine a set of exposures that were made on the mobile unit that was routinely used to x-ray neonatal chests. The results for the final set of exposures are included in Tables 4.20 and 4.21. In Table 4.22 the quantitative image quality rankings for the final set of exposures for the neonatal chest simulation phantom and those of the physics image quality assessment phantom were compared.

Table 4.13: First preliminary exposure set results.

Focus	kV	mAs	FFD (cm)	Filtration	Relative dose (µGy)	SNR	SDNR
Fine	50	2	100	Inherent	44.9	18.7	22.5
Fine	40	2	100	Inherent	21.9	28.1	38.0
Fine	70	2	100	Inherent	95.7	18.8	27.6
Fine	50	2	100	0.1 mm Cu + 1 mm Al	11.2	146.5	19.2
Fine	50	2	80	Inherent	73.1	28.1	47.7
Fine	50	2	120	Inherent	30.1	26.9	24.7

Table 4.14: Second preliminary exposure set results for raw images.

Focus	kV	mAs	FFD (cm)	Filtration	Sternum	Central line	Healthy lung	Sick lung	Overall	Total	SNR healthy lung	SNR sick lung	SDNR healthy lung	SDNR sick lung	CNR
Fine	50	2	100	Inherent	5	1	3	1	4	14	15.4	25.5	25.6	1.6	219.1
Fine	40	2	100	Inherent	2	0	3	1	1	7	15.2	59.3	38.3	2.3	47.6
Fine	45	2	100	Inherent	5	1	3	1	3	13	16.8	25.0	19.5	1.2	309.4
Fine	55	2	100	Inherent	4	1	3	0	2	10	21.2	59.7	57.1	0.5	77.7
Fine	60	2	100	Inherent	5	3	2	0	3	13	51.6	42.2	28.7	1.8	309.4
Fine	70	2	100	Inherent	5	3	2	0	1	11	35.7	40.3	30.3	4.2	401.7
Fine	50	2	100	0.1 mm Cu + 1 mm Al	4	1	2	0	1	8	17.0	21.4	14.3	0.8	189.8
Fine	50	2	100	1 mm Al	4	2	2	0	1	9	15.7	48.0	38.4	1.0	74.3
Large	50	2	100	Inherent	5	1	3	1	4	14	14.8	30.7	28.9	1.7	203.3
Fine	50	2	120	Inherent	4	1	2	0	1	8	14.1	31.8	28.5	0.5	165.1

Table 4.15: Second preliminary exposure set results for processed images.

Focus	kV	mAs	FFD (cm)	Filtration	Sternum	Central line	Healthy lung	Sick lung	Overall	Total	SNR healthy lung	SNR sick lung	SDNR healthy lung	SDNR sick lung	CNR
Fine	50	2	100	Inherent	5	1	3	0	2	11	30.0	84.8	35.7	2.9	39.4
Fine	40	2	100	Inherent	2	0	3	0	1	6	23.1	64.8	27.0	5.8	28.6
Fine	45	2	100	Inherent	4	0	3	0	1	8	28.7	96.6	25.2	8.4	34.8
Fine	55	2	100	Inherent	5	1	3	0	2	11	39.9	94.6	51.0	1.0	43.6
Fine	60	2	100	Inherent	5	1	3	0	2	11	43.7	129.6	49.9	1.6	47.7
Fine	70	2	100	Inherent	5	1	3	0	2	11	39.3	149.3	55.2	0.6	41.8
Fine	50	2	100	0.1 mm Cu + 1 mm Al	5	1	3	0	1	10	33.5	65.3	22.0	0.9	36.1
Fine	50	2	100	1 mm Al	5	1	3	0	1	10	19.7	49.2	45.3	0.4	45.3
Large	50	2	100	Inherent	5	1	3	0	2	11	32.1	102.5	30.7	3.0	36.0
Fine	50	2	120	Inherent	3	0	3	0	1	7	61.1	136.2	34.1	1.2	33.0

Table 4.16: Third preliminary exposure set results for raw images.

Focus	kV	mAs	Filtration	Relative dose (µGy)	Sternum	Central line	Healthy lung	Sick lung	Overall	Total	SNR healthy lung	SNR sick lung	SDNR healthy lung	SDNR sick lung	CNR
Fine	50	2.00	Inherent	45.9	5	2	3	1	3	14	16.8	37.6	34.0	1.2	193.0
Large	50	2.00	Inherent	48.1	4	1	3	0	2	10	16.3	40.4	32.2	0.5	200.6
Fine	50	3.20	1 mm Al	49.6	2	1	3	0	1	7	16.7	49.0	42.4	0.9	80.1
Fine	50	3.20	0.1 mm Cu + 1 mm Al	19.0	5	3	1	0	2	11	23.0	20.5	16.9	0.3	308.1
Fine	50	4.00	1 mm Al	62.4	2	1	3	1	0	7	19.1	59.9	46.4	1.4	76.5
Fine	50	4.00	0.1 mm Cu + 1 mm Al	24.1	5	3	1	0	3	12	21.5	22.1	19.8	0.1	301.1
Fine	70	2.00	1 mm Al	72.6	5	3	3	1	4	16	20.8	36.4	30.5	0.9	172.4
Fine	70	2.00	0.1 mm Cu + 1 mm Al	36.8	2	1	3	0	0	6	36.5	115.4	71.3	2.5	38.9
Fine	55	1.60	Inherent	45.7	4	1	3	0	3	11	16.8	60.8	39.4	1.4	74.7
Fine	55	1.25	Inherent	35.1	2	1	3	0	1	7	13.7	39.0	34.1	1.1	60.5
Fine	55	0.80	Inherent	21.4	1	1	3	0	0	5	14.8	39.8	32.2	1.5	62.8
Fine	60	1.40	Inherent	48.3	5	3	3	0	4	15	14.6	39.0	38.4	0.3	119.0
Fine	60	1.00	Inherent	33.6	5	1	2	1	3	12	17.3	32.2	28.9	0.1	105.6
Fine	60	0.80	Inherent	26.2	4	1	3	0	3	11	15.9	29.1	22.5	0.1	106.4
Fine	65	1.25	Inherent	51.5	5	3	3	1	5	17	18.7	29.7	23.3	0.4	212.9
Fine	65	0.80	Inherent	30.8	5	2	2	0	3	12	23.9	24.6	20.5	0.5	304.8
Fine	65	0.50	Inherent	18.0	4	1	1	0	1	7	13.8	31.8	22.9	0.1	95.5
Fine	70	1.00	Inherent	47.5	5	3	0	0	1	9	24.6	33.3	28.1	0.9	280.1
Fine	70	0.50	Inherent	21.1	5	3	0	0	0	8	21.9	23.9	17.9	0.2	265.4

Table 4.17: Third preliminary exposure set results for processed images.

Focus	kV	mAs	Filtration	Relative dose (µGy)	Sternum	Central line	Healthy lung	Sick lung	Overall	Total	SNR healthy lung	SNR sick lung	SDNR healthy lung	SDNR sick lung	CNR
Fine	50	2.00	Inherent	45.9	2	1	3	0	3	9	57.2	129.9	0.6	44.8	40.4
Large	50	2.00	Inherent	48.1	4	1	3	0	2	10	33.9	109.6	1.9	38.7	37.7
Fine	50	3.20	1 mm Al	49.6	2	1	3	1	1	8	73.9	152.5	1.4	40.5	40.2
Fine	50	3.20	0.1 mm Cu + 1 mm Al	19.0	4	1	3	0	3	11	57.7	143.9	1.0	33.3	28.2
Fine	50	4.00	1 mm Al	62.4	2	1	3	1	1	8	78.7	181.8	0.7	39.9	39.8
Fine	50	4.00	0.1 mm Cu + 1 mm Al	24.1	4	1	3	0	3	11	57.2	138.7	0.5	32.2	30.1
Fine	70	2.00	1 mm Al	72.6	5	3	3	0	4	15	32.1	78.6	5.1	43.3	46.5
Fine	70	2.00	0.1 mm Cu + 1 mm Al	36.8	5	3	3	0	3	14	76.7	190.7	2.1	37.9	39.0
Fine	55	1.60	Inherent	45.7	2	1	3	0	2	8	71.8	178.7	0.8	38.6	36.1
Fine	55	1.25	Inherent	35.1	2	1	3	0	2	8	59.5	133.5	0.8	30.0	31.5
Fine	55	0.80	Inherent	21.4	2	1	3	0	2	8	72.8	106.9	0.3	24.7	38.7
Fine	60	1.40	Inherent	48.3	5	1	2	0	3	11	76.0	155.6	2.1	42.4	36.3
Fine	60	1.00	Inherent	33.6	5	1	2	0	3	11	77.8	143.8	1.8	39.5	38.3
Fine	60	0.80	Inherent	26.2	4	1	2	0	2	9	65.1	127.6	0.6	27.5	33.3
Fine	65	1.25	Inherent	51.5	5	1	3	0	4	13	77.7	175.0	1.3	42.6	35.8
Fine	65	0.80	Inherent	30.8	5	1	3	0	3	12	77.6	172.5	0.8	33.1	38.9
Fine	65	0.50	Inherent	18.0	5	1	3	0	3	12	69.0	135.9	0.3	26.0	35.8
Fine	70	1.00	Inherent	47.5	5	1	3	0	3	12	80.3	178.3	1.7	41.4	37.2
Fine	70	0.50	Inherent	21.1	5	1	3	0	3	12	58.0	140.4	0.6	31.1	30.8

Table 4.18: Fourth preliminary exposure set results for raw images.

kV	mAs	Filtration	Relative dose (µGy)	Sternum	Central line	Healthy lung	Sick lung	Overall	Total	SNR healthy lung	SNR sick lung	SDNR healthy lung	SDNR sick lung	CNR
50	2.00	Inherent	45.3	4	1	2	0	3	10	14.6	37.0	29.9	1.4	131.3
53	3.20	0.1 mm Cu + 1 mm Al	23.4	5	3	1	0	1	10	29.3	22.4	19.4	0.2	366.6
55	2.00	0.1 mm Cu + 1 mm Al	16.2	5	3	1	0	1	10	18.5	19.8	12.9	0.4	192.2
55	2.50	0.1 mm Cu + 1 mm Al	20.6	5	3	1	0	1	10	52.9	23.6	18.6	0.3	624.9
55	3.20	0.1 mm Cu + 1 mm Al	26.8	5	3	1	0	1	10	28.9	24.5	18.1	0.5	345.1
55	4.00	0.1 mm Cu + 1 mm Al	34.0	5	3	1	1	1	11	25.9	32.2	25.4	0.3	300.1
57	2.00	0.1 mm Cu + 1 mm Al	18.7	5	3	1	1	1	11	16.3	17.8	15.7	0.7	164.0
57	3.20	0.1 mm Cu + 1 mm Al	31.0	5	3	1	1	1	11	22.3	27.2	24.2	0.6	237.6
60	2.00	0.1 mm Cu + 1 mm Al	22.8	5	1	3	0	3	12	17.0	29.5	27.2	0.4	77.3
60	3.20	0.1 mm Cu + 1 mm Al	37.6	5	1	3	0	3	12	20.7	41.3	40.5	0.8	79.2
63	2.00	0.1 mm Cu + 1 mm Al	26.6	4	1	3	0	2	10	24.1	50.9	38.2	0.4	66.3
64	2.00	0.1 mm Cu + 1 mm Al	27.7	5	3	2	0	3	13	18.8	44.3	27.8	0.8	94.0
65	2.00	0.1 mm Cu + 1 mm Al	29.1	5	1	1	0	1	8	26.7	57.3	38.1	0.2	68.8
58	1.25	Inherent	39.1	4	1	3	0	3	11	13.8	40.7	30.7	1.0	78.4
58	1.00	Inherent	30.9	4	1	3	0	3	11	15.9	43.9	36.6	1.1	79.2
59	1.25	Inherent	41.2	4	1	3	0	3	11	16.2	43.2	37.4	0.3	55.5
59	1.00	Inherent	32.4	4	1	3	0	2	10	17.2	48.3	36.9	0.4	69.9
61	1.10	Inherent	38.0	5	1	2	0	3	11	14.4	40.6	32.0	0.4	76.8
61	0.80	Inherent	26.7	5	1	2	0	3	11	14.1	27.9	26.2	0.6	89.1
62	1.10	Inherent	40.0	5	1	2	0	3	11	14.7	36.9	30.2	0.4	103.8
62	0.80	Inherent	28.2	5	1	2	0	3	11	16.3	33.5	28.4	0.8	121.4
63	1.10	Inherent	40.6	5	3	2	0	3	13	18.1	44.3	34.2	0.3	133.4
63	0.80	Inherent	29.1	5	3	1	0	2	11	18.9	16.5	16.2	0.4	230.6
64	1.00	Inherent	38.2	5	3	1	0	2	11	22.7	29.8	19.9	0.1	265.8
64	0.80	Inherent	29.5	5	3	1	0	2	11	16.2	29.8	21.5	0.5	170.7
64	0.50	Inherent	17.8	3	1	2	0	2	8	12.4	32.5	25.4	0.8	67.4
68	0.80	Inherent	33.6	5	3	1	0	1	10	27.6	26.0	22.1	0.3	322.9
68	0.50	Inherent	19.9	5	3	1	0	1	10	15.8	18.7	16.2	0.2	177.5

Table 4.19: Fourth preliminary exposure set results for processed images.

Focus	kV	mAs	Filtration	Relative dose (µGy)	Sternum	Central line	Healthy lung	Sick lung	Overall	Total	SNR healthy lung	SNR sick lung	SDNR healthy lung	SDNR sick lung	CNR
Fine	50	2.00	Inherent	45.3	2	1	3	0	2	8	75.2	156.7	37.1	1.1	37.9
Fine	53	3.20	0.1 mm Cu + 1 mm Al	23.4	5	1	3	0	3	12	79.9	160.4	30.1	1.7	36.6
Fine	55	2.00	0.1 mm Cu + 1 mm Al	16.2	5	1	3	0	3	12	77.7	142.2	27.5	0.7	35.7
Fine	55	2.50	0.1 mm Cu + 1 mm Al	20.6	5	1	3	0	3	12	68.7	138.1	32.8	1.7	32.0
Fine	55	3.20	0.1 mm Cu + 1 mm Al	26.8	5	2	3	0	3	13	85.1	151.9	39.4	0.8	40.1
Fine	55	4.00	0.1 mm Cu + 1 mm Al	34.0	5	2	3	0	3	13	82.1	205.3	40.8	0.7	36.8
Fine	57	2.00	0.1 mm Cu + 1 mm Al	18.7	5	3	3	1	3	15	69.0	152.6	32.8	2.0	30.3
Fine	57	3.20	0.1 mm Cu + 1 mm Al	31.0	5	3	3	1	4	16	77.3	155.1	39.8	1.1	37.3
Fine	60	2.00	0.1 mm Cu + 1 mm Al	22.8	5	3	3	0	4	15	82.8	158.8	30.3	0.5	37.0
Fine	60	3.20	0.1 mm Cu + 1 mm Al	37.6	5	3	3	0	4	15	86.8	156.2	41.7	1.5	39.0
Fine	63	2.00	0.1 mm Cu + 1 mm Al	26.6	5	3	3	0	4	15	82.1	148.0	37.6	2.0	34.8
Fine	64	2.00	0.1 mm Cu + 1 mm Al	27.7	5	3	3	0	4	15	81.9	168.4	32.7	1.3	34.0
Fine	65	2.00	0.1 mm Cu + 1 mm Al	29.1	5	3	3	0	4	15	77.2	171.1	37.9	0.6	34.2
Fine	58	1.25	Inherent	39.1	5	1	3	0	3	12	73.0	163.7	33.2	1.6	33.1
Fine	58	1.00	Inherent	30.9	5	1	3	0	3	12	82.0	141.1	33.8	1.3	38.6
Fine	59	1.25	Inherent	41.2	4	1	3	0	3	11	82.5	150.2	34.8	1.6	38.8
Fine	59	1.00	Inherent	32.4	5	1	3	0	3	12	78.0	143.3	34.5	1.9	37.0
Fine	61	1.10	Inherent	38.0	5	1	3	0	3	12	81.9	163.6	33.4	2.0	37.4
Fine	61	0.80	Inherent	26.7	5	1	3	0	3	12	69.4	146.1	29.8	1.5	32.9
Fine	62	1.10	Inherent	40.0	5	1	3	0	3	12	75.2	154.9	33.6	1.7	33.8
Fine	62	0.80	Inherent	28.2	5	1	3	0	3	12	71.2	149.3	28.4	0.9	32.9
Fine	63	1.10	Inherent	40.6	5	1	3	0	3	12	87.7	173.6	35.2	2.2	39.5
Fine	63	0.80	Inherent	29.1	5	1	3	0	3	12	86.1	139.9	32.3	1.4	39.3
Fine	64	1.00	Inherent	38.2	5	1	3	0	3	12	84.4	177.2	34.9	1.9	37.4
Fine	64	0.80	Inherent	29.5	5	1	3	0	3	12	64.2	178.7	37.5	1.3	30.7
Fine	64	0.50	Inherent	17.8	5	1	3	0	2	11	69.5	124.1	23.9	1.7	32.4
Fine	68	0.80	Inherent	33.6	5	1	3	0	3	12	72.9	148.9	38.5	2.0	32.7
Fine	68	0.50	Inherent	19.9	5	1	3	0	2	11	65.5	129.5	28.1	2.0	30.1

Table 4.20: Final exposure set quantitative image quality and ESD results.

Image number	Image mode	Focus	kV	mAs	FFD (cm)	Filtration	Absolute dose (µGy)	Dose ranking	SNR healthy lung	SNR sick lung	SDNR healthy lung	SDNR sick lung	CNR	Quantitative image quality ranking
1	Processed	Fine	50	2.0	100	Inherent	44.0 ± 2.2	6	45.5	86.3	24.5	0.5	32.8	2
2	Raw	Fine	60	2.0	100	0.1 mm Cu + 1 mm Al	19.1 ± 1.0	2	17.7	17.3	13.6	1.2	137.0	9
3	Raw	Fine	64	2.0	100	0.1 mm Cu + 1 mm Al	22.8 ± 1.1	3	16.2	30.9	21.0	0.7	59.0	6
4	Raw	Fine	61	0.8	100	Inherent	25.8 ± 1.3	4	13.2	24.0	19.7	2.2	78.4	8
5	Raw	Fine	62	0.8	100	Inherent	26.4 ± 1.3	5	12.7	24.5	17.0	2.5	96.6	7
6	Processed	Fine	57	2.0	100	0.1 mm Cu + 1 mm Al	16.2 ± 0.8	1	43.6	78.7	23.2	2.5	32.6	1
7	Processed	Fine	57	3.2	100	0.1 mm Cu + 1 mm Al	26.3 ± 1.3	5	25.4	60.0	24.5	3.0	38.6	4
8	Processed	Fine	60	2.0	100	0.1 mm Cu + 1 mm Al	19.1 ± 1.0	2	34.4	65.8	23.1	2.1	33.5	5
9	Processed	Fine	61	0.8	100	Inherent	25.8 ± 1.3	4	46.0	74.1	24.3	0.8	31.4	3

Table 4.21: Final exposure set visual image quality results.

Observer number	Sternum	Central line	Healthy lung	Sick lung	Overall	Total
Image number 1						
1	4	3	3	0	4	14
2	3	0	3	0	2	8
3	5	2	3	0	5	15
4	4	2	3	0	3	12
5	0	3	3	1	4	11
6	5	1	3	0	2	11
7	5	3	3	1	1	13
8	5	2	3	0	4	14
9	3	2	3	0	2	10
10	5	1	3	0	0	9
11	2	0	3	0	3	8
Average	3.7	1.7	3.0	0.2	2.7	11.4
Image number 2						
1	5	3	2	0	3	13
2	5	3	2	0	4	14
3	5	3	2	0	4	14
4	5	3	1	0	1	10
5	5	3	1	1	2	12
6	5	3	3	0	3	14
7	5	3	3	1	4	16
8	5	3	2	0	4	14
9	5	2	3	0	1	11
10	5	3	2	1	3	14
11	5	1	3	0	3	12
Average	5.0	2.7	2.2	0.3	2.9	13.1
Image number 3						
1	5	3	2	0	4	14
2	4	2	2	0	3	11
3	5	3	2	0	4	14
4	4	3	3	0	4	14
5	3	3	2	1	4	13
6	5	3	3	0	3	14
7	5	3	3	1	4	16
8	5	3	3	0	4	15
9	5	3	3	0	3	14
10	5	3	3	0	3	14
11	4	1	2	0	3	10
Average	4.5	2.7	2.5	0.2	3.5	13.5
Image number 4						
1	4	3	2	0	3	12
2	3	0	3	0	2	8
3	2	2	1	0	2	7
4	4	3	2	0	3	12
5	1	3	2	1	4	11
6	5	2	3	0	3	13
7	5	3	3	0	3	14
8	5	2	2	0	3	12
9	5	2	3	0	2	12
10	5	3	3	0	3	14
11	5	1	3	0	3	12
Average	4.0	2.2	2.5	0.1	2.8	11.5
Image number 5						
1	4	3	3	0	3	13
2	5	2	2	0	3	12
3	5	2	1	0	3	11
4	4	3	2	0	2	11
5	5	3	2	1	3	14
6	5	3	3	0	4	15
7	5	3	3	1	4	16
8	5	3	3	0	4	15
9	5	2	3	0	2	12
10	5	3	3	1	3	15
11	4	2	3	0	3	12
Average	4.7	2.6	2.5	0.3	3.1	13.3
Image number 6						
1	5	3	2	0	3	13
2	5	2	2	0	4	13
3	5	2	2	0	3	12
4	5	3	3	0	4	15
5	2	3	2	0	2	9
6	5	2	2	0	1	10
7	2	2	3	1	2	10
8	5	3	3	0	4	15
9	5	2	3	0	4	14
10	5	3	3	0	2	13
11	2	1	2	0	2	7
Average	4.2	2.4	2.5	0.1	2.8	11.9
Image number 7						
1	5	3	2	0	2	12
2	5	2	3	0	4	14
3	5	2	3	0	4	14
4	5	3	3	0	5	16
5	4	3	2	1	3	13
6	5	3	2	0	2	12
7	5	3	3	1	5	17
8	5	3	3	0	5	16
9	5	3	3	1	5	17
10	5	3	3	1	3	15
11	5	2	3	0	3	13
Average	4.9	2.7	2.7	0.4	3.7	14.5
Image number 8						
1	4	3	2	0	2	11
2	4	1	3	0	3	11
3	5	1	3	0	3	12
4	5	3	3	0	4	15
5	3	3	2	1	3	12
6	5	1	2	0	1	9
7	5	3	3	1	4	16
8	5	3	3	0	4	15
9	5	2	3	0	3	13
10	5	3	3	0	2	13
11	4	2	3	0	3	12
Average	4.5	2.3	2.7	0.2	2.9	12.6
Image number 9						
1	5	3	2	0	3	13
2	5	2	2	0	3	12
3	4	1	2	0	3	10
4	5	3	3	0	3	14
5	0	3	2	1	3	9
6	5	1	2	0	1	9
7	2	0	3	1	2	8
8	5	2	2	0	3	12
9	4	2	3	0	3	12
10	5	3	3	0	1	12
11	4	2	3	0	2	11
Average	4.0	2.0	2.5	0.2	2.5	11.1

Table 4.22: Comparison of quantitative image quality rankings for the neonatal chest simulation and physics image quality assessment phantoms for the final exposure set.

Image number	Neonatal chest simulation phantom ranking	Physics image quality assessment phantom ranking
1	2	1
2	9	7
3	6	6
4	8	9
5	7	8
6	1	5
7	4	2
8	5	4
9	3	3

4.5 Uncertainties in dose measurements

The random uncertainty in the ESD measurements with the PTW Conny II detector was determined by repositioning the neonatal chest simulation phantom and detector repeatedly and measuring the dose for the same exposure factors. The results are recorded in Table 4.23.

Table 4.23: Random uncertainty in ESD measurements with PTW Conny II detector.

Random uncertainty in absolute dose measurement	
	Dose (µGy)
	44.0
	43.8
	44.0
	43.4
	43.9
Average	43.8
Standard deviation	0.2
Coefficient of variation (%)	0.5

The systematic uncertainty in the calibration of the detector was 5%, obtained from the calibration certificate. Using Equation 3.4 the total uncertainty in absolute dose measurement was 5%.

4.6 Cancer induction risk calculation

Cancer induction risk was calculated as the product of effective dose and published ICRP risk factors. In the current study, entrance surface dose was measured and it was converted to effective dose using NRPB conversion coefficients from the published NRPB Report R262 tables. Only chest AP x-rays were considered and the calculations were done for the final exposure set, as in Table 3.8. The results are tabulated in Table 4.24. The risk per 1 000 000 of the population, for a single radiograph and the risk from an average of 15 radiographs, which was the average number of chest AP x-rays performed on a neonate during its stay in Tygerberg Academic Hospital, were calculated and recorded in Table 4.24.

Table 4.24: Cancer induction risks.

Image number	ESD (mGy)	NRPB onversion coefficient (mSv/mGy)	Effective dose (mSv)	Minimum risk with ICRP fetal irradiation coefficient, $2.8x10^{-2}$ Sv^{-1}			Maximum risk with ICRP fetal irradiation coefficient, $13x10^{-2}$ Sv^{-1}			Minimum risk with ICRP fetal irradiation coefficient, 0.1 Sv^{-1}			Maximum risk with ICRP fetal irradiation coefficient, 0.15 Sv^{-1}		
				Risk	Risk for 1 000 000 population per x-ray	Risk for 1 000 000 population per 15 x-rays	Risk	Risk for 1 000 000 population per x-ray	Risk for 1 000 000 population per 15 x-rays	Risk	Risk for 1 000 000 population per x-ray	Risk for 1 000 000 population per 15 x-rays	Risk	Risk for 1 000 000 population per x-ray	Risk for 1 000 000 population per 15 x-rays
1	4.4±0.2E-2	0.097	4.3±0.2E-3	1.2E-07	0.1	1.8	5.5E-07	0.6	8.3	4.3E-07	0.4	6.4	6.4E-07	0.6	9.6
2	1.9±0.1E-2	0.170	3.2±0.2E-3	9.1E-08	0.1	1.4	4.2E-07	0.4	6.3	3.2E-07	0.3	4.9	4.9E-07	0.5	7.3
3	2.3±0.1E-2	0.178	4.1±0.2E-3	1.1E-07	0.1	1.7	5.3E-07	0.5	7.9	4.1E-07	0.4	6.1	6.1E-07	0.6	9.1
4	2.6±0.1E-2	0.118	3.0±0.1E-3	8.5E-08	0.1	1.3	4.0E-07	0.4	5.9	3.0E-07	0.3	4.6	4.6E-07	0.5	6.8
5	2.6±0.1E-2	0.119	3.1±0.1E-3	8.8E-08	0.1	1.3	4.1E-07	0.4	6.1	3.1E-07	0.3	4.7	4.7E-07	0.5	7.1
6	1.6±0.1E-2	0.159	2.6±0.2E-3	7.2E-08	0.1	1.1	3.3E-07	0.3	5.0	2.6E-07	0.3	3.9	3.9E-07	0.4	5.8
7	2.6±0.1E-2	0.159	4.2±0.2E-3	1.2E-07	0.1	1.8	5.4E-07	0.5	8.1	4.2E-07	0.4	6.3	6.3E-07	0.6	9.4
8	1.9±0.1E-2	0.170	3.2±0.2E-3	9.1E-08	0.1	1.4	4.2E-07	0.4	6.3	3.2E-07	0.3	4.9	4.9E-07	0.5	7.3
9	2.6±0.1E-2	0.118	3.0±0.1E-3	8.5E-08	0.1	1.3	4.0E-07	0.4	5.9	3.0E-07	0.3	4.6	4.6E-07	0.5	6.8

Chapter 5

Discussion

The results of the phantom design and validation, image quality and dose assessment, possible dose reduction techniques and the effects of these on image quality and cancer induction risks are deliberated in this chapter. Based on these results recommendations were made to the Diagnostic Radiology Division at Tygerberg Academic Hospital.

5.1 The design of a neonatal chest simulation phantom

One of the aims of the current study is to design and construct a neonatal chest simulation phantom that is as close as possible to an anatomical and radiological simulation of a real neonatal chest, as discussed in sections 5.1.1 and 5.1.2.

5.1.1 Anatomical equivalence

Figure 4.1 shows a schematic version of the posterior ribs and vertebral column. Compared with real neonatal posterior ribs the design of the phantom's ribs is more rigid, geometrical and has sharper edges and points. Limitations of the machining process made cutting soft, rounded edges impossible.

The soft tissue areas were cut out of a slab of bone equivalent tissue substitute. The cuts were made at different diameters and angles to account for differences in rib widths and for the sloping, or "Christmas tree" effect, of posterior ribs. An edge of

bony material was left around the posterior ribs, i.e. the soft tissue was not cut right through to the bony material, in order to add stability to the structure, which could easily break if the ribs were loose at the ends with no support. The bony edge accounted for the increased density of the ribs in the areas where they curled up anteriorly. It proved to be impossible to machine the anterior curl of the ribs.

The flat section in the middle of the posterior ribs accounted for the transverse processes of the vertebrae which formed the posterior part of the spinal column. Because of machining limitations it was necessary to assume that transverse processes are a solid slab. Although not a perfect anatomical replica of true posterior ribs, the general shape and size of the posterior ribs simulate that of real ribs fairly accurately.

The vertebral column was designed to be a solid column of bone equivalent Gammex SB3 material. Real vertebrae have gaps between the bony structures and are not all similar in size. The spinal cord was not taken into account. The postulation was again necessary to simplify machining of the structure. The solid column accounted for the body and spinous processes of the vertebrae.

The lungs were mirror images of each other. The design, as in Figure 4.2, was again more rigid than real lungs, but machining was again a limiting factor. The general shape and size of the lungs were simulations of real neonatal lungs. The lung simulations had an elongated design laterally, to account for the inferior extension of the lungs posteriorly. Real lungs do not have the same thickness throughout. Differences in thickness were taken into consideration by making angled cuttings on the lateral part of the lung structures.

It was assumed that anterior ribs are rectangular in shape. These ribs and the sternal blocks are shown in Figure 4.3. The ribs were again surrounded with a bony edge to account for the curling effect of the ribs anteriorly and to add support to the structure. The ribs were assumed to be similar in length, which was calculated as an average length of the different ribs from the cadaver CT scan. The anterior ribs structure consisted of a clavicle most superiorly, with 7 ribs following, as was seen on the CT scan of the neonatal cadaver. The thickness of the ribs was 2 mm,

slightly thicker than that of an actual neonate but again, because of machining limitations, it was considered acceptable for the purposes of the current study.

The sternum consisted of three sternal blocks. These blocks were cubic in design, whereas real sternum segments are more spherical in shape but again, machining limitations necessitated simplification. The blocks were 5, 3 and 2 cm^3 respectively for the manubrium and two of the body segments. At this early age the sternum is not solid and fused yet, as seen on the neonatal cadaver CT scan. The separate sternal blocks mimicked this accurately.

The chest circumference of the phantom, measured with a ruler, was 280 mm. According to Gray[7] typical neonatal chest circumferences are about 330 mm. Various samples of phantoms were measured at the Skills Laboratory of Tygerberg Campus Medical Faculty and these chest circumferences were 280 - 350 mm. The chest length of these samples was 60 mm, i.e. from clavicle to last rib, and the chest thickness was 70 mm, i.e. anterior to posterior. The chest length of the final neonatal chest simulation phantom was 61 mm and the thickness was 53 mm. The thickness of the phantom chest, as determined from the sectional view of its constituent materials in Figure 4.4 b.), was 51 mm.

The chest circumference of the simulation phantom was within the range obtained from the Skills Laboratory and about 15% smaller than that mentioned in literature. The age of the neonate considered influenced chest circumference to a great extent, and as this phantom was a simulation of a very small 7 month old preterm cadaver, the chest circumference of the phantom was indicative of neonates of this very young age. The chest length of the simulation phantom was almost the same as that of the phantoms from the Skills Laboratory, although the simulation phantom's chest thickness was 17 mm less. When phantom chest thickness was considered it was seen that the phantom was constructed quite closely to the working drawings, as the actual phantom chest thickness was 2 mm more than that of the sectional working drawing in Figure 4.4 b.). The chest circumference, length and thickness of the neonatal chest simulation phantom were therefore in good agreement with literature and samples in the Skills Laboratory. These measurements showed that the

neonatal chest simulation phantom simulated a real neonatal chest in terms of chest size.

By measuring the cylindrical object which had been placed at the feet of the cadaver, it was possible to establish that no scaling or magnification occurred with the scan and that the measurements, as obtained with the software tools on the CT scanner, were accurate and acceptable, with the largest deviation being 0.4 mm or 1.4%. The deviation could be ascribed to difficulty in placing the start and end points of the measuring line on the exact edges of the cylinder, as the edges were substantially pixelated when the image was zoomed in.

5.1.2 Radiological equivalence

Table 4.1 shows that RM/G1 gel was the best substitute for newborn skeletal muscle. Details about its construction were not readily obtainable, and its cost could not be determined. Agar gel mix, which was second best according to the results of the analysis, was therefore used as body or muscle substitute in the current study. Agar is easily obtainable from a local supplier and not very expensive. It is a liquid when heated and sets into a firm gel. It is easy to mix and to pour around the anatomical structures of the phantom in layers. The only drawback Agar has is that it is a growth medium for bacteria and fungi. As a preventative measure, all structures, instruments and the finished phantom were thoroughly cleaned with Sporekill. Although these measures had been followed meticulously, fungi still grew on the simulation phantom and the phantom had to be remade before the final set of exposures could be obtained.

The overall results for the three bone substitute materials were very similar. Gammex SB3 is available from a local vendor, at a specified cost. It was chosen as newborn cortical bone substitute material. The construction and cost data for B110 and SB5 could not be obtained.

With foetal inflated or healthy lung, Griffith lung was the best substitute, with Gammex LN300 a close second option. Obtainability and cost were again

determining factors. The Gammex LN300 is available from a local vendor at a specified cost and was therefore used as substitute.

For sick or foetal deflated lung Gammex solid water was the best choice in this case. Gammex CT solid water was comparable to Gammex solid water, and although both could be obtained from a local representative, Gammex solid water was R570 per slab less costly than Gammex CT solid water and was therefore selected as substitute material.

The determinants leading to these conclusions are discussed in subsections 5.1.2.1 to 5.1.2.3 and 5.1.3.

5.1.2.1 Density and elemental composition matching

The densities and elemental compositions, or mass fractions by weight, of the different real neonatal tissues and possible substitute materials were obtained from literature.[6,46,47] In respect of the Agar gel mix these compositions were calculated as shown in Appendix B. Main composition elements were hydrogen, carbon, nitrogen and oxygen. Trace elements that were considered included calcium, sodium, chlorine, magnesium, titanium, zinc, potassium, sulphur, phosphorus, antimony and silicon. In Figure 4.6 a.) and d.) a comparison is made between the elemental composition (on the y-axis) of each element (on the x-axis) of real neonatal tissue and possible substitute materials.

Figure 4.6 a.) shows the comparison of elemental body composition. Generally, all the possible substitute materials matched the composition of real muscle well, except for Polystyrene, Temex and Gammex solid water, which had a very high concentration of carbon and did not contain enough oxygen. Agar gel mix was 0.1% by mass and 7.2% by mass richer in hydrogen and oxygen respectively and 4.2% by mass and 2.4% by mass poorer in carbon and nitrogen, compared to newborn skeletal muscle. Differences of 0.1 - 0.2% by mass were seen in trace elements. Rossi gel was comparable to the Agar gel mix, with -0.6% by mass for hydrogen, +5.4% by mass for carbon, +1.2% by mass for nitrogen and -5.3% by mass for

oxygen. Trace element differences were 0.1 - 0.2% by mass. Frigerio gel performed better than Agar gel mix, as well as Rossi gel. Compared with newborn skeletal muscle Frigerio gel was 0.4% by mass lower in hydrogen, 1.7% higher in carbon, 1.6% higher in nitrogen, 2.9% lower in oxygen and 0.1 - 0.3% different in the trace elements. The best performer was RM/G1 gel, which was 0.2 % and 0.9 % by mass poorer in hydrogen and carbon respectively, 1.2% by mass richer in oxygen and had the same concentration of nitrogen than newborn skeletal muscle. Trace element differences were again 0.1 - 0.2% by mass. It was found that Polystyrene, Temex and Gammex solid water were not acceptable substitutes for newborn skeletal muscle based on elemental composition. The other possible substitutes were considered based on the elemental composition criterion, with RM/G1 gel being the best option, followed by Frigerio gel, Agar gel mix and Rossi gel.

Bone elemental composition comparison is shown in Figure 4.6 b.). Significant differences between the possible substitute materials and real neonatal cortical bone were seen in the case of carbon, with all substitutes having a higher concentration of carbon than real bone. It was 15.3%, 21.1% and 16.1% by mass for SB5, B110 and SB3 respectively. Differences were also seen in the case of oxygen, where the concentration in real bone was higher than in the substitutes. With the oxygen concentration, Gammex SB3 performed better than B110, with -11.2% by mass compared to -42.9% by mass. SB5 had the smallest oxygen difference of -8.8% by mass, compared to neonatal cortical bone. B110 also contained fluorine, which was not present in neonatal cortical bone. All the substitutes lacked phosphorus. The hydrogen, nitrogen, calcium and trace element concentrations in the different substitute materials were comparable, with B110 performing slightly better here than SB3 and SB5. These results showed that, based on elemental composition data, Gammex SB3 and SB5 were better substitutes than B110. Gammex SB3 and SB5 results were reasonably comparable with each other.

The inflated or healthy lung results are shown in Figure 4.6 c.). All the substitutes measured higher in carbon concentration than foetal inflated lung, i.e. by 53.2%, 52.8% and 51.8% by mass for Griffith lung, LN10/75 and Gammex LN300. Based on oxygen concentration LN10/75 and Gammex LN300 were comparable by 61.9% versus 61.6% by mass, respectively. The oxygen concentration for Griffith lung was

54.4% by mass too low compared with foetal inflated lung. LN10/75 and Gammex LN300 contained about 11.0% by mass magnesium and about 0.7% by mass silicon, while Griffith lung contained 2.1 % by mass calcium, which was not present in foetal inflated lung. The hydrogen and trace element concentrations of the substitutes were comparable. The concentration of nitrogen was similar for LN10/75 and Gammex LN300, 0.1% and 0.2% by mass respectively. In the case of Griffith lung the nitrogen concentration of 2.4% was too high. Griffith lung seemed to be a better match than LN10/75 and Gammex LN300 on elemental composition, and LN10/75 and Gammex LN300 were comparable overall.

Figure 4.6 d.) shows the comparison results of elemental composition in deflated lung. According to ICRU Report 44[46] the elemental composition of inflated and deflated lung could be assumed to be the same, with differences in density only.[46] The carbon and oxygen contents of the substitute materials were significantly higher and lower respectively, compared with real foetal deflated lung. The carbon concentrations were 84.7%, 59.7% and 59.6% in the case of Polystyrene, Gammex CT solid water and Gammex solid water respectively, and were considered too high compared to foetal deflated lung. Gammex CT solid water and Gammex solid water were 59.3% by mass poorer in oxygen. Polystyrene contained no oxygen, and was therefore not a good substitute for sick lung. Hydrogen concentration was comparable in the case of these three substitutes. Polystyrene was 1.8% by mass richer in nitrogen and Gammex CT solid water and Gammex solid water were 0.6% by mass poorer in nitrogen than foetal deflated lung. The Gammex materials also contained calcium, which was not present in foetal deflated lung. Differences of 0.1 - 0.2% by mass existed in the trace elements. The results showed little difference between Gammex CT solid water and Gammex solid water, which performed better than Polystyrene in the comparison.

In the density comparison, Polystyrene proved to be a perfect match to newborn skeletal muscle. Gammex solid water, with a density difference of 0.6% from newborn skeletal muscle, was also an option. RM/G1 gel, 1.9% higher, and Temex, 3.8% lower, were second best. Rossi gel and Agar gel mix had comparable results, i.e. a density difference of 4.8% higher from newborn skeletal muscle. Frigerio gel

performed worst in the density analysis, with a difference of 6.7% above newborn skeletal muscle.

For newborn cortical bone substitute B110, Gammex SB3 and SB5 were ranked from best to worst based on the density criterion. Here the density differences were 4.1%, 5.8% and 8.7% higher respectively, compared with newborn cortical bone.

Foetal inflated lung was accurately simulated by Griffith lung in density. For the density comparison, Gammex LN300 and LN10/75 did not compare well with real foetal inflated lung, with densities higher by 15.4% and 19.2% respectively. Gammex LN300 had slightly better results than LN10/75.

Polystyrene and Gammex solid water, with a density difference of 1.0% and 0.6% higher respectively than foetal deflated lung, were the best substitutes on a density analysis. Gammex CT solid water was further from unity, i.e. -2.4%, but was also a possible substitute.

5.1.2.2 Attenuation and scatter coefficients

Image quality is influenced by attenuation and scatter coefficients. The total attenuation coefficient takes into account coherent (Compton) and incoherent scatter, photoelectric absorption and pair production, although pair production does not occur in the energy range considered. Between coherent or Compton scatter and incoherent scatter, the Compton scatter coefficients were largest, and the chance of Compton scatter occurring was greater than for incoherent scatter. It implied that Compton scatter would have a greater influence on image quality and was therefore considered for analysis.

The total attenuation and Compton scatter coefficients for the possible substitute data were normalised to that of real neonatal tissues. A value of 1 therefore indicated a good match, as shown in Figures 4.8 and 4.9 a.) – d.)

Figure 4.8 a.) shows the results of the possible substitutes for newborn skeletal muscle or body. RM/G1 gel, Gammex solid water, Agar gel mix and Frigerio gel all proved to be possible substitutes based on the criteria. The largest deviations from unity for these substitutes were 0.2% at 10, 65 and 70 kV for RM/G1 gel, 2.8% at 10 kV for Gammex solid water, 2.9% at 15 kV for Agar gel mix and 4.3% at 10 and 15 kV for Frigerio gel. Rossi gel and Temex performed poorer and Polystyrene was not an option based on attenuation data.

The bone substitutes are evaluated in Figure 4.8 b.). The substitutes were ranked, best to worst, as B110, Gammex SB3 and SB5, although all were reasonably comparable. The total attenuation coefficients of the substitutes were all higher than that of newborn cortical bone, considered over the whole energy range, with the comparison being closer to unity at the higher energy end. For Gammex SB3 the largest percentage difference from unity was 12.5% at 20 kV. It was 12.9% at 20 kV for SB5 and 11.8% at 20 kV for B110.

For healthy lung, LN10/75 and Gammex LN300 were comparable, as seen in Figure 4.8 c.). Gammex LN300 was slightly better than LN10/75, with a maximum deviation of 1.9% below unity at 65 and 70 kV. The largest deviation from unity for LN10/75 was 2.0% at 10, 65 ad 70 kV. The total attenuation coefficient of Griffith lung was very low at 10 kV, 5.0% below unity.

In Figure 4.8 d.) Polystyrene was not an option as a substitute for sick lung, based on total attenuation coefficient results. Gammex solid water and Gammex CT solid water had very similar results, with Gammex solid water being 0.1% higher than Gammex CT solid water at 25 kV and Gammex CT solid water was 0.1% higher than Gammex solid water at 45 kV. The largest difference from unity for Gammex CT solid water and Gammex solid water was 4.1% from unity at 10 kV.

Although slightly above unity, with a maximum deviation of 0.1% over the energy range considered, Agar gel mix was the best substitute for a neonatal body, or newborn skeletal muscle, based on Compton scatter coefficients, as Figure 4.9 a.) indicates. RM/G1gel, with the largest deviation of 0.3% from unity at 10, 15 and 20 kV, Frigerio gel, with a maximum deviation of 0.5% at 10 kV, and Rossi gel, with

0.5% deviation from unity at 10 - 20 kV and 55 - 70 kV, were also possible substitutes. Here Temex, Polystyrene and Gammex solid water did not show good results.

The best substitute for bone was Gammex SB3. In Figure 4.9 b.) the Gammex SB3 substitute's Compton scatter coefficients were below that of newborn cortical bone considered over the energy range, with the largest deviation being 0.8% at 10 and 15 kV. SB5 performed slightly better than B110 over the entire energy range in the comparison, although its maximum deviation of 2.3% at 10 kV was larger than the 2.0% at 10 kV of B110.

Inflated lung was best matched by Griffith lung, with Gammex LN300 and LN10/75 following, as seen in Figure 4.9 c.). These three substitutes were comparable with each other to a high degree regarding the calculated Compton scatter coefficients, but they all deviated from unity. Griffith lung's coefficients were slightly closer to unity at 10 - 25 kV. Its largest deviation was 2.1% from unity at 10 kV and 60 - 70 kV. It was slightly further from unity at 60, 65 and 70 kV, compared with Gammex LN300 and LN10/75. The biggest difference in Compton scatter coefficient between Gammex LN300 and foetal inflated lung was at 10 kV, a 2.6% difference. LN10/75 had a maximum deviation at 10 kV of 2.7% from unity.

Figure 4.9 d.) shows that Polystyrene was the best match to foetal deflated lung on a Compton scatter coefficient comparison, being closer to unity at lower energies. All three of the possible substitutes differed from foetal deflated lung in the criteria, with the most substantial deviation from unity of 2.1% at 65 and 70 kV.

5.1.2.3 Mass energy absorption coefficients.

The mass energy absorption coefficient influences dosimetry by serving as an indication of the absorption of radiation dose at different energies. In this thesis this coefficient was calculated by applying the mixture rule, using published data. By weighing these energy specific results over a typical incident x-ray spectrum, a single value for a spectral weighted mass energy absorption coefficient was obtained

using the program written by Mr EA de Kock[37]. This was essential since an incident x-ray beam consisted of a range of different energy photons.

Using the program, it was also possible to determine the spectral weighted mass energy absorption coefficients at different depths, i.e. for different thicknesses of muscle attenuator in the path of the incident beam or emission spectrum. These depth specific results showed how the spectral weighted mass energy absorption coefficient changed with depth, i.e. how dose was absorbed at different depths, and aided towards a more realistic comparison of possible substitute materials and real tissues.

The foundation of these calculations was the mixture rule, as in Equation 2.13, which was proven to hold for calculations of the mass energy absorption coefficient of a compound based on its elemental composition. The rule was applied to water, A150 and adipose tissue and the results were compared to published values of mass energy absorption coefficients obtained from Hubbel and Seltzer[38]. For water, the largest found difference was 0.06% at 15 kV, for A150 the largest difference of 1.30% occurred at 30 kV and for adipose tissue the difference was 0.04% at 3 kV, as shown in Table 4.7.

The average deviation from newborn skeletal muscle was calculated over all the different thicknesses of muscle attenuator considered. In Figure 4.10 a.) it was seen that RM/G1 gel was an accurate simulator of newborn muscle with regard to the mass energy absorption coefficient. Temex, with an average deviation of 2.0%, was better than Agar gel mix, with an average difference of 4.3%, at greater thicknesses of attenuating muscle. Frigerio gel, 5.0% on average below newborn skeletal muscle, was also a good simulator. The average results for Rossi gel, 11.0% deviation, was preceded by 8.6% average difference of Gammex solid water, with Gammex solid water being above and Rossi gel below unity. Polystyrene was not suitable as muscle substitute with mass energy absorption coefficient as criterion.

The mass energy absorption coefficient results for the bone substitutes were all higher than that of newborn cortical bone. Although these substitutes were comparable with the criteria, B110 performed slightly better than Gammex SB3 and

SB5 performed worst. The average deviations from newborn cortical bone, over the different thicknesses of attenuating muscle considered, were 13.2%, 14.1% and 14.3% for B110, Gammex SB3 and SB5 respectively. These results are obtained from the analysis of Figure 4.10 b.).

Figure 4.10 c.) shows that Griffith lung best simulated the mass energy absorption coefficient of the foetal inflated lung. The average error for the substitute was 5.1% across the muscle attenuator thickness range considered. The coefficients for LN10/75 and Gammex LN300 were much higher than that of real healthy lung. Here LN10/75 performed slightly better than Gammex LN300, which differed by 59.1% on average from foetal inflated or healthy lung. The average deviation of LN10/75 was 53.2%.

Gammex CT solid water and Gammex solid water showed exactly the same results for sick lung absorption coefficient simulation, i.e. an average difference of 7.5% above that of foetal deflated lung. Polystyrene was not an acceptable substitute according to the criteria, having an average deviation of 57.2%, as is seen in Figure 4.10 d.).

5.1.3 Obtainability and cost

Details on the production of many of the possible substitutes mentioned in literature were not available, but it was possible to obtain composition data and costs details from the Gammex representative in South Africa. The Gammex materials were readily available for import, with delivery within 4 - 6 weeks after ordering. For the neonatal chest simulation phantom, Gammex SB3 bone, Gammex LN300 lung and Gammex solid water were procured. Agar was easily obtainable from the vendors mentioned in section 4.1.3, as it was used as a biological growth medium for bacteria and fungi.

iThemba LABS collaborated on the project by assisting in the design and manufacture of the phantoms. The CT scan of the neonatal cadaver was performed at iThemba LABS. All perspex, torlon, high density polyethylene and wires needed

for the neonatal chest simulation and physics image quality assessment phantoms were supplied by iThemba LABS. The machining of the different neonatal anatomy structures was also done by iThemba LABS. The Agar used in the preparation of the Agar gel mix was supplied by the radiation biology department at iThemba LABS. All the products used and the work done as mentioned above were provided and done free of charge. The staff of iThemba LABS further contributed to this project by offering their time and expertise.

5.1.4 Validation of phantom

The results in Table 4.10 show that the average intensities in the ROIs in the neonatal chest simulation phantom were larger than those in the real neonate, while the average standard deviations were smaller. The smaller standard deviations were indicative of a more uniform material. This was expected since a real neonate was quite inhomogeneous, as seen from Figure 4.11, and the simulation phantom materials were completely homogeneous, with no density differences in different areas. The neonatal chest simulation phantom did not account for any inhomogeneities which exist in a real neonatal chest.

A difference of 33.7% was found between real neonatal muscle and Agar gel mix. It was noted that the average standard deviation of Agar gel mix was lower than that of real neonatal muscle, as Agar gel mix was a homogeneous mixture. Skin folds and tissue inhomogeneities, as seen on a real neonate, were not present in the phantom. A real neonate's thickness was also not the same over the extent of the chest, i.e. it was not a rectangular block like the simulation phantom, it was therefore possible that the areas used for measurements were not made up of the same thickness of muscle as those used in the phantom, which would influence the measurements. It was very difficult to find an area in the real neonatal image that was made up of muscle only. Most real tissue or muscle areas were over- or underlain by other structures. Uniform Agar gel mix areas were present in the phantom.

For the bone comparison, ROIs were drawn in the ribs and not in the vertebrae, as was done with the neonatal chest simulation phantom for image quality analysis in

section 4.4. The vertebral column of the phantom was a solid slab of bone equivalent material, according to the simplifying assumption. Real neonatal vertebrae were separate structures and housed a spinal cord. It was therefore expected that there would be a difference in measurements of the vertebral area between the phantom and a real neonate. A difference of 28.2% was found. The phantom was constructed of a solid bone equivalent material, whereas real bone did not have the same density all over. It was confirmed by the significantly smaller standard deviation in the phantom measurements, i.e. the phantom material was completely homogeneous. The phantom also assumed a fixed thickness for ribs, i.e. 2 mm, but the thickness of real neonatal ribs were not constant everywhere. The thickness of the area in the ROI and the material above and below the area also influenced the obtained measurements.

The largest deviation, 45.0%, was seen in healthy lung. The homogeneity of the substitute material was again confirmed by the smaller standard deviation. Real neonatal lung did not have an almost even grey scale value, as was the case with the healthy lung in the simulation phantom. It was difficult to place the ROIs in areas that were uniform. These non-uniformities are apparent in Figure 4.11.

The smallest difference was shown in sick or deflated lung, i.e. 23.2%. The sick lung in the neonatal chest simulation phantom simulated a completely collapsed lung. The sick lung in the real image was not complete since “white lung” areas were still aerated, therefore it was again difficult to find uniform sick lung areas for the analysis. In the case of the phantom it was also assumed that the healthy and sick lungs had the same thickness throughout, although real lung thicknesses varied over the area of the lung. There were therefore uncertainties in the thickness of the areas used for the ROI analysis.

In the case of real neonates, variable density and thickness of the different structures, different over- and underlying materials around the structures and non-uniformities in the different organs and structures existed. These were not present in the neonatal chest simulation phantom, which was much more uniform with regard to organ and structure size, shape, density and composition, because of simplifying geometrical assumptions for easier phantom design. The images of the real neonate

and the simulation phantom were also not acquired on the same imaging unit, using the same imaging cassettes, which could also influence the obtained measurements. The neonatal chest simulation phantom was an approximation of a real neonatal chest, and taking these complicating factors into account, an overall deviation of 32.5% from a real neonate was deemed acceptable for the current study. The phantom was still a better simulation of a neonatal chest than most of the options discussed in literature in section 2.4.

5.2 The design of a physics image quality assessment phantom

The designed physics image quality assessment phantom enabled quantification of image quality on non-clinical phantom components. These components are torlon and high density polyethylene disks of different thicknesses, for low contrast detectability and SNR, SDNR and CNR calculations, a copper plate for obtaining a MTF from an ESF of the plate, and a perspex holder with wires of different diameters, for MTF calculation. The calculations done in respect of the phantom for the final exposure set are discussed in section 5.3.1.

5.3 Image quality analysis

The quantitative image quality results for the neonatal chest simulation and physics image quality assessment phantoms for the final set of exposures were compared and the obtained images were ranked best to worst. Ranking of visual image quality regarding the neonatal chest simulation phantom for the final exposure set was done by independent medical physicists and radiographers. Quantitative and visual rankings were compared for the neonatal chest simulation phantom, and overall image quality was compared to the ESDs delivered in obtaining the images. These results are discussed in sections 5.3.1 and 5.3.2 below.

5.3.1 Evaluation of the physics image quality assessment phantom

The MTFs were calculated using two methods for the images of the physics image quality assessment phantom in the final exposure set. Figure 4.13 shows the results. In this figure high frequencies i.e. larger values for line pairs per millimetre (lppmm) or pixels per centimetre (pixels/cm) represent smaller objects and vice versa.

Figure 4.13 a.) and b.) show the results using the resolution wires and Equation 3.2. It was found that image 4 had the best resolution as it had the highest MTF value at 5 lppmm. This was followed by images 5 and 3. The results for images 6, 7, 8, 1 and 9 were comparable at 5 lppmm and the resolution of these images were poorer than that of images 4, 5, 3 and 2 overall. It showed that small objects were best visualised in images 4, 5 and 3. The graphs of images 4 and 5 were overall comparable, image 4 being slightly better than image 5. In these images small objects of high frequencies could still be seen well. Image 3 also had good resolution, but small objects were not as clear as in images 4 and 5. Overall the graph was also below that of images 4 and 5, therefore the resolution of image 3 was poorer than that of images 4 and 5. With image 2 a sharp drop off in MTF was not seen as the frequency increased, i.e. the graph was more gradual with a smaller difference in the visibility of large and small objects. It was also seen in images 6, 1, 7, 8 and 9, where large objects were not much more visible than small objects. Image 4 is a raw image obtained with 61 kV, 0.8 mAs and inherent filtration and it had the best resolution.

Figure 4.13 c.) and d.) show the results for MTF calculation with the Fourier Analysis tool in Microsoft Excel. Image 3 had the best resolution for large objects, as is seen in Figure 4.13 c.). Large object resolution was also acceptable in the case of images 5, 4 and 2, image 6 following. The large object resolution was comparable for images 7 and 8 and for images 1 and 9, which had the lowest resolution for large objects. A substantial difference was seen in the visibility of large and small objects in image 3. At 5 pixels/cm images 3, 4 and 5 were comparable in resolution and at lower frequencies, 10 - 50 pixels/cm, image 4 was generally better than image 5. In Figure 4.13 d.) it is seen that image 4 was the best at high frequencies, i.e. had the

best visualisation of small objects. Here the results for images 3 and 5 were comparable. The resolution of image 2 was poorer than that of images 3, 4 and 5, but better overall than the resolution of images 6, 7, 8, 1 and 9. The figure shows that the resolution for images 7, 8, 9 and 1 were comparable at high frequencies, with images 6 and 2 being slightly better here. Images 1 and 9 had the poorest resolution overall. Large and small objects were not distinctly visible, i.e. the ratio between low and high frequencies was smaller. From these results image 4 again had the best resolution overall, although that of image 3 was higher at low frequencies.

When the results from the two methods of MTF determination were compared, similar trends were observed. For the resolution wire method the images were ranked, from best to worst overall resolution, as image 4, 5, 3, 2, 6, 1, 7, 8 and 9. For the Fourier Analysis method the ranking was image 4, 3, 5, 2, 6, 7, 8, 1 and 9. With both methods of MTF calculation, images 4 and 9 had the best and worst resolution respectively.

The results showed that the MTF resolution was better for raw images than for processed images. Images 4, 5, 3 and 2 were raw images. It was expected as the raw images had no image processing or smoothing, therefore small differences in pixel values were more obvious. The processed images with additional filtration of 0.1 mm Cu + 1 mm Al, i.e. images 6, 7, and 8, performed better than the processed images with inherent filtration only, i.e. images 1 and 9.

The results shown in Table 4.11 were used to rank the images of the physics image quality assessment phantom from best to worst based on the quantitative analysis results.

The best ranked image was image 1, i.e. the image obtained with the standard exposure factors. In this image the thinnest disks, 3 mm, of torlon and high density polyethylene were seen. It also had the highest SDNR for torlon, 2.3, and high density polyethylene, 7.3. The SNR for torlon, 86.9, and high density polyethylene, 80.3, were also acceptable, although not the highest values.

Image 7 was ranked second. It had the best SNR values for torlon, 94.6, and high density polyethylene, 92.5. Although these values were better than that of the image ranked first, the other criteria measured image 7 worse than image 1. With image 7 the signals for torlon and Agar were almost the same, thus the SDNR for torlon was not high. It also influenced the low contrast detectability of the torlon disks, therefore the thinnest disk seen was 4 mm for torlon and 5 mm for high density polyethylene. It was attributed to the image being a processed image, which underwent inherent image processing on readout, i.e. the image was smoothed. The SDNR for high density polyethylene of the image was comparable to that of most of the other images.

Image 9 was placed third. The SNRs for torlon and high density polyethylene, 78.5 and 75.5, were lower than that of the image that was ranked fourth, i.e. 83.9 and 85.2 for SNR torlon and high density polyethylene respectively, but the 4 mm torlon disk was visible in the image. The SDNR for torlon, 1.1, was better than that of the fourth image although the SDNR for high density polyethylene was comparable.

Image 8 was ranked fourth. The SNRs for torlon and high density polyethylene of the image was comparable to that of the image ranked first, but the low contrast detectability of the image was only 5 mm torlon and high density polyethylene disks. The SDNR for high density polyethylene of image 8 was comparable to that of image 7, which was ranked second, but the SDNR for torlon was poorer, i.e. 0.1. The signals in the ROIs in Agar gel mix and torlon disks were almost the same as a result of the image being processed and smoothed. It was also the reason for the thinner torlon disks not being visible in the Agar gel mix.

Image 6 was ranked fifth. The SDNR for torlon shown in the image was 2.6. It was better than that of the images ranked second to fourth, but its SDNR for high density polyethylene was poorer than that of these images, i.e. a value of only 0.1. The SNRs for torlon and high density polyethylene, 60.7 and 54.4 respectively, were also lower than that of the higher ranked images. The 5 mm disks were seen with low contrast detectability.

The processed images were shown to be better than the raw images in the analysis, which was attributed to the large standard deviation or noise levels in the ROIs used for analysing raw images. As these images did not undergo inherent image processing or smoothing more obvious differences were seen between the signals in the ROIs in the different structures, but these were accompanied by larger noise values.

Image 3 was ranked sixth. The low contrast detectability for torlon was 3 mm but the SNRs for torlon and high density polyethylene were low, due to large noise values in the raw image ROIs. Significant differences were seen between the signals of high density polyethylene and Agar gel mix, which explains the higher value for SDNR for high density polyethylene of 5.0. Although this was the second best SDNR value for high density polyethylene, the SNRs for torlon and high density polyethylene were much poorer than those of some of the other exposures and therefore the image could not rank better. The value for SDNR for torlon was not high, although a substantial difference was seen between the signals for torlon and Agar gel mix, which explained why thinner torlon disks were visible, but the large noise values of the raw image suppressed the effect and reduced the SDNR for torlon.

Image 2 was ranked seventh. The 4 mm torlon disk was visible, which was better than the results for the images ranked fourth and fifth, but the SNRs for torlon and high density polyethylene for the image was much lower. The SDNR for torlon was comparable to that of the image ranked sixth, i.e. 2.0 versus 1.8, but the SDNR for high density polyethylene was worse, 4.1 versus 5.0. The SNRs for torlon and high density polyethylene were also comparable to that of the sixth ranked image, but the low contrast detectability for torlon in the sixth image was 3 mm and for image 2 it was 4 mm. The large standard deviations or noise values were again seen and accounted for the smaller ratios.

The eighth ranking position was image 5. For low contrast detectability 4 mm torlon and 5 mm high density polyethylene were seen, which were the same as for image 2 that ranked seventh. Compared with image 2, the SNRs for torlon and high density polyethylene were lower for image 5. For image 2 these values were 24.7 and 22.6 for torlon and high density polyethylene respectively and for image 5 these were 21.5

and 18.4. The SDNRs for torlon and high density polyethylene in this image were also slightly poorer than that of the seventh ranked image. Differences in signals between Agar gel mix, torlon and high density polyethylene were again seen, but these were shadowed by the larger noise values inherent in the raw image.

The worst image quantitatively for the physics image quality assessment phantom was image 4. It was ranked ninth. Similar to the images ranked seventh and eighth, low contrast detectability was 4 mm for torlon. However, it had the highest noise levels of all the raw images and therefore the poorest SNRs for torlon and high density polyethylene, i.e. 17.9 and 14.1 respectively. The SDNRs for torlon and high density polyethylene were comparable to that of the eighth ranked image.

Quantitative image quality ranking best to worst was therefore image 1, 7, 9, 8, 6, 3, 2, 5 and 4.

The rankings of the images, based on MTF analysis and quantitative image quality, were compared. The images that had better resolution, i.e. images 4, 5, 3 and 2, were raw images. Images 1, 7, 9 and 8 were better images quantitatively. These were processed images. The processed images did not have good resolution, with images 1, 7, 8 and 9 having the poorest MTF results for both methods of calculation. Images 4, 5, 3 and 2 were the lowest ranked quantitatively. Only image 6 had the same ranking position for MTF and quantitative image quality, owing to the result of smoothing which has the effect of reducing pixel difference between neighbouring regions in an image. Therefore the MTFs for these images did not have large ratios between low- and high frequency MTF values. Image smoothing also decreased the noise levels in ROIs used for quantitative image quality analysis, which resulted in larger SNRs and SDNRs. In the case of the raw images, smoothing did not occur, therefore small differences in neighbouring pixel values were more apparent, with higher noise levels in ROI analysis. The result was smaller SNRs and SDNRs and therefore poorer quantitative image quality.

The physics image quality assessment phantom images for the final exposure set were ranked best to worst 4, 5, 3, 2, 6, 1, 7, 8 and 9, based on MTF calculation using Equation 3.2. The ranking positions were image 4, 3, 5, 2, 6, 7, 8, 1 and 9, based on

MTF calculation from the ESF of the copper plate. Quantitative image quality analysis ranked the images 1, 7, 9, 8, 6, 3, 2, 5 and 4.

5.3.2 Neonatal chest simulation phantom evaluation

The results for the preliminary exposure sets for the neonatal chest simulation phantom are discussed in sections 5.4.1 to 5.4.4. The final exposure set results are discussed in section 5.4.5, and an overall comparison of visual and quantitative image quality and delivered ESD set out in Table 4.12. The final exposure set results for the physics image quality assessment phantom are given in section 5.3.1.

The aim of the current study is to reduce the delivered radiation dose (ESD) per radiograph while maintaining acceptable clinical (or visual) image quality, as well as considering cancer induction risks. Visual or clinical image quality is deemed more important than quantitative image quality, as radiographs of real neonates are visually investigated in Tygerberg Academic Hospital.

Table 4.12 is an overall comparison and ranking of the images obtained in the final exposure set for the neonatal chest simulation phantom. It considers the delivered ESD, the visual or clinical image quality, as averaged from the scores of eleven independent medical physicists and radiographers, and the quantitative image quality as calculated by the principal investigator.

It was possible to obtain an image that was visually poor and quantitatively acceptable, such as image 1 which was ranked eighth for visual image quality and second for quantitative image quality. The opposite was also possible, for example image 2, which was visually satisfactory and ranked third, but quantitatively poor, therefore ranked ninth. Some of the quantitative results were acceptable as the signal differences between ROIs were large, but this could imply a black lung for example, making the image visually unacceptable. In Table 4.12 no correspondence between visual and quantitative image quality rankings was seen.

Acquiring images by way of additional filtration was problematic. Additional filtration was not available on the mobile units used routinely to image neonates at Tygerberg Academic Hospital. To produce such an exposure radiographers will have to fix filtration plates to the exit window after the neonate is set up and before the exposure is made, as the plates block the light field that is used for setup and centring. Since these small patients cannot stay perfectly immobile retakes often need to be done, in this way dishonouring the ALARA principle. A solution would be if only experienced radiographers are allowed to image neonatal patients. Another option is to buy the filter assembly for the units used routinely for imaging of neonates. The assembly fits onto the x-ray unit and does not obstruct the light field. When new mobile units are procured for the neonatal division, specifications can be written for the acquisition of a commercially available mobile unit, which is fitted with additional filtration on a selection dial.

Another problem was obtaining image in raw mode, since the default acquisition method with image plate readout produced processed images. To obtain raw images radiographers are compelled to perform an extra step at readout of the imaging plate, i.e. the selection of the raw processing mode, UM Chest Paediatrics. The option is available on the readout computer screen. Simple instructions and a demonstration will be sufficient to achieve this.

All three the criteria were considered, i.e. ESD, visual and quantitative image quality, to rank the images overall.

Image 6 was the best image overall. It had the largest ESD reduction from the standard exposure, i.e. ranked first on dose, and was the best image quantitatively. However, it was ranked only sixth for visual image quality.

Image 7 was second. It was the best image visually, ranked fourth quantitatively and still had a significant ESD reduction of about 40% from the standard exposure, i.e. image 1.

Image 3 was third. Visually it was ranked second, on dose it was ranked third and quantitatively it was sixth. The image had a satisfactory clinical image quality, better

than that of the standard exposure image, at a significantly reduced dose, but quantitatively it did not perform well. Considering all three criteria the image was not a good option, but based on dose and clinical image quality only, it was acceptable.

The fourth position overall, based on all three criteria, was image 8. It had a dose reduction of about 56% from the standard exposure and ranked fifth for visual and quantitative image quality.

Image 2 was ranked fifth. It had the second largest ESD reduction and third best visual image quality, but as its quantitative image quality was ranked worst its overall ranking was poor. However, considering ESD and visual image quality only, the image was one of the best options.

Image 5 was ranked sixth. It was rated average according to all three criteria, i.e. ranked fifth on ESD, fourth on visual image quality and seventh on quantitative image quality.

Image 9 was ranked seventh. Although it had a third ranking quantitatively, it was visually the poorest image and ranked fourth on dose. It was therefore expected that such an image would not be optimal, based on the poor clinical image quality, and overall should have a very poor rank.

The standard exposure image, image 1, was ranked eighth overall. It was an acceptable image quantitatively, ranked second, but ranked only eighth on visual image quality and had the highest ESD. This image would therefore be the worst overall, i.e. it was obtained at a high ESD and had a poor visual image quality.

The analysis ranked image 4 ninth. It had a dose ranking of fourth, but visually and quantitatively it was not acceptable, being ranked seventh and eighth respectively. However, due to its ESD reduction from the standard exposure of about 41%, it was expected to rank better overall than the standard exposure image, i.e. image 1.

Considering all three criteria, i.e. measured ESD, visual or clinical image quality and quantitative image quality, the ranking of the images, from best to worst was Image 6, 7, 3, 8, 2, 5, 9, 1 and 4.

These results illustrated clearly that visual image quality and ESD reduction were more important than quantitative image quality in determining the overall ranking of the images in the final exposure set. The overall ranking positions in Table 4.12 were therefore determined in this way, i.e. giving more importance to ESD reduction and visual image quality maintenance than to good quantitative image quality results.

Another analysis focusing primarily on ESD and visual image quality was done.

This analysis illustrated that the overall best image was Image 3. This image was obtained at an ESD of 3.7 µGy higher than Image 2, but it had the second best visual image quality. The slight increase in ESD was justified by the improvement in visual image quality, as the ESD was still about 48% less than that of the standard exposure. Its visual image quality was also higher than that of the standard exposure, as seen in Figure 5.10 a.) and c.) on page 184. Image 3 was acquired with 0.1 mm Cu + 1 mm Al additional filtration at 64 kV and 2 mAs and it was a raw image. The image was acquired at a higher kV than was used for routine exposures on neonates in Tygerberg Academic Hospital. It had no image processing, which meant the image was not smoothed. Small differences in image grey scales were therefore perceivable. However, it also increased image noise, or ROI standard deviations, but the effect was not unacceptably large. The identified problems regarding additional filtration and raw image mode were applicable in the case of this image.

Image 2 was ranked second overall. It was ranked second on dose and third on visual image quality. It was a raw image, acquired at 60 kV, 2 mAs and with additional filtration. Its kV was also higher than that of the standard exposure, but lower than that of Image 3. It explained the slight reduction in image quality, as fewer photons were available to contribute to image formation. The exposure therefore had the same acquisition and readout concerns as Image 3.

Overall, Image 7 was third best. This image was the best visually, as seen in Figure 5.10 g.) on page 185. Its ESD was about 40% less than that of the standard exposure. It still showed a significant ESD reduction, although the image ranked only fifth on ESD. The higher ESD was justified by the high visual image quality, which was not only maintained, but also an improvement on the exposure protocol routinely used at Tygerberg Academic Hospital. The image was acquired with the additional filtration, posing the same acquisition challenges, but it was obtained as a processed image and therefore needed no intervention in the readout process.

Images 6 and 8 were ranked fourth and fifth overall respectively. Image 6 had the lowest ESD, about 63% less than that of the standard exposure. Visually it was ranked sixth. Image 8 was ranked second on dose and fifth on visual image quality. The lower ESD of Image 6 at a comparable overall visual image quality, compared with Image 8, made it a better option. Both these images were processed with no changes required on the readout process. Image 8 was acquired at a higher kV than Image 6, which explained its slightly higher visual image quality, i.e. a higher kV increased x-ray beam quality, therefore it had better penetration and beam quantity, i.e. the number of photons available for image formation. Both of these images were obtained with added additional copper and aluminium filtration, and therefore required extra steps in image acquisition, as discussed previously.

Image 5 was ranked sixth. It had a dose ranking of fifth and a visual image quality ranking of fourth. Image 7, which was the third best image overall, also had a dose ranking of fifth, i.e. images were acquired with the same exposure factors, but different readout techniques were used, therefore its visual image quality ranking position differed. Image 5 was better than the ranking of fourth for dose and seventh for visual image quality of Image 4. Image 4 was ranked seventh overall. Images 4 and 5 were raw images obtained with inherent filtration. Readout intervention was therefore required to obtain the images, but additional filtration was not needed and image acquisition could be done as usual. Image 5 was obtained at a slightly higher kV than Image 4. The higher kV again gave improved image quality, due to the increase in the number of photons and energy of the x-ray beam. Both these images were obtained at higher kV and lower mAs setting than used routinely for neonatal chest x-rays in Tygerberg Academic Hospital.

Image 9 was ranked fourth on dose, similar to Image 4, since it was obtained with the same exposure factors, but it had the lowest visual image quality ranking, therefore overall it was ranked eighth. The image was processed, therefore smoothed, and at the reduced mAs of 0.8 mAs, compared with 2 mAs for the standard exposure, it reduced the image quality although the kV was increased. The image did not require additional filtration or readout intervention and was obtained as routinely done at Tygerberg Academic Hospital. Exposure of Image 9 would have been a feasible option if it were possible to fit a copper and aluminium plate to the exit window of the mobile x-ray unit without leading to retakes. This option also implied that mobile units were to be assembled with filters or, new units with filters on a selection dial were to be bought, which would incur substantial financial costs. Its visual image quality was comparable to that of the standard exposure image, Image 1, with an overall averaged observer score of 11 for both of these images, and it was obtained at an ESD of about 41% less than image 1. It was therefore still within the aim of the current study of ESD reduction while maintaining image quality.

Image 1, the standard exposure image, was ranked ninth overall. Although it was ranked eighth visually, i.e. better than Image 9 as explained in section 5.4.5, its ESD was the highest of the acquisitions in the final exposure set.

It was therefore possible, with all of the exposures other than the standard exposure, to obtain images that were visually equivalent to or better than the standard exposure image at an ESD that was significantly less than that of the standard exposure. When ESD and visual image quality were the preferred ranking criteria, the overall ranking position of the images, from best to worst, was Image 3, 2, 7, 6, 8, 5, 4, 9 and 1.

These results clearly demonstrated that the aim of the current study was reached, i.e. new exposure protocols were developed that reduced the ESD delivered per x-ray, while the clinical image quality was maintained. It was also apparent that such dose reductions were possible with improved clinical image quality in some cases. The risks for cancer induction in the young child now had to be investigated.

5.4 Dose reduction versus image quality

Most of the research available in literature was performed on film-screen systems. Tygerberg Academic Hospital uses a digital CR system for x-ray imaging. It was therefore difficult to extrapolate the literature data to CR imaging systems. The results as described in literature were also quite variable, as seen in Table 3.3. Different publications offered different exposure factor combinations to achieve reduced ESD with acceptable image quality, with the kV ranging from 40 - 80 kV, 0.5 - 4 mAs, 80 - 115 cm FFD with different types of added filtration suggested.[13,14,15,21,28] Therefore a number of trial runs or preliminary exposures were made in order to determine the response of the CR system and to derive a range of kV, mAs, FFD and filtration for the system where it was possible to achieve an ESD reduction with maintenance of acceptable clinical image quality.

According to suggestions in literature it was clear that collimation should be performed as tightly as possible in order to decrease the delivered ESD and the total area exposed to radiation. For neonatal chest AP x-rays it was possible to collimate in such a way that the gonads and head were not in the primary exposure beam. However, it was important to ensure that the collimation was not so tight that structures of interest would be missed due to movement of neonates, which would result in retakes. Such collimation was in accordance with the ALARA principle and was general practice at Tygerberg Academic Hospital. Therefore collimation was not investigated. The other possible exposure factors, i.e. kV, mAs, focal spot size, FFD and filtration were considered in the preliminary exposures.

The preliminary exposures were made on a fixed unit at the Oncology Division at Tygerberg Academic Hospital. It was logistically easier for all parties involved in the measurements and the unit was available for long periods of time, which was ideal for research purposes. The mobile unit for neonatal chest imaging was used continually and could only be accessed for short periods of time. Quality assurance was done on both units by a SANAS accredited Inspection body. The results obtained from the fixed unit were only used to derive a final set of measurements to be done on the mobile unit. The final set of measurements was used for final calculations, image evaluations and recommendations.

The standard exposure factors used at Tygerberg Academic Hospital for neonatal chest AP examinations are processed images obtained with small focus, 50 kV, 2 mAs, 100 cm FFD with inherent filtration only and collimation as tightly as possible. Such an exposure is referred to as the standard exposure. Results obtained in the four preliminary and final exposure sets are discussed in terms of comparison to the standard exposure.

5.4.1 First preliminary exposure set

Image quality was calculated as the SNR of healthy lung and the SDNR between healthy lung and Agar gel mix for the first preliminary exposure set.

Table 4.13 shows that the dose increased as the kV was increased due to the mAs being kept constant at 2 mAs. Despite the dose increase there was no real gain in image quality. An increase in kV increased the penetrability of the beam and the efficiency of x-ray production, therefore the increase in ESD. These results clearly demonstrated that an increase in kV should be accompanied by a decrease in mAs. As the beam quality and x-ray production efficiency were improved, more photons were reaching the CR plate to contribute to image formation, which offset the reduction in the number of photons when the mAs was reduced. Literature confirmed the statement that an increase in kV, with an associated reduction in mAs, resulted in the maintenance of a certain level of image quality, at a reduced ESD.[4,5] This concept was employed in the following preliminary exposure sets.

It was seen that the ESD could be halved if the kV was reduced from 50 to 40 kV with a constant 2 mAs. It gave improved SNR and SDNR compared with the standard. Addition of 0.1 mm Cu + 1 mm Al filtration gave a dramatic ESD reduction from the standard exposure. Here the SNR was much better and the SDNR was comparable to that of the standard exposure. This was a result of filtration absorbing low energy photons that contributed to delivered dose only and not to image formation.

A FFD of 80 cm caused an increase in ESD, which could not be justified by the slight gain in SDNR. At 120 cm FFD there was a slight ESD reduction, showing a slight improvement in SNR, but the SDNR was comparable to that of the standard exposure. It was important that the optimal FFD was used as FFD influenced magnification and image sharpness. Theoretically a shorter FFD would increase ESD and reduce the image sharpness with increased magnification.[16] A standard FFD should therefore be used. This was equal to 100 cm in Tygerberg Academic Hospital.

These were all processed images. Image processing occurred when the CR plate was read in the CR reader. Image processing was automatically performed by the software to create an image that shows the results of a radiological investigation in a much more accessible and optically pleasing way, although post acquisition image manipulation was available with a CR system. These images gave reason for the decision to examine raw images as well, i.e. images that had no image processing at readout. The second set of preliminary exposures was therefore acquired as raw and processed images.

5.4.2 Second preliminary exposure set

The results of the second set of preliminary exposures are included in Tables 4.14 and 4.15. In this set the mAs was again kept constant at 2 mAs in order to investigate the effect of raw images and to compare the raw and processed images. In this set of exposures doses were not measured. Analysis was therefore purely based on image quality, quantitatively and visually.

The raw image data, Table 4.14, was considered.

Visually 40 kV performed the worst, so although the 40 kV image had good quantification results, it was decided not to work at such a low kV owing to the poor visual image quality. The best range for good visual and quantitative image quality proved to be 50 - 70 kV. This range was combined with the ESD results for the first

set, which indicated that an increase in kV must have a compensatory decrease in mAs. It was employed in the third set of preliminary exposures.

In this thesis the effect of additional filtration on ESD and image quality was investigated to gain a more complete overview, even though additional filtration was not an inherent feature of the x-ray units used to image neonates routinely. With added filtration at 50 kV, 2 mAs, 100 cm FFD and small focus, the visual image quality reduced significantly. The first set of preliminary exposures showed that the ESD decreased with added filtration, but the visual and quantified image quality was much lower. The second set gave reason to examine the effect of added filtration with an increase in kV and/or an increase in mAs. Theoretically it would take advantage of the dramatic ESD drop with added filtration, and compensate for the reduction in image quality with the kV and/or mAs increase. It implied a greater beam intensity and number of photons which should increase the image quality and ESD, but the reduction in ESD with the additional filtration seemed significant enough to counter the resultant ESD increase. Additional filtration caused dramatic dose reductions, which warranted further investigation.

By changing the focus from small, or fine, to large the visual and quantified image quality was comparable to that of the standard exposure. Theoretically a small focal spot size should give a geometrically sharper image. For the third set of preliminary exposures it was therefore necessary to determine if there was an ESD difference between the two focal spot sizes.

The image at 120 cm FFD was visually much poorer than the standard exposure image. The first preliminary exposure set showed that the ESD decreased by about 34%, but it did not justify the reduction in image quality and the magnification effect. Changing the FFD also changed the magnification of the image, and as organ size was important in many chest AP investigations, it was decided to use an FFD of 100 cm, which was standard use at Tygerberg Academic Hospital.

The processed image set, Table 4.15, was then considered.

By changing the kV from 50 kV to70 kV the visual image quality was not influenced. These images again showed that the 50 - 70 kV range required further investigation, as with the raw images. However, in the case of the processed images, changing the kV did not have much impact on the quantified image quality and no influence on the visual image quality, compared to the effect seen in the case of the raw images. It was expected since the image processing that occurred with the processed images counteracted image quality degradation.

Added filtration made no significant difference in the visual image quality of the processed images, while a significant reduction was seen in the raw images. When using a large focus, the SNR for sick lung was better than that of the standard exposure, while other image quality parameters were comparable.

At 120 cm FFD the visual image quality was decreased compared with the standard exposure. Visually the processed and raw images were comparable, but the quantification of the processed image was better than that of the raw image, except for the CNR. As in the case of the raw image it was concluded that the reduction in image quality was not justified by the reduced ESD.

The processed images performed better quantitatively than the raw images, except for the CNR. These images were smoothed and therefore the noise values in the ROIs used for analysis were smaller. The signal values in these ROIs were generally also larger and more uniform than those of the raw images. No significant changes were seen in signal values as exposure parameters were changed, although substantial changes were apparent in the raw images. In general the noise levels for healthy lung were higher for processed than for raw images. The processed images underwent inherent image processing that smoothed the images and made them more uniform. These images were processed to appear almost similar, regardless of the exposure factors used. It explained the more subtle changes in the signal values between the processed images and the lower noise levels. The CNRs of the processed images were therefore poorer than those of the raw images, as the differences in signals were smaller on the processed images.

Visually the raw images were better than the processed ones. This is indicated in Figure 5.1 on page 150, where the grey scale of the raw image was adjusted to appear to be similar to that of the processed image. Both these images were acquired at 60 kV, 2 mAs, 100 cm FFD, small focus and inherent filtration. In Figure 5.1 the central line and sternum were clearer on the raw than on the processed image.

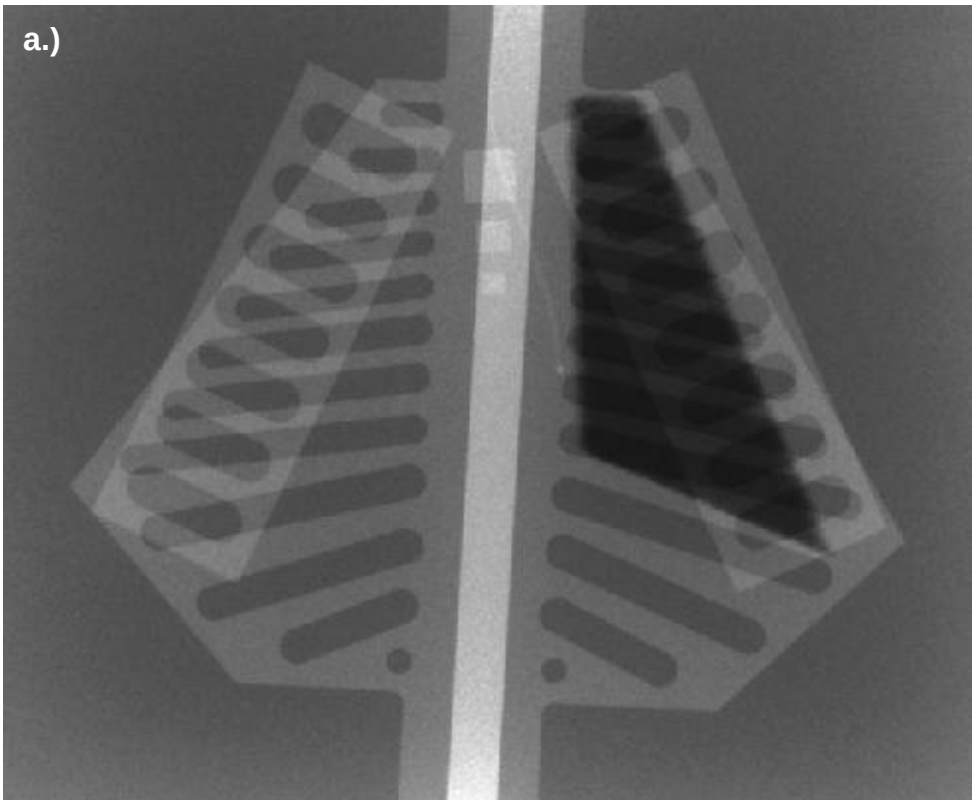

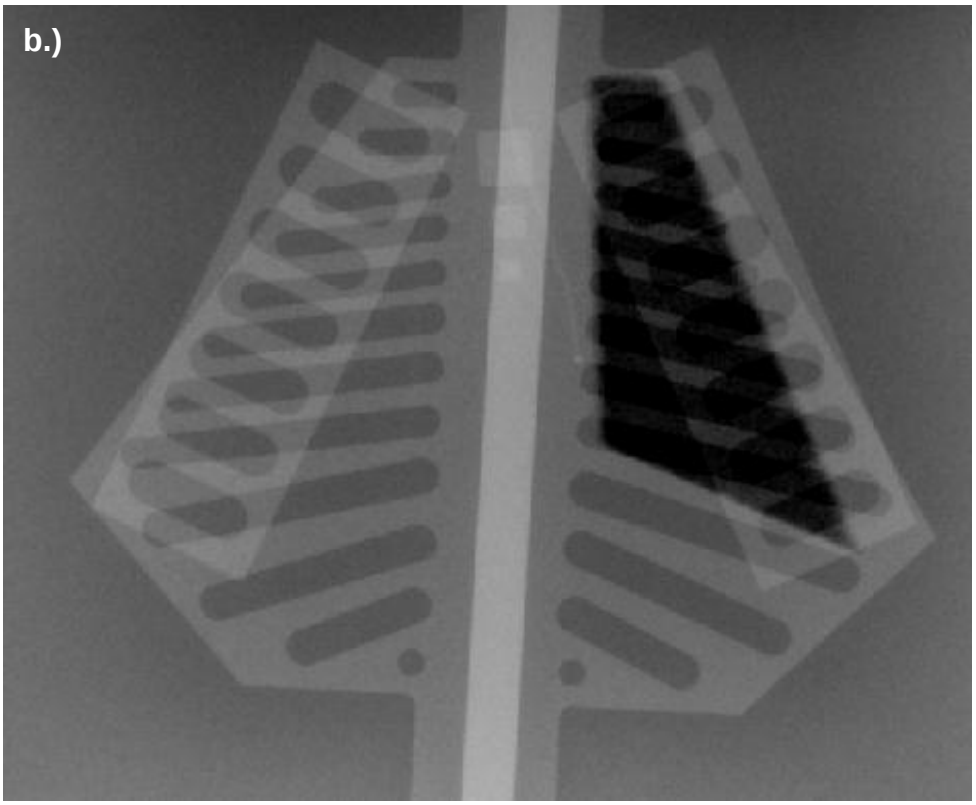

Figure 5.1: a.) 60kV, 2 mAs and inherent filtration raw image. b.) 60kV, 2 mAs and inherent filtration processed image.

The processed images quantified better than the raw images, but visually the images were less clear due to image processing. The visual scores for the raw images were higher than those of the processed images, where many of the images had the same total score of 11. As radiologists are used to viewing processed images in Tygerberg Academic Hospital, and there is no direct correspondence between visual and quantified image quality, it was therefore possible to reduce the ESD with little or no effect on the visual image quality, although the quantified image quality might be affected.

The raw images were visually much better, showing more detail and small differences in grey scale value, since they had not been processed and smoothed out. It also implied that the raw images would be more grainy in appearance, although the graininess in Figure 5.1 a.) on page 150 was quite acceptable. The graininess was another explanation for the poorer scoring quantitatively.

From the second set of preliminary exposures it could be deduced that dose reduction with minimal or no effect on image quality was indeed possible using processed images. It was also postulated that, with raw images, the initial better visual image quality could be used to obtain a dose reduction with a slight associated decrease in image quality, resulting in a raw image that was comparable to the initial visual image quality of a processed image. A dose decrease was possible with raw images. The third set of preliminary exposures therefore also considered raw and processed images.

5.4.3 Third preliminary exposure set

In the third set of preliminary exposures relative doses were measured with the Unfors XI view detector available at Tygerberg Academic Hospital. If the measured dose for a certain exposure was greater than that of the standard exposure (50 kV, 2 mAs, 100 cm FFD and inherent filtration) the objective of the study, i.e. dose reduction, would not be achieved. Such exposures could therefore not be considered as acceptable in the current study, irrespective of the visual and quantified image quality.

The raw images, with results recorded in Table 4.16, were considered first.

Table 4.16 shows that the raw standard image scored a total of 12 for visual image quality. The relative dose for the exposure was 45.9 µGy. An exposure that resulted in a dose reduction with similar or improved image quality would be an advancement compared with the standard used at Tygerberg Academic Hospital. Focus size, filtration and kV and mAs variation were investigated.

A large focus increased the ESD to a level higher than standard exposure. The visual image quality was also poorer, although the quantification was similar to the standard. It was therefore decided that a small or fine focus should be used, with a lower dose and better image quality. This was applied in the fourth and final exposure sets.

As additional filtration had proven results in literature, its effect had to be investigated, therefore the addition of 1 mm Al and 0.1 mm Cu + 1 mm Al filtration was considered. At 50 kV and 4 mAs, with the 1 mm Al filter, the visual image quality was comparable to that of the 50 kV and 3.2 mAs image with this filtration, but the quantitative image quality was only slightly improved. Increasing the mAs therefore did not improve the image quality, but the ESD was increased 6% and 36% above the standard, for 3.2 mAs and 4 mAs respectively. It was in contradiction with the aim and therefore not an option. At 70 kV, 2 mAs and 1 mm Al added filtration the visual image quality was better than that of the standard, but this improvement occurred at a 58% ESD increase above the standard exposure ESD. Due to the ESD increase and no apparent gain in image quality, it was decided that the addition of 1 mm Al filtration was not feasible for the current study. The 1mm Al filter alone only absorbed the very low energy photons. The 0.1 mm Cu + 1 mm Al filtration results looked more promising, as the Cu filtered a greater energy range of photons and the Al absorbed the characteristic x-rays generated in the Cu. Filtration reduced the number of low energy photons, which contributed to dose only and not to image quality formation.

An exposure with 50 kV, 3.2 mAs and 0.1 mm Cu + 1 mm Al filtration resulted in an image with a total visual image quality score of 11. It was considered a good score,

but it was not possible to see through the healthy lung in the image, i.e. the healthy lung was almost blacked out, so the image was not usable. The high CNR was also explained by this, i.e. there was a very large difference between the signals of bone and healthy lung, although it was not a true reflection of the actual image quality. The ESD was dramatically reduced by 58%, compared with the standard exposure.

The image obtained with the filter at 50 kV and 4 mAs was comparable to the 3.2 mAs image visually and quantitatively. Its dose was about 3% higher than at 3.2 mAs, but the ESD was still only half of the standard exposure. Compared to the image obtained in the second set of preliminary exposures, at 50 kV, 2 mAs with 0.1 mm Cu + 1 mm Al added filtration, the visual image quality was improved but the quantification results were similar. At 70 kV, 2 mAs with the added filtration the visual image quality deteriorated, although quantified image quality was better, except for CNR which was lower, due to healthy lung having a larger signal than that of the other images obtained with the filter. The image also quantified better than the standard image and had an ESD reduction of nearly 20%. These results showed that the addition of a 0.1 mm Cu + 1 mm Al filter held significant dose reduction advantages, although visual image quality was lower compared to the standard. It therefore warranted investigation of the filtering option further, with other combinations of kV and mAs, in the fourth preliminary exposure set.

The ESD at 55 kV, 1.6 mAs, 100 cm FFD with inherent filtration was comparable to that of the standard exposure, but visually it was poorer. At the higher kV, the intensities in the ROIs used in quantitative analysis were higher, therefore the SNR sick lung was better, but the CNR was poorer, as healthy lung, in this case as well, had a larger signal. The exposure was not an option, as the ESD was not decreased and visual image quality was reduced. In order to obtain an ESD reduction the mAs was reduced to 1.25 mAs, but it resulted in a drop in visual image quality, compared with the 1.6 mAs image and the standard. The quantitative analysis results were as satisfactory as those of the standard image, only the CNR was reduced as the signal in the healthy lung was increased. The reduction in dose achieved in this case was not justified by the loss in visual image quality. It was also the conclusion when the mAs was decreased to 0.8 mAs, i.e. ESD reduced by about 53%, but visual image quality had a total score of only 5.

Three mAs settings were used with 60 kV. At 1.4 mAs the ESD was increased to higher than the standard, the visual image quality had an increased total score of 15, and quantitatively it scored similar to the standard image, except for SDNR sick lung. However, due to the dose increase the exposure was not adequate. The mAs was lowered to 1 mAs, which gave an approximate 27% decrease in ESD compared with the standard exposure. Visually the total score of 12 was comparable to that of the standard image and quantitatively the image scored worse on SDNR sick lung and CNR, although the rest of the scores were also similar to that of the standard. It was due to the lowered mAs resulting in larger standard deviations or noise in the analysis ROIs and a very small difference in intensity or signal between Agar gel mix and sick lung. The image was also found to be the best raw image, compared with the standard image, of all the exposures made in preliminary set three. It is shown in Figure 5.2 a.) on page 155. With 0.8 mAs, a further reduction in ESD was achieved although image quality was slightly reduced. The exposure was still considered an option for the current study.

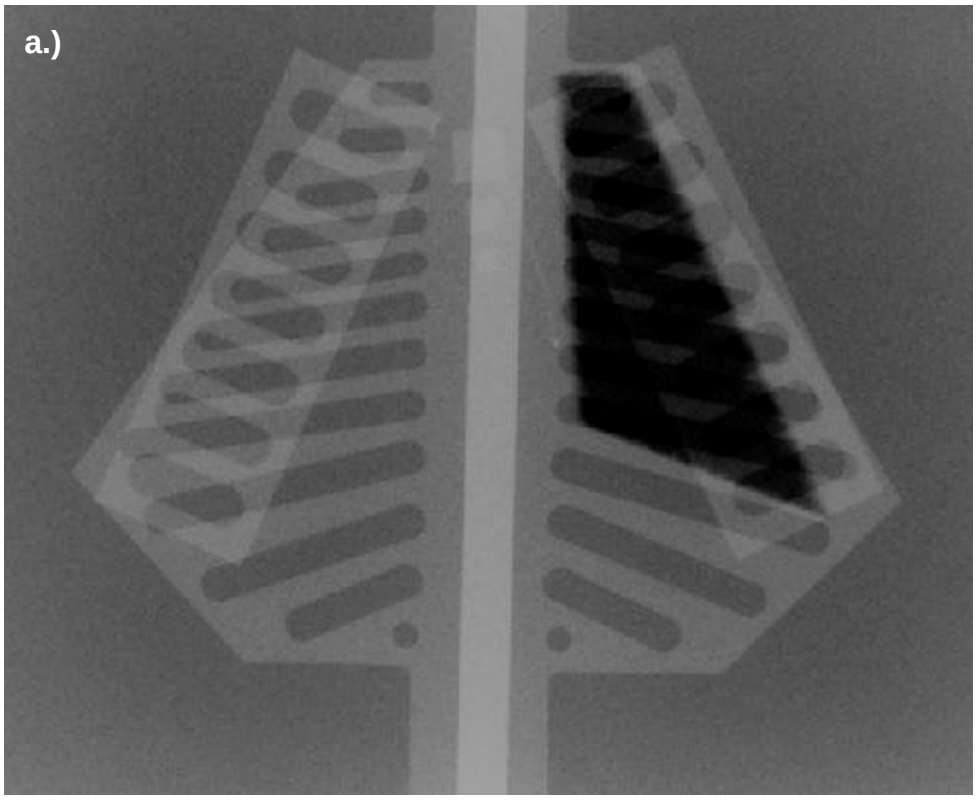

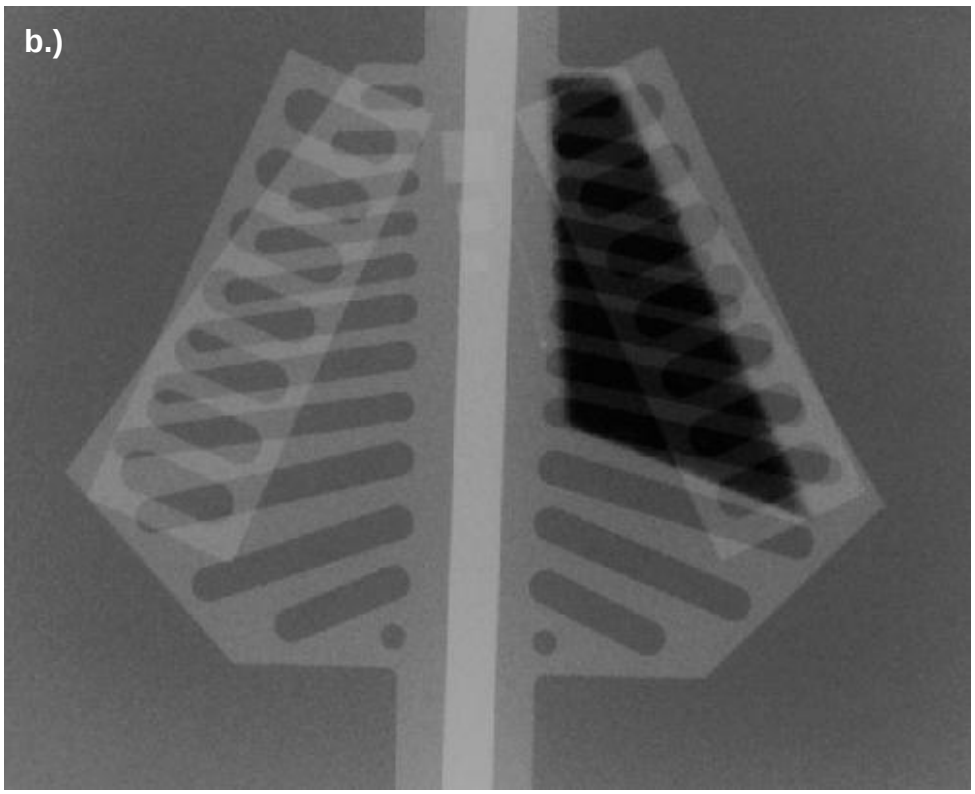

Figure 5.2: a.) Raw image obtained with 60 kV and 1 mAs. b.) Standard exposure raw image.

The ESD increased by 12% when an exposure was made with 65 kV and 1.25 mAs, although the visual image quality was higher than that of the standard image. With a reduction in mAs to 0.8 mAs, the ESD was about 33% lower than that of the standard exposure, obtaining an acceptable visual image quality comparable to that of the standard. Quantitatively the image was comparable to the image obtained with 1.25 mAs, except the CNR. When the mAs was dropped further, to 0.5 mAs, visual image quality was unacceptably degraded, although the ESD was greatly reduced.

Exposures were made at 70 kV with two mAs settings, 1 mAs and 0.5 mAs. At 1 mAs the ESD, was higher than with the standard exposure and the visual image quality poorer and this setting was therefore not an option. With a mAs reduction of 0.5 mAs, the ESD showed a 50% decrease compared with the standard, but the visual image quality was poor and overall the image was unacceptable. Exposures at 70 kV were therefore considered unacceptable.

The conclusion here was that dose reduction, using raw images, was possible, with maintenance of acceptable clinical image quality, by increasing the kV from 50 to 60 kV and reducing the mAs from 2 to 1 mAs. Further and finer investigation in the exposure range was necessary and was done in the fourth set of preliminary exposures.

Table 4.17 shows the results for the processed images of the third preliminary exposure set. These are discussed below.

The standard exposure processed image here had a lower visual image quality than the corresponding raw image, as shown in Figure 5.3 on page 157. The central line and sternal blocks were more clearly visible in the raw image, although the healthy lung was darker. Quantitatively the processed image was better than the raw image, except for SDNR sick lung and CNR. It was due to the processed image signals being larger and more uniform and having smaller standard deviations. The processed image is the image generally used in Tygerberg Academic Hospital, therefore a visual image quality above 9 implied an improvement compared with the image quality routinely used at the hospital.

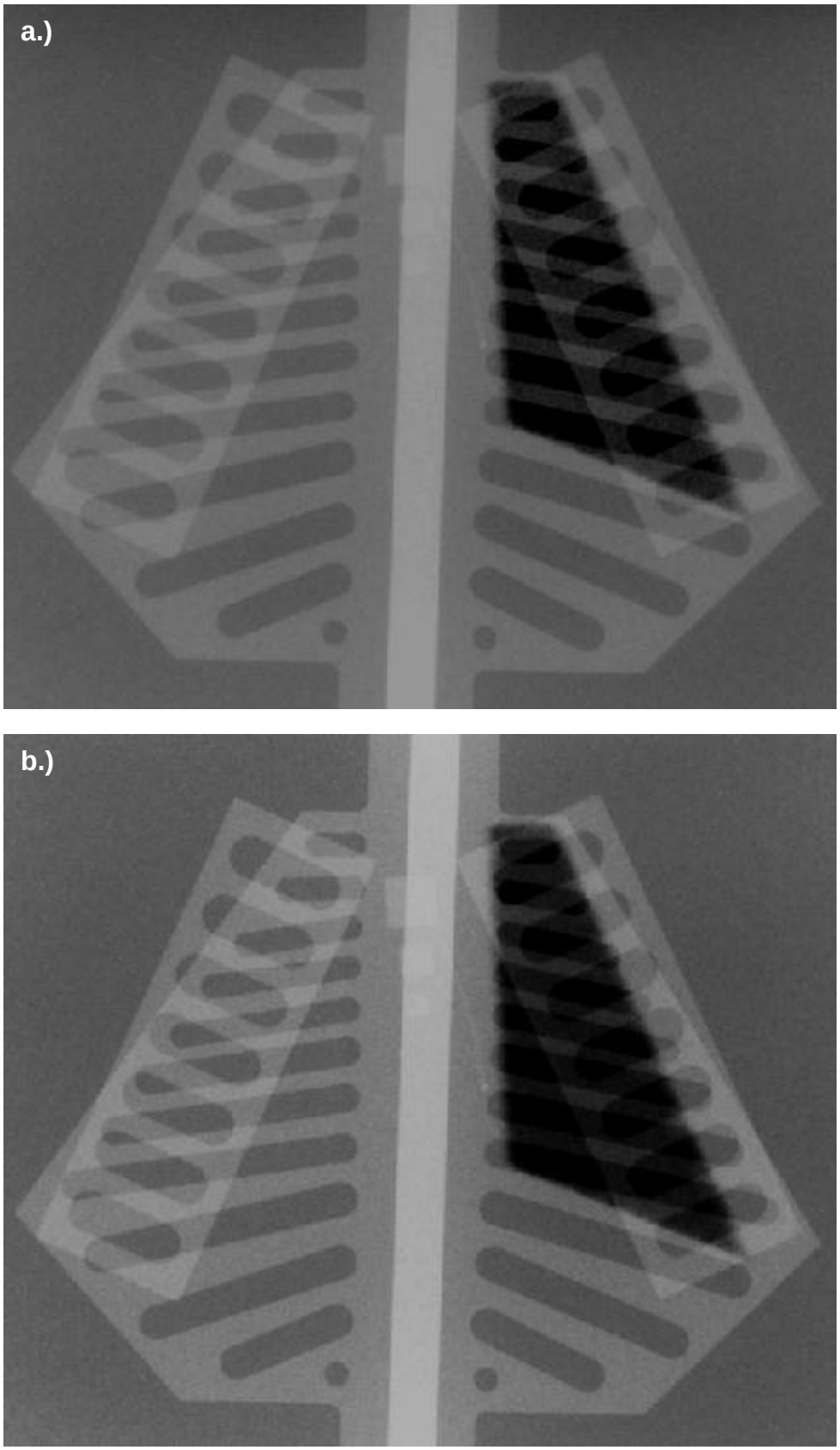

Figure 5.3: a.)Processed standard exposure image. b.) Raw standard exposure image.

The processed large focus image was visually comparable to the processed standard image, but the ESD had increased, therefore small focus was decided on for all further exposures. Quantitatively this image was poorer than the processed standard image, except on SDNR sick lung, as there was a larger signal intensity difference between Agar gel mix and sick lung. It was expected, as fine or small focus was supposed to give more detail theoretically.

With added 1 mm Al filtration, the processed images at 50 kV, 3.2 mAs and 4 mAs were visually and quantitatively comparable to the standard, at an increased ESD. And therefore these exposures were not justifiable.

At 70 kV and 2 mAs the additional 1 mm Al filter gave very high visual image quality, a total score of 15, but the ESD was increased by around 58%, therefore the exposure did not meet the requirements of dose reduction. The image is included as Figure 5.4 on page 159, in comparison with the standard processed image.

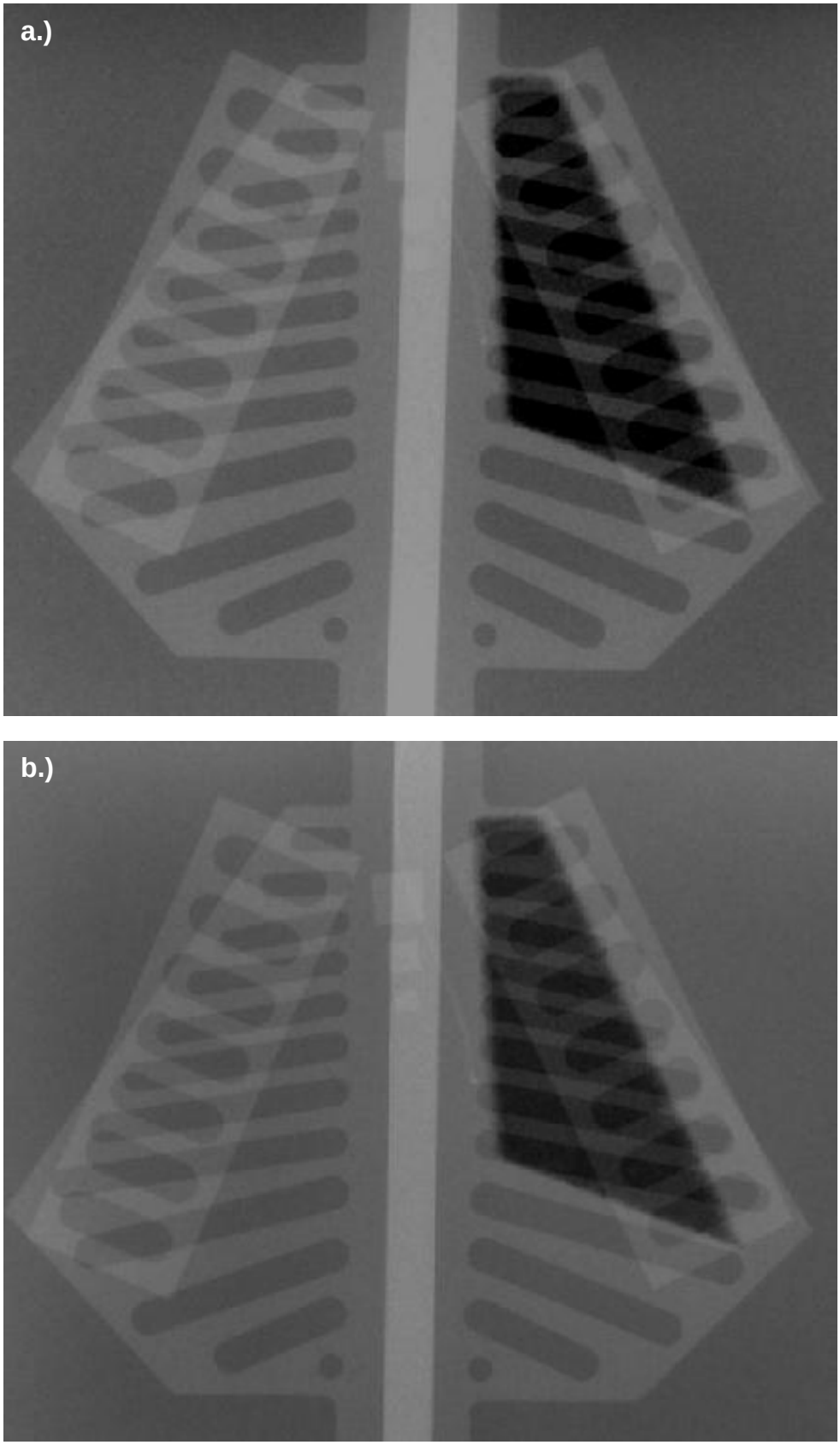

Figure 5.4: a.) Processed standard exposure image. b.) Processed image obtained at 70 kV, 2 mAs with 1 mm Al added filtration.

By adding 0.1 mm Cu + 1 mm Al additional filtration, significant ESD reductions as well as improved visual image quality were achieved, compared with the processed standard image. This type of exposure therefore met the requirements of the current study of ESD reduction, but had another advantage of visual image quality being higher than what was generally used in Tygerberg Academic Hospital. Apart from maintaining acceptable clinical image quality at a reduced ESD per x-ray, image quality was also improved.

At 50 kV and 3.2 mAs the visual image quality was slightly higher than that of the processed standard image, and the quantified results showed reduced CNR and better SNR sick lung. It was also the case at 50 kV and 4 mAs. The ESD was reduced by about 58% at 3.2 mAs and about 47% at 4 mAs. As the image quality was comparable visually and quantitatively between these two exposures, the 3.2 mAs exposure was deemed better, as it had a greater ESD reduction.

The exposure at 70 kV and 2 mAs yielded a total visual score of 14, which was much higher than the processed standard image score of 9. It was similar to the processed standard image quantitatively and was obtained at about 20% less ESD. It proved to be the best processed image and was considered an option for real neonatal imaging. The image is shown in comparison with the standard processed image in Figure 5.5 on page 161. The filtered image showed the central line and sternal blocks more clearly and the healthy lung was not as dark, showing the posterior ribs more clearly.

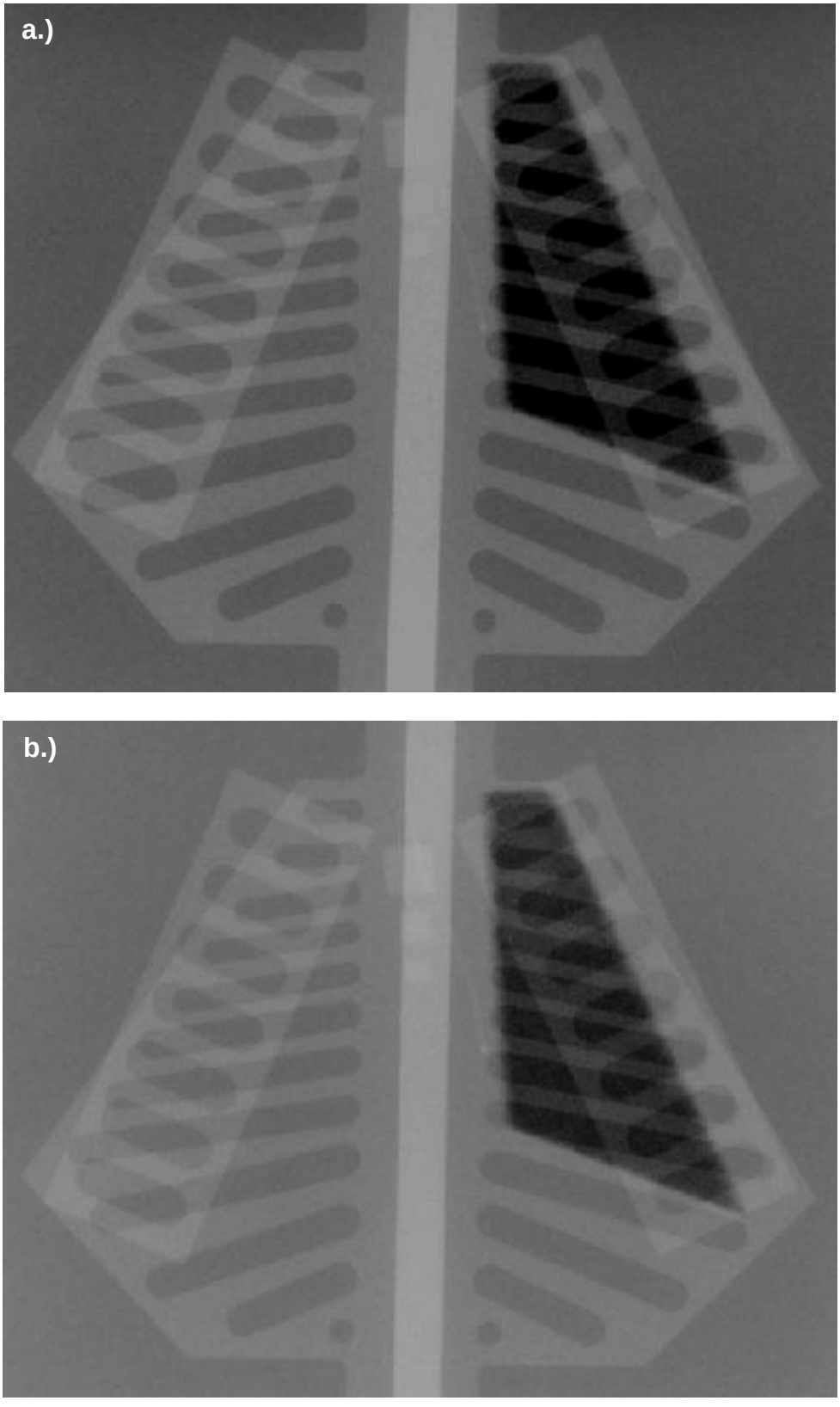

Figure 5.5: a.) Processed standard exposure image. b.) Processed image obtained at 70 kV, 2 mAs with 0.1 mm Cu + 1 mm Al added filtration.

Exposures were made at 55 kV with 1.6, 1.25 and 0.8 mAs respectively. Visually these images were comparable to the standard processed image, but the visual image quality was lower than was achieved with added 0.1 mm Cu + 1 mm Al filtration and at higher kV settings. The ESD was reduced at 1.25 and 0.8 mAs. At 1.6 mAs the image quantified better on SNR healthy and sick lung, with similar results for other criteria. The SDNR healthy lung and CNR were reduced at 1.25 mAs, compared to the standard processed image. At 0.8 mAs the SNR healthy lung was better, the CNR was comparable, but on all other criteria measured worse than the standard processed image. Overall the processed images at 55 kV were better than the corresponding raw images. However, the reduction in ESD at 1.25 and 0.8 mAs was not justified by the obtained image quality. The kV was therefore increased.

At 60 kV and 1.4 mAs, the visual image quality was better than that of the processed standard image, but the ESD was slightly increased, and therefore the exposure was not a good option. A mAs reduction to 1 mAs gave an ESD reduction of around 27% from the standard, with a slightly improved visual image quality total score of 11. Quantitatively the image was better than the standard. The image was visually and quantitatively comparable to the image obtained at 60 kV and 1.4 mAs, but had a lower ESD, and was therefore considered better than the 1.4 mAs image. At 0.8 mAs the ESD was about 43% less than the standard exposure, with the same visual image quality and similar quantified image quality as the standard image.

It was therefore possible to obtain an image at a reduced ESD while maintaining image quality. This set of preliminary exposures showed it may be possible to reduce ESD while achieving an improvement in the image quality at the same time, compared with the standard exposure of small focus, 100 cm FFD, inherent filtration, 50 kV and 2 mAs.

At 65 kV and 1.25 mAs the ESD was higher than that of the standard exposure, therefore the improved visual image quality was not justified. By reducing the mAs to 0.8 mAs the ESD was decreased by 33%, with a visual and quantitative image quality that were comparable to that obtained at 1.25 mAs and better than the standard image. The exposure, at 65 kV and 0.8 mAs, was therefore an option for

the current study. A further ESD reduction was obtained by decreasing the mAs to 0.5 mAs. The significant ESD reduction of about 61% from the standard exposure had a visual image quality that was higher than that of the standard exposure. Quantitatively it was also comparable to the standard processed image. The processed image was better than its corresponding raw image regarding visual image quality. The images are included in Figure 5.6 on page 164. Image quality was visually higher since the sternal blocks were clearer and also resulted in significant ESD reduction. Exposures in this range had therefore to be more closely evaluated in the fourth preliminary exposure set.

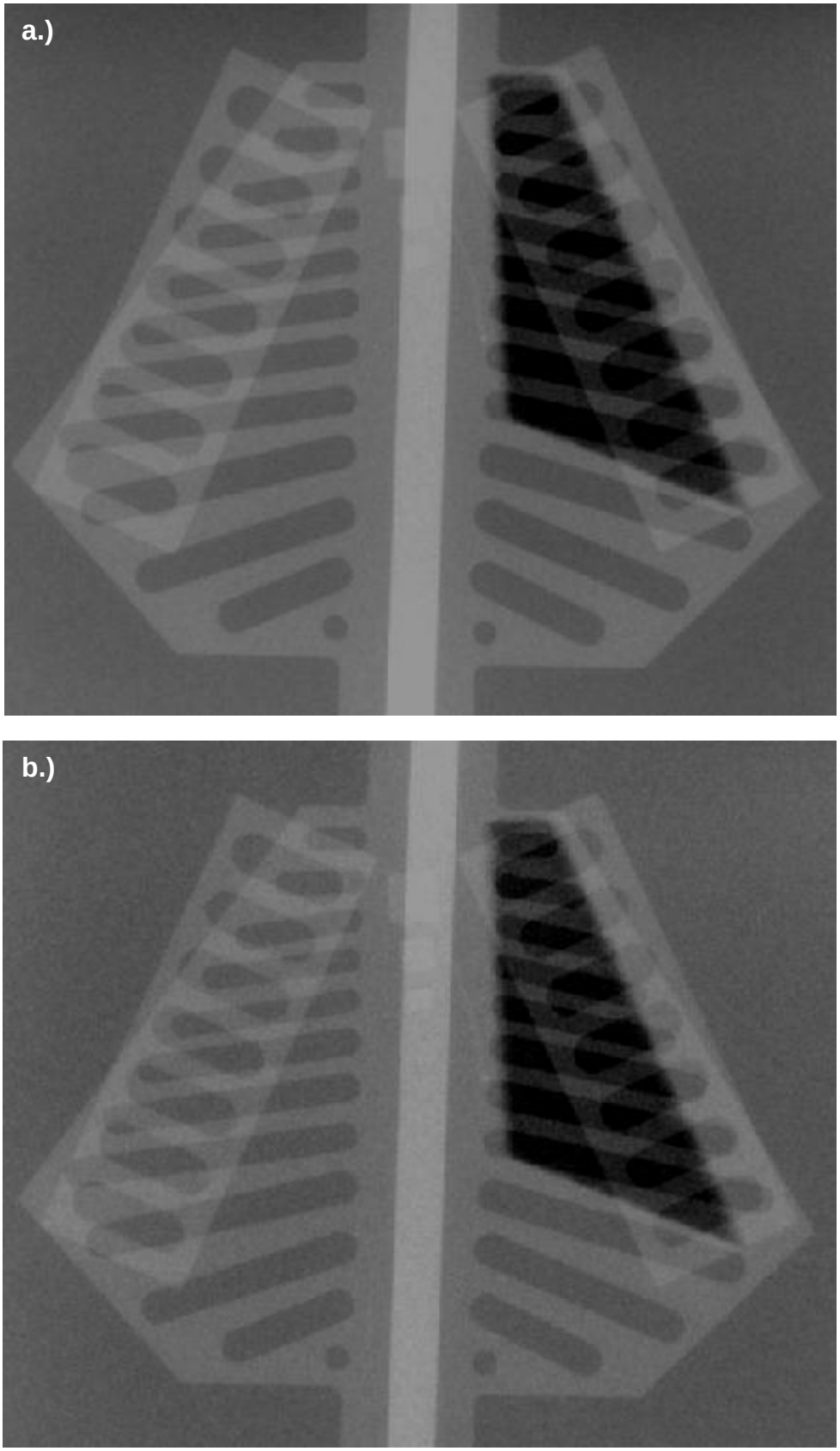

Figure 5.6: a.) Processed standard exposure image. b.) Processed image obtained at 65 kV and 0.5 mAs.

At 70 kV and 1 mAs no ESD reduction was obtained. The same total visual image quality score could be obtained with reduced ESDs at 65 kV and 0.5 mAs and 65 kV and 0.8 mAs. Similar scores were also reached with added 0.1 mm Cu + 1 mm Al filtration. Therefore the exposure was not considered feasible for the current study. An ESD reduction of about 54% was obtained when the mAs was decreased to 0.5 mAs, i.e. the lower mAs limit of the fixed x-ray unit. Visually the image was better than the standard processed image and the same as the image obtained at 70 kV and 1 mAs, although it was quantitatively poorer than this image. The image was also an option for the current study.

The processed images in the third preliminary exposure run showed that the best option was 70 kV, 2 mAs and added 0.1 mm Cu + 1 mm Al filtration, as seen in Figure 5.5 b.) on page 161.

The third preliminary exposure set showed that a definite, and significant, ESD reduction from the standard exposure was indeed possible. It was found that dose reduction could include an improvement in visual image quality, when using processed images, compared with standard practice at Tygerberg Academic Hospital. A narrower range was therefore proposed for investigation in the fourth preliminary exposure set.

5.4.4 Fourth preliminary exposure set

In the fourth set of preliminary exposures, a smaller range with finer sampling was used. Additional filtration of 0.1 mm Cu + 1 mm Al and changes in kV and mAs for raw and processed images were considered.

Table 4.18 shows the results for the raw images. Although no significant improvements in visual image quality were found in the case of raw images, visual image quality was maintained, at a reduced ESD, in most of these images. These results are discussed below.

Figure 5.7 shows some of the raw images obtained with additional filtration of 0.1 mm Cu + 1 mm Al.

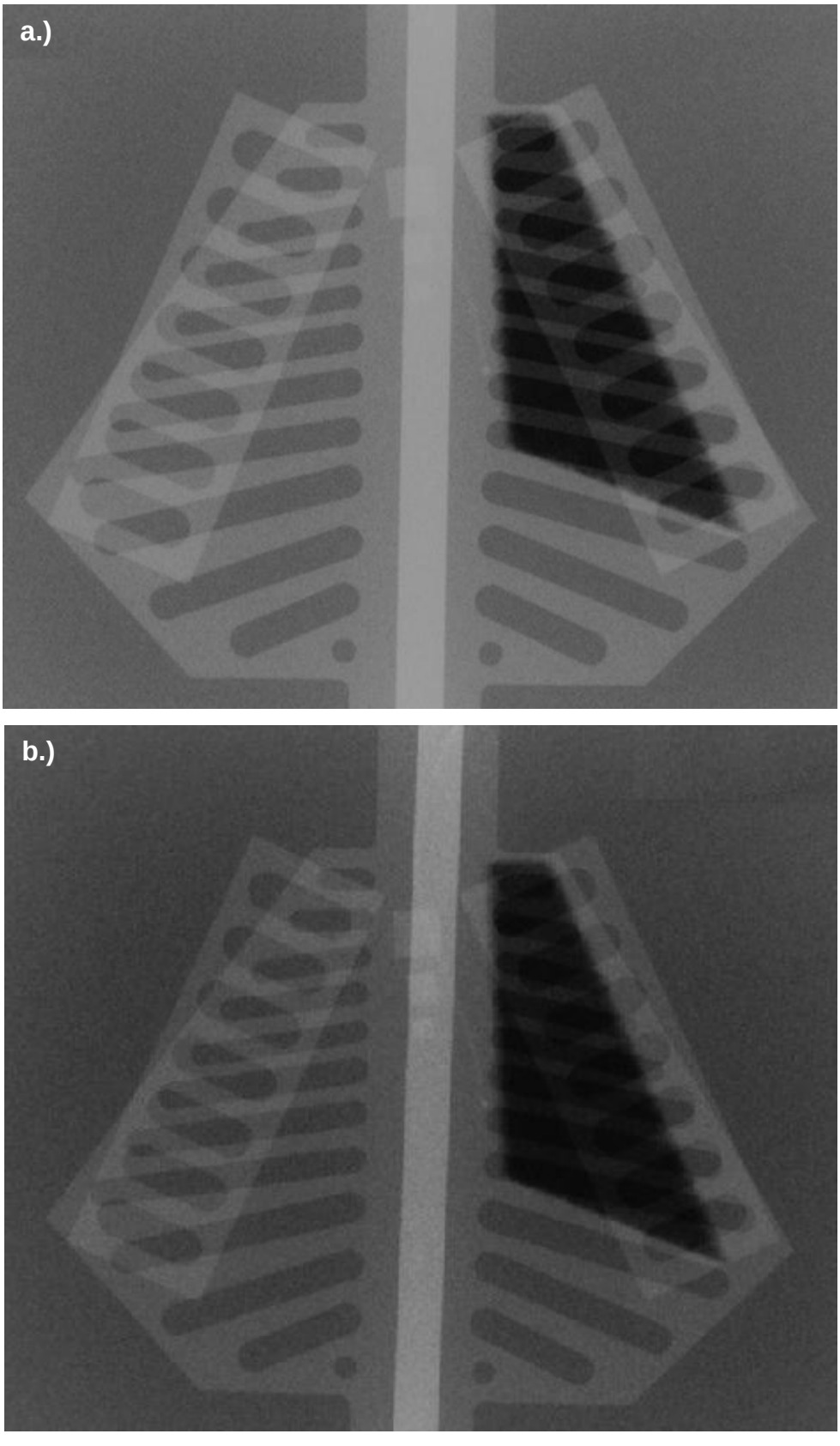

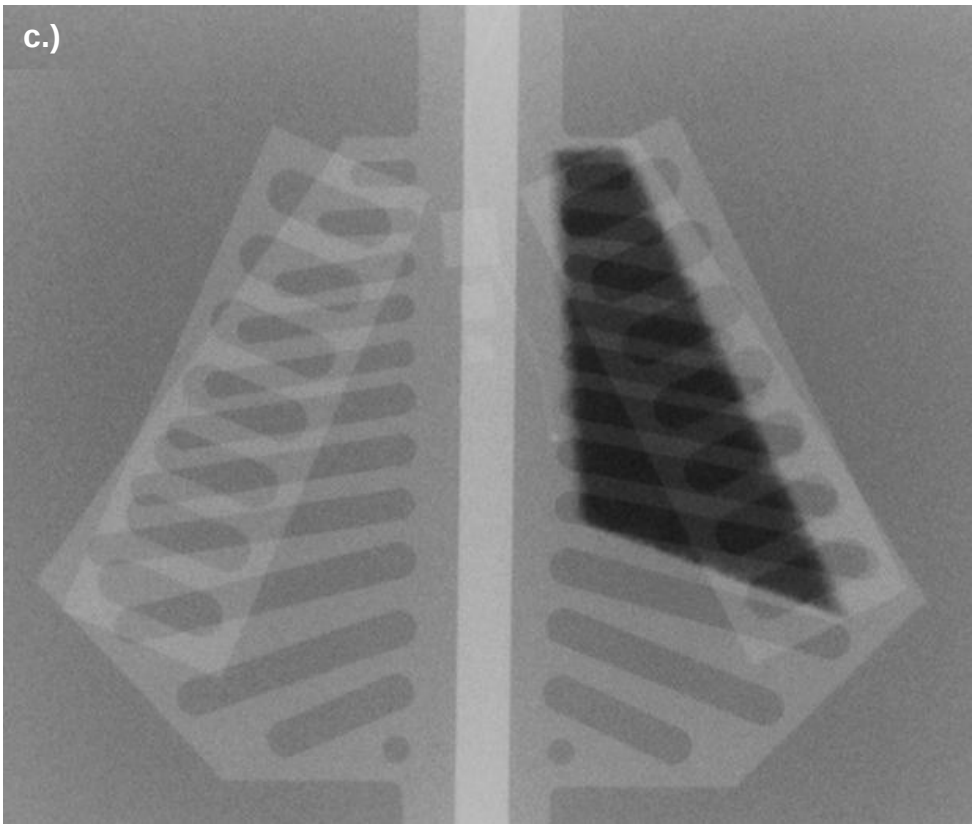

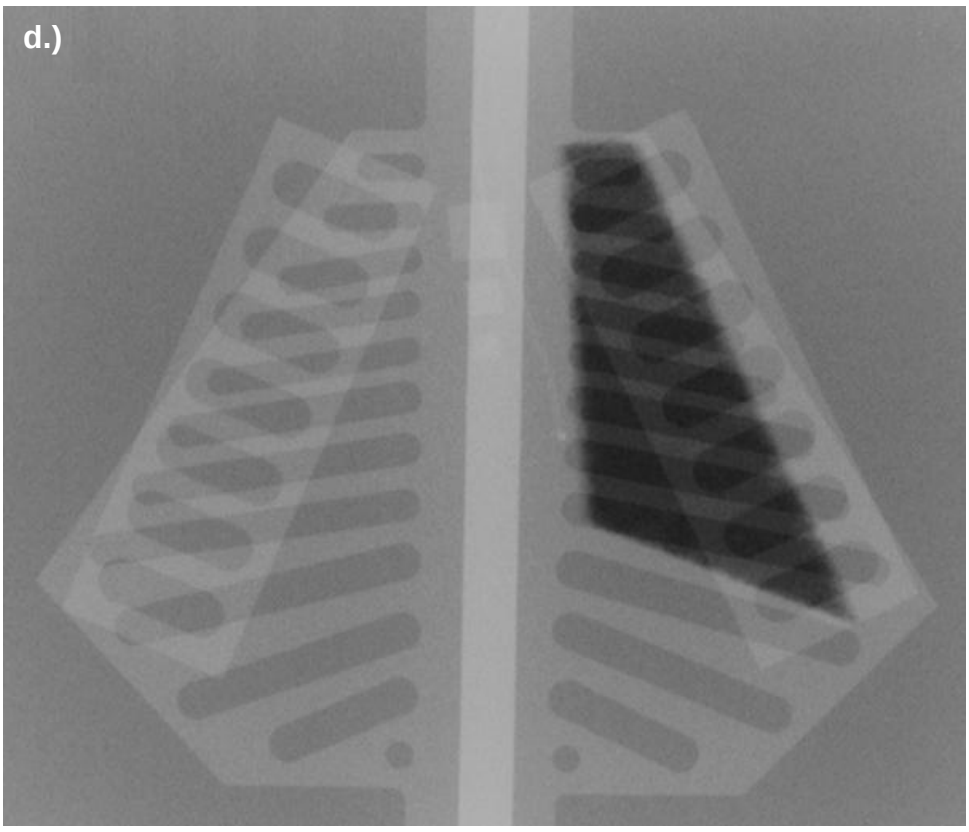

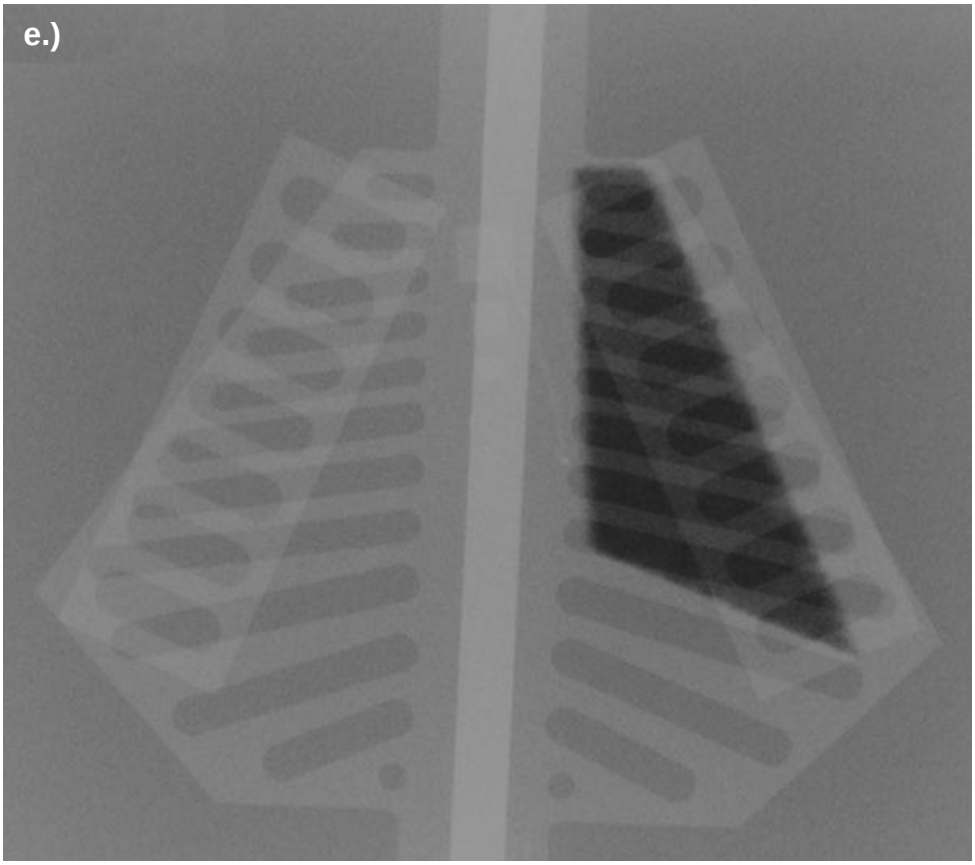

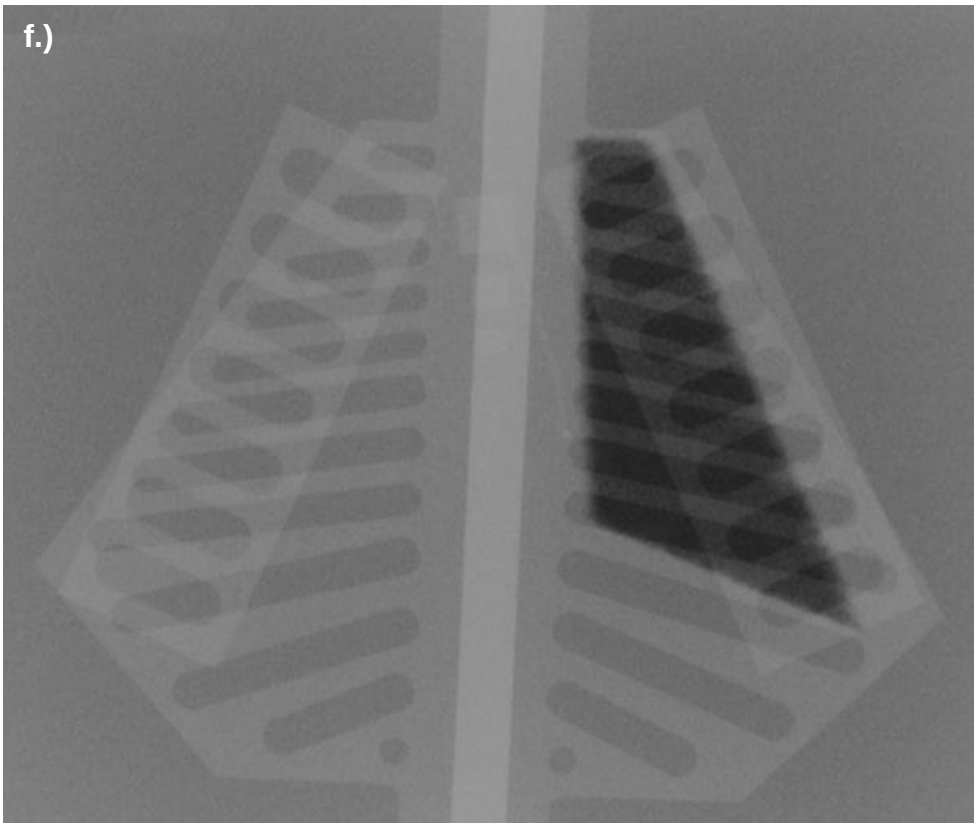

Figure 5.7: a.) Raw standard exposure image. b.) Raw image at 55 kV, 2 mAs with 0.1 mm Cu + 1 mm Al added filtration. c.) Raw image at 60 kV, 2 mAs with 0.1 mm Cu + 1 mm Al added filtration.

d.) Raw image at 60 kV, 3.2 mAs with 0.1 mm Cu + 1 mm Al added filtration. e.) Raw image at 64 kV, 2 mAs with 0.1 mm Cu + 1 mm Al added filtration. f.) Raw image at 63 kV, 2 mAs with 0.1 mm Cu + 1 mm Al added filtration.

Most of the raw images obtained at 53 - 57 kV and 65 kV with the additional 0.1 mm Cu + 1 mm Al filtration were actually visually poor. It seemed that visual image quality was maintained, with total scores of 10 or 11, but this was not true. These images scored a value of 1 for healthy lung, which implied that the healthy lung was almost black. An example is shown in Figure 5.7 b.), on page 166, of the 55 kV and 2 mAs filtered image. Although the image had an ESD reduction of approximately 64% and the central line and sternal blocks were clearly visible, the almost black lung made it unusable. Chest AP x-rays were used to investigate disease conditions of the lungs, and if the lungs were black no information could be obtained from such an exposure.

At 60 kV and 2 mAs with the added filtration, the obtained total visual image quality was higher than that of the standard raw image, i.e. a total score of 12. It showed the sternal blocks better and the healthy lung was more transparent. This image, Figure 5.7 c.) on page 167, is compared with the standard raw image, Figure 5.7 a.) on page 166. Quantitatively it was better than the standard raw image on SNR healthy lung, comparable on SDNR healthy lung but scored lower in respect of the other criteria. The image was obtained at an ESD of about half of the standard raw image. It was therefore considered an option for final evaluation.

The mAs was increased to 3.2 mAs at 60 kV and applied together with the additional filtration. The image quantified better than the corresponding image at 2 mAs, although its visual image quality was comparable to that of the 2 mAs image. Its ESD was only about 17% less than that of the standard, and so the image was not included in the final evaluation. The images are compared in Figure 5.7, i.e. Figure 5.7 a.) on page 166, for the standard raw image, and Figure 5.7 d.) on page 167.

The image obtained at 64 kV, 2 mAs and additional 0.1 mm Cu + 1 mm Al filtration was the best raw filtered image visually totalling visual image quality score of 13. Visually it was better than the images acquired at 60 and 63 kV with 2 mAs and the additional filtration, but it had a slightly higher ESD than these images. Its ESD was still nearly 39% less than the standard image, so the slight increase in ESD was justified by the improved visual image quality. This image quantified better than the standard raw image in SNR healthy and sick lung, similar in SDNR healthy lung and poorer in SDNR sick lung and CNR. Figure 5.7 a.), c.), e.) and f.), on pages 166 - 168, show these images.

In the case of inherent filtration, different combinations of kV and mAs were used. These images all achieved a total visual image quality score of 10 or 11, except for the 63 kV and 1.1 mAs and 64 kV and 0.5 mAs images, which had a total score of 13 and 8 respectively. By using this technique, the visual image quality was maintained overall and ESD was reduced as well.

Figure 5.8 on pages 171 - 175 shows the images obtained with inherent filtration.

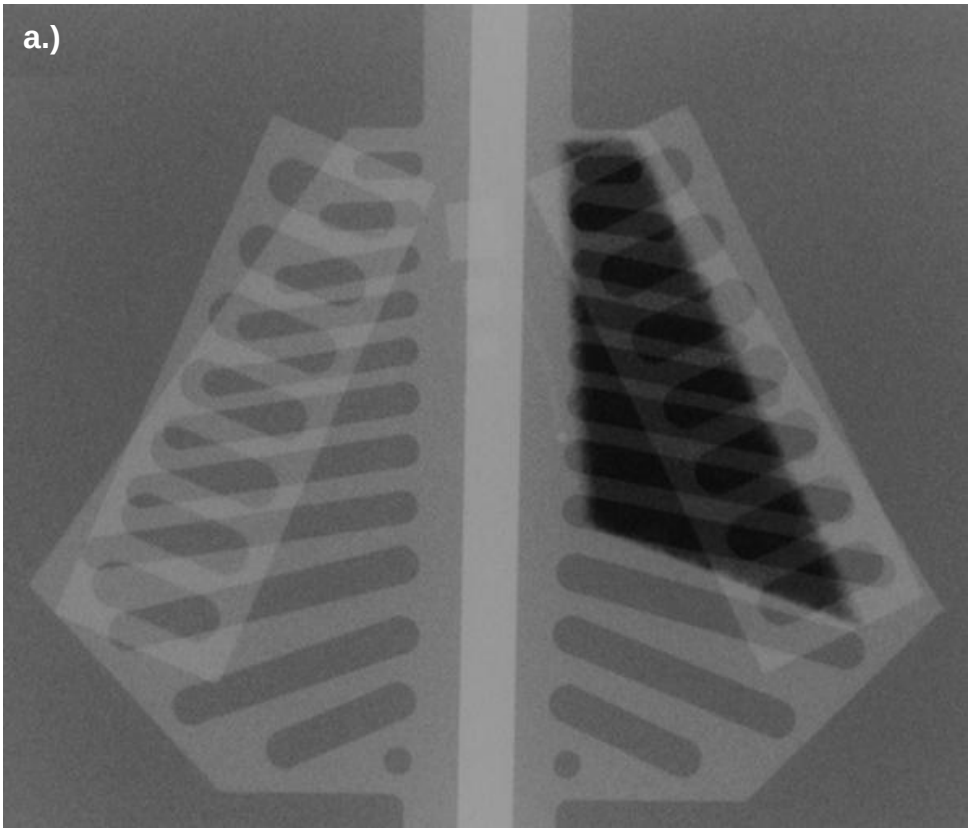

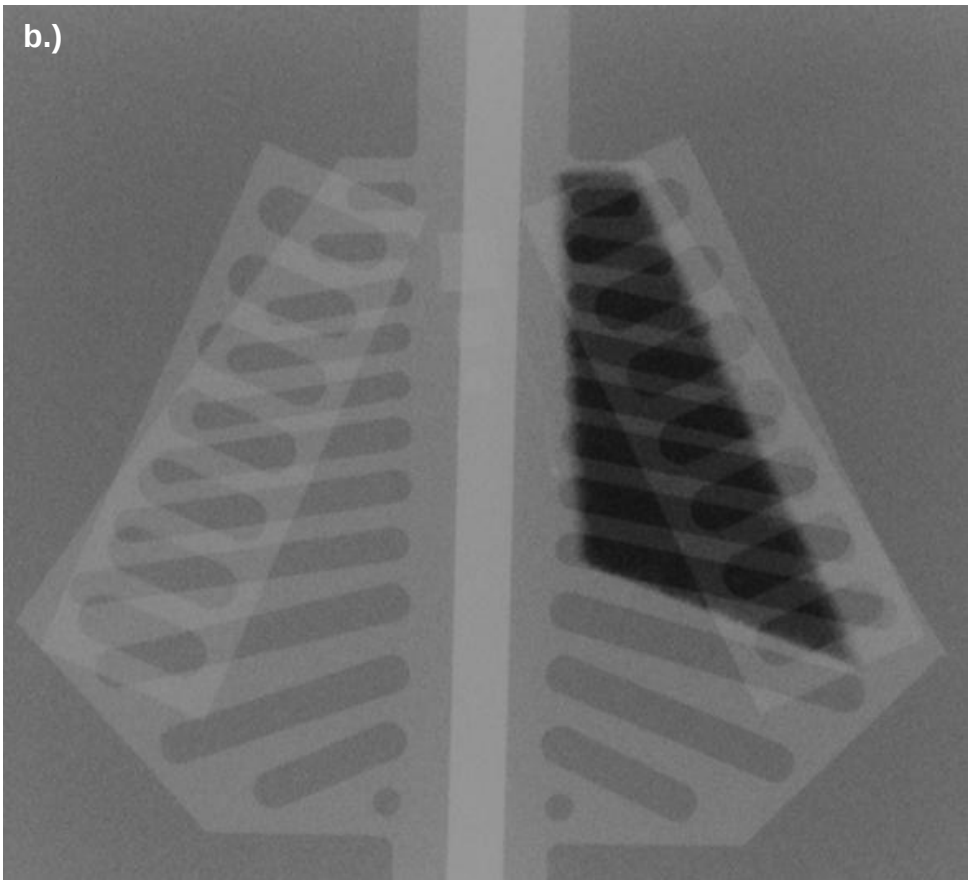

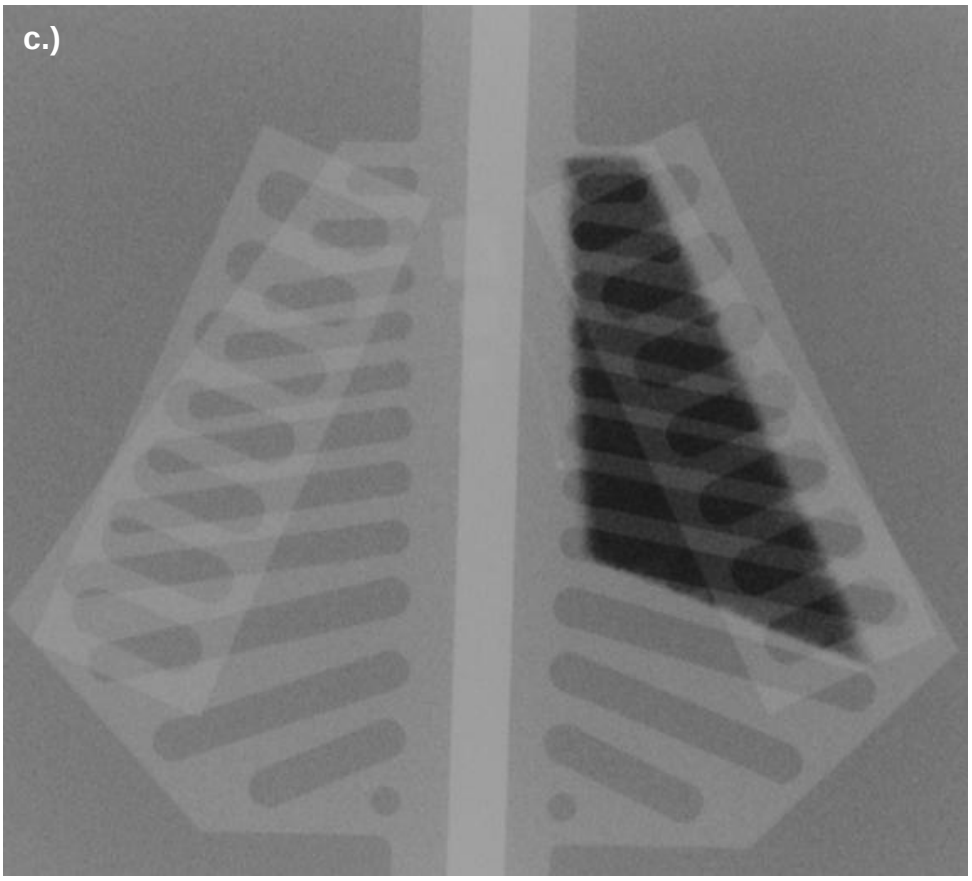

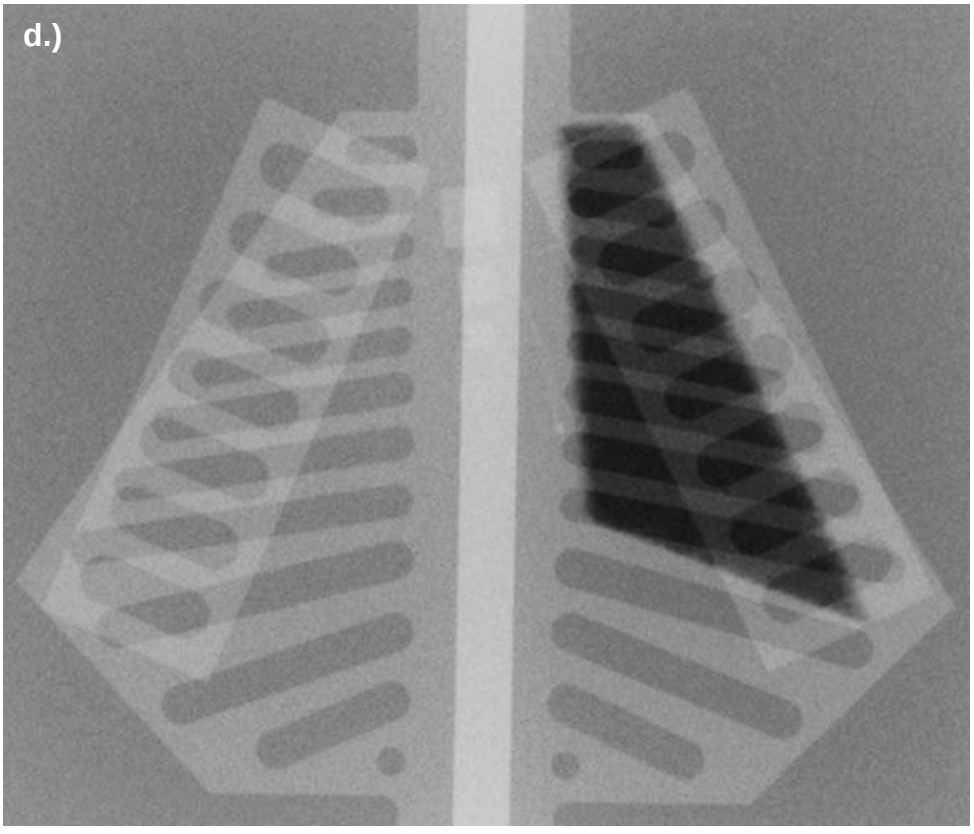

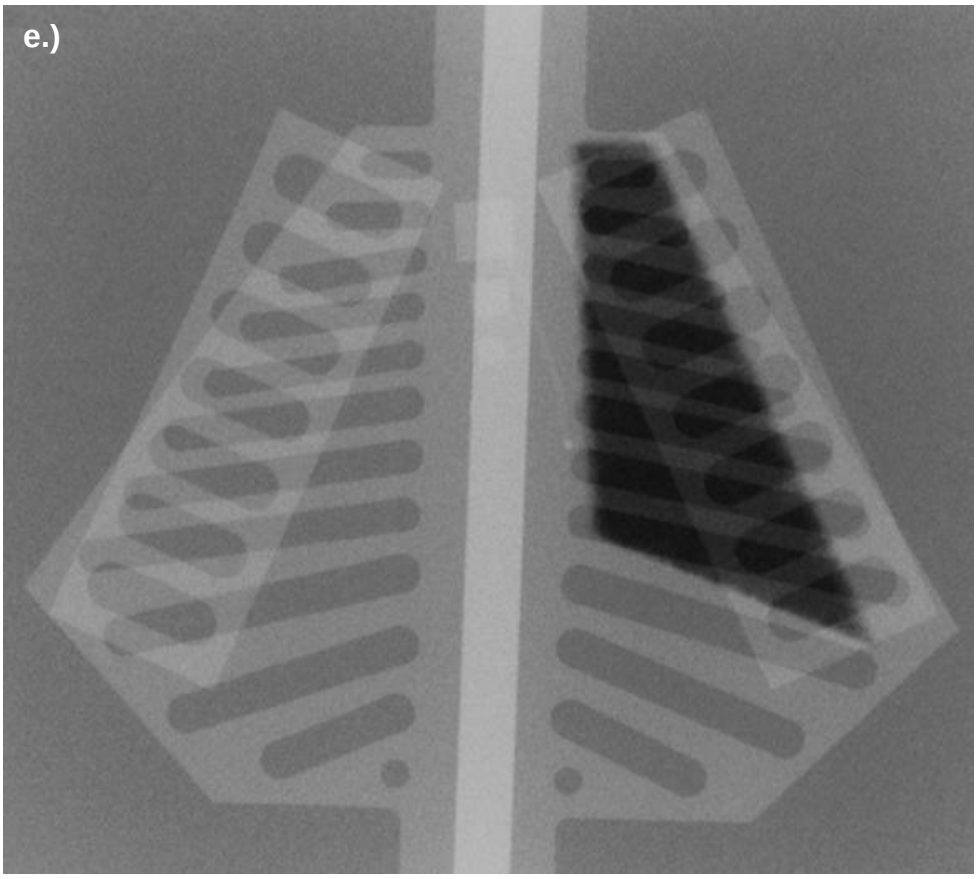

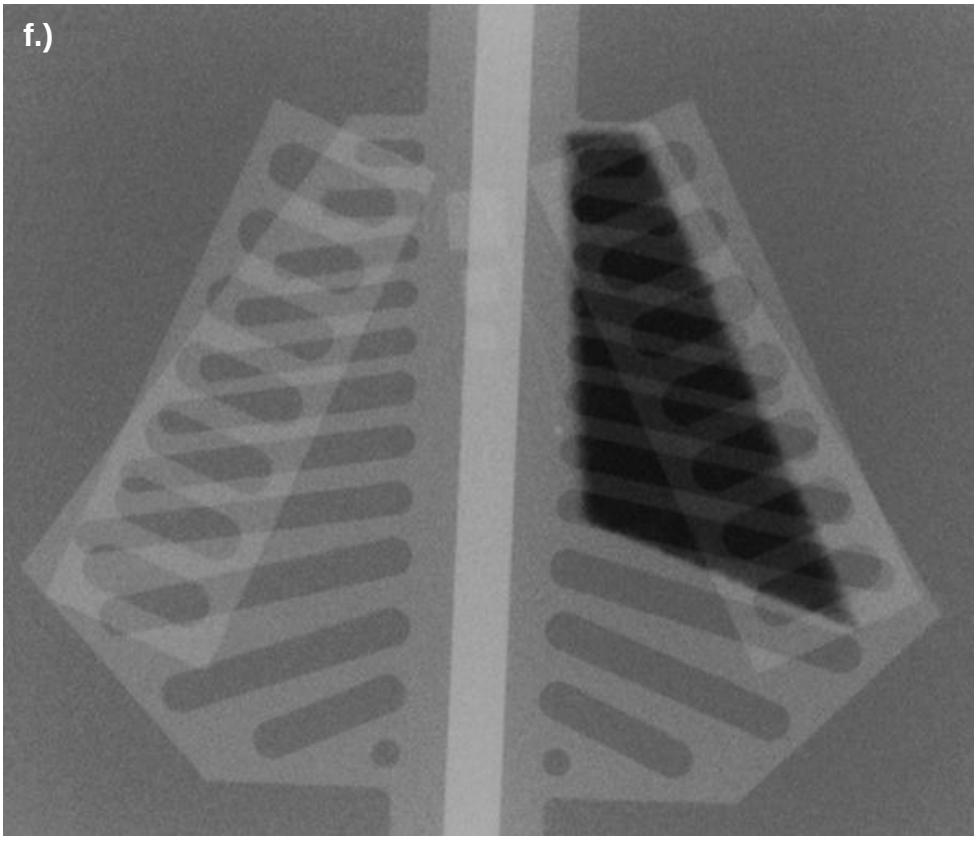

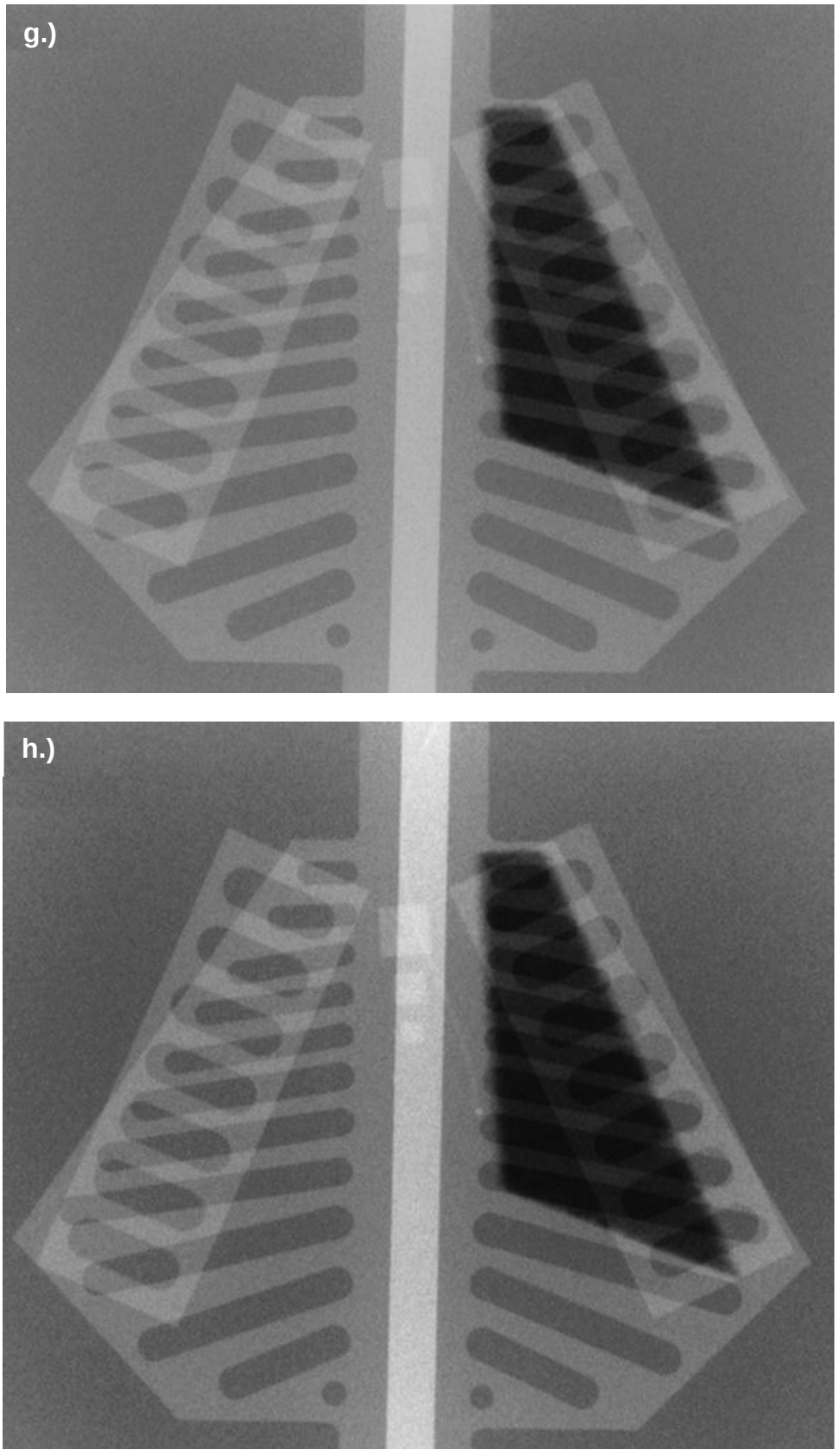

Figure 5.8: a.) Raw standard exposure image. b.) Raw image at 58 kV, 1mAs with inherent filtration. c.) Raw image at 59 kV, 1 mAs with inherent filtration. d.) Raw image at 61 kV, 0.8 mAs with

inherent filtration. e.) Raw image at 62 kV, 1.1 mAs with inherent filtration. f.) Raw image at 62 kV, 0.8 mAs with inherent filtration. g.) Raw image at 63 kV, 1.1 mAs with inherent filtration. h.) Raw image at 64 kV, 1 mAs with inherent filtration.

The image at 58 kV and 1 mAs was better than the one at 59 kV and 1 mAs, although it was more grainy. It showed more detail than the 59 kV 1 mAs image, which was smoother, and had a slightly lower ESD. These images are included in Figure 5.8 b.) and c.) on pages 171 and 172. These images were not considered in the final assessment since they obtained scores of 4 for sternum, while similar images at similar doses were recorded with sternum scores of 5. It was also the case in the images at 58 and 59 kV and 1.25 mAs, which were comparable visually. Overall these images were also comparable to the standard raw image quantitatively, but with worse performance on CNR.

At 61 kV, images were obtained at 1.1 and 0.8 mAs. These images were comparable to the standard raw image and to each other. The image at 0.8 mAs was therefore considered to be better, as it had a lower ESD than the 1.1 mAs image. The image was also considered an option for the final exposure set. It had an ESD reduction of about 41% from the standard exposure. Quantitatively it was slightly poorer than standard raw image. It was slightly grainier than the image at 1.1 mAs, but the slight effect on image quality was justified by the reduced ESD. Visually it was comparable to the standard raw image, so visual image quality was maintained. These images are included in Figure 5.8 a.) and d.) on pages 171 and 172.

Images were also recorded at 0.8 and 1.1 mAs at 62 kV. The 62 kV and 1.1 mAs image was slightly better, at a slightly increased ESD, compared with the image at 61 kV and 1.1 mAs. The image still had an ESD reduction of about 12%, compared with the standard exposure. The image at 0.8 mAs and 62 kV was slightly grainier than the 1.1 mAs image, but its ESD was about 30% less than for the1.1 mAs image. The medial line of the sick lung was visible, it was not the case at 61 kV and 0.8 mAs, so the 62 kV 0.8 mAs image was considered the better of the two, although it

had a slightly higher ESD. The image was still slightly better than the standard raw image, with an ESD reduction in the order of 38%, and it was considered an option for final evaluation. These images are included in Figure 5.8 e.) and f.) on page 173.

The image at 63 kV, 1.1 mAs and inherent filtration, in Figure 5.8 g.) on page 174, achieved the best visual image quality results with change in kV and mAs in raw images. It had a total visual image quality score of 13, but its ESD was only about 10% less than the standard exposure. The small improvement in image quality did not justify the higher ESD, compared with other kV and mAs combinations, therefore the image was not considered for the final exposure set. Similar results were obtainable at substantially lower ESDs.

The rest of the kV and mAs combination images in Table 4.18 were not considered as options for final evaluation, as the healthy lung was again nearly black in these images. In general, these images were grainier but showed more contrast. For example, sternal blocks and the whole central line were clearly seen, as shown in Figure 5.8 h.) on page 174.

The processed images of the fourth preliminary exposure set, as in Table 4.19, showed that additional filtration of 0.1 mm Cu + 1 mm Al actually caused an improvement in visual image quality, compared with the standard processed image, and all of these exposures had an associated ESD reduction from the standard. The best image visually was obtained at 57 kV and 3.2 mAs with added filtration. Visually the image scored a total of 16, i.e. twice as high as the standard processed image. The image also quantified very similar to the standard processed image in respect of all criteria and its ESD was about 32% lower.

As shown in the third set of preliminary exposures, exposures around 50 kV with added filtration were too low. As the kV was increased, and the beam penetrability was increased, more photons were reaching the imaging plate to contribute to image formation. In Table 4.19 it was seen that the visual image quality improved as the kV was increased above 55 kV, with the optimal range of 57 to 65 kV. The added filtration absorbed the lower energy photons, which only contributed to dose and not to image formation, as illustrated by the significant ESD reductions from the standard

in Table 4.19. The processed images of importance are included in Figure 5.9 on pages 177 - 179.

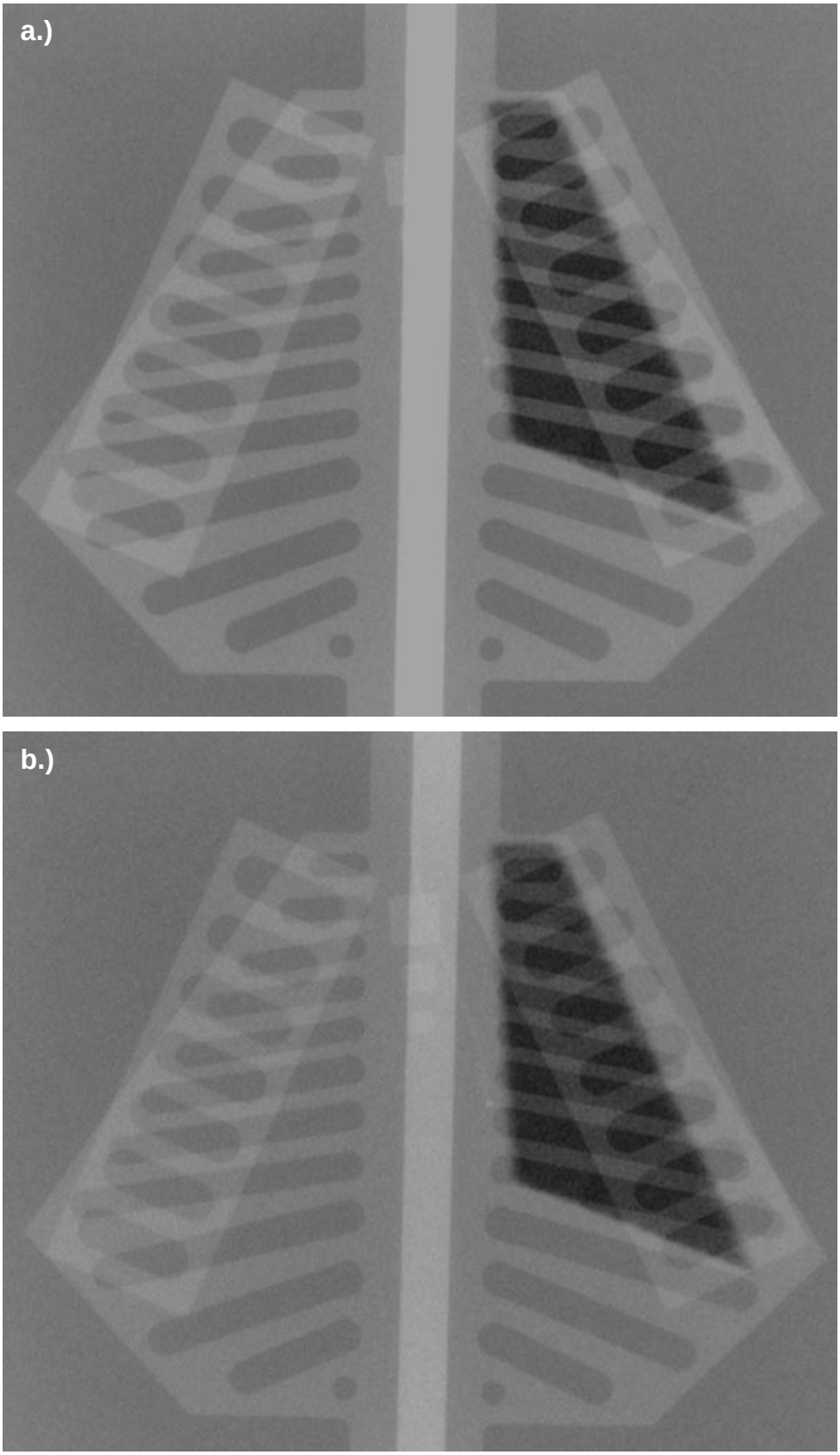

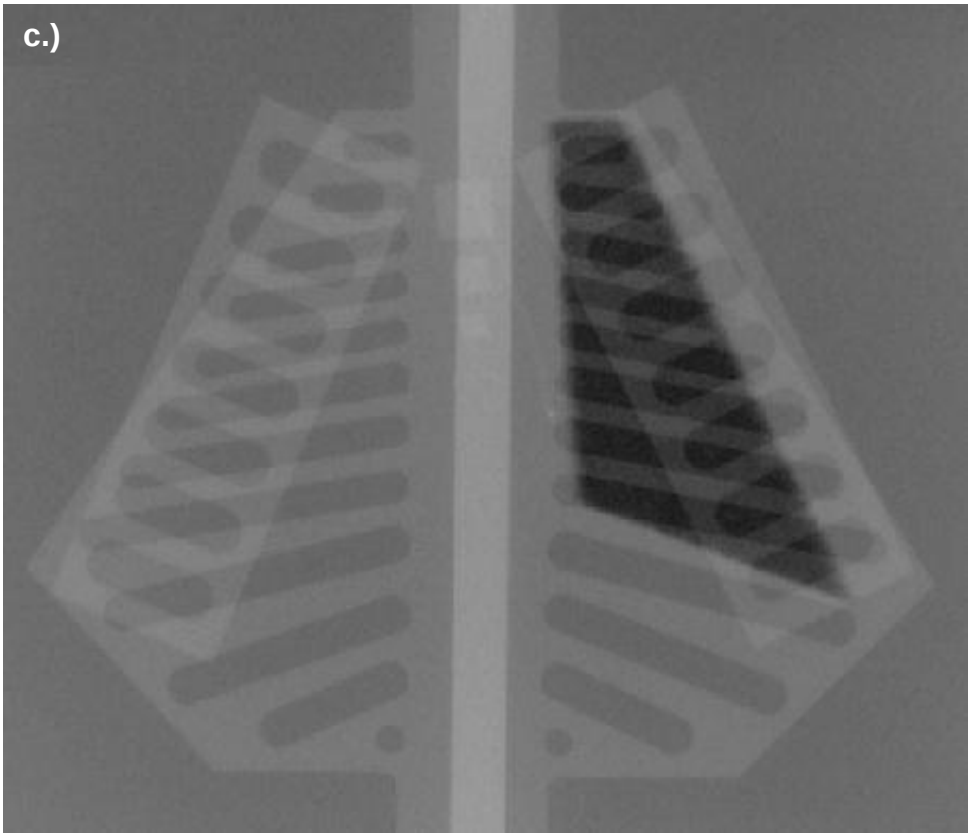

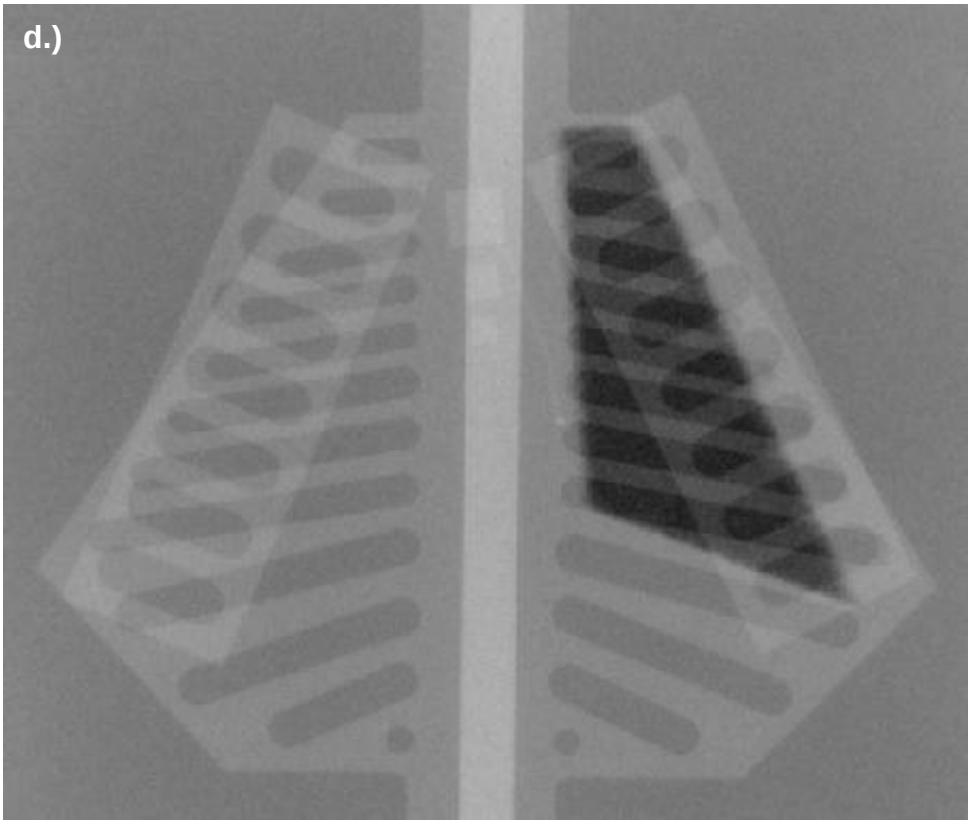

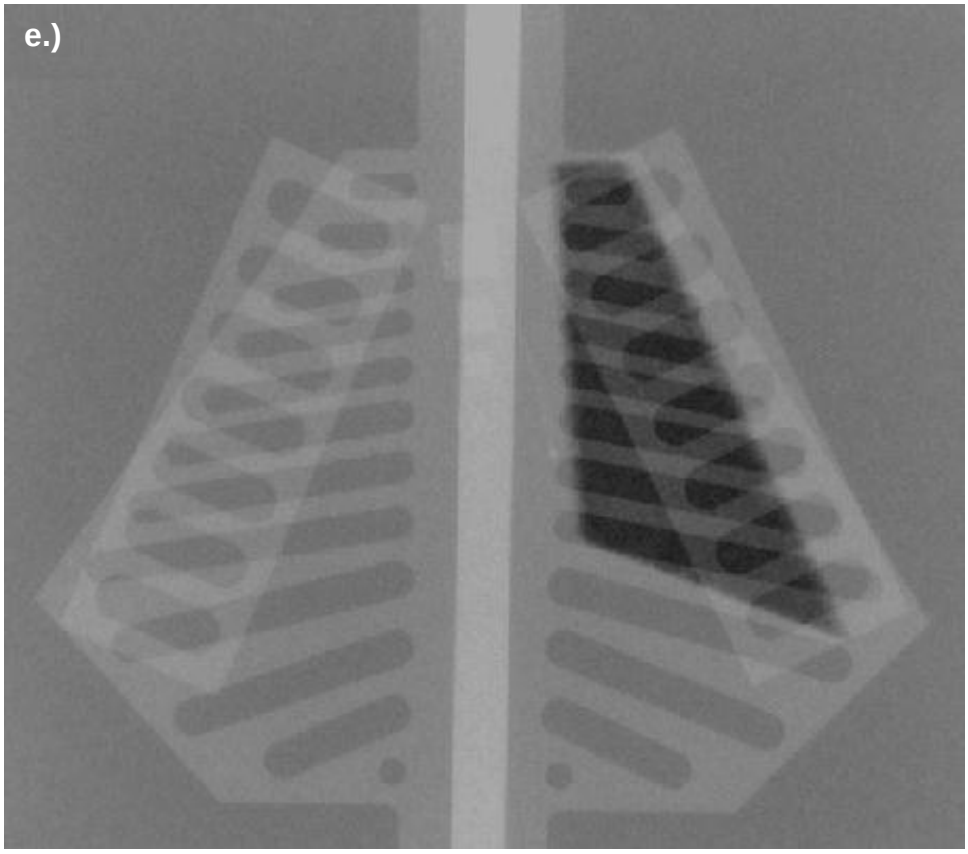

Figure 5.9: a.) Processed standard exposure image. b.) Processed image at 57 kV, 2 mAs with 0.1 mm Cu + 1 mm Al added filtration. c.) Processed image at 57 kV, 3.2 mAs with 0.1 mm Cu + 1 mm Al added filtration. d.) Processed image at 60 kV, 2 mAs with 0.1 mm Cu + 1 mm Al added filtration. e.) Processed image at 61 kV, 0.8 mAs and inherent filtration.

At 57 kV, Figure 5.9 b.) and c.) on pages 177 and 178, with added filtration, visual image quality was slightly improved as the mAs was increased from 2 to 3.2 mAs. Quantitative image quality was also improved. The ESD was about 40% higher at 3.2 mAs than at 2 mAs, but as there was still a significant ESD reduction from the standard (nearly 32%) at 3.2 mAs, this increase in ESD was still justifiable. Compared with the processed standard image, Figure 5.9 a.) on page 177, the filtered image at 57 kV and 2 mAs was quantitatively lower and visually better. The image was obtained at an ESD of about 59% less than that of the standard exposure. The tremendous ESD reduction made the exposure, which also brought about improved image quality compared with the standard used at Tygerberg Academic Hospital, a definite option for final assessment.

An ESD increase with increased mAs was also seen at 60 kV, as dose was directly proportional to mAs. An increase in mAs from 2 to 3.2 mAs achieved about 65% increase in ESD, however the ESD was still about 17% lower than that of the standard exposure. The ESD values at 60 kV were also higher than those obtained at 57 kV with the same mAs values. This was expected since an increase in kV influenced beam quality and quantity. Visually and quantitatively the images at 60 kV and 2 and 3.2 mAs with added filtration were comparable. The filtered 60 kV and 2 mAs image had an ESD of approximately 50% lower than the standard and was therefore considered in final evaluation. It is included in Figure 5.9 d.) on page 178.

The image obtained at 60 kV and 3.2 mAs with the added filtration had a visual image quality total score of 15. It was comparable to the standard processed image quantitatively and had an ESD reduction of approximately 17%. Since its visual score and ESD reduction were lower than that of the 57 kV and 3.2 mAs with added filtration image, the 57 kV image was deemed better. These images are included in Figure 5.9 c.) and d.), on page 178.

The results achieved by added filtration were better than those obtained with inherent filtration and changes in kV and mAs only. The total visual image quality scores with the change in kV and mAs at inherent filtration images were still higher than those of the standard processed image. Visually most of these images had a total score of 12. Quantitatively these images were comparable to each other and to the standard processed image, due to the image processing which created more uniform signals regardless of the exposure parameters used.

The lowest ESD achieved, using these exposures, was at 61 kV and 0.8 mAs, i.e. almost 41% less than in the standard exposure. Other combinations of kV and mAs did not give improved visual image quality, although ESD was increased. In the case of processed inherently filtered images the image was therefore better. The image was compared with the standard processed and the better filtered image in Figure 5.9 on pages 177 - 179.

All of the exposures in the fourth preliminary set were achieved with ESDs lower than that of the standard exposure. By applying the procedures used in this set of

exposures it was therefore not only possible to reduce ESD, but also to improve clinical image quality. These exposures were therefore considered for the final exposure set for processed images with 0.1 mm Cu + 1 mm Al added filtration at 57 kV and 2 and 3.2 mAs and 60 kV and 2 mAs. These images are shown in Figure 5.9 b.), c.) and d.) on pages 177 and 178. An exposure at 61 kV and 0.8 mAs with inherent filtration was also an option.

5.4.5 Final exposure set

The quantitative image quality results and the measured ESDs were recorded in Table 4.20.

If only ESDs were considered, the lowest ESD would be regarded as the best option since one of the aims of the current study was to decrease the ESD. This applied to image 6 with an ESD of 16.2 µGy. If the uncertainty in the ESD measurements, as determined in section 4.5 i.e. 5%, was taken into account, the dose was 16.2 ± 0.8 µGy. It was therefore significantly lower than any of the other ESDs. Images 2 and 8 were both ranked second, with an ESD of 19.10 ± 1.0 µGy. These images were obtained with the same exposure factors, which determined the delivered dose. Image 2 was raw and image 8 was processed. Image 3 was ranked third. The ESD for the image was 22.8 ± 1.1 µGy. These images were all obtained with 0.1 mm Cu + 1 mm Al additional filtration. The advantage of additional filtration was clear. It absorbed the low energy photons, which only contributed to radiation dose and not to image formation. These results showed that additional filtration seemed necessary for all neonatal chest x-ray exposures.

Image 7 was also had additional filtration, but at a higher mAs of 3.2 mAs compared to 2 mAs for the other filtered images. It resulted in an increased ESD of 26.3 ± 1.3 µGy for the image. The image was ranked fifth on ESD. Image 5 was also ranked fifth, with an ESD of 26.4 ± 1.3 µGy. The ESD difference between these images was not statistically significant. The images that were ranked fourth were images 4 and 9. These images were obtained with the same exposure factors. Image 9 was a processed version of the raw image 4 and therefore these images had the same

ESD of 25.8 ± 1.3 µGy. The worst image, based on ESD only, was the standard exposure image, Image 1. This image had an ESD of 44.0 ± 2.2 µGy, which was the highest dose obtained in the final exposure set.

These results proved that all of the exposures in the final exposure set were obtained at ESDs lower than that of the standard exposure (50 kV, 2 mAs, 100 cm FFD, fine focus, inherent filtration). All of these exposures therefore achieved the objective of the current study, i.e. to reduce the radiation dose per chest x-ray to a lower quantity, compared with standard procedure.

The ESD ranking of the images, from best to worst, was therefore image 6, 2 & 8, 3, 4 & 9 and 7 & 5. As the ESDs of these exposures were acceptable, it was necessary to evaluate the clinical acceptability of these images. The cancer induction risks for these exposures also had to be evaluated.

Images were evaluated on quantitative and visual quality and they were ranked accordingly. The quantitative image quality results are included in Table 4.20.

A higher value for the SNRs, SDNRs and CNR was indicative of a better image. Image 6 was considered the best image here and was ranked first. It had a SNR healthy lung of 43.6, SNR sick lung of 78.7, SDNR healthy lung of 23.2, SDNR sick lung of 2.5 and CNR of 32.6. The SNR healthy and sick lung in images 1 and 9 were similar to those of image 6. Images 1, 7, 8 and 9 had comparable SDNR healthy lung values. The SDNR sick lung in Images 5 and 8 were also similar to that of Image 6. Some of these values were slightly larger than those of Image 6. The CNR of Images 2, 3, 4 and 5 was larger than that of image 6. Image 6 was preferred above Images 1 and 9 based on its higher SDNR sick lung of 2.5 compared to 0.5 and 0.8 respectively.

Image 1 was ranked second. It was slightly better than Image 6 on SNR sick lung, 86.3, and comparable, on SNR and SDNR healthy lung and CNR. Only its SDNR sick lung was poorer than that of Image 6. Image 9 was placed third. It was poorer than image 1 in SNR sick lung. All the other results compared well with that of Image 1.

Image 7 was better on SDNR sick lung and CNR, while Image 8 was better on SNR healthy and sick lung. The SDNR healthy lung results for the two images were comparable. Based on SDNR sick lung, 3.0 for Image 7 and 2.1 for Image 8, Image 7 was ranked fourth and Image 8 was placed fifth. As signal differences between Agar gel mix and the simulated sick lung were not large, i.e. the sick lung was not clearly visible on the images of the phantom, this criterion was considered most important. A slight difference in image quality was therefore most likely to show in this ratio.

Image 4 had a SNR healthy lung comparable to that of Image 5. The SNR healthy lung of Image 3 was comparable to that of Image 2. The SDNR healthy lung of Image 4 was slightly lower than that of image 3, but higher than that of image 5. Image 2 had the lowest SDNR for healthy lung. The SDNR for sick lung in Image 4 was comparable to that of Image 5. These values for images 2 and 3 were lower than the values for Images 4 and 5 but similar to each other. The CNR for image 2 was the highest. The CNR of Image 5 was higher than Image 4 but lower than Image 3. The SNR sick lung was highest for Image 3, followed by Images 4 and 5, which had comparable results. The SNR sick lung for Image 2 was the lowest. Image 2 was better than Image 3 on CNR, comparable to Image 3 on SNR healthy lung and SDNR sick lung and worse than Image 3 on SNR sick lung. The results for Image 3 were overall better than those of Images 4 ad 5 and therefore Image 3 was ranked sixth.

Images 4 and 5 were better than image 2 on SNR sick lung and SDNR healthy and sick lung and worse on SNR healthy lung and CNR. Image 5 was better than Image 4 on CNR, 96.6 versus 78.4, and it also had a better SDNR sick lung. Image 5 was therefore ranked seventh and image 4 was placed eighth. Image 2 was quantitatively the poorest image. Although it had the highest CNR, it had the lowest results for SNR sick lung and SDNR healthy lung.

The overall quantitative image quality ranking, form best to worst, was therefore image 6, 1, 9, 7, 8, 3, 5, 4 and 2.

The visual image quality was assessed by independent medical physicists and radiographers. The results of the scoring by different observers are included in Table 4.21. The final exposure set of images are included in Figure 5.10, on pages 184 and 185. Enlarged copies of the images are included as Appendix C.

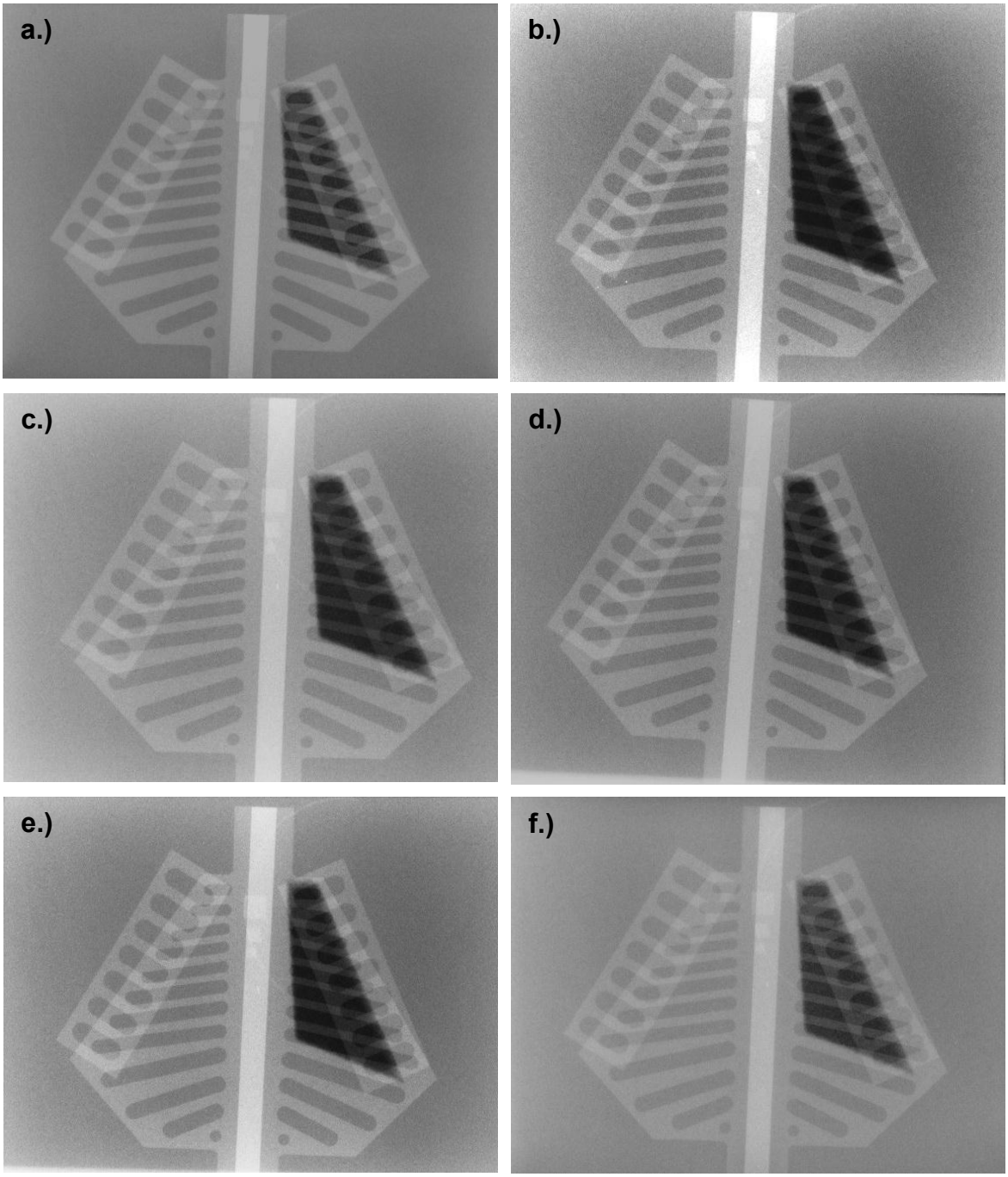

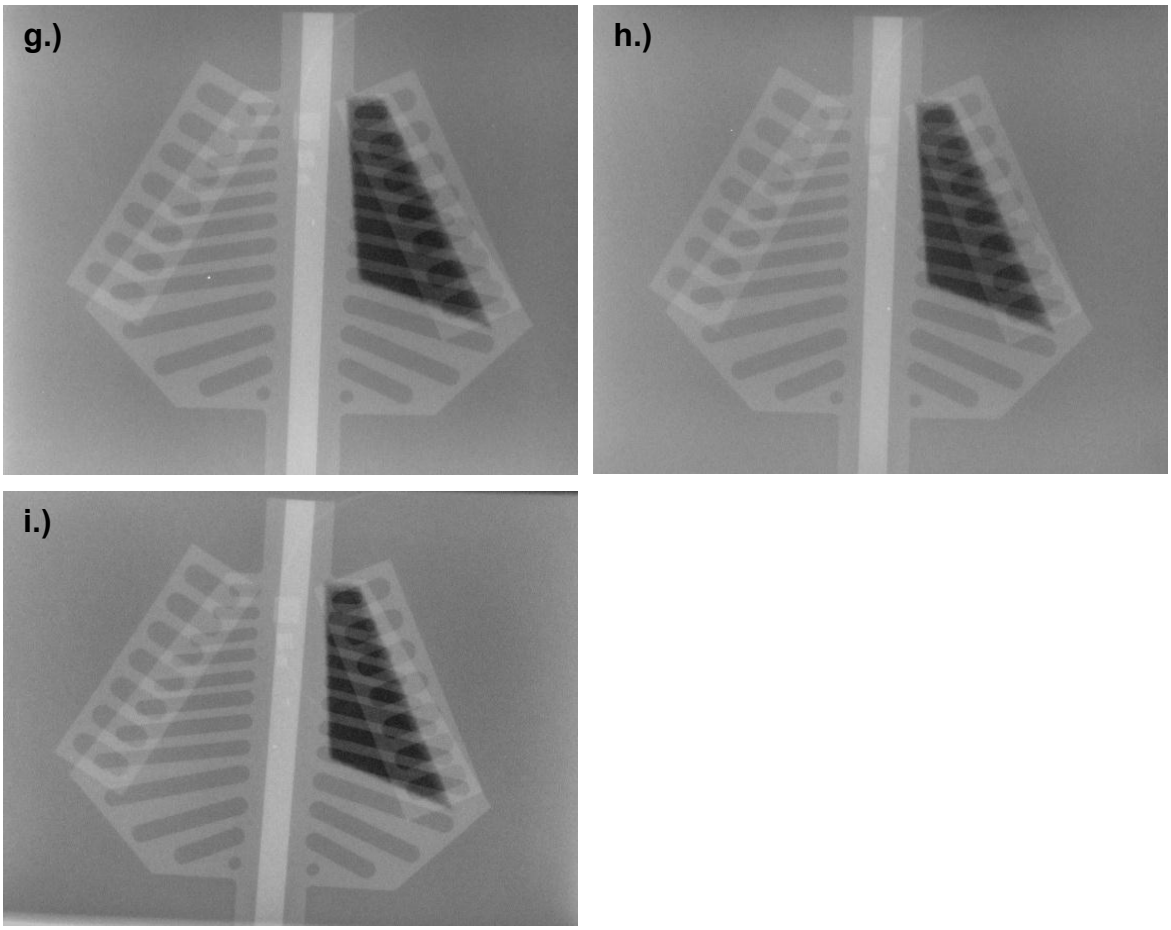

Figure 5.10: a.) Image 1, 50 kV, 2 mAs, inherent filtration, processed. b.) Image 2, 60 kV, 2 mAs, 0.1 mm Cu + 1 mm Al filtration, raw. c.) Image 3, 64 kV, 2 mAs, 0.1 mm Cu + 1 mm Al filtration, raw. d.) Image 4, 61 kV, 0.8 mAs, inherent filtration, raw. e.) Image 5, 62 kV, 0.8 mAs, inherent filtration, raw. f.) Image 6, 57 kV, 2 mAs, 0.1 mm Cu + 1 mm Al filtration, processed. g.) Image 7, 57 kV, 3.2 mAs, 0.1 mm Cu + 1 mm Al filtration, processed. h.) Image 8, 60 kV, 2 mAs, 0.1 mm Cu + 1 mm Al filtration, processed. i.) Image 9, 61 kV, 0.8 mAs, inherent filtration, processed.

Table 4.20 showed that all of these images were obtained at reduced radiation doses. To meet the aim of the current study of reducing radiation dose with maintenance of acceptable clinical image quality an average total image quality score of at least 11 was required, i.e. the score of Image 1. Image 1 was the standard exposure image obtained with 50 kV, 2 mAs, 100 cm FFD, small focus and inherent filtration, a process followed at Tygerberg Academic Hospital to image neonates.

The visual image quality of the neonatal chest simulation phantom was assessed by eleven independent observers, i.e. practising medical physicists and radiographers. The results are recorded in Table 4.21. The table shows that the total visual image quality scores, averaged over the 11 observers, ranged between 11 and 14 for the different images. The scoring criteria in Table 3.2 were used by the observers. The results of the scoring implied that the aim of the current study was indeed met in all of these exposures, i.e. the obtained image quality was maintained at a reduced radiation dose. Any one of these exposures was therefore acceptable for neonatal chest x-ray imaging. The final aspect to consider was the risk for cancer induction, an inherent part of this study.

Image 3, Figure 5.10 c.) on page 184, and Image 7, Figure 5.10 g.) on page 185, had the highest total averaged scores of 14. Image 3 was a raw image obtained at 64 kV, 2 mAs, 100 cm FFD, small focus with added 0.1 mm Cu + 1mm Al filtration. The total scores of most of the observers were comparable, ranging within ± 15% of the total average score, i.e. 13 - 16. Observers 2 and 11 scored the image slightly lower. Most observers saw all three of the sternal blocks. The central line was clear across the entire phantom for most of the observers. Observers 5 and 7 saw the medial outline of the sick lung. None of the observers could see the sick lung. For all of the observers the posterior ribs were visible behind the healthy lung. None of the observers saw the healthy lung as black lung. Based on the criteria the image was therefore definitely usable and an overall score of more than 2 was expected. Overall scores of 3 and 4, i.e. acceptable and good, were indicated. The highest total score of 16 was allocated by observer 7. These results indicated that the image was indeed an acceptable option visually for all of the observers.

Image 3 was obtained at an ESD of 22.8 µGy, which was about 48% less than that of the standard exposure. However, it was a raw image, which implied selection of UM Chest Paediatrics on the readout computer. The readout process defaulted to UNIQUE Chest Portable, i.e. processed images, and the extra step in the imaging process would have to be communicated to all staff that image neonates. It was also acquired with additional 0.1 mm Cu + 1 mm Al filtration. The filtration was not available as a standard feature on the mobile x-ray units currently used to image neonates. Plates of copper and aluminium could be fixed to the exit window, as was

done for the experimental acquisition of these images, but it was another extra step in the imaging process. As mentioned in Section 3.4 external filters which can be fitted onto these units and x-ray units with additional filtration incorporated on a selection dial, is available commercially. Exposures with these parameters were therefore possible, requiring extra effort from the imaging radiographers.

Figure 5.10 g.) on page 185 shows Image 7 which also had an averaged total score of 14. It was a processed image obtained at 57 kV, 3.2 mAs, 100 cm FFD, small focus and with 0.1 mm Cu + 1 mm Al additional filtration. Observers 7 and 9 allocated total scores of 17 for the image. Only observer 5 did not see all the sternal blocks clearly. The central line was totally visible for most of the observers. The medial outline for the sick lung was seen by observers 5, 7, 9 and 10. The posterior ribs were clearly visible behind the healthy lung for most of the observers. According to observers 4, 7, 8 and 9 the image was very good overall, with a score of 5 for this criterion. The exposure was made at an ESD of 26.3 µGy, about 40% less than the standard exposure dose. As it was a processed image, special intervention with readout was not needed. However it did need additional filtration.

For visual image quality ranking, Images 3 and 7 were compared. Image 7 was scored better than image 3 by more observers. Image 7 got 5 scores, which Image 3 did not. Image 7 scored 2 and 3 for central line visibility. According to these allocations Image 7 was ranked first and Image 3 second, although both had an average total score of 14. Both of these images were visually better than the standard exposure image. It did not only meet the aim of the current study, but advanced it by achieving reduced radiation dose and improved image quality at the same time. Image 7 was obtained at an ESD of 3.5 µGy more than image 3, but the improved visual image quality and the fact that it was a processed image justified the slight increase in ESD. The ESD of Image 7 was still significantly less than that of the standard exposure, or Image 1.

The next highest total score, averaged over the 11 observers, was 13. It was achieved by Images 2 and 5, Figures 5.10 b.) and e.) on page 184, and Image 8, Figure 5.10 h.) on page 185. Image 2 was a raw image acquired with 60 kV, 2 mAs, 100 cm FFD, small focus and additional filtration of 0.1 mm Cu + 1 mm Al. The

same factors were used to acquire image 8, a processed image. Image 5 was obtained with 62 kV, 0.8 mAs, 100 cm FFD, small focus and inherent filtration as a raw image.

In Image 2 all the observers were able to see all three of the sternal blocks. The central line was also completely visible, except for observers 9 and 11. The medial outline of the sick lung was seen by observers 5, 7 and 10. The posterior ribs behind the healthy lung were clearly visible only to observers 6, 7, 9 and 11. Black lung was not observed by any of the observers, but the score of 1 for healthy lung implied weaker overall scores. Observers 4 and 9 and observer 5 scored the image as poor and not good respectively. Observer 7 scored the image the highest, i.e. 16. The ESD for the image was 19.1 µGy, about 56% lower than that of the standard exposure image and its visual image quality was evaluated as higher than that of the standard exposure image. It was acquired as a raw image with additional filtration, so the additional commitments from the imaging radiographers, as described above for such acquisitions, were again needed.

In the case of Image 5, the three sternal blocks were not clear to all observers. The visibility of the central line was also slightly poorer than in Image 2, since four observers could not see them across the spinal column. Observers 5, 7 and 10 did see the medial outline of the sick lung, as in Image 2. In this image the posterior ribs were clearer behind the healthy lung than in Image 2. Overall the image was acceptable or good, except for observers 4 and 9 who scored it as not good. Image 2 had poor scores overall and was scored lower than Image 5. The ESD of image 5 was 26.4 µGy, about 40% lower than that of the standard exposure. The image was also a raw image, with the additional requirement of selecting UM Chest Paediatrics on readout, but it was obtained with inherent filtration and therefore did not require the addition of filtration plates or a commercial filtration system. Image 2 was ranked better than image 5, i.e. third versus fourth, for overall visual image quality.

Image 8 was poorer than images 2 and 5, although it also had a total score of 13. Most of the observers could see all three sternal blocks clearly in this image. The central line was less visible in the image. A score of 1 was given by observers 2, 3 and 6, while observers 9 and 11 scored it as 2. The rest of the observers saw the

entire central line clearly. The medial outline of the sick lung was seen by only two observers. Healthy lung scores were good, with the posterior ribs either clearly or partially visible behind the healthy lung. Overall the image was poor according to observer 6 and observers 1 and 10 decided that the image was not good. The ESD for Image 8 was also 19.1 µGy, the same as for Image 2, as these images were obtained within the same parameters. Image 8 was processed and Image 2 raw. It could be derived from the results that the raw image was preferred. Image 8 was ranked fifth. Image 8 was also obtained with additional filtration, so although the readout process was the same as the radiographers were used to, additional filtration plates or a filtration system or a new mobile x-ray unit with available additional filtration was needed. None of the observers gave Images 2, 5 and 8 an overall score of 5, which showed that these images were visually poorer than Image 7.

Image 6, Figure 5.10 f.) on page 184, and image 4, shown in Figure 5.10 d.) on page 184, had the same averaged total score of 12. Image 6 was ranked sixth and Image 4 was ranked seventh on visual image quality. The sternum visibility of Image 6 was better than that of Image 4. With image 6 all three the sternal blocks were clearly visible to eight of the observers. In Image 4 three sternal blocks were clearly visible to six observers. The central line scored 2 and 3 for all the observers in Image 6, except for observer 1 who saw it towards the healthy lung only. It was also the case with Image 4, where observer 2 did not see it at all. The sick lung's medial outline was seen by observer 5 in Image 4 and by observer 7 in Image 6. The healthy lung in Image 4 was scored 1, i.e. the posterior ribs were not clear, as decided by observer 3. Image 6 had five scores of 3 and six scores of 2 for healthy lung. Three observers decided that Image 4 was not good, seven considered it acceptable and observer 5 stated it was good. Observer 6 scored Image 6 as poor. Four observers scored it as not good, two as acceptable and four as good. The lowest total score for image 6 was from observer 11, i.e. 7, and the highest scores were 15, by observers 4 and 8. A total score of 7 was also the lowest score for image 4 by observer 3, while observer 2 scored it as 8 in total. The best score for the image was 14 by observers 7 and 10. Image 4 was therefore visually poorer than Image 6.

Image 4 was acquired with 61 kV, 0.8 mAs, 100 cm FFD, small focus and inherent filtration. It was a raw image with an ESD of 25.8 µGy, about 41% less than the standard exposure. Image 6 was acquired with 57 kV, 2 mAs, 100 cm FFD, small focus and 0.1 mm Cu + 1 mm Al additional filtration at the lowest ESD of 16.2 µGy, which was about 63% less than that of Image 1, the standard exposure image. Image 6 was better than Image 4, based on ESD and visual image quality, although both images had total average visual image quality scores of 12. Analysis of Image 6 showed that its visual image quality was better than that of Image 4, and it was obtained at 9.6 µGy less. Image 4 was raw and image 6 processed, therefore it was easier to obtain Image 6, from a readout perspective. However, Image 6 was obtained by means of additional filtration and Image 4 with inherent filtration, therefore additional effort was needed to acquire Image 6. For both of these images the overall averaged visual image quality was still better than that of the standard exposure image.

The standard exposure image, Image 1, in Figure 5.10 a.) on page 184, and Image 9, in Figure 5.10 i.) on page 185, had the same averaged overall visual image quality scores of 11. It implied that even Image 9, which was ranked ninth, was still acceptable in terms of the aim of the current study, i.e. it had a reduced ESD of 41% less than that of the standard exposure, at an image quality that was visually comparable to that of the standard exposure image, i.e. an acceptable clinical image quality. Image 1 was a processed image obtained at 50 kV, 2 mAs, 100 cm FFD, small focus with inherent filtration. Image 9 was also a processed image acquired with 61 kV, 0.8 mAs, 100 cm FFD, small focus and inherent filtration. Both of these images were obtained without any additional intervention in the acquisition and readout processes and did not require additional staff training or extra cost. Image 1 was ranked eighth.

Image 9 was scored better on sternum visibility than Image 1. Six observers saw the three blocks clearly. In Image 1 only five observers saw all the blocks clearly. More observers saw the central line with scores of 3 and 2 in Image 9 than did in Image 1. The medial outline of the sick lung was seen by observers 5 and 7 in Images 1 and 9. Based on this criterion the images were therefore comparable. Image 1 obtained the highest score of 3 for healthy lung by all the observers. Most of the observers

scored Image 9 as 2. Here Image 1 was again better than Image 9. For the overall score Image 1 received a score of very good from observer 3 and a score of good from observers 1, 5 and 8. The highest overall score achieved by Image 9 was 3, i.e. acceptable. Only images 1 and 7 reached overall scores of 5 from some observers.

The visual image ranking, based on the scores by the eleven independent observers, was therefore, from best to worst, image 7, 3, 2, 5, 8, 6, 4, 1 and 9.

Differences in scoring among the observers were evaluated. The results showed that observer 7 allocated the highest scores to six of the nine images. The total scores for observer 7 were also higher than the total score averaged over all the observers, except for images 6 and 9. The lowest scores for the sternum were most often allocated by observer 5. None of the other observers allocated such low scores to the sternum criterion. The central line was not seen by observers 2, 11 and 7 in certain images. The black lung criterion, i.e. posterior ribs were not visible behind the healthy lung, was seen by observer 7 in Image 9 only. The medial outline of the sick lung was seen by observers 5 and 7 in every case. Observer 7 generally gave higher scores in other criteria. These variations could be attributed to differences in viewing conditions and eyesight. Such differences were also possible in radiology at Tygerberg Academic Hospital, implying that images that were better for some radiologists could be seen by others as poorer.

Observer differences will exist, it is impossible to find an image that would appeal to all observers similarly, so the image that was acceptable to most observers had to be sought. Image 7, which was ranked first visually, was such an image. It had a minimum and maximum total score by all observers of 12 and 17 respectively. It was seen as the same as, or better than, the standard exposure image, i.e. none of the observers scored it lower than the standard exposure image.

The overall averaged visual image quality results showed that images obtained by means of additional filtration of 0.1 mm Cu + 1 mm Al were generally ranked better than those obtained with inherent filtration. The images ranked first, second, third, fifth and sixth were obtained with the additional filtration. Ranks 7, 8 and 9 were for

inherent filtration acquisitions. Only image 5, obtained with inherent filtration, was ranked fourth. Greater ESD reductions were found in the case of additional filtration, except for image 7, ranked first visually, which had an ESD reduction comparable to that obtained with the inherent filtration acquisitions. In producing this image a higher level of improvement in visual image quality was achieved, compared with the standard exposure, and this could be considered a success of this study. The results showed that the effect of the added filtration contributed to a substantial reduction in dose while not reducing image quality.

The complete sick lung was not visible in any of the images, due to the similarity in density between Gammex solid water and Agar gel mix. The grey scale values of these structures were therefore much the same. It explained the small differences in ROI signals in these areas and the associated small SDNR sick lung values under quantitative analysis. Small changes in image quality were therefore most pronounced with this criterion. It was confirmed with image 7, the best image visually, in which case four observers saw the medial outline of the sick lung. In the case of Image 2, which was ranked third visually, three observers allocated a score of 1 to the sick lung criterion.

Quantitative image quality was compared for the two phantoms in Table 4.22. Overall, the quantitative image quality ranking for the two phantoms was acceptably comparable, i.e. images that were considered to be better quantitatively in respect of the neonatal chest simulation phantom and had the same rating as the physics image quality assessment phantom.

Image 1, obtained with the standard exposure factors, was quantitatively the better image and ranked first and second for the neonatal chest simulation and physics image quality assessment phantoms respectively. In Image 3 both phantoms were ranked sixth. Image 4 was overall the poorest image quantitatively, with eighth and ninth position for the neonatal chest simulation and physics image quality assessment phantoms respectively. It was preceded by Image 5, which again had comparable results in position seventh, for the neonatal chest simulation phantom, and eighth, for the physics image quality assessment phantom. A comparable result was also shown in Image 8, ranking fifth and fourth respectively for the neonatal

chest simulation phantom and the physics image quality assessment phantom. For Image 9 the ranking results for the two phantoms were the same, i.e. third place. Image 2 had the worst quantitative image quality for the neonatal chest simulation phantom and was ranked seventh for the physics image quality assessment phantom. Although these results were not as close as those of the images discussed previously, it was, overall, still not a good image quantitatively. This was also seen in the case of Image 7, which was ranked fourth in the case of the neonatal chest simulation phantom and second for the physics image quality assessment phantom. The biggest difference in ranking between these phantoms was in respect of Image 6. The best quantitative image quality ranking for the neonatal chest simulation phantom was achieved in respect of Image 6, but the image was ranked fifth within the case of the physics image quality assessment phantom.

Overall the quantitative image quality rankings of the neonatal chest simulation and physics image quality assessment phantoms were therefore comparable. Comparable results in two different phantoms highlighted that the obtained image quality, with the final exposure set, was indeed clinically acceptable therefore in line with the aim of the current study. To achieve the aim of the current study fully, cancer induction risks now had to be considered.

Table 5.1 shows all of the rankings, for the physics image quality assessment phantom and the neonatal chest simulation phantom, discussed in the preceding sections.

Table 5.1: Overall rankings for the images of the final exposure set for different criteria.

Physics image quality assessment phantom										
Rank		**1**	**2**	**3**	**4**	**5**	**6**	**7**	**8**	**9**
Criteria	MTF from wires and Equation 3.2	4	5	3	2	6	1	7	8	9
	MTF from copper plate ESF	4	3	5	2	6	7	8	1	9
	Quantitative image quality	1	7	9	8	6	3	2	5	4
Neonatal chest simulation phantom										
	ESD, visual and quantitative image quality	6	7	3	8	2	5	9	1	4
	ESD and visual image quality	3	2	7	6	8	5	4	9	1
	ESD	6	2 & 8	3	4 & 9	7 & 5				
	Quantitative image quality	6	1	9	7	8	3	5	4	2
	Visual image quality	7	3	2	5	8	6	4	1	9

5.5 Uncertainties in dose measurements

Uncertainty in measuring absolute doses, i.e. ESDs, included random and systematic uncertainties as explained in Section 3.5. The random uncertainties were classified type as type A and can be determined by repeated measurements. The sources of the random uncertainties included uncertainty in the positioning of the phantom and detector, i.e. experimental errors, the response of the detector, i.e. instrumental measurement errors, and the stability, reproducibility and linearity of the x-ray tube. By performing the measurements repeatedly, as shown in Table 4.23, all of these sources of random error were taken into account. An estimation of random error in the measurements was 0.5%. Table 4.23 clearly shows that there were no outlying results. Systematic uncertainty was included in the measurements due to the uncertainty in the calibration factor of the detector. This was estimated as 5%, provided by information on the calibration certificate of the detector.

The random and systematic uncertainties were combined using Equation 3.4 and the total uncertainty was 5%. The random uncertainties measured much lower than the value of the systematic uncertainty. The effect of the former was thus negligible.

5.6 Cancer induction risk calculation

Exposure of a neonate to x-ray radiation could increase the risk of cancer, such as leukaemia[3], developing in the young child. The risk is stochastic in nature, i.e. no threshold dose exists below which cancer induction cannot occur. Therefore any dose of radiation, regardless of how small, has a chance of inducing cancer in the child. As neonates have a relatively longer life expectancy and higher sensitivity to radiation, these radiation risks should be minimised, i.e. the ALARA principle should be upheld.

The risk for cancer induction is calculated as the product of the effective dose and the ICRP published risk factors for the irradiation of children and foetuses. Risks for cancer induction are expected to be higher for babies than for adults, due to their increased radiosensitivity and longer life expectancy.[2] These factors are representative of the average population, and as radiosensitivity varied among individuals, the factors were over- and underestimations for certain individuals.[19] The risk factors for foetal irradiation assumed whole body exposure to radiation[15], and with neonatal chest AP x-ray imaging, this was not the case. The risks for cancer induction in the child based on these factors were therefore overestimations. Calculated cancer induction risks represented the risk up to the age of 15 years, but the life time risk could be two to four times higher, according to Chapple et al[32]. It was therefore clear that these risks could not be ignored and that every effort had to be made to decrease the risk for cancer induction, as mentioned in literature[3,31,32] The current study also aims to achieve this.

Huda[2] and Roebuck[19] suggested that effective dose should be used to estimate the cancer induction risk.[2,19] The effective dose can be calculated with Equation 2.1, as suggested by Roebuck[19], using published tissue weighting factors[14]. It can also be derived from the measured ESD using conversion coefficients published by the NRPB in report R262[52].

NRPB conversion coefficients[52] are based on ICRP Publication 60, considering adult tissue weighting factors only. ICRP Publication 103 has tissue weighting factors representative of the average population, taking different ages and gender into

account. More accurate and neonatal appropriate risks can be calculated if conversion coefficients based on ICRP Publication 103 are used. It is available in the PCXMC computer program[55] which costs in the region of R 7 500 and could not be purchased for the current study. The aim of this dissertation was to investigate whether cancer induction risk reduction was achievable and therefore, although the calculated risks are based on adult data using the NRPB conversion coefficients, trends in risk increases or reductions were still observed.

Applying the above mentioned method the results for 9 images were recorded in Table 4.24 where it was shown that the risk for cancer induction, for an average of 15 chest AP x-rays, was 1.8 - 8.3 and 6.4 - 9.6 per million for Image 1, with foetal and child ICRP risk factors respectively. Image 1 was the standard exposure, i.e. 50 kV, 2 mAs, 100 cm FFD, small focus and inherent filtration that was routinely used to image neonates at Tygerberg Academic Hospital. The aim was therefore to obtain an exposure with a risk lower than that of Image 1.

It was found that the risks for Images 3 and 7 were comparable to that of Image 1, as shown in Table 4.24, although these images were obtained at ESDs of about 48% and 40% lower than that of Image 1 respectively. The results in Table 4.24 were calculated with the available conversion coefficients in the NRPB tables, i.e. the coefficient for 2 mm Al filtration was used for inherent filtration of 1.5 mm Al and that of 5 mm Al was used for additional filtration, which was equivalent to 6 mm Al. The coefficient for 1.5 mm Al filtration was expected to be lower than the one at 2 mm Al filtration, therefore the risk with such an exposure was also expected to be lower. An estimation, based on extrapolation of data, would be about 1.6 - 7.6 and 5.8 - 8.7 per million of the population for foetal and child risk factors for Image 1 for 15 chest AP x-rays. Similarly, the coefficient for 6 mm Al filtration was anticipated to be larger than that of 5 mm Al filtration, which would result in a higher risk for images 3 and 7. It was probably 1.8 - 8.2 and 6.3 - 9.4 per million for image 3 and 1.9 - 8.7 and 6.7 - 10.0 per million for Image 7 for foetal and child risk factors respectively, again based on extrapolation of the conversion coefficients. These were estimations only.

It meant that the risks calculated for Images 3 and 7 could potentially be higher than that of Image 1. Since it was the aim of the current study to reduce the risk for

cancer induction, these exposures, for Images 3 and 7, were therefore not acceptable, confirming that ESD and image quality analysis alone were not the only aspects to be considered. A 40 - 48% reduction in ESD with an associated improvement in visual image quality from the standard exposure resulted in a higher risk for cancer developing in the young child, contradictory to what was expected. It was expected that such a dramatic ESD reduction would imply a lower cancer induction risk, but the conversion coefficients were kV and filtration dependent, and were larger at higher kV and filtration values, which resulted in larger effective doses. Therefore cancer induction risk analysis was of utmost importance.

The image that was ranked second overall in Table 4.12, Image 2, had a lower risk for cancer induction than Image 1. The risk with foetal risk factors was 1.4 - 6.3 per million and with child risk factors it was 4.9 - 7.3 per million for 15 chest AP x-rays. The visual image quality for the image was ranked third and the ESD ranking was second in Table 4.12, but the acquisition again posed raw image and additional filtration challenges. However, these challenges could be overcome, and the cancer induction risk reduction from the standard made the exposure an option for recommendation.

Table 4.12 shows that Image 6 was ranked fourth overall. This image had a significant risk reduction compared with Image 1, as shown in Table 4.24. The risk was also lower than that of Image 2. The risk for cancer induction for Image 6 was 0.7 - 3.3 per million and 2.5 - 3.8 per million, as calculated with foetal and child ICRP risk factors, lower than that of Image 1. Visually the image was ranked sixth, although the visual image quality was still slightly higher than that of Image 1, and it was obtained at the lowest ESD. It was a processed image, and obtaining extra filtration remained a problem. Due to the larger risk reduction and processed readout method, Image 6 was deemed better than Image 2 and was an option for recommendation.

Image 8 was ranked fifth overall in Table 4.12. Visual image quality was ranked fifth and ESD second. The cancer induction risk indicated in this exposure was the same as that of Image 2. The visual image quality of Image 2 was ranked higher than that of Image 8, although the total visual image quality score of Images 2 and 8 was 13, it

was still lower than that of Image 1. Image 8 was a processed image, therefore readout intervention was not required, but it also needed additional filtration. Image 8 was considered to be better than Image 2, as a result of this, but poorer than Image 6, which had a greater risk reduction.

In Table 4.12 Image 5 was ranked sixth overall, with a fourth position for visual image quality, a total visual image quality score of 13, and a fifth position for dose. The cancer induction risk suggested in the image was slightly higher than that of Image 6 and somewhat lower than that of Images 2 and 8, as Table 4.24 shows. Image 5 was acquired as a raw image with inherent filtration. No additional filtration was needed, as for Images 2 and 8, but raw readout intervention was required. Image 5 was considered better than Images 2 and 8. These three images had the same visual image quality score, but the cancer induction risk shown in Image 5 was slightly lower and did not require additional filtration.

The image that was ranked seventh overall in Table 4.12 was Image 4. Image 9 was ranked eighth overall. Image 4 was a raw version of Image 9, therefore these images had the same cancer induction risk of 1.3 - 5.9 per million for foetal risk factors and 4.6 - 6.8 per million for child risk factors. The risk was comparable to that of Image 5, and lower than that of Image 1, as Table 4.24 shows. These images were acquired with inherent filtration. The visual image quality of Image 4 was lower than that of Image 5, i.e. it was ranked seventh visually with a total score of 12, but it was higher than that of Image 9, which was ranked ninth visually. The visual image quality total score of Image 9 was still comparable to that of Image 1. Image 9 was now deemed better than Image 4, although its image quality was slightly lower, as it did not require any readout or additional filtration intervention. Image 9, overall ranked eighth in Table 4.12, was obtained at an ESD of about 41% less than the standard exposure. It had an acceptable clinical image quality and was comparable to the standard exposure routinely used and showed a cancer induction risk lower than standard exposure.

None of the risks were higher than that of the standard exposure in Table 4.24, being either comparable or lower. However, it was important to remember that these risks were calculated with 2 mm and 5 mm Al equivalent filtration conversion coefficients

and that 1.5 mm and 6 mm Al equivalent filtration were actually used. The risks for inherent exposures were expected to be lower than those in Table 4.24 and those for the additional exposure images were expected to be higher than those shown in Table 4.24. Except for Images 3 and 7, the risks in Table 4.24 were substantially reduced from that of Image 1. The other exposures in the final exposure set were therefore considered possible options for recommendation to the diagnostic radiology department at Tygerberg Academic Hospital.

It was decided that the best option for recommendation was Image 6. Images 5, 8, 2, 9 and 4 were also options. Image 1 was the standard and the aim was to improve on the exposure. Images 3 and 7 were not considered feasible options, due to the possibility of increasing cancer induction risk to above the standard exposure.

The obtained results were compared with literature. The derived optimised exposures were acquired with 57 - 62 kV, 0.8 - 2 mAs, 100 cm FFD, small focus with or without 0.1 mm Cu + 1 mm Al additional filtration. Additional filtration, kV ranges around 60 kV and a FFD of between 80 and 150 cm were recommended in literature.[14,21,28,29,30,31] The acquisition protocols of the proposed optimised exposures were therefore well in agreement with these researchers. The measured ESDs were 16.2 - 26.4 µGy with a 0.5% uncertainty. The measured doses in the current study were much smaller than those reported by most researchers.[14,15,21,28,30] The results from the current study agreed to a great extent with that of Armpilia et al[31], 18 - 58 µGy, and Makri et al[3], who reported ESDs of 44 ± 16 µGy.

These ESD values were used to obtain effective doses, which ranged between 8 - 40 µSv per chest x-ray as calculated by means of the Child Dose program.[14,15,30] For the derived optimised exposures the effective doses were about 3 µSv. The lower effective dose was expected due to the NRPB conversion coefficients that were based on adult and not on neonatal data, but these were not available for 1.5 mm and 6 mm Al filtration. The effective doses for neonates were expected to be higher than those for adults, due to relatively longer life expectancy, higher radiosensitivity and smaller body size, and higher in the case of increased Al filtration. For the current study the minimum to maximum risk per million of the population per x-ray was 0.1 - 0.5. The risks mentioned in literature were generally higher.[3,14,15,30,31,32]

Monte Carlo simulations and the Child Dose program were used by these researchers, while NRPB conversion coefficients were used in the current study.

5.7 Strengths and limitations of the project

The first aim of this thesis was to design and construct a neonatal chest simulation phantom. The constructed phantom proved to be a reasonable and practical anatomical representation of a real neonatal chest. Radiologically it was a highly acceptable approximation, mimicking real-tissue density, elemental composition and attenuation, absorption and scattering characteristics. The phantom allowed for experimentation and provided the opportunity to collect and analyse data, to reach conclusions and make recommendations and it was an improvement on the phantoms suggested in literature, as summarised in Section 2.4. The design of the phantom was based on medical physics principles, where attenuation, absorption and scatter coefficients were calculated and evaluated. A muscle equivalent substitute material was developed as Agar gel mix.

However, the phantom did have limitations. The vertebral column was assumed solid. A possible improvement would be the inclusion of a spinal cord, by drilling a hole through the solid column structure and filling it with Agar gel mix. Vertebrae could also be simulated by separate cuboids, and not by a solid column structure. Machining limitations were restrictive in the construction of the neonatal chest simulation phantom. If more intricate structure machining was available, an improvement would be more rounded structures and edges, making the phantom less rigid. The sick lung simulated a completely collapsed lung in the neonatal chest simulation phantom, but in reality there are often still aerated areas in sick lungs. It could be simulated by the introduction of aerated pockets in the sick lung. The thickness of real lungs also varied over the area of the lungs. More angled cuttings could be made on the simulation lungs to account for this to a greater extent. For improved visual image quality analysis, more catheters and tubes could be included in the phantom.

All the exposures were performed on the neonatal chest simulation phantom, and although the phantom simulated a real neonatal chest anatomically and radiologically, the obtained recommendations and conclusions were not implemented on real neonatal patients. Exposure of real neonates, according to the proposed protocols, and obtaining similar results would be a definitive test to prove the equivalence of the phantom to a real neonatal chest, and verify the results of the current study.

The simultaneous evaluation of radiation dose and visual and quantitative image quality was also a strength of the study. In many cases published in literature either dose or image quality was assessed separately. The method of evaluation in this thesis implied that the recommended exposures resulted in a proven dose reduction, with associated maintenance or improvement of image quality. The fact that certain exposures achieved a substantial improvement in the image quality compared with standard practice at Tygerberg Academic Hospital as was one of the strengths of this research.

The current study also considered cancer induction risks calculations. After an ESD reduction was established, with maintenance or improvement of image quality, it was necessary to evaluate the risk of inducing cancer in the young child. It was possible that an exposure with ESD reduction could result in an increased risk for cancer induction, and this had to be avoided. In the current study the importance of such evaluation was proved when it was established that the image that was ranked the best with regard to ESD reduction and overall total visual image quality could potentially have a higher risk for cancer induction.

The study used NRPB Report R262 conversion coefficients to convert from measured ESD to effective dose. These coefficients were based on ICRP 60 tissue weighting factors, which applied to adults only. Neonates were more sensitive to radiation, experienced rapid cell division, had a small body size, which meant that organs at risk could be included in the primary x-ray beam, and had a relatively longer life expectancy than adults. These coefficients underestimated the effective dose for neonates. A possible solution was the Child Dose or PCXMC computer based programs for calculating effective doses from ESDs, as these programs used

ICRP 103 tissue weighting factors, which were averaged over the entire population and were therefore representative of adults and children and of different gender. These programs also used neonatal or baby simulation phantoms for the calculations, and provided more appropriate and neonate specific results.

Chapter 6

Conclusions and recommendations

Only chest AP x-rays on neonatal patients were considered in the current study. These investigations were done in order to assist in the diagnosis and follow-up treatment of neonates, especially when the condition of the heart and/or lungs had to be examined radiologically. As the cancer induction risk analysis of the current study showed, these exposures had a chance of inducing cancer in the young child. The risk did not have a threshold dose, which meant that there was a risk for cancer developing in the child exposed to radiation as neonate.

Neonates have a relatively long life expectancy, undergo rapid cell division and growth and are more sensitive to radiation. Because of the small physical size of these patients the risk exists that organs in close proximity to the chest are included in the x-ray field. Numerous x-rays are also taken of these babies, for the duration of their stay in hospital. It is therefore clear that all exposures of these patients to x-rays have to be justified and be in accordance with the ALARA principle. Optimisation of the exposure protocols used to image neonates can achieve this and it was accomplished in the current study.

This dissertation had two aims. The first was to develop a neonatal chest simulation phantom that simulated a real neonatal chest anatomically and radiologically. The phantom presented in the current study was based on medical physics principles and neonatal cadaver anatomy for radiological and anatomical equivalence. Although limited by machining capabilities, the constructed phantom was superior to those presented in literature. It was comparable to the Gammex RMI© 610 anthropomorphic phantom. The Gammex RMI© 610 phantom had more rounded edges, segmented vertebrae, curved ribs and a better presentation of a mediastinum, but the radiological equivalence of the phantom could not be

established. In this regard, the presented neonatal chest simulation phantom was an improvement on the commercially available phantom.

The second aim was to develop new exposure protocols that would be more efficient than the standard used routinely in Tygerberg Academic Hospital. The new protocols had to achieve a lower ESD, while the clinical image quality had to remain at least the same as that of the standard exposure. The risk for cancer induction of these new protocols also had to be lower than the standard exposure. The current study showed that it was possible to obtain exposures at lower ESDs but with increased cancer induction risks, which defeated the aim of this thesis. It was therefore of utmost importance that ESD, visual image quality and cancer induction risks had to be considered in conjunction with one another. Since this aim was achieved in the current study the following recommendations could be made to the diagnostic radiology department at Tygerberg Academic Hospital.

For chest AP x-rays on neonatal patients the current study found six possible exposures that decreased the ESD, maintained or improved the visual image quality and resulted in a reduced cancer induction risk compared to the standard exposure that was currently used. From the final set of exposures these were:

a.) Image 6 acquired with 57 kV, 2.0 mAs, 100 cm FFD, small focus, 1 mm Al + 0.1 mm Cu additional filtration and processed readout.
b.) Image 5 acquired with62 kV, 0.8 mAs, 100 cm FFD, small focus, inherent filtration and raw readout.
c.) Image 8 acquired with 60 kV, 2.0 mAs, 100 cm FFD, small focus, 1 mm Al + 0.1 mm Cu additional filtration and processed readout.
d.) Image 2 acquired with 60 kV, 2.0 mAs, 100 cm FFD, small focus, 1 mm Al + 0.1 mm Cu additional filtration and raw readout.
e.) Image 9 acquired with 61kV, 0.8 mAs, 100 cm FFD, small focus, inherent filtration and processed readout.
f.) Image 4 acquired with 61 kV, 0.8 mAs, 100 cm FFD, small focus, inherent filtration and raw readout.

Additional filtration was not available on the mobile x-ray units used for imaging neonates. As discussed, it could be overcome by using copper and aluminium plates fitted to the exit window of the unit, or by purchasing a commercially available PMMA filter that can be fitted to the x-ray unit, or by motivating management to purchase a commercially available x-ray unit with additional filtration on a selection dial. In order to obtain raw images a selection had to be made on the readout computer. Staff therefore needed new information on, and training in, these new protocols. In the case of Image 9 this was not necessary, as the image was acquired with filtration and readout as routinely used. It only had kV and mAs changes, which were easy to set on the mobile unit.

These problems could be overcome, especially if the advantages of these proposed exposures were considered. Dose and cancer induction risk reductions were successfully achieved and therefore recommended. The visual image quality of Image 9 was maintained, compared to the standard exposure, and that of Images 6, 5, 8, 2 and 4 was improved. By producing these images and by enhancing visual image quality in certain cases, as compared to standard use, the aim of the study was achieved.

Recommendations on how to change the current standard exposure protocols for x-ray imaging of neonates were based on a phantom that was an anatomical and radiological simulation of a real neonatal chest, sound medical physics principles and thorough experimental work. Based on these recommendations the Diagnostic Radiology Department at Tygerberg Academic Hospital could consider any of the options mentioned above for the imaging of neonatal chests, depending on availability of funds for filtration, staff willingness for raw-image readout training and radiologists' acceptance of looking at images that were slightly different to what they were used to. To achieve this, educational sessions could be arranged to inform staff of the results of this dissertation and of the importance of the ALARA principle.

Neonatal sensitivity to radiation is proved in literature, as is the stochastic nature of cancer induction in the young child due to exposures to radiation as a neonate. As seen in studies available in literature, radiation dose reduction, image quality and cancer induction risk analysis were generally not investigated in conjunction with one

another. Dose and image quality were examined, but without considering the implications of cancer induction, which the current study clearly proved to be essential for realistic results. Dose and image quality analysis alone was not enough since it was shown in this study that it is possible to decrease the delivered dose and improve the image quality, but at a higher risk for cancer induction.

Implementation of the derived optimised protocols in practice would confirm the obtained results for neonatal chest AP x-rays clinically. Such clinical proof would warrant similar studies on other types of x-ray investigations on neonates, but it should also be extended to all x-ray imaging of all patients. The ALARA principle should be the foundation for x-ray imaging in a diagnostic radiology department. By applying the recommended exposure protocols, this foundation would be reaffirmed by reducing the danger of cancer induction as far as possible during repeated chest AP x-rays of neonates under medical care.

Bibliography

1. Bushberg, J.T., Seibert, J.A., Leidholdt, E.M. & Boone, J.M., 2002. *The essential physics of medical imaging*. 2nd ed. Philadelphia: Lippincott Williams &Wilkens.
2. Huda, W., 2004. Assessment of the problem: pediatric doses in screen-film and digital radiography. *Pediatric Radiology*, 34(3), p.173-182.
3. Makri, T. et al., 2006. Radiation risk assessment in neonatal radiographic examinations of the chest and abdomen: a clinical and Monte Carlo dosimetry study. *Physics in Medicine and Biology*, 51, p.5023-5033.
4. Dougeni, E.D. et al., 2007. Dose and image quality optimization in neonatal radiography.*TheBrittish Journal of Radiology*, 80, p.807-815.
5. McParland, B.J. et al., 1996. Radiology in the neonatal intensive care unit: dose reduction and image quality. *The British Journal of Radiology*, 69, p.929-937.
6. White, D.R., Widdowson, E.M., Woodard, H.Q. & Dickerson, J.W.T., 1991. The composition of body tissues.*The British Journal of Radiology*, 64, p.149-159.
7. Gray, H., 2004. *The anatomy of full term neonate*.In H. Gray.Gray's anatomy.[e-book]. 39thed.Elsevier: Churchill Livingstone. Available at: http://e-medicaltextbook.blogspot.com/2008/08/anatomy-of-neonates.html [accessed 24 January 2012]
8. Odita, J.C., Okolo, A.A. &Omene, J.A., 1985. Sternal ossification in normal newborn infants.*Pediatric Radiology*, 15, p.165-167.
9. Arthur, R., 2001. The neonatal chest x-ray.*Paediatric Respiratory Reviews*, 2, p.311-323.
10. Sophomore pediatric chest. [online]. Available at: http://www.indyrad.iupui.edu/rtf/teaching/medstudents/pedcest.htm [accessed 25 June 2012]

11. Smans, K. et al., 2010. Cu filtration for dose reduction in neonatal chest imaging.*Radiation Protection Dosimetry*, 139(1-3), p.281-286.
12. Ono, K. et al., 2003. Neonatal doses from x-ray examinations by birth weight in a neonatal intensive care unit. *Radiation Protection Dosimetry*, 103(2), p.155-162.
13. Gutteling, J.W.A., Oetomo, S.B. &Wijn, P.F.F., 2009. Trends in dosimetry at the neonatal intensive care unit.*IFMBE Proceedings*, 25(3), p.333-335.
14. Brindhaban, A. &Eze, C.U., 2006. Estimation of radiation dose during diagnostic x-ray examinations of newborn babies and 1-year-old infants.*Medical Principles and Practice*, 15, p.260-265.
15. Brindhaban, A. & Al-Khalifah, K., 2004. Radiation dose to premature infants in neonatal intensive care units in Kuwait.*Radiation Protection Dosimetry*, 111(3), p.275-281.
16. Malekzadeh, M. et al., 2009. First report of radiation dose to pediatric patients arising from diagnostic chest and abdomen examination.*IFMBE Proceedings*, 25(3), p.93-95.
17. Duggan, L. et al., 1999. Suitability of LiF:Mg,Cu,P and Al_2O_3:C for low dose measurements in medical imaging. *Radiation Protection Dosimetry*, 85(1-4), p.425-428).
18. Lowe, A. et al., 1999. Diagnostic image quality of mobile neonatal chest x-rays and the radiation exposure incurred*. The British Journal of Radiology*, 72, p.55-61.
19. Roebuck, D.J., 1999. Risk and benefit in paediatric radiology. *Pediatric Radiology*, 29, p.637-640.
20. Le Heron, J.C., 1997. *Child dose: a user guide*. National Radiation Laboratory. In A. Brindhaban, ed. Estimation of radiation dose during diagnostic x-ray examinations of newborn babies and 1-year-old infants. *Medical Principles and Practice*, 2006, 15, p.260-265.
21. Wraith, C.M. et al., 1995. An investigation into techniques for reducing doses from neonatal radiographic examinations.*The British Journal of Radiology*, 68, p.1074-1082.
22. Barcham, N., Egan, I. & Dowd, S.B., 1997. Gonadal protection methods in neonatal chest radiography.*Radiologic Technology*, 69(2), p.157-161.

23. Wilson-Costello, D.W., Rao, P.S., Morrison, S. & Hack, M., 1996. Radiation exposure from diagnostic radiographs in extremely low birth weight infants. *Pediatrics*, 97(3), p.369-374.

24. Egan, I. & Dowd, S.B., 1997. Gonadal protection methods in neonatal radiography.*Radiologic Technology*, [online]. Nov-Dec. Available at: http://entrepreneur.com/tradejournals/article/20176493_2.html [accessed 10 August 2009]

25. Loovere, L. et al., 2008. Quality improvement in radiography in a neonatal intensive care unit.*Canadian Association of Radiologists Journal*, 59(4), p.197-202.

26. Duggan, L. et al., 2004. Variations in dose response with x-ray energy of LiF:Mg,Cu,Pthermoluminescence dosimeters: implications for clinical dosimetry. *Physics in Medicine and Biology*, 49, p.3831-3845.

27. Edwards, C.R. et al., 2005. The low energy x-ray response of the LiF:Mg,Cu,Pthermoluminescentdosemeter: a comparison with LiF:Mg,Ti. *The British Journal of Radiology*, 78, p.543-547.

28. Duggan, L., Warren-Forward, H., Smith, T. &Kron, T., 2003. Investigation of dose reduction in neonatal radiography using specially designed phantoms and LiF:Mg,Cu,P TLDs. *The British Journal of Radiology*, 76, p.232-237.

29. Akahane, K. et al., 2000. Development of neonate phantom for estimating medical exposure. IRPA 10, [online]. Available at: http://www.irpa.net/irpa10/cdrom/00582.pdf [accessed 19 December 2011]

30. Olgar, T., et al., 2008. Radiation exposure to premature infants in a neonatal intensive care unit in Turkey.*Korean Journal of Radiology*, 9(5), p.416-419.

31. Armpilia, C.I., Fife, I.A.J. &Croasdale, P.L., 2002. Radiation dose quantities and risk in neonates in a special care baby unit. *The British Journal of Radiology*, 75, p.590-595.

32. Chapple, C.L., Faulkner, K. & Hunter, E.W., 1994. Energy imparted to neonates during x-ray examinations in a special care baby unit. *The British Journal of Radiology*, 67, p.366-370.

33. Mak, B., 2001. Attenuation. [online]. Available at:http://bennymak.com/Attenuation.htm [accessed 11 October 2011]

34. Berger, M.J., et al. XCOM: Photon cross section database. 1998. NIST, [online]. Available at: http://www.nist.gov/pml/data/xcom/index.cfm [accessed 23 January 2012]

35. Turgut, U., Simsek, O. &Büyükkasap, E., 2007. Measurement of mass attenuation coefficients in some Cr, Co and Fe compounds around the absorption edge and the validity of the mixture rule. *Pramana Journal of Physics*, 69(2), p.199-207.

36. Tucker, D.M. &Chakraborty, D.P., 1991. Semiemperical model for generating tungsten target x-ray spectra.*Medical Physics*, 18(2), p.211-217.

37. de Kock, E.A.,2010. Spectra_Weighted_Att program. [Author of calculation program and program prologue] (Personal communication, 15 October 2010)

38. Hubbell, J.H. & Seltzer, S.M., 1995. Tables of x-ray mass attenuation coefficients and mass energy-absorption coefficients 1 keV to 20 MeV for elements Z=1 to 92 and 48 additional substances of dosimetric interest. NIST, [online]. Available at: http://www.nist.gov/physlab/data/xraycoef/index.cfm [accessed 30 September 2010]

39. Constantinou, C., 1982. Phantom materials for radiation dosimetry: Liquids and gels. *The British Journal of Radiology*, 55, p.217-224.

40. Hubbell, J.H., 1982. Photon mass attenuation and energy-absorption coefficients from 1 keV to 20 MeV.*The International Journal of Applied radiation and Isotopes*, 33, p.1269-1290.

41. White, D.R., et al., 1986. Foamed epoxy resin-based lung substitutes. *The British Journal of Radiology*, 59, p.787-790.

42. Jones, A.K., Hintenlang, D.E., Bolch, W.E., 2003. Tissue-equivalent materials for construction of tomographic dosimetry phantoms in pediatricradiology.*Medical Physics*, 30(8), p.2072-2081.

43. Vergara, J.C.S., et al., 1999. Dose measurements in a phantom simulating neonates by using different TL materials: LiF:Mg,Cu,P and LiF:Mg,Ti. *Radiation Protection Dosimetry*, 85(1-4), p.345-348.

44. Seifert, H., et al., 1998. Dose reduction in thorax radiography in simulated neonates with additional filtration and digital luminescence radiography.*ActaRadiologica*, 39(5), p.514-519.

45. Neonatal chest phantom Gammex 610. Gammex RMI©, [online]. Available at:

http://www.gammex.com/nportfolio/productpage.asp?id=317&category=Diagnostic+Radiology&name=Neonatal+Chest+Phantom%2C+Gammex+610 [accessed 17 June 2010]

46. International Commission on Radiation Units and Measurements., 1989. *Tissue substitutes in radiation dosimetry and measurement,* (ICRU Report 44), USA:ICRU.
47. Gammex RMI©.*Specifications Gammex 457, 450, 452, 453, 454, 455, 456*. [Email] (Personal communication with local Gammex representative, Mr G Corazza from CM Nuclear Systems c.c., 8 December 2010)
48. Milne, G.W.A., 2005. Gardner's commercially important chemicals:synonyms, trade names and properties. [e-book]. Canada:John Wiley & Sons. Available at http://books.google.co.za/books?id=qzFpFxBtYeUC&pg=PA664&lpg=PA664&dq=Gardner%E2%80%99s+commercially+important+chemicals+c12h18o9&source=bl&ots=sAPkdFzJ0I&sig=Qk2Ny86vgwRuV1b5JZ3yyMcdmOw&hl=en&sa=X&ei=fBMhUPDiGcHBhAeFkoGgCw&ved=0CDgQ6AEwAg#v=onepage&q=Gardner%E2%80%99s%20commercially%20important%20chemicals%20c12h18o9&f=false [accessed 20 March 2012]
49. Goodfellow Catalogue., 2012. Polyamide/imide sheet and Polyethylene – High density, [online]. Available at: http://www.goodfellow.com/catalogue/GFCat4I.php?ewd_token=0Y9CN4JVgdK5y9KGVVhgouqGzH18H5&n=jxvmp1eovwkOSDjYtCKcq9lU46UMPK&ewd_urlNo=GFCat411&Catite=AM313050&CatSearNum=1 and http://www.goodfellowusa.com/A/Polyethylene-High-density.html [accessed 22 March 2012]
50. Atkins, B., 2007. Modulation transfer function – what is it and why does it matter, [online]. Available at: http://photo.net/learn/optics/mtf [accessed 7 July 2011]
51. Klingenberg, L., 2005. *Frequency domain using Excel*, [online]. Available at: http://online.sfsu.edu/~larryk/Common%20Files/Excel.FFT.pdf [accessed 5 September 2012]
52. Hart, D., Jones, D.G. & Wall, B.F., 1994.*Estimation of effective dose in diagnostic radiology from entrance surface dose and dose-area product measurements*, (NRPB-R262), UK:NRPB.
53. Shimadzu product data. *Radiographic mobile x-ray system – Mobile Art Evolution*, [online]. Available at:

http://www.alphaimaging.com/files/document%20library/shimadzu/shimadzu%20brochures/mobileart%20evolution%20product%20data%20-%20pd504-005b.pdf [accessed 5 September 2012]

54. Hertrich, P., 2005. Practical radiography. [e-book]. p.49-50. Erlangen: Publicis Corporate Publishing. Available at: http://books.google.co.za/books?id=GSd0IqSt3bsC&printsec=frontcover&source=gbs_ge_summary_r&cad=0#v=onepage&q&f=false [accessed 5 September 2012]

55. STUK – Radiation and nuclear safety authority, 2012. *PCXMC - A PC-based Monte Carlo program for calculating patient doses in medical x-ray examinations*, [online]. Available at: http://www.stuk.fi/sateilyn_kaytto/ohjelmat/PCXMC/en_GB/pcxmc/ [accessed 1 August 2012]

Appendices

Appendix A: Ethical committee approval letter

UNIVERSITEIT·STELLENBOSCH·UNIVERSITY
jou kennisvennoot · your knowledge partner

03 March 2011 **MAILED**

Miss A Korf
PO Box 3301
Paarl
7620

Dear Miss Korf

Organ size measurements from a neonatal cadaver Computer Tomography (CT) scan for phantom construction.

ETHICS REFERENCE NO: N10/12/400

RE : APPROVAL

A panel of the Health Research Ethics Committee reviewed this project on 8 February 2010; the above project was approved on condition that further information is submitted.

This information was supplied and the project was finally approved on 2 March 2011 for a period of one year from this date. This project is therefore now registered and you can proceed with the work.

Please quote the above-mentioned project number in ALL future correspondence.

Please note that a progress report (obtainable on the website of our Division: www.sun.ac.za/rds should be submitted to the Committee before the year has expired. The Committee will then consider the continuation of the project for a further year (if necessary). Annually a number of projects may be selected randomly and subjected to an external audit.
Translations of the consent document in the languages applicable to the study participants should be submitted.

Federal Wide Assurance Number: 00001372
Institutional Review Board (IRB) Number: IRB0005239
The Health Research Ethics Committee complies with the SA National Health Act No.61 2003 as it pertains to health research and the United States Code of Federal Regulations Title 45 Part 46. This committee abides by the ethical norms and principles for research, established by the Declaration of Helsinki, the South African Medical Research Council Guidelines as well as the Guidelines for Ethical Research: Principles Structures and Processes 2004 (Department of Health).

Please note that for research at a primary or secondary healthcare facility permission must still be obtained from the relevant authorities (Western Cape Department of Health and/or City Health) to conduct the research as stated in the protocol. Contact persons are Ms Claudette Abrahams at Western Cape Department of Health (healthres@pgwc.gov.za Tel: +27 21 483 9907) and Dr Helene Visser at City Health (Helena.Visser@capetown.gov.za Tel: +27 21 400 3981). Research that will be conducted at any tertiary academic institution requires approval from the relevant hospital manager. Ethics approval is required BEFORE approval can be obtained from these health authorities.

Approval Date: 2 March 2011 Expiry Date: 2 March 2012

Fakulteit Gesondheidswetenskappe - Faculty of Health Sciences

Verbind tot Optimale Gesondheid · Committed to Optimal Health
Afdeling Navorsingsontwikkeling en -steun · Division of Research Development and Support
Posbus/PO Box 19063 · Tygerberg 7505 · Suid-Afrika/South Africa
Tel: +27 21 938 9075 · Faks/Fax: +27 21 931 3352

UNIVERSITEIT·STELLENBOSCH·UNIVERSITY
jou kennisvennoot · your knowledge partner

Yours faithfully

MS CARLI SAGER
RESEARCH DEVELOPMENT AND SUPPORT
Tel: +27 21 938 9140 / E-mail: carlis@sun.ac.za
Fax: +27 21 931 3352

Fakulteit Gesondheidswetenskappe - Faculty of Health Sciences

Appendix B: Calculation of Agar gel mix mass fraction by weight

Atomic weights:

C 12.011

H 1.0079

O 15.999

Molecular weights:

$Molecular\ weight = Atomic\ weight \times Number\ of\ atoms\ in\ molecule$

Agar 306.2652 g/mol

Sucrose 342.2948 g/mol

Water 18.0148 g/mol

Mole:

$$Mole = \frac{Weight}{Molecular\ weight}$$

Agar (4 g) 1.306×10^{-2}mol

Sucrose (10 g) 2.921×10^{-2}mol

Water (86 g) 4.774 mol

Molecules:

$Molecules = Mole \times N_A$ where N_A is Avogadro's constant, i.e. 6.0221415×10^{23}.

Agar 7.865×10^{21}

Sucrose 1.759×10^{22}

Water 2.875×10^{24}

Atoms:

$Atoms = Molecules \times Number\ of\ atoms\ in\ molecule$

Agar – C 9.438×10^{22}

Agar – H 1.416×10^{23}

Agar – O 7.079×10^{22}

Sucrose – C 2.111×10^{23}

Sucrose – H 3.870×10^{23}

Sucrose – O	1.935×10^{23}
Water – H	5.750×10^{24}
Water – O	2.875×10^{24}

Total number of atoms in mixture:

$$Atoms\ in\ mixture = Atoms_{Agar} + Atoms_{Sucrose} + Atoms_{Water}$$

C	3.055×10^{23}
H	6.279×10^{24}
O	3.139×10^{24}

Total weight of element in mixture:

$$Total\ elemental\ weight = Atomic\ weight \times Atoms\ in\ mixture$$

C	3.669×10^{24}
H	6.329×10^{24}
O	5.022×10^{25}
Total weight of mixture	6.022×10^{25}

Mass fraction of element in mixture:

$$Mass\ fraction = \frac{Elemental\ weight}{Total\ mixture\ weight}$$

C	0.06093
H	0.1051
O	0.8339

These values are included in Table 4.2 for further calculations.

Appendix C: Final exposure set images of the neonatal chest simulation phantom for visual image quality assessment

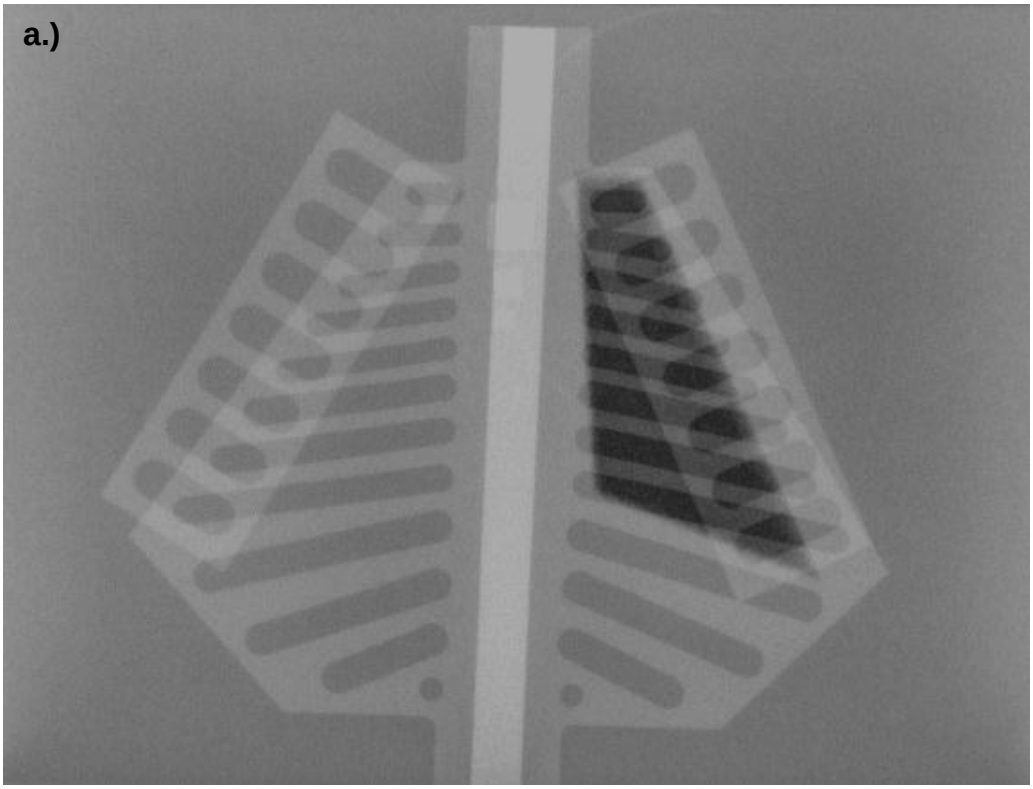

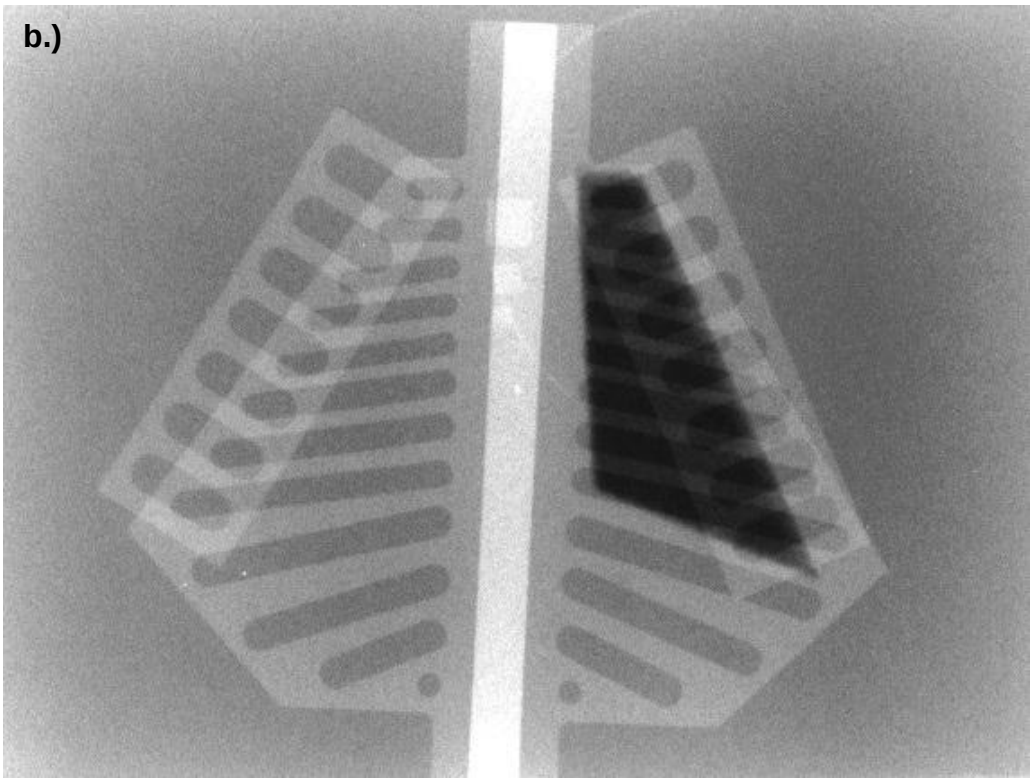

c.)

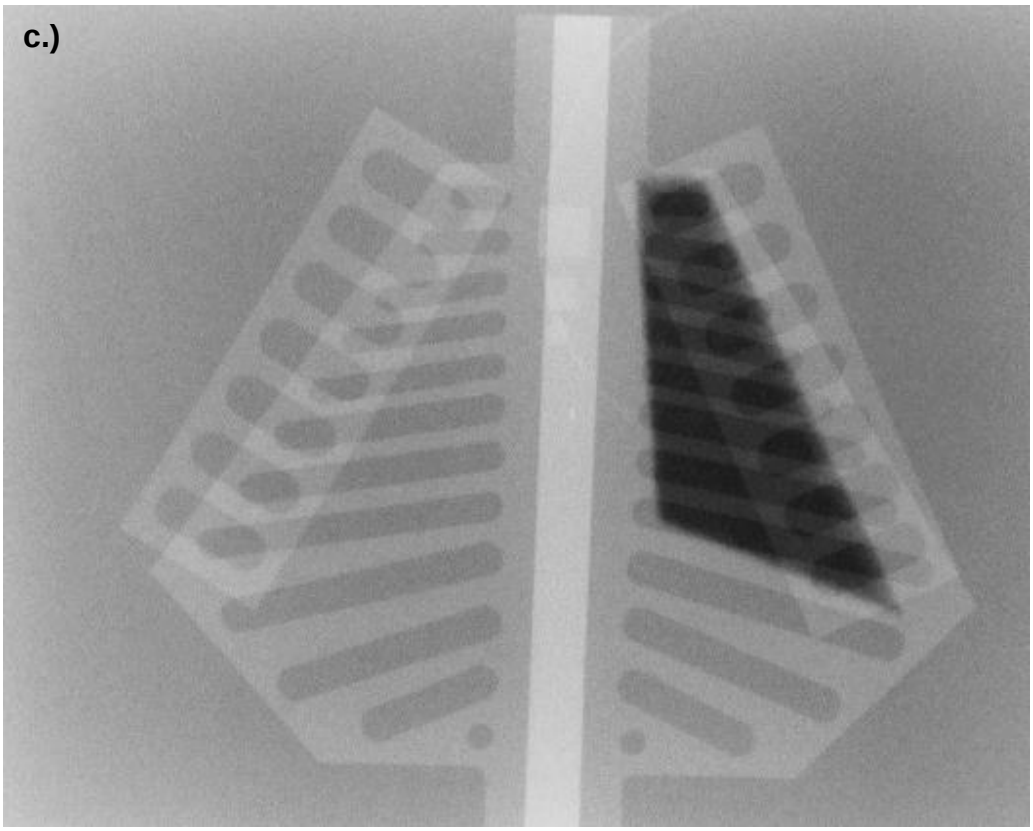

d.)

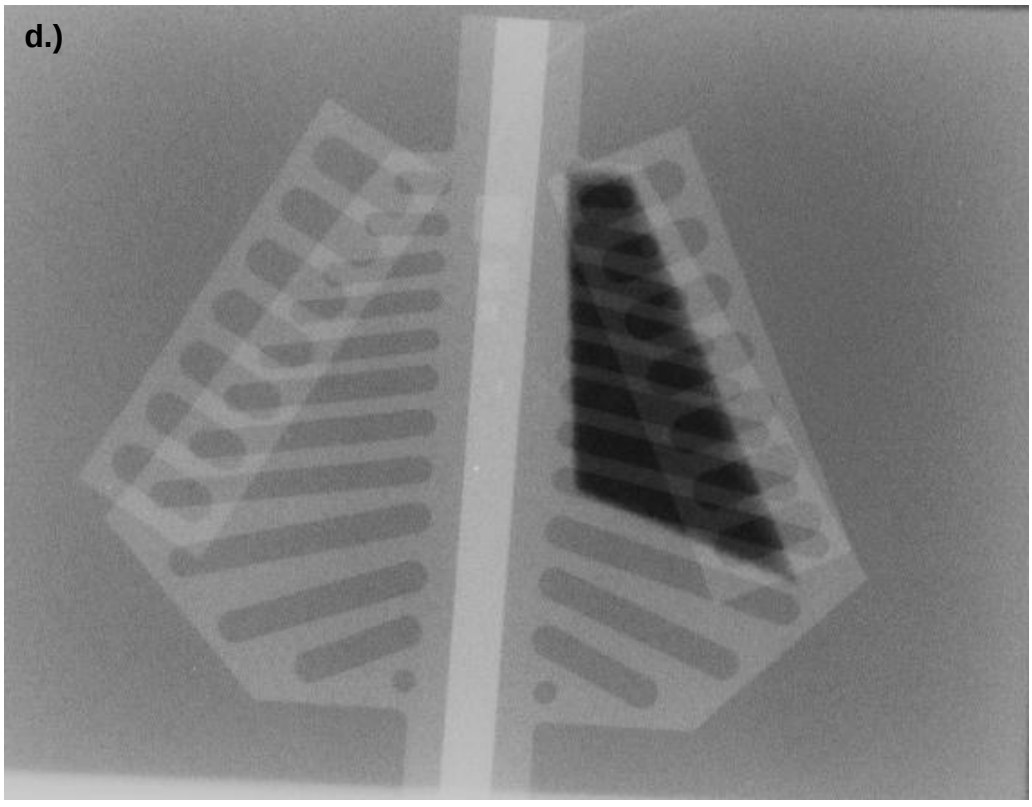

e.)

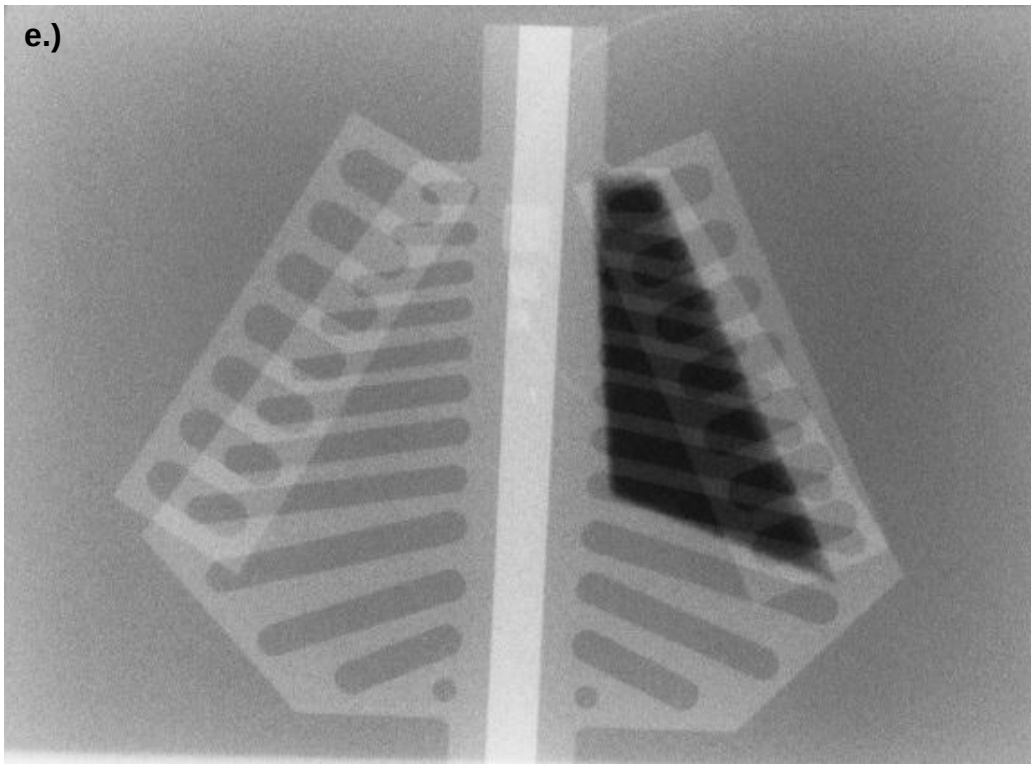

f.)

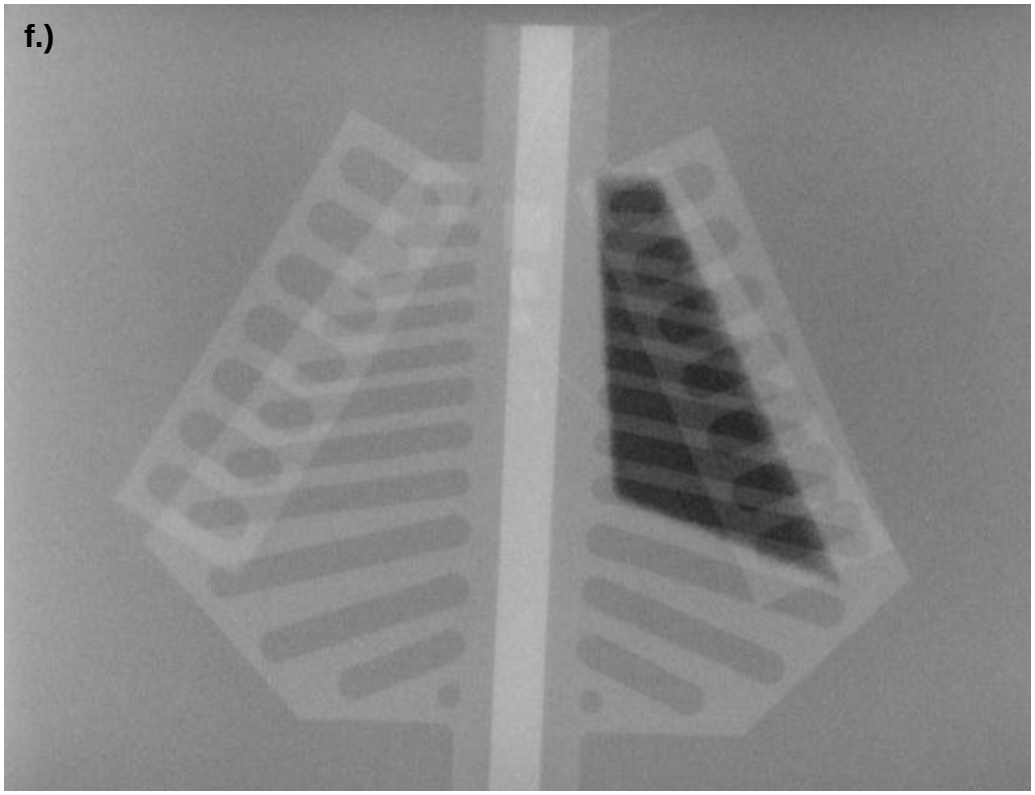

g.)

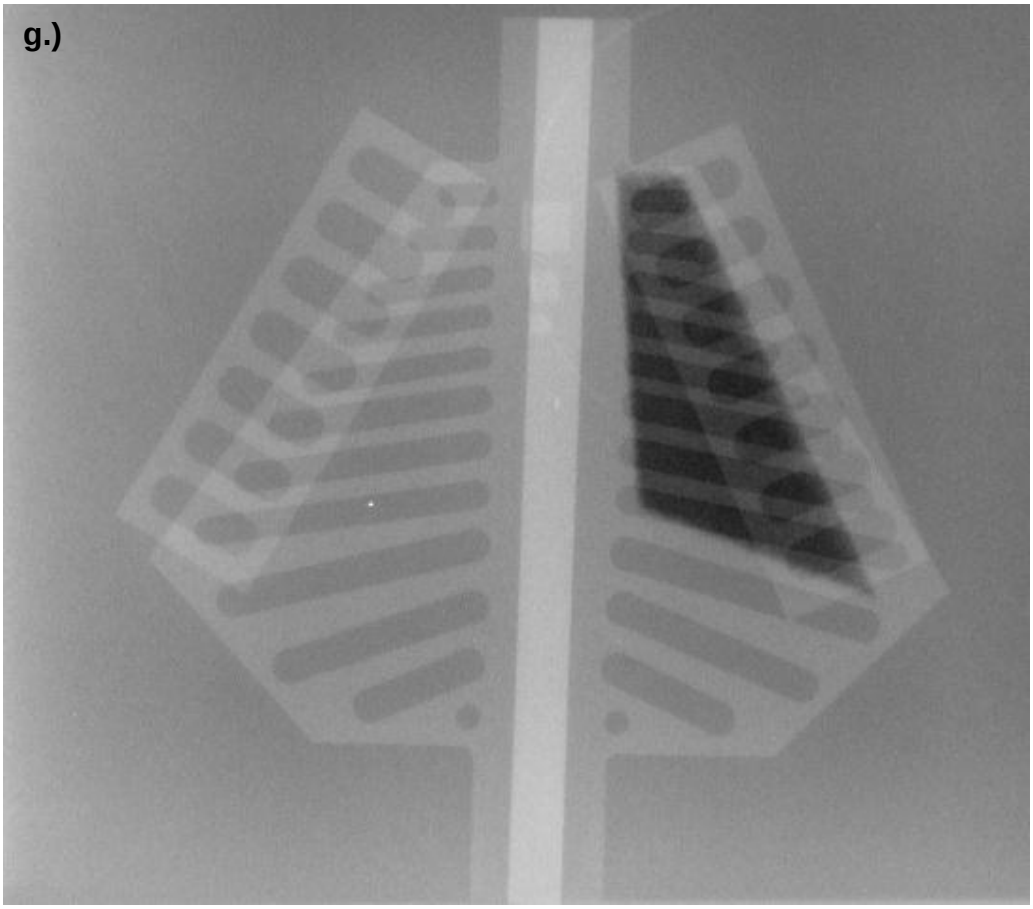

h.)

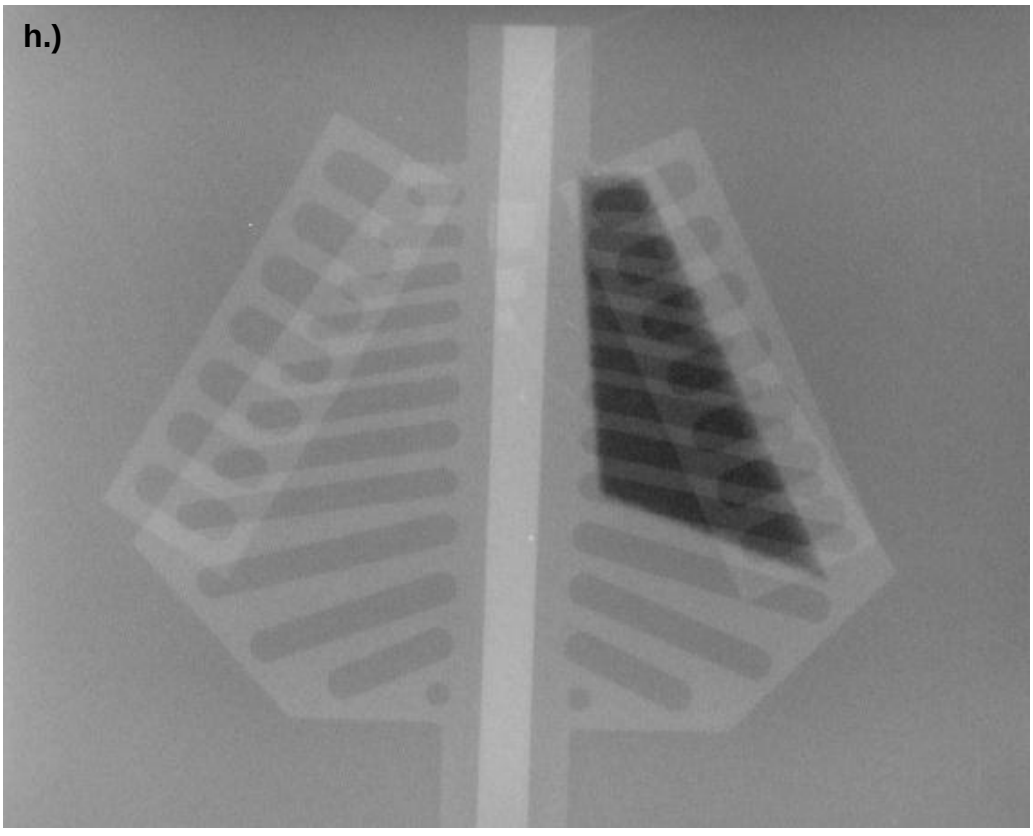

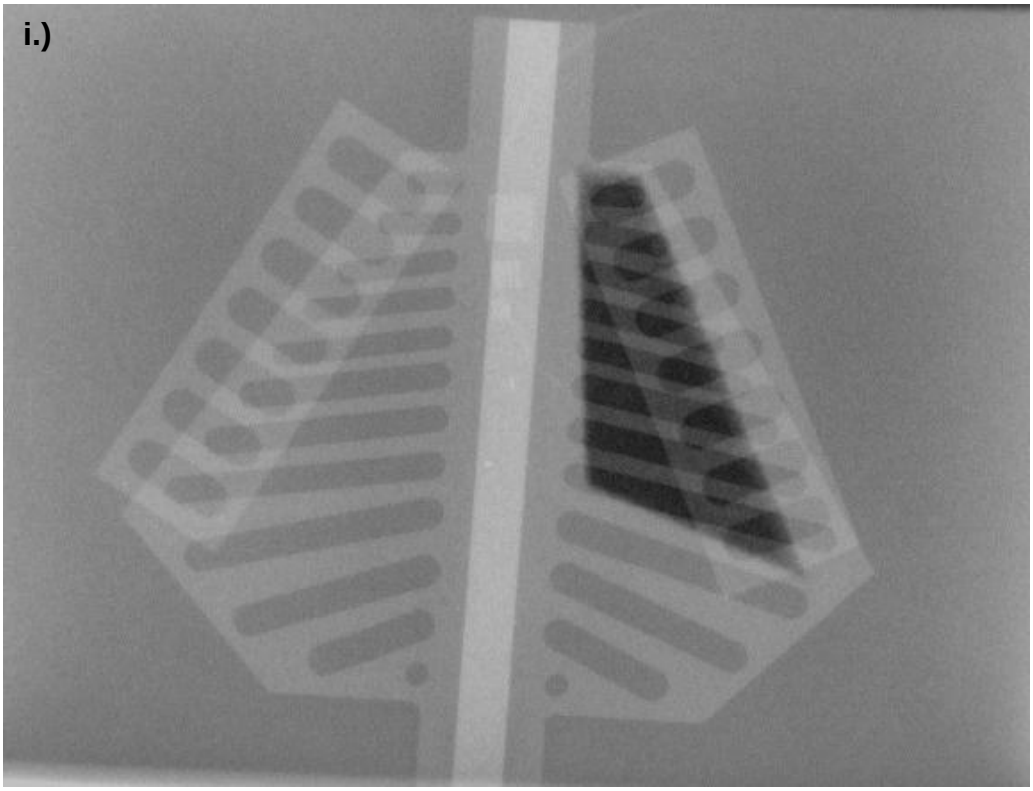

Figure 5.10: a.) Image 1, 50 kV, 2 mAs, inherent filtration, processed. b.) Image 2, 60 kV, 2 mAs, 0.1 mm Cu + 1 mm Al filtration, raw. c.) Image 3, 64 kV, 2 mAs, 0.1 mm Cu + 1 mm Al filtration, raw. d.) Image 4, 61 kV, 0.8 mAs, inherent filtration, raw. e.) Image 5, 62 kV, 0.8 mAs, inherent filtration, raw. f.) Image 6, 57 kV, 2 mAs, 0.1 mm Cu + 1 mm Al filtration, processed. g.) Image 7, 57 kV, 3.2 mAs, 0.1 mm Cu + 1 mm Al filtration, processed. h.) Image 8, 60 kV, 2 mAs, 0.1 mm Cu + 1 mm Al filtration, processed. i.) Image 9, 61 kV, 0.8 mAs, inherent filtration, processed.